Synthesis and Applications of Nanostructured Metal Oxide Films

By

Brnyia Omar Salem Alwhshe

A Thesis Submitted for the Degree of Doctor of Philosophy

School of Life Sciences

University of Sussex

April 2016

Acknowledgments

First of all, I would like to express my sincere gratitude and obligation to my main supervisor, Dr. Qiao Chen, for the patient guidance, encouragement and advice he has provided throughout my time as his student. I have been extremely lucky to have a supervisor who has cared so much about my work. I also would like to thank my second supervisor, Dr Mark Osborne for his advice, help and support.

I would also like to extend my appreciation to Edward Hill and Declan Rowlands, former Mchem students, who assisted me in some of my experimental work with immense enthusiasm and proficiency. I would like to thank all my amazing nanogroup members for their interest and some fruitful discussions about the project including, Zainab Al-Abdullah, Ali Shahroozi, Thomas Draper, Giacomo Canciani, Wei Cheat Lee and Yuanxing Fang. Many thanks to all of them for helping me with any technical difficulties and with using various computer software.

I must also acknowledge some members of staff at the University of Sussex, who have provided me with invaluable help including, Julian Thorpe for his assistance in SEM imaging and permission to use the Gold sputtering coater, Mr Michael Henry and Miss Frances Chick for providing me with chemicals and glassware every time I needed them.

I like to dedicate my most special thanks to my family for the support they provided me through my entire life and in particular, I must acknowledge my husband and lovely son for their moral support and precious love, who were always standing by me in my hard times during this work. Thanks for all of my family and husband's family for their great support.

In conclusion, I recognize that this research would not have been possible without the financial assistance from the ministry of higher education and scientific research in

Libya and the Libyan Embassy in London, giving me this great opportunity and sponsoring my PhD study.

To

My beloved country

Libya

University of Sussex

Brnyia Omar Salem Alwhshe

PhD

Synthesis and Applications of Metal Oxide Nanostructure Films

Summary

This research project focuses on the creation and optimisation of the nanomaterial films for enhancing their medical and photocatalytic applications. Developing controlled drug delivery systems has been gaining increasing interest. Processing of metal oxides into porous nanostructures has been considered as a promising strategy. In this work, the morphology of TiO_2 nanotubes was modified and tubes with a bottle shape were designed and used for controlled drug delivery. It was found that, the drug loading and release kinetics can be controlled by adjusting the nanotubes and nanobottles morphology.

Moreover, there is increasing interest of using metal oxides as photocatalyst for capturing solar energy and converting it to chemical energy in the form of hydrogen. However, the current photoconversion efficiency over nanostructured metal oxides is limited by a number of factors such as low surface area, limited light absorption, poor conductivity, poor electron mobility and high rate of electron-hole recombination. In this project, a number of strategies have been developed to overcome these difficulties.

Firstly, optimizing the film morphology, density and thickness helps to increase the photoconversion efficiency. 1-D nanorods with relatively low densities offer high surface area with a large number of reaction sites to be in contact with the electrolyte. In addition, the small film thickness allows light to illuminate through the whole nanorods layer. This offers good electron conductivity through the rods, reducing the rate of electron-hole recombination. TiO_2 nanorods (TNR) with optimised structures were prepared and the photoelectrochemical measurements revealed that a tilted TNR film at

the density of 14 μm^{-2} and the thickness of 2.2 μm exhibited optimal photocatalytic performance.

Secondly, the surface treatment over TNRs, through a reduction in hydrogen and re-oxidation in air, was demonstrated in order to improve electron mobility and inhibit the electron-hole recombination. The measurements revealed that a sequence of reduction and re-oxidation helps to achieve an enhancement in the photoelectrochemical water splitting efficiency.

Thirdly, copper doped TiO_2 nanorods were synthesized through one step hydrothermal synthesis for enhancing their photoelectrochemical (PEC) water splitting performance. The performance of the Cu doped TNRs was improved by at least a factor of 3 due to the improved light absorption, charge separation and transportation and appropriate nanorods morphology.

Finally, a three dimensional photoanode was designed and fabricated for a PEC device in order to enhance the photocatalytic performance. Clear conductive glass rods decorated with a zinc oxide thin film were attached to a copper disc, forming a three dimensional photoanode. It was observed that, high photocurrent can be achieved by using this 3-D photoanode configuration. The efficiency of this electrode can be further enhanced by improving the conductivity of the ITO film and the light leakage from the side of the glass rods (with increased roughness of the glass surface). In addition, by adding organic compounds to the PEC system, the photocurrent density could also be further enhanced.

Further effort was involved in the developing of perovskite copper titanate. Cubic shaped $CuTiO_3$ crystals were successfully synthesised with molten salt synthesis. The reaction conditions have been investigated in order to achieve high purity $CuTiO_3$.

In summary, different strategies and nanomaterials have been developed and demonstrated in this thesis for specific applications.

Table of Contents

List of Abbreviations

(A)	Absorbance
Am	Air mass
α	Absorption coefficient
(θ)	Angle (°)
Eg	Band gap energy
CB	Conduction band
CBD	Chemical bath deposition
CBM	Conduction band minimum
CVD	Chemical vapour deposition
D_{hkl}	Crystal size (nm) perpendicularly to the hkl crystal plane
Csc	Capacitance of the space charge region
CTO	Copper titanate
D	Crystal domain size
ε	Dielectric constant
N_D	Donor density
D	Diameter (nm)
DI	Deionised
β_{hkl}	Diffraction peak width
DSSCs	Dye sensitised solar cells
EES	Electrochemical energy storage devices
(e^-)	Electron
eV	Electron volte [1.602×10^{-19} joules]
EDTA	Ethylenediaminetetraacetic acid
EDX	Energy dispersive x-ray diffraction

EG	Ethylene glycol
EIS	Electrochemical impedance spectroscopy
FTO	Fluorine doped tin oxide
E_F	Fermi level
V_{FB}	Flat band potential
FWHM	Full width of half maximum
f_g	Growth factor
HOMOs	Highest occupied molecular orbitals
P^H	Hydrogen concentration
(h^+)	Hole
HMT	Hexmethylene tetramine
IR	Infrared light (> 700nm of electromagnetic radiation)
ID	Inner diameter
IPA	Isopropyl alcohol
ITO	Indium doped tin oxide
IPCE	Incident photon to current efficiency
JCPDS	Joint Committee on Powder Diffraction Standards
KHz	kilohertz
LIBs	Lithium ions batteries
LUMOs	Lowest unoccupied molecular orbitals
L	Length (µm)
L_N	Length of tube neck
L_B	Length of tube base
(I)	Light intensity
(µm)	Micrometre

R_{max}	Maximum reflectance
R_{min}	Minimum reflectance
MB	Methylene blue
MP	Melting point
MSS	Molten salt synthesis
M-S	Mott-Schottky
NPs	Nanoparticles
NWs	Nanowires
NFs	Nanofibers
NRs	Nanorods
NTs	Nanotubes
NBs	Nanobottles
(nm)	Nanometre
NHE	Normal hydrogen electrode
1-D	One dimension
OD	Outer diameter
ODPA	Octadecylphosphonic acid
Ω	Ohm
(h)	Planck constant [6.62×10^{-34}J/s]
PEC	Photoelectrochemical system
PV	Photovoltaic
PL	Photoluminescence
η or PE	Photoconversion efficiency
PVA	Polyvinyl alcohol
D	Particle size

I-V	Photocurrent density vs applied voltage
QDs	Quantum dots
$E_{F(redox)}$	Redox potential of electrolyte solution
K (h^{-1})	Release kinetic constant
SAVR	Surface area to volume ratio
(c)	Speed of light through a vacuum [3×10^{8}m/s]
SCs	Super capacitors
SEM	Scanning electron microscopy
STH	Solar to hydrogen conversion efficiency
TEM	Transmission electron microscopy
TNRs	Titanium dioxide nanorods
TNTs	Titanium dioxide nanotubes
TNBs	Titanium dioxide bottles
2-D	Two dimensions
3-D	Three dimensions
(%T)	Transmission
TBO	Titanium butoxide
TSD	Titanium dioxide surface defects
TTFT	Transparent thin film transistor
TCO	Transparent conductive oxides
TSDs	Titanium surface defects
UV	Ultraviolet light [100-400 nm of electromagnetic radiation]
Vis	Visible light [400-700 nm of electromagnetic radiation]
V	Voltage
VB	Valence band

VBM	Valence band maximum
W	Wall thickness
(λ)	Wave length (nm)
(wt%)	Wight percent
XRD	X-ray diffraction
0-D	Zero-dimensional

List of Figures

List of Tables

Chapter 1 Introduction to metal oxide nanomaterials

Metal oxides play important roles in many areas of chemistry, physics and materials science [1, 2]. By employing various synthetic techniques, elemental metals can form a variety of oxide compounds with controllable nanomorphologies and crystal structures. They can be either a conductor [3], a semiconductor [4], or an insulator [5], depending on their electronic structures, which will be discussed in the next section. Transition metal oxides have been intensively investigated for their complex phases and structures, metal-insulator transitions and magnetic ordering transitions [6]. These properties make metal oxides the ideal materials for a wide range of applications, including electronic components [7], sensors [8], piezoelectric devices [9], corrosion protection coatings [10], as well as catalysts in the chemical industries [11, 12].

One of the key applications of metal oxides as photocatalysts is in the field of energy production from renewable resources. Renewable energy industry focuses on harvesting natural energy sources, such as solar energy, and to convert them either to chemical energy or electricity for later consumption. There is an increasing interest in renewable energy systems for several reasons such as the fact that all the renewable energy systems are constantly replenished, unlike the fossil fuels that are likely to run out in years to come. The other reason is related to the positive environmental impact. Using renewable energy sources plays a key role in decreasing the total amount of pollution gas emissions. These gases, such as carbon dioxide (CO_2) and sulphur dioxide (SO_2), are generated mainly from the combustion of fossil fuels and therefore directly harvesting solar energy would help to prevent negative impacts in climate change.

For harvesting the solar energy, there are two major categories of technologies: photovoltaic (PV) cells and photoelectrochemical (PEC) hydrogen generation. Both

systems depend on semiconductor materials to be photosensitive and/or choice of electrolytes. PV cells could consist of either a solid state solar cell with a junction between p- and n-type semiconductors that does not require an electrolyte, or at least one semiconducting material in contact with liquid electrolyte. The metal oxide semiconductor can also be sensitised by organic dyes or quantum dots, in order to expand the spectrum of the light absorption with photogenerated charges injected into the semiconductor, producing a voltage. This system is known as a dye sensitised solar cell (DSSC)[13-18]. The photoconversion efficiency of this system can be increased by engineering a nanostructured electrode, which increases dye loading [19-22] and improves the electron transport properties [23].

Alternatively, solar energy can be harvested through photoelectrochemical water hydrolysis on a semiconductor surface to produce hydrogen in a water splitting process[24-27]. The photocatalytic performance of the semiconductor in this system can be enhanced by modifying its electronic structure and morphology [28]. Variety metal oxide semiconductors have been investigated as efficient photocatalyst for water splitting into H_2 and O_2, including TiO_2, ZnO and WO3, which act as photocatalyst for the oxidation of water by photogenerated holes.

Metal oxides are also widely utilized in electrochemical energy storage (EES) devices, such as batteries [29, 30] and supercapacitors (SCs) [31, 32]. Lithium ion batteries (LIBs) are currently the most efficient batteries. It has the advantages of a high working voltage, high capacity and long cycling life [29]. Supercapacitors also have an important role in complementing batteries in the field of energy storage due to their unique properties of high power density, long cycling life and fast recharge capability. Both systems consist of a positive electrode, negative electrode, separator and electrolyte. The performance of such EES system is determined by the morphology and electronic

structure of electrode materials and the properties of electrolyte. Among various electrode materials, transition metal oxides, such as RuO_2, MnO_2, Fe_2O_3, TiO_2, CoO and SnO_2, have been found to be important classes of semiconductors in the EES system, due to their unique electrochemical reactivity [33]. Transition metal oxides, especially in the form of nanostructures, have potential to be used as electrode materials for LIBs and SCs devices. The ease of large scale fabrication, where the size, morphology and orientation can be easily tuned, in addition to their rich redox reactions involving different ions, contributes to their high specific capacitance and facilitates the systematic investigation of structure-electrochemical property relationship. For instance, CoO, have capability of storing lithium by the conversion mechanism, which differs from the classical lithium insertion/de-insertion and involves the formation and decomposition of Li_2O associating with the reduction and oxidation of the metal oxide. Since most of metal oxides crystallize in a rock-salt structure that does not contain empty sites for hosting Li ion, therefore, the reversible electrochemical reaction mechanism of Li ion with these materials such as CoO follows the reversible formation and decomposition of Li_2O as shown in Equations 1.1 and 1.2:

$$\mathrm{CoO} + 2\mathrm{Li} + 2\mathrm{e}^- \rightleftharpoons \mathrm{Li_2O} + \mathrm{C} \qquad \text{(Equation 1.1)}$$

$$2Li \leftrightarrow 2Li^+ + 2e^- \qquad \text{(Equation 1.2)}$$

Therefore, the overall reaction can be written as following:

$$\mathrm{CoO} + 2\mathrm{Li} \leftrightarrow \mathrm{li_2O} + \mathrm{Co} \qquad \text{(Equation1.3)}$$

In addition, some metal oxides such as iron and manganese oxides are abundant in nature and therefore are low cost.

Metal oxides have also shown potential applications in biological and medical sciences such as drug delivery for cancer treatment and fluorescent imaging[34-36]. For instance, TiO_2 has been commonly used in biomedical components and devices. It is widely used for the fabrication of hard tissue replacement such as dental implants, bone plates and hip joints. In addition, TiO_2 films on the surface of titanium show good blood compatibility. The bioactivity of TiO_2 is due to the existence of surface hydroxyl (Ti-OH) group and the induced negative charge, which draws calcium and phosphorus ions from the body fluid to the surface of the implant.

1.1 Fundamentals of metal oxide

The performance of metal oxide devices rely on the electronic properties and morphologies of the solid state materials. The electronic structure of metal oxide can be described by the formation of molecular orbitals. In solids, molecular orbitals are modelled by the linear combination of multiple periodically arranged atomic orbitals. When a large number of orbitals overlap they form essentially continuous bands with s, p and d orbital character. Such orbitals can therefore be considered as continuum of energy levels or an energy band.

The band edges are referred to as the highest and lowest energy levels within a band. The highest (energy) occupied molecular orbitals (HOMOs) form the valence band (VB) and the electrons in this band are responsible for covalent bonding. They can move from one atom to another if they can find a vacant position in the neighbour's orbital. On the other hand, the lowest unoccupied molecular orbitals (LUMOs) form the conduction band (CB), where electrons move freely and conduct in this band. Obtaining an extra

energy is required to excite the electrons, moving from their level to the higher levels. Moving to conduction band can only takes place in a band (from atom to atom at given level) if the band is partly empty. The free electrons can then move around in response to an applied electric field (produced by an end-to-end voltage difference applied to the lump of material). The free movement of the electrons make the material conductive. There are no electron states between the top of the VB and the bottom of the CB. The energy difference between the upper edge of the valance band (valance band maximum, VBM) and the lower edge of the conduction band (conduction band minimum, CBM) is defined as the band gap energy (E_g). It corresponds to the minimum energy required to promote an electronic excitation from the valence band to the conduction band. Any additional energy will be used for vibration of excitation of the atoms at the electronic excitation states. The band gap structure, which involves the band gap and the positions of VBM and CBM, is the key properties of a photocatalyst. It regulates the light absorption property and the redox capability of the metal oxide.

The band gap influences the optical and electronic properties of solid state materials, according to Planck's equation (Equation 1.4).

$$E_g = hc/\lambda \qquad \text{(Equation 1.4)}$$

Where h and c are Planck's constant and speed of light through vacuum respectively. E_g is the band gap energy forming the optical transition, while λ is the wavelength of the photons absorbed by the solid. The electronic excitation from the valence band to the conduction band can be driven through the absorbance of a photon with energy equal or greater than the band gap energy E_g of the material. The electron excitation to conduction band will leave a positive charge in the valence band called hole. The holes are considered

as electric charge carriers, equal in magnitude but opposite in polarity to the charge on the electrons. Holes and electrons are the two types of charge carrier responsible for electrical current in material.

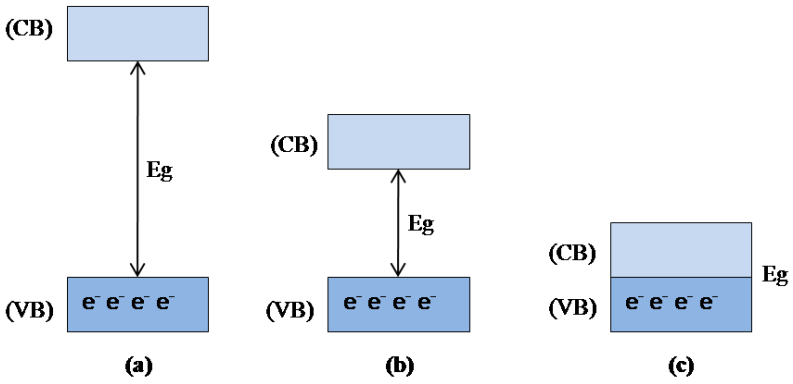

Figure 1.1 The electronic structure of solid materials. (a) insulator, (b) semiconductor and (c) conductor.

The band gap also plays an important role in determining the electronic properties of the solid material, as shown in Fig. 1.1. If the energy band gap is large (over 4 eV) and cannot be easily overcome, the material does not conduct electricity under normal conditions because the electronic transition could not be promoted at low temperatures with UV-Visible photons. These materials are defined as insulator. Al_2O_3 and SiO_2 are considered as insulating materials, since their band gaps are 8.8 and 8.9 eV, respectively [6]. Both have good dielectric properties, therefore they are widely used as inert, low expansion, dielectric filling material for epoxy resins in electronic circuits.

If the valence band overlaps with the conduction band or the valence band is not fully filled, the electrons can move freely without any barrier and the material is electrically conductive [37]. Rhenium oxide ReO_3 for instance is a typical conductive ionic crystal. It was reported that, the conductivity of ReO_3 is higher than the Re metal and is equivalent to that of silver. It is unstable at temperature above 300°C in a vacuum and decomposes into Re_2O_7 and ReO_2 [38].

Materials with intermediate band gaps in between those of conductors and insulators are defined as semiconductors. The valence band electrons can be excited to the conduction band by absorbing energy (voltage bias, heat or UV Vis irradiation) equal to or larger than the band gap energy. Semiconducting materials with band gaps less than 3 eV, such as CdSe (1.7 eV), GaAs (1.4 eV) and WO_3 (2.6 eV), are considered as narrow band gap semiconductors. A wide band gap semiconductor refers to a semiconductor material with band gap of at least 3 eV, such as TiO_2 (3.2 eV for anatase, 3.03 eV for rutile), ZnO (3.37 eV) and SiC (3 eV) [39].

The material's colour is determined by its band gap energy. If *Eg* is less than the lowest energy of visible light (*Eg*= 1.7 eV, red, λ= 700 nm), the material can absorb any wavelength of the light and appears in black or metallic colour. For instance, Si (*Eg*= 1.1 eV) has gray metallic colour and GaAs (*Eg*= 1.4 eV) has black colour. On the other hand, when the material has *Eg* more than the highest energy of visible light (*Eg*= 3 eV, violet, λ= 400 nm), no visible light is absorbed and the material is colourless/transparent, such as diamond (*Eg*= 5.4 eV). If *Eg* falls between the range of visible light, the material has a complementary colour to the absorbed wavelength. For instance, CdS (*Eg*= 2.5 eV) permits the absorption of violet and some blue, therefore it has yellow colour.

The electronic structure of TiO_2, for instance, as a wide band gap semiconductor, can be described by the formation of molecular orbitals that are formed with a large number of overlapped atomic orbitals. Continuous bands with s, p and d orbitals characters from Ti and O are formed. The valence band (VB) in anatase and rutile TiO_2 is dominated by O 2p and the conduction band (CB) is formed from the Ti 3d (TiO_2 orbital formation). This is because the O^{2-} has its atomic orbitals fully occupied, while the Ti^{4+} has an empty 3d orbital. An electronic transition could happen by promoting an electron

from the occupied O^{2-} 2p state (valence band) to the unoccupied Ti^{4+} 3d state (conduction band) by absorbing a photon with energy larger than the band gap.

The difference in the size of band gap between both materials, 3.0 eV for rutile and 3.2 eV for anatase, is due to their differences in lattice structure, which affects the periodic arrangement and subsequently the overlap of the atomic orbitals. This causes different densities and electronic band structures, leading to different band gaps. This difference affects the optical properties of both phases, where anatase absorbs light at 388 nm and rutile absorbs at 415 nm.

1.1.1 n- and p-type semiconductors

For a semiconductor, the promotion of electrons to the conduction band results in the formation of positively charged holes in the valence band. Both electrons and holes can move causing an increase in the conductivity. The properties of the semiconductor are determined by the charge carrier density near the top of the valence band and the bottom of the conduction band.

Non-doped semiconductors are known as intrinsic semiconductors. In a doping process, impurities are introduced as defects into the intrinsic semiconductor structure, in order to modify its optical and electronic properties [40]. The introduced impurities can be assigned into two categories: donors and acceptors. Donors are elements that donate electrons to the conduction band of the semiconductor, such as doping of a tetravalent semiconductor, Si, with a pentavalent donor element, P. Sufficient electrons are provided to form the usual four covalent bonds to its neighbours, leaving the fifth electron free. In this type of semiconductors, electrons are the majority charge carriers and are called n-type semiconductors. Acceptors are elements that accept electrons and create holes in the valence band of the semiconductor, such as doping a tetravalent semiconductor, Si, with

a trivalent element (acceptor), B. In such a case, there is one electron too few to complete the bonding to neighbouring atoms. This type of semiconductors with holes as the majority charge carriers are called p-type semiconductors.

The Fermi level of solid state materials can be affected by the doping. It is used to describe the thermodynamic equilibrium of charges, defined as the energy level at which the probability of occupation by an electron is exactly 1/2. As shown in Fig. 1.2(a), for intrinsic semiconductors, the Fermi level lies approximately in the mid-point of the band gap. Doping changes the electron distribution in the solid material, therefore the position of the Fermi level is altered too. For an n-type semiconductors, the Fermi level shifts up and lies below the conduction band edge, while for a p-type semiconductors, it lies just above the valence band edge [41].

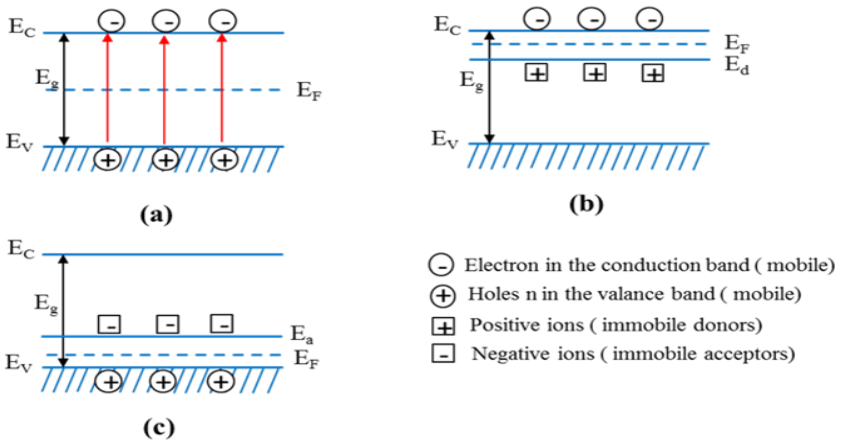

Figure 1.2 Semiconductor types: (a) intrinsic semiconductor. (b) n-type semiconductor. (c) p-type semiconductor. E_V: valance band, E_C: conduction band and E_F: Fermi level in semiconductor, Eg: band gap energy, E_d: donor state and E_a: acceptor state.

The addition of controlled amounts of certain impurities can significantly affect the charge carrier densities and the electronic properties of a semiconductor. Such modification is vital in the development of electronic devices based upon semiconductors. Lightly and moderately doped semiconductors are defined as extrinsic semiconductors,

while heavily doped semiconductor will increase the conductivity significantly and behave more like metal than a semiconductor. Transparent conductive oxides (TCO) such as aluminium doped zinc oxide (AZO) and fluorine doped indium oxide (FTO) are typical examples of heavily doped of semiconductors [42, 43]. High density semiconductor defects (vacancies, impurities, dislocations) are not desirable for photoexcitation. This is due to the fact that high density defects could act as charge trapping sites and hence can promote charger recombination.

The band gap energy can also be controlled by managing the size of the semiconductor crystals due to the quantum size effects. This effect occurs when the size of the semiconductor particles ranges from 2-20 nanometres (10-100 atoms) in diameter [44]. The decrease in the particle size to this scale leads to dramatic changes in the key properties of semiconductor. Firstly, by decreasing the size to quantum size (Q-size), the charge confinement leads to series of discrete electronic states. In the quantum dots structure, the charge carriers are confined in all three dimensions, forming zero-dimensional dots. In such cases the charge carriers behave like a particle in a box, showing discrete allowed energy states. The separation of these energy levels depends on the size of the dots. Subsequently, there will be an increase in the effective band gap and a shift in the band edges. The valance band levels are moderately shifted to lower energies, while the conduction band levels are strongly shifted to higher energies [44]. The increase in the band gap energy, *Eg*, depends on the radius of the particles, *R*, the reduced effective mass of the excitons, μ and the dielectric constant of semiconductor, ε as shown in equation 1.5:

$$E_g = \frac{h^2}{8\mu R^2} - \frac{1.8e^2}{\varepsilon R} \qquad \text{(Equation 1.5)}$$

where h is Planck constant = 6.626×10^{-34} J.s and e is the electron charge = 1.602×10^{-19} C. The reduced effective mass of the excitons is related to the effective masses of the charge carrier (m_e, m_h) according to the following expression:

$$\mu^{-1} = m_e^{-1} + m_h^{-1} \qquad \text{(Equation 1.6)}$$

From equation 1.5 it can be seen that *Eg* depends critically on the effective masses of the electrons and holes. The quantisation phenomenon also has a significant effect on the optical properties of the semiconductor, as a result of changing electronic properties. For instance, with decreasing particle size, the optical transition energy will increase therefore the Q-particles can have different colours depending on their size. Cadmium sulphide for instance normally exists as a yellow material, when its particle size decreases to 22Å it becomes colourless. The normal black colour of the cadmium phosphide can be changed to various colours by changing its particles size. Thus, by varying the size of the semiconductor particles, the redox potential of the valance band holes and conduction band electrons can be controlled.

1.1.2 Direct and indirect band gap of semiconductors

The top of the valence band and the bottom of the conduction band do not usually have the same value of electron momentum in *k* space. The *k* space is constructed on one of three vectors in the *p* space, usually three dimensional but in general could have any finite number of dimensions. While *r* space, is a set of position vectors, which has dimensions of length and defines a point in space, *p* space is a set of momentum vectors in a physical system with the units of [mass] [length] $[time]^{-1}$. The *k* space is set of all wave vectors; which has dimensions of reciprocal length. The electronic transition from the valence

band to the conduction band can be associated with a forbidden change in momentum. According to that, semiconductors are classified as direct and indirect band gap semiconductors, as shown in Fig. 1.3. For direct band gap semiconductors (Fig. 1.3a) the VBM has the same electronic momentum as the CBM. Its electronic transition is described as a direct transition, since the momentum is conserved during the excitation. Due to the tendency of electrons to lower their energy, they can rapidly recombine with the holes for a direct band gap semiconductor. The recombination process in this transition is associated with emitting photons with energy (*hv*) with no change in the electron momentum (red arrow). Such a transition process is normally allowed and relatively effective. For the indirect semiconductor as shown in Fig. 1.3b, the conduction band minimum and the valance band maximum have different values of electronic momentum. Subsequently, the electronic transition from the valence band to the conduction band requires a change in momentum. In addition, the excited electron cannot relax back from the lowest-energy state in the conduction band to the highest-energy state in the valence band without the change of momentum. For such indirect band gap system, the momentum required during the excitation and relaxation process is normally supplied in the form of phonons (which are the vibration of atoms in the crystal lattice). After relaxation, the electrons recombine with the valance band holes and emit photons with energy (*hv*) (dark red arrow). These transitions are generally forbidden and relatively slow. In most cases, the recombination in the indirect band gap semiconductor is non-irradiative in nature and usually results in heat (green arrow), due to the energy coupling with the phonons.

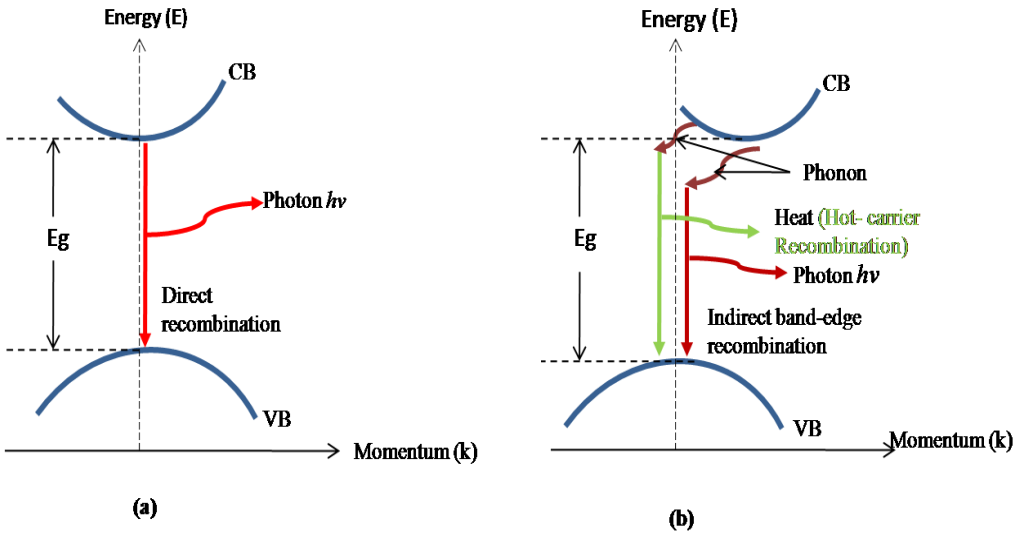

Figure 1.3 Schematic diagram shows the band gap for different semiconductors as a function of electrons momentum. (a) Direct semiconductor, a direct electron transition is possible due to the match in momentum. (b) Indirect semiconductor, an indirect electron transition is required due to change in momentum.

The properties and performance of metal oxide semiconductors are partly affected by crystal type, size and morphology. Nanostructured metal oxides with dimensions ranging from a few nanometres to several hundred nanometres offer a large surface to volume ratio which is significantly larger than that of the bulk material. Therefore, the performance of these materials could effectively be enhanced by synthesising the metal oxides into nanostructure [13, 45, 46].

1.2 Nanostructured metal oxides semiconductors and their applications

Metal oxide nanostructured films have been attracting great attention in the research community for a period of time, due to their superior properties over densely packed polycrystalline films. These properties derive from structural features such as particle size or layer thickness on a scale 1-100 nm, much smaller than that found in conventional materials. Furthermore, the highly porous nanostructured films also offer a large surface to volume ratio. With respect to the bulk material, nanostructured oxides of metals,

including titanium, zinc, iron, cerium, tin, zirconium and magnesium, have been found to exhibit interesting nano morphology. These materials also exhibit interesting functional properties, such as biocompatible, non-toxic and catalytic properties. The enhanced electron-transfer kinetics and strong adsorption capability offer the potential for immobilizing and sensing of biomolecules [47].

Nanomaterials can be classified as zero, one and two dimensional structures. Firstly, zero-dimensional (0-D) nanostructures are referred to as nanoparticles (NPs), polycrystalline and amorphous with possible morphologies being spheres, cubes and platelets [48]. In general, the particles are less than one hundred nanometres in size and if the nanoparticles are single crystal they are often referred to as nanocrystals. One-dimensional (1-D) nanostructures can be classified to four categories; nanowires (NWs) [49, 50], nanorods (NRs) [51], nanobelts (NBs) [52] and nanotubes (NTs) [53]. The first three categories have solid structure, while the nanotubes have hollow centre. In general, NWs are NRs with large aspect ratio (long NRs), which appear less rigid and straight compared to NRs. Some times when the NWs are very long and not single crystalline, they are described as nanofibers. NBs are special NWs structure with rectangular cross-section. Two dimensional (2-D) nanostructures are referred to as thin films, an important nanostructure class, which have been the subject of intensive research efforts for a long period of time [54, 55].

Metal oxides nanostructures based on TiO_2 and ZnO have been receiving a great interest in nanotechnology since Ti and Zn are two of the most abundant minerals on Earth [56]. The vital properties of these materials encouraged many researchers over the past decades to focus their studies on the producing and processing the nanostructured materials of these oxides. In the present work, TiO_2 is the main metal oxide being studied. ZnO has also been used as a photocatalyst as discussed in chapter 8. Therefore, the

properties, synthesis methods and the potential applications of each material will be discussed in details.

1.3 Titanium dioxide (TiO_2) nanostructure and applications

1.3.1 TiO_2 properties

Titanium dioxide (titania, TiO_2) represents one of the most important compound of titanium and oxygen. This compound has been the subject of enormous research interest over the past decades, due to its interesting properties, such as high photocatalytic activity [57-59], high chemical and thermal stability [60], biocompatibility [61], non-toxicity [62] and low cost [63]. Therefore, many studies have been focused on the producing and processing of nanostructured titania. TiO_2 arises in nature in three distinct crystal structures, including anatase (tetragonal), rutile (tetragonal) and brookite (orthorhombic) [64], in addition to other two high pressure forms, a monoclinic baddeleyite-like form (TiO_2-B) and an orthorhombic α-PbO_2-like form [65]. The first three crystal structures are more commonly known forms of titania than others (more studied) [66]. Rutile is the most common naturally occurring form [67]. Anatase, which is less naturally abundant, is also of great interest, primarily for its role in the transport of electrons in photovoltaic devices [68]. Brookite phase is the rarest form of the mineral and is least studied due to the difficulty of synthesising it in a laboratory [69].

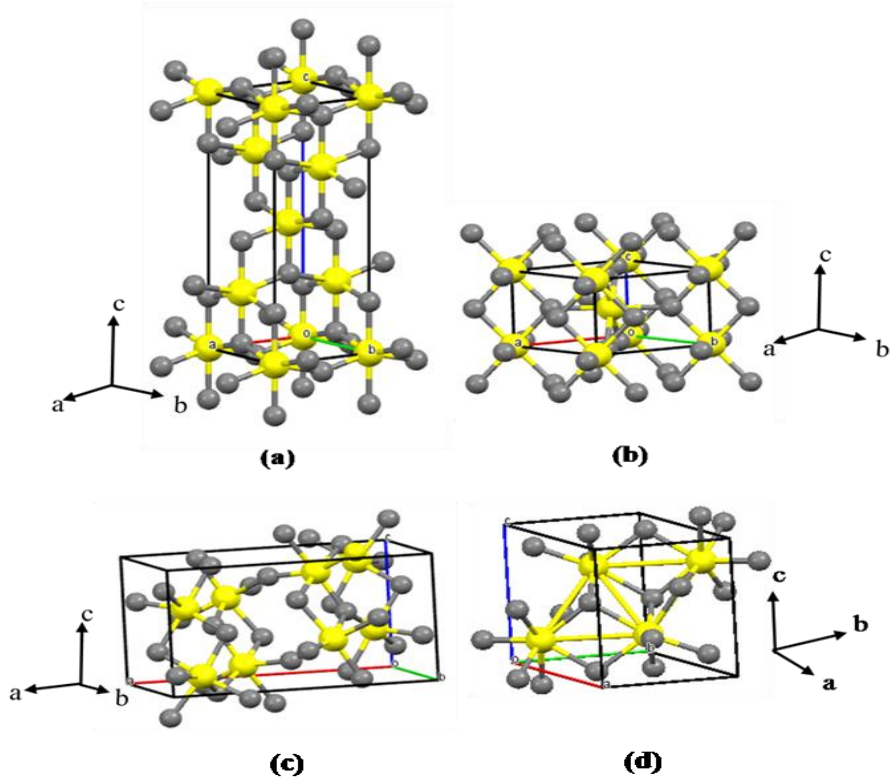

Figure 1.4 Crystal structures of TiO_2 (a) anatase, (b) rutile, (c) brookite and (d) baddeleyite (TiO_2-B). Ti (yellow) and O (grey). The wireframes represent the unit cell of the TiO_2 phases and the coloured frames identify a, b and c directions.

Fig. 1.4 shows the crystal structures of anatase, rutile, brookite and TiO_2-B. The crystal structures of TiO_2 in all these phases are made up of distorted octahedra. Each octahedron is formed with a TiO_6 unit with Ti^{4+} central and coordinated with six O^{2-} ions. The characteristics of each polymorph depend on the assembly of the octahedra to form TiO_6 chains. Anatase has four corners shared per octahedron with neighbours and shares edges with four other neighbours. This connection gives the crystal structure of anatase a zigzag chain with a screw axis. In rutile, each octahedron shares corner with eight neighbours and shares edges with two other neighbours, forming liner chains along [001] direction. In the brookite phase the octahedra share three edges and corners. TiO_2-B comprises of edge and corner sharing TiO_6 octahedra with an open channel parallel to the b-axis between axial oxygens. Table 1.1 lists some of the important physical properties of the four polymorphs of TiO_2. TiO_2-B has the widest bans gap (~ 3.22 eV) with the

lowest refractive index and material density. In contrast, rutile has the lowest band gap with the highest density and refractive index. Brookite and anatase come between the TiO_2-B and rutile in terms of its properties (density, band gap and refractive index).

Table 1.1 Different TiO_2 crystal structure and their physical properties [67, 70-73].

Structure	Refractive index	Crystal system	Band gap (eV)	Density (g/m^3)	Unit cell Volume ($Å^3$)	O-Ti-O bond angle
Rutile	2.72	Tetragonal	3.02	4.13	31.2160	81.2º-90.0º
Anatase	2.52	Tetragonal	3.20	3.79	34.0610	77.7º-92.6º
Brookite	2.63	Orthorhombic	3.11	3.99	32.1720	77.0º-105º
TiO_2(B)	2.45	Monoclinic	3.22	3.64	35.27	-

Among the different polymorphs, rutile is generally considered to be the most thermodynamically stable phase while anatase, brookite and TiO_2-B are metastable. The irreversible transformation of the metastable phases of anatase, brookite to rutile happens at high temperature (> 600°C). The high thermal stability of rutile may be related to the strong crystallinity as the result of its synthesis conditions. It is mainly prepared by hydrothermal method, since the rutile formation requires hard conditions such as acidic media, high temperature and relatively long aging time. Furthermore, the stability of anatase, rutile, brookite and TiO_2-B greatly relies on the particle size, *d*, of the TiO_2 nanocrystals [60]. While anatase is thermodynamically most stable when $d < 11$ nm and brookite is the most stable when $11 < d < 35$ nm. Meanwhile, rutile is the most stable when $d > 35$ nm [71]. In addition, the phase transformation of anatase nanoparticles is affected by density of defect sites on their surface., which determines the surface energy on the crystal. If the defect sites are blocked by some additives, the phase transformation can be effectively prohibited [74]

As being mentioned in Section 1.1, the valance band VB of TiO_2 is formed by fully occupied O 2p states (in particular, non-bonding p_π states) and the unoccupied conduction band CB is formed by the empty Ti 3d, 4s, 4p states [75, 76]. The presence of defects and dopants provides additional states in the band gap near the valance band or the conduction band. Ti^{+3} and oxygen vacancy are the most important defects which dominate optical and electrical properties of TiO_2 [77]. Ti^{+3} states were reported to lie about 0.2-0.8 eV below the conduction band [78, 79]. These defects may be generated by annealing under vacuum or in inert-gas. Such defects can effectively reduce the band gap energy and easily release trapped charge carriers to the nearby conduction band by thermal excitation [79].

The four polymorphs of TiO_2 have been applied in different fields based on their different physical/chemical properties. For instance, the high refractive index and bright white colour of rutile makes it an appropriate material as a white pigment in paint. Anatase usually exhibits much higher photocatalytic activity than rutile, due to the difference in the band gap structures. The open crystal structure of TiO_2-B with significant voids and continuous channels make it an ideal host for lithium intercalation in lithium ion batteries (LIBs).

1.3.2 TiO_2 nanostructures

The photocatalytic performance of TiO_2 can be enhanced by controlling the nanostructures of TiO_2. As mentioned previously, by decreasing the dimensions to the nanoscale, the electronic properties may also change considerably due to the quantum size effects. For many applications it is also vital to maximize the specific surface area to achieve maximum overall efficiency for surface reactions. In such cases, the fraction of the atoms those are located at the surface is very large due to a high surface area to volume

ratio (*SAVR*). This can dramatically increase the surface reaction sites to enhance the catalytic activity of the surface atoms.

Over the past few years, several TiO_2 nanostructures, including nanowires [80, 81], nanorods [46, 82], nanobelts [83], nanotubes [53, 84], nanofibers [85], nanoparticles [63] and nanospheres [86], have been synthesised for different applications. A part of this project focuses on TiO_2 nanotubes and nanorods, which were synthesised by electrochemical anodisation of Ti metal and by the hydrothermal synthesis method respectively.

1.3.2.1 TiO_2 nanotubes

Vertically oriented, highly ordered TiO_2 nanotube (TNTs) structure is one of the widely studied structures of titanium dioxide. It has the combined advantages of one dimensional tubular structure and large surface areas, in addition to the improvement of electronic and mechanical properties. One-dimensional (1-D) nanotube structures offer large internal surface area with highly ordered geometric structure, these features possess excellent charge transportation [87], providing higher charge carrier mobility and longer lifetime. In addition, the processing of titana into nanotube structure could provide quantum confinement effects with high mechanical strength. Therefore, this material is suitable for novel applications, including gas sensing [88] photocatalysis of hydrogen generation [89-92], dye-sensitized solar cells [28, 53, 93, 94] and drug delivery [95-99].

A simple electrochemical anodic oxidation of a metallic titanium substrate is one of the most efficient ways of creating highly ordered TiO_2 nanotubular arrays [89, 100]. Nanoporous and nanotubular TiO_2 are synthesised by passing an anodisation current through a fluoride-containing electrolyte. The concept and operation conditions of this method will be discussed in the next chapter. Sol-gel [101], microwave irradiation [102], hydrothermal [103] and templating [104] are also used for the fabrication of TiO_2 nanotube

arrays. However, most of these methods have limitations. For instance, the templating technique requires high temperature calcination to remove the template, resulting in possible collapse of the tubular structure [105]. For hydrothermal methods, the TNTs are not able to assemble into closely packed vertically oriented structures, which limit their use in photoelectrochemical applications. The titania nanotubes grown owith anodisation method are vertically aligned and close packed with well defined tubular morphology. The nanotube layer with controlled top openings is suitable for size-selective applications (filters) or for templating secondary nanomaterial. The inside volume is regular and well-defined, thus the TNTs can be used as nano test tubes [106] and nanobottles, which can be used for drug delivery.

1.3.2.2 TiO_2 nanowires, nanorods and nanobelts

Titanium dioxide can be synthesized as nanowires (TNWs), nanorods (TNRs) and nanobelts (TNBs) as well. These are important 1-D nanostructures since they offer large surface area, more reaction sites, high volume of depletion regions and possible quantum conferment effect compared to the bulk structure. The synergy of these advantages with the high photocatalytic activity of TiO_2 could enhance the performances of energy harvesting, sensing and catalysis. In contrast, for the nanoparticular films, the electron conductivity is restricted by limited contact between particles, resulting in charge scattering and a high probability of charge recombination. 1-D TiO_2 nanostructures such as TNWs and TNRs may serve as constricted conductive channels, where their longer charge carrier diffusion length could reduce charge recombination and assist charge transportation [45]. The similarity between their physical dimensions and carrier diffusion length facilitates the collection of free charge carriers. They also provide appropriate geometric configurations for the effective trapping of the illuminated photons in the

excitation step. Based on that, TNRs, TNWs are considered as a highly efficient framework in electronical applications, such as photovoltaic, photocatalysis, energy storage system and sensors devices.

To date, 1-D titanium oxide, TNWs, TNRs, TNBs, can be synthesised by many methods, including oxidation of Ti substrate [80, 107], template-assisted synthesis [108], metal-organic chemical vapour deposition [82, 109] and hydrothermal synthesis [46, 110]. Among the previous described methods, hydrothermal synthesis is a relatively simple, low cost process and has the potential for large scale production. The general concept of the hydrothermal method is discussed in next chapter.

1.3.2.3 TiO_2 nanoparticles

Titanium oxide nanoparticles are an important zero dimensional nanostructure of titania, since they are used in many applications, including catalysis [111], drug delivery [112], bactericidal agents [113] and gas sensing [114]. Large amount of research is being diverted towards the controlling of the TiO_2 nanoparticle size distribution and crystal morphology. There are a number of methods to produce TiO_2 nanoparticles, such as sol-gel synthesis, hydrothermal and biosynthesis.

1.3.3 Applications of titanium dioxide

In light of the interesting properties of TiO_2 nanostructures, the main motivation behind research on these materials is their possible impact upon a wide range of technologies, particularly photocatalysis including photo-splitting of water, photovoltaic and gas sensing, in addition to the biomedical applications.

1.3.3.1 Photocatalytic degradation of organic pollutants

Photocatalysis by a solid state system occurs when electron-hole pairs (generated by photoexcitation) react with molecules close to the catalyst's surface. TiO_2 is one of the most active photocatalysts in the degradation of organic and inorganic pollutants. Organic materials can be decomposed under illumination of UV light to yield CO_2 and water oxidatively. Fig. 1.5 presents schematic diagram of a typical photocatalytic reaction mechanism.

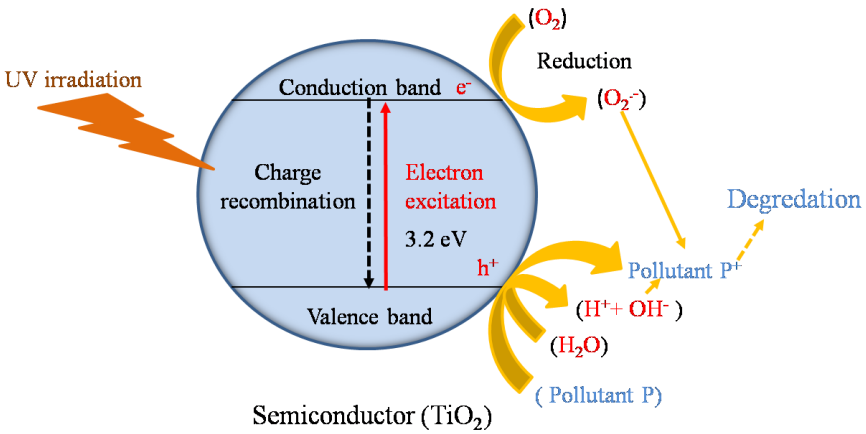

Figure 1.5 Mechanism of photocatalysis by TiO_2. The band gap is 3.2 eV.

By absorbing photons with energies equal or higher than the band gap energy of TiO_2, electrons are excited from the valence band to the conduction band, leaving an equal number of positively charged holes in the valence band. The generated charge carriers (electron-hole pairs) can recombine or migrate to the catalyst surface to promote reactions with adsorbed molecules. For degradation of pollutants in water, the photogenerated charge carriers participate in reactions with the adsorbed water molecules. Surface hydroxyl groups and dissolved molecules oxygen are reacted with excited electrons and holes, generating highly reactive hydroxyl and superoxide radicals.

Both species are recognized as active agents in the degradation of organic compounds on a TiO_2 surface. The formation of these radicals can be illustrated in the following equations:

$$TiO_2 + hv \rightarrow e^- + h^+ \quad \text{(Equation 1.7)}$$

$$O_2 + e^- \rightarrow O_2^{\cdot -} \quad \text{(Equation 1.8)}$$

$$H_2O + h^+ \rightarrow OH^{\cdot} + H^+ \quad \text{(Equation 1.9)}$$

The photocatalytic reaction is initiated from the generation of electron-hole pairs upon light irradiation. When TiO_2 absorbs photons with energy equal or greater than 3 eV, electrons in VB are excited to CB, leaving holes in VB, shown in equation 1.7. The reduction of the adsorbed O_2 forms superoxide radical as shown in equation 1.8, while the hydroxide radical is formed by the oxidation of water shown in equation 1.9. The organic pollutants are degraded by the oxidative action of superoxide and hydroxyl radicals that break the C-C and C-O bonds in the organic molecules.

The photocatalytic activity of the semiconductor is determined by its light absorption ability and the recombination rate of the generated charge carriers. It also depends on the rate of surface reduction and oxidation by the electrons-holes pairs. The reductive power of the excited electrons is determined by the CBM of the semiconductor. This must be higher than the reduction potential of O_2/O_2^-. Meanwhile, the potential of the maximum of valence band of the semiconductor must be lower than the water oxidation potential. Subsequently, the reduction process is driven by the difference between the electron-hole potentials and the H_2O/O_2 redox potential.

The photocatalytic activity also depends on the crystal structure. Anatase and rutile show photocatalytic activity but brookite and TiO_2-B do not. Anatase exhibits

higher photocatalytic activity than rutile. The differences in lattice structures of anatase and rutile TiO_2 cause different densities and electronic band structures, leading to different band gaps in the bulk material: 3.02 eV for rutile and 3.2 eV for anatase (table 1.2). This difference gives the anatase a slightly higher redox driving force than rutile, although the range of the light absorption by the anatase is less than that absorbed by retile. The higher top edge of its valance band maximum increases the oxidation power of the holes and facilitates electron transfer from the adsorbed molecules to the anatase [115].

Table 1.2 The band gap structure of anatase and rutile TiO_2 [115, 116] referring to the redox potential of H^+/H_2 (0 V *vs.* NHE).

TiO_2	Band gap	VBM	CBM
anatase	3.20 eV	3.00 eV	-0.20 eV
rutile	3.02 eV	2.93 eV	-0.09 eV

Anatase has an indirect band gap, while rutile has a direct band bap [115]. For the indirect band gap semiconductor, the light absorption and creation of excited electron-hole pairs are kinetically limited. However, the recombination of electron-hole pairs is also slower [117]. To some extent, the low light absorption efficiency can be compensated by increasing the film thickness. For a direct band gap material, the light absorption is efficient, but the charge recombination will also be faster. This recombination can be manipulated either by increasing the charge mobility within the materials by introducing defects and dopants; or by reducing the dimension of the nanomaterials. In this work, I will present the enhancement of photoefficiency from the reduced or doped rutile nanorods.

Moreover, anatase formed at lower temperatures generally has higher surface area and higher density of active sites, such as oxygen vacancies, than rutile due to limited

sintering, leading to faster reaction rates in heterogeneous gas/solid reactions. The presence of more oxygen vacancies in the anatase crystal offers the possibility of efficient charge separation, although rutile has better charge carrier mobility due to its higher crystallinity. Because of these advantages, anatase usually exhibits much higher photocatalytic activity than rutile as will be discussed later.

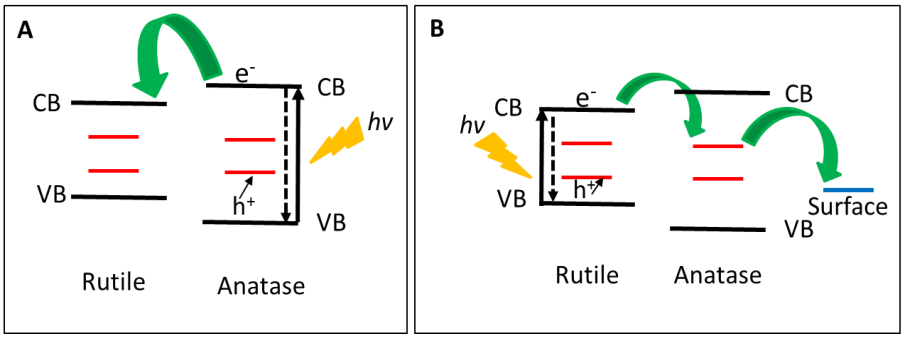

Figure 1.6 Proposed models of P25 activity. (a) Bickley model where charge separation occurs on anatase and rutile acts as electrons sink. (b) Hurum model where anatase facilitates charge separation on rutile by trapping the transferred electrons from rutile on its trapping sites [121].

Degussa P25 is a commercial form of TiO_2 nanoparticles with an average diameter of 25 nm. It is a mixture of anatase and rutile with a ratio of 3:1. It exhibits a higher photocatalytic activity than either pure phases alone [118, 119]. Different investigations have been reported to explain the high photoactivity of this mixture as proposed in Fig. 1.6. Bickley and co-workers [120] attributed that to the presence of anatase and rutile, which promotes the transferring of the photoexcited electrons and positive holes between interconnecting anatase and rutile nanoparticles (Fig. 1.6a). When the electrons are transferred from the anatase to the lower energy levels of rutile, the mixed phase in this case serves to reduce the recombination rate of anatase, leading to more efficient electron-hole separation and greater catalytic reactivity. Hurum and co-workers [121] proposed an opposite model to explain the photoactivity of P25 (Fig. 1.6b). Their study illustrated that,

while the rutile phase extends the photocatalytic activity to the visible region due to its smaller band gap, the presence of anatase particles close to rutile particles serve to trap the photoexcited electrons from rutile to lower energy lattice trapping sites (red lines) under visible illumination. Therefore, the charge carrier separation is improved in the photocatalytic reaction. The anatase trapping sites have been reported to lie at 0.8 eV lower in energy than the CB of the anatase and below the CB of rutile [122].

1.3.3.2 Photoelectrochemical water splitting

Solar energy conversion by water electrolysis to generate hydrogen as an alternative energy source is an ideal system to reduce our dependence on fossil fuels and to control the emission of greenhouse gases. Since Fujishima and Honda [58] discovered the high photocatalytic activity of TiO_2 electrode in water splitting process under UV light, it has become one of the most studied materials for use as photoanodes in a photoelectrochemical system (PEC).

The water splitting reaction generally is similar to the oxidation of organic molecules as described above. The only difference is that here water, instead of organics, is oxidised and reduced. In fact, in some research work, organic molecules, such as ethanol, were used as hole scavengers to improve the hydrogen generation. A standard water splitting process involves a sequence of chain reactions, as shown in Fig. 1.7. First, a semiconductor is excited by a photon ($h\nu$) with energy higher than its band gap (E_g) and electrons are transferred from the VB to the CB, generating a hole in the VB (Equation 1.10). Second, the photogenerated holes migrate to the anode surface and oxidize water generating oxygen. The excited electron in the CB is transported through the external circuit to the cathode for the reduction of water to produce hydrogen, as described in (Equations 1.11 and 1.12).

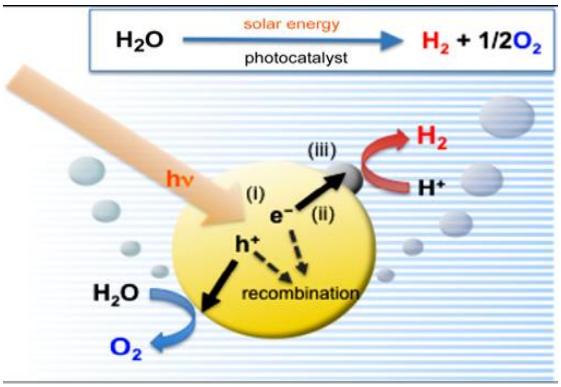

Figure 1.7 Scheme of the main processes in the photocatalytic water splitting [123].

$$TiO_2 + hv \rightarrow e^-(TiO_2) + h^+(TiO_2) \quad \text{(Equation 1.10)}$$

$$4h^+ + H_2O \rightarrow O_2 + 4H^+ + 4e^- \quad \text{(Equation 1.11)}$$

$$4H^+ + 4e^- \rightarrow 2H_2 \quad \text{(Equation 1.12)}$$

The first two steps are significantly influenced by the morphology and electronic properties of the photocatalyst, such as crystallinity, defect density, charge-transfer pathways, band gap and surface area. These factors affect photon absorption efficiency, exciton generation and the charge re-combination rate. Therefore, the design of the photoanode in a PEC system is crucial in maximising the efficiency of the PEC system. The water oxidation process is normally the rate limiting process, since it involves 4 electrons. A high reaction barrier defined as over potential is normally observed for this step.

It is worth mentioning that, the photogenerated electron-hole pairs may be involved in three possible processes: (i) successful migration to the surface of the semiconductor, where it could be available for the photocatalytic reactions, (ii) capturing by the defect sites in the bulk and/or on the surface region of the semiconductor and (iii) recombining and releasing the absorbed energy in the form of heat or a photon[123]. The defect sites in the bulk and on the surface may also serve as the recombination centres for

the photogenerated charge carriers, which will decrease the efficiency of the photocatalytic reaction[65]. The recombination rate is determined by the charge diffusion length and exciton lifetime. The optimum thickness of the film should be less than the charge diffusion length[115]. However, if the film is too thin, the light absorption will be greatly reduced, following the Beer-Lambert law. For a planar thin film electrode, a trade-off between light absorption and charge transport must be achieved. However, for a 3-D nanostructured thin film, these issues can be separately optimised without the restriction between each other.

There are also several intrinsic stringent requirements for a photocatalyst to be efficient in water splitting. Firstly, the band edge positions of the semiconductor are important. The top of the valence band edge must be more positive than the oxidation potential of water for the production of O_2 (+1.23V *vs* normal hydrogen electrode, NHE). The lower edge of the conduction band must be more negative than the reduction potential of water for the generation of H_2 (0V *vs.* NHE*)*. Thus, the minimum semiconductor band gap for water splitting is 1.23 eV. Additional potential is needed to overcome the over potential arising from energy barrier for electron transfer at the semiconductor-electrolyte interface. Therefore, the practical band gap is required between 1.6-2.4 eV [124]. Finally, Semiconductor should pose a high chemical stability in the chosen electrolyte and under light illumination.

Fig. 1.8 shows the CBM and the VBM positions of selected common semiconductors. Some of them absorb visible light, such as (WO_3 and Fe_2O_3) but with a conduction band edge below the potential required to produce H_2. Thus external potential bias will be needed between the anode and cathode in order to shift the CBM towards the negative potential. GaAs, GaP, Cu_2O, $CuLnS_3$ and C_3N_4 are semiconductors with a relative small band gap (1.4-2.25 eV) with capability of absorbing visible light. However,

their VBM potentials are all less positive than the water oxidation potential (1.23 eV). Therefore the production of O_2 cannot be directly facilitated. On the other hand, CdS has a band gap of 2.25 eV which is visible light sensitive and its band edge positions are appropriate for the water splitting. However, CdS is chemically unstable and suffers from photocorrosion rather than forming O_2.

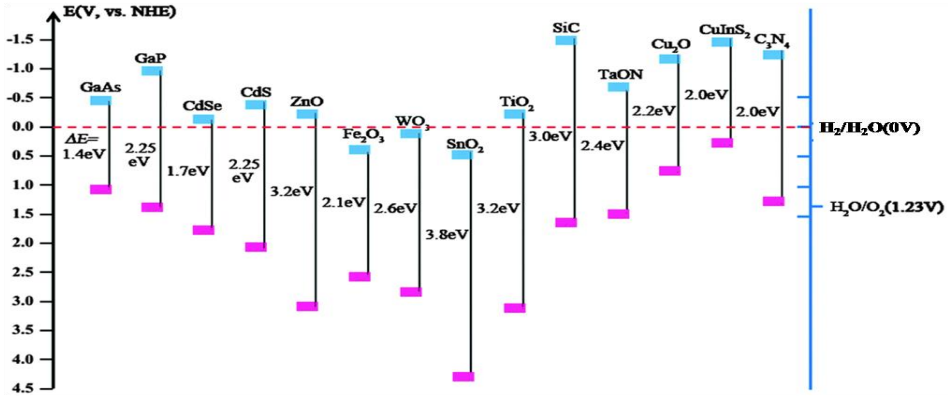

Figure 1.8 A schematic diagram of the band gap position of some semiconductors with respect to the redox potential of water [39].

Among those semiconductors shown in Fig. 1.8, TiO_2 is very stable, non-corrosive, environmentally friendly, abundant and low cost. More importantly, its valance band edge is more positive than oxidation potential of water for oxygen generation, while its conduction band lies at a potential more negative than the reduction potential of water for hydrogen production. Therefore it can produce both H_2 and O_2 without the need of direct bias. The main drawback of this catalyst is the large band gap, which restricts its spectral absorption to the UV region. Another problem of using TiO_2 is the fast recombination rate of its photogenerated charge carriers.

Despite many advantages of TiO_2 as photoanode material in the PEC system, its photocatalytic efficiency under solar energy is still very low, due to its wide band gap (3.0 eV for rutile and 3.2 eV for anatase). TiO_2 can only be excited by the UV light, which

accounts for less than 5% of the total incident solar radiation. This can be extended to the visible region (> 400 nm) by band gap engineering, which refers to narrowing the band gap by a doping (mentioned in Section 1.1.1) or by surface sensitising.

The doping process involves introducing controlled impurities into TiO_2 lattices. These impurities could be metallic or non-metallic docents. Metallic ions, such as Fe [125], Ca [126] and La [127] as well as non-metallic elements, such as C [128] and N [122], have been used as dopants. Since the VB of TiO_2 is made up of contributing O 2p orbitals and Ti 3d, 4s and 4p orbitales contribute to the CB, by introducing these impurities, additional dopant states can be created within the band gap. As shown in Fig. 1.9, by the incorporation of metal ions into the TiO_2 lattice, the cationic doping replaces the Ti cations and introduces energy levels near the conduction band. These levels can act as electron donor or acceptor and contribute to the reduction of the band gap energy and allow absorbing the visible light. A systematic study was carried out by Choi et al [129] on the effect of doping 21 different metal ions into TiO_2 upon its photoreactivity. Their results show the evidence of extended absorption of visible light.

Conversely, non-metallic doping such as N and C, could hardly affect the CB of TiO_2, since they usually give impurity energy levels near the valence band VB, due to their electronegativity. The p orbit of the dopant ions will mix with the O 2p orbit of TiO_2 and shift the valance band up, narrowing the band gap. Therefore, the electrical absorption of this material could be also modified as the electronic transitions from the dopant 2p or 3p to the Ti 3d orbital. Meanwhile, the oxidative power of the photoexcited hole is also reduced. Therefore, a fine balance between the reduction of band gap and the oxidation power has to be optimised. Experimentally, Asahi et al demonstrated the enhancement of the TiO_2 photocatalytic activity due to the narrowing of the TiO_2 band gap by doping with

nitrogen [122]. They proposed that nitrogen doping was associated with the formation of oxygen vacancies.

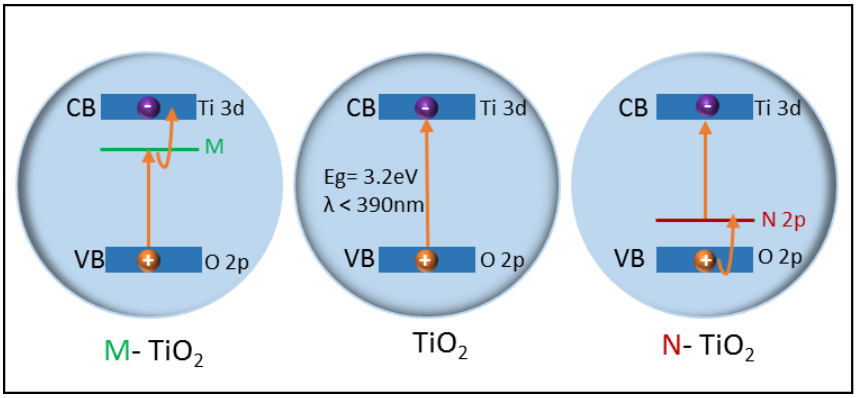

Figure 1.9 Schematic diagrams represents doping of TiO_2 with metal (M-TiO_2) and non-metal (N-TiO_2), which results in a mid-band gap energy levels near the conduction band or the valance band respectively. These reduce the energy gap required for charge separation.

Apart from band gap engineering, creating surface defects and increasing the donor density can also introduce new energy states within the band gap. The formation of surface defects introduces energy states close to the VB, acting as hole trapping. While the presence of oxygen vacancies, which are known as electron donor, increases the electrical conductivity of TiO_2 in addition to forming energy levels near the CB minimum. In both cases, the formed energy levels contribute in the reduction of the band gap and improving the visible light absorption. For multivalent atoms, such as Ti and Fe, the defects can be introduced by the reduction treatment of the metal oxides in a hydrogen environment or annealing in vacuum. It was reported that the reduction of the anatase TiO_2 nano particles narrows the optical band gap from 3.2 eV to 1.0 eV and shifts the optical absorption from UV energies towards the near infrared (IR) [130]. Wang *et al* [131] found that the reduction treatment of rutile TiO_2 nanowires improved photoactivity of the TiO_2 in the UV region according to their IPCE (incident photon-to-current efficiency)

analysis. IPCE evaluates the current density that the cell produces when irradiated by photon of a particular wavelength. The hydrogen treatment increases the donor density of the TiO_2 nanowire by three orders of magnitudes, via creating a high density of the oxygen vacancies that act as electron donors. The energy levels of the oxygen vacancies in hydrogenated rutile TiO_2 are located below the conduction band. Subsequently, the electron transitions from the TiO_2 valance band to the oxygen vacancy level or from the oxygen vacancies to the conduction band, which are associated with the light absorptions in the visible and near infrared respectively. The work attributed the high efficiency of the reduced sample in water splitting experiments to the surface disorder after the hydrogen treatment [131]. Higher degrees of lattice disorder in the semiconductor could produce mid-gap states. These states can form an extended band which overlaps with either the conduction band or the valance band, resulting in a reduced band gap. The surface defects can also act as trapping sites for photogenerated charge carriers to prevent them from rapid recombination. Therefore, the electrons transfer and the photocatalytic reaction will be promoted.

The photocatalytic hydrogen production can also be enhanced using hydrocarbons as hole scavengers. Hydrocarbons can be oxidized by the holes in VB while allowing the electrons in CB to reduce water. In such a process, the anodic reaction is changed from water oxidation to a relative easy hydrocarbon oxidation. Different hydrocarbons have been studied as hole scavengers, several compounds showed high efficiency in the enhancement of hydrogen production following the order of improvement: EDTA >methanol >ethanol >lactic acid with hydrogen generation of 140, 110, 85 and 60 µmol respectively within photolysis time of 6h [132]. The surface area to volume ratio (SAVR) of the catalyst also plays a key role in determining the hydrogen generation rate. Compared to the thin film, for instance, 1-D nanostructure film provides high SAVR

value with large number of surface reaction centres. Therefore, higher rate of the hydrogen generation can be obtained by using this structure in comparison with solid thin film photoanode. In this research, we tried to improve the photocatalytic activity of TiO_2 by synthesising 1-D nanorods of this semiconductor with optimum performance.

One of the drawbacks of TiO_2 as photocatalyst is the fast recombination rate of the generated charge carriers, where the photoexcited electrons return to the valence band to combine with the holes rather than being involved in a water splitting reaction. Subsequently, the energy conversion efficiency of TiO_2 from solar to hydrogen by photocatalytic water splitting is limited. It is worth mentioning that the charge carrier recombination occurs mainly at the surface of the catalyst, where it competes strongly with the photocatalytic process. This phenomenon is usually associated with the release of energy; therefore, transient photoluminescence measurements can be employed to study the recombination kinetics.

Several strategies have been developed to reduce the recombination rate of the TiO_2 photoanode material. Coating TiO_2 nanocrystals with materials of different electronic structures, such as small band gap semiconductors, is one of the most efficient techniques. For instance, TiO_2 nanostructures sensitised by CdS quantum dots improve the photoefficiency significantly. It was reported in recent study that nearly 3.5 times higher of photoefficiency was achieved [133]. That was attributed to enhancing the light harvesting efficiency and suppressing the recombination of photogenerated electron-hole pair through the sensitizing TiO_2 with CdS QDs. With the small band gap of CdS (2.4 eV), more visible light can be absorbed. In addition, CdS QDs also have the ability of generating multiple excitons from the absorption of single photon. In the model nanostructure of TiO_2/CdS, a possible charge-transfer mechanism was proposed, shown in Fig. 1.10. The conduction band energy of the CdS is more negative (E_{CB}= -0.52 eV)

than that of rutile TiO_2 (E_{CB}= -0.09 eV), therefore the generated electrons in CdS, as result of the visible light absorption, can be readily transferred into the CB of TiO_2 and then to the substrate to be passed through the external circuit to the cathode for reduction process. While the formed holes in the VB of TiO_2 (E_{VB}= +2.91 eV) can be easily transferred to the less positive VB of CdS (E_{VB}= +1.73 eV), which are still more positive than the oxidation potential of water (H_2O/O_2= +1.23). These holes will be available at the surface for the oxidation reaction.

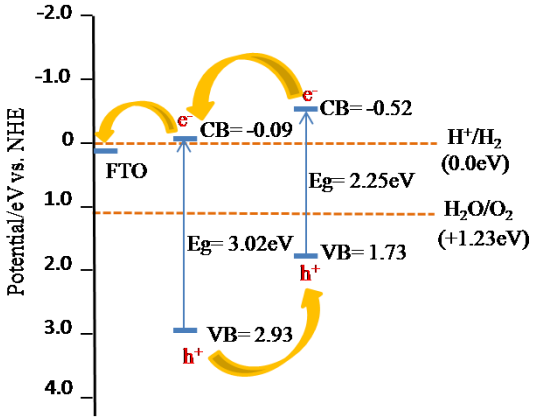

Figure 1.10 Schematic diagram for the band gap alignment model in CdS QDs synthesised TiO_2 photo electrode.

Nevertheless, surface coating treatment has the disadvantage of instability, low homogeneity and the lack of adhesion to the metal oxide substrate. For instance, CdS is chemically unstable material and shows high photocorrosion in the electrolyte. Therefore, direct doping is more desirable strategy for enhancing the photocatalytic efficiency of metal oxides.

Furthermore, the nano morphology of semiconductors has also been considered as an important factor in influencing the charge carrier separation and transportation. 1-D metal oxide nanostructures, such as nanorods, nanowires and nanotubes, can facilitate the charge carrier diffusion and interaction with electrolytes crossing the width of the 1-D structures. These morphological effects become more important when the nano

dimension is equal or less than the charge carrier diffusing length or the mean free path. The short pathways for photogenerated charges to reach the solid surfaces and large surface area can significantly suppress charge recombination[45, 92, 133].

The performance of the semiconductor in PEC systems can be also affected by the design of the photoanode. For instance, TiO_2 nanotube arrays grown on Ti meshes improve the photocurrent by 36.4% for water photoelectrolysis compared with TiO_2 nanotube arrays on a flat substrate under the same light irradiance[90]. The nanotubes grown on meshes form a 3-D configuration with higher surface area. This structure provides massive number of the reaction centres at the interface with the electrolyte which significantly reduces the loss of the excitons. Such a large effective surface area is expected to achieve high photoconversion efficiency. Moreover, the radial nature of 3-D arrays on a mesh is capable of harvesting the incident light from different directions with multiple internal light scattering effects. Therefore, more light is being trapped and utilised in the water splitting reaction. [134].

The water splitting efficiency is also restricted by the reverse reactions between the generated hydrogen and oxygen. Using a two-compartment electrochemical cell separated by an ion exchange membrane can be a good solution to circumvent this problem [135].

1.3.3.3 Metal oxide semiconductor photovoltaics (PV)

In a photovoltaic cell, sunlight is absorbed and converted directly to electrical energy. Nanostructured TiO_2 offers large surface area to enhance the efficiency when capturing solar energy. For a PV cell, the band edges are not restricted and the visible light absorption can be enhanced by using organic dyes, defined as dye sensitised solar cell (DSSCs). A typical DSSC is shown in Fig. 1.11. The cell consists of a nanostructured

TiO_2 film coated with a monolayer of specially designed dye capable of visible light photoexcitation and effective charge transfer. In such a case, the electron in the excited states of the dye must have more negative potential than the conduction band of the TiO_2. An organic hole conductor, in the form of redox couples (iodide/triiodide is a popular system used in DSSCs) is used as electrolyte.

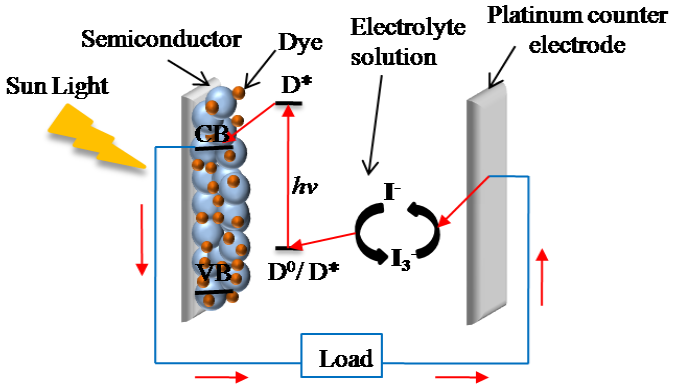

Figure 1.11 Schematic principle of operation in DSSC (red arrows represent the movement of electrons).

The nanostructures of TiO_2 exhibit mesoporousity with large surface areas, which enables a large amount of dye to be adsorbed. By illuminating with sun light, electrons are excited in the dye and are readily released into the conduction band of TiO_2. These electrons are protected from being recombined with the holes in the excited dye. The holes will be filled by the oxidation of iodide in the electrolyte, which regenerates the reduced dye monolayer. The electron in the conduction band of TiO_2 will move around the external circuit to produce direct current. The triiodide in the electrolyte will be reduced of iodide at the counter electrode. The voltage generated under illumination corresponds to the energy difference between the Fermi level of TiO_2 and the ground state of the dye. The electrical power can be generated in the DSSCs under illumination by sunlight without any irreversible chemical transformations.

Many shapes of TiO_2 nanostructure have been explored for use as anode in DSSCs including commercial nanoparticles [136, 137], nanotubes [84], nanorods[46], nanowires[81] and nanoparticles decorated nanorods [93]. Higher efficiencies were achieved using nanotubes and nanorods than nanoparticles, which can be explained by the better charge mobility along the 1-D nanostructure in addition to the greater amount of dye that can be loaded [59].

1.3.3.4 Nanostructures for drug delivery

The unique tubular structure, which has the top end open, alongside the biocompatibility makes a TiO_2 nanotube an ideal candidate as a capsule for drug delivery. Moreover, it may also be filled with magnetic particles, such as Fe_3O_4, and guided to the desired location to enhance imaging as well as to deliver drug locally. It combines the enhanced diagnosis with targeted treatment. The tube can also be coated with proteins that can recognize viruses or infected cells, forming a self-guided drug delivery. The drug loaded nanotubes can also be sealed with polymer for a delayed release or controlled using voltage induced catalysis. The underlying of this catalytic reaction is that, electron-hole pairs are generated on the catalysis surface by applying a bias voltage that is larger than the semiconductor band gap. The generated valance holes are ejected to the surrounding environment, body fluid and create OH^- radicals. These radicals can be used to trigger chain scission in the attached polymer and thus liberate terminal payloads [138]. UV light or X-ray radiation also can be used for *in vivo* treatment [139].

Song *et al* [140] studied the effect of using amphiphilic coated TiO_2 nanotubes for drug storage and release. The tube had a hydrophobic cap to restrict the release of loaded hydrophilic drug. This cap could be directly removed by photocatalytic oxidation, allowing the aqueous body fluid to enter the tubes and flush out the drug. Peng *et al* [141]

studied the drug release kinetics finding that the size of the loaded substrate molecules plays a key role for determining the elution time. Diffusion of small molecules may take weeks, while larger molecules can take up to a month to diffuse from the tubes. Achieving a controlled and sustained release pattern with uniform drug release over the time is a crucial goal for this application of the titanium dioxide nanotubes TNTs. This is the underlying topic of investigation in the fourth chapter of the thesis.

1.3.3.5 Other applications

Apart from the applications mentioned previously, TiO_2 nanomaterials are also used in electrochemical gas sensors. The adsorbed target gas modifies the electronic states of the TiO_2. The electrical resistance is measured to indicate the gas pressure. TiO_2 nanotubes show excellent H_2 response in air at raised temperature [142]. The selectivity towards hydrogen is related to the tube diameter, smaller tube diameters give higher sensitivity.

TiO_2 is well known for its use as self-cleaning building materials [143]. The excitation of TiO_2 with UV photon generates an electron-hole pair, which can create oxidative radicals, such as super oxide and hydroxyl radicals. These radicals oxidize any organic contamination forming gas phase CO_2 and H_2O. TiO_2 films also show the ability to switch from hydrophobic to hydrophilic surfaces after UV light illumination. This property with the photocatalytic activity provides antifogging and self-cleaning capability.

As an effective photocatalyst, TiO_2 is also used in antiseptic paints and coatings, air purification, as well as the decontamination of water by degrading bacteria, organic compounds and viruses [144]. It has been tested the potential in skin and stomach anticancer treatments [57]. Another application of TiO_2 is for charge storage in lithium ion batteries (LIB). Nanostructures of TiO_2, including nanorods, nanotube and nanoparticles, allow

increased capacity of the stored charge [145]. The effective capacity can be further increased by using TiO_2 composite with carbon [146], RuO_2 [147], SnO_2 [148], ZnO [149] or Si [150].

1.4 Zinc oxide (ZnO) nanostructure and application

1.4.1. ZnO properties

Zinc oxide (ZnO) is another adaptable and important semiconductor material, which has been a research subject in the scientific community for a long time. ZnO is an n-type direct wide band gap (3.37 eV) semiconductor, which makes it transparent in the visible region with most of its activities in UV/blue region. It has high thermal, mechanical and photostability with good charge mobility[151]. Thus, ZnO is an ideal candidate for applications like transparent conduction electrodes, flat panel displays and window layers for solar cells.

ZnO has been considered as an important material in the ceramic industry due to its hardness property, rigidity and piezoelectric response. Its hardness is related to its resistance to deformation, indentation, or penetration by means such as abrasion, drilling, impact, scratching. In addition, low toxicity, biocompatibility and biodegradability properties also make it a suitable candidate for the use in biomedicine and in biological system [152, 153].

Although TiO_2 is the most studied photocatalyst material, ZnO has also been considered as a key alternative material to TiO_2. This can be attributed to its comparability with TiO_2 in terms of the band gap energy and its relatively lower cost of production [154]. It has a slightly more negative conduction band potential than TiO_2, which, in principle, have a higher reduction potential. ZnO has a large exciton binding energy of 60 meV, which offers higher exciton populations under photoexcitation. Furthermore, ZnO also exhibits better electron mobility [151, 155] and longer lifetime than TiO_2 [156]. These properties

are favourable for electron transportation by reducing the recombination losses. Therefore, ZnO could exhibit a higher photocatalytic activity compared to TiO_2. Some studies reported a better photocatalytic activity of ZnO for the degradation of organic molecules in comparison with TiO_2 [128, 157]. However, the efficiency of ZnO based photocatalyst is still limited due to its photocorrosion upon irradiation and the poor stability under high acidic or basic conditions.

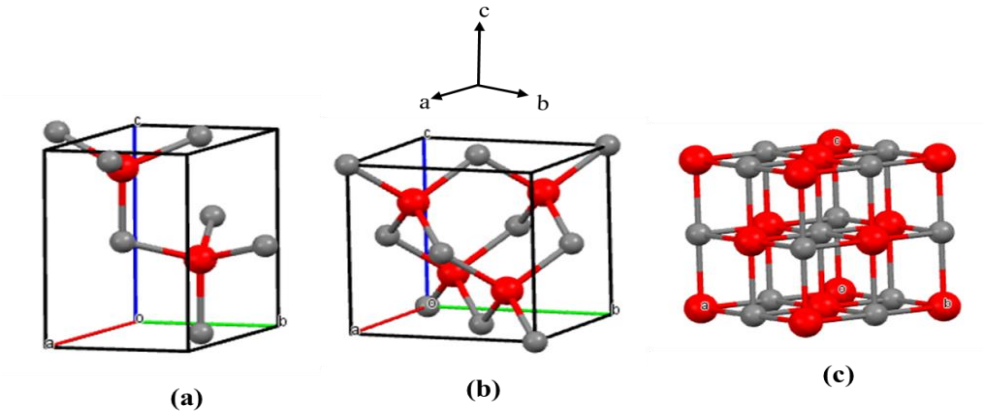

Figure 1.12 Crystal structures of ZnO, (a) wurtzite, (b) zincblende and (c) rocksalt. Zn (red) and O (grey).

Pure ZnO is a white powder and commonly referred as zinc white. ZnO occurs in three crystal forms: hexagonal wurtzite, cubic zincblende and cubic rocksalt. Under normal conditions, ZnO exhibits a hexagonal wurtzite structure which is the most thermodynamically stable phase, while the rocksalt phase is less abundant. Fig. 1.12 shows the structures of these three crystals. In both the wurtzite and zincblende crystals, the Zn^{2+} occupied in the centre of a tetrahedron that formed by four O^{2-}, while in the rocksalt, the Zn^{2+} occupies the octahedral sites. The lack of centre of symmetry in wurtzite ZnO Fig. 1.12a generates piezoelectric and pyroelectric characteristics. A polar surface is another key property of ZnO. The alternating layers of $Zn^{2+}$and O^{2-} along the c-axis results in the formation of positively charged Zn-terminated (0001) and negatively

charged O-terminated $(000\bar{1})$ surfaces, resulting in a dipole moment and polarization along the c-axis with divergence in surface energy [158].

Due to the high surface energy of the Zn-terminated (0001) plane, the anions are absorbed favourably on this polar surface. This causes a fast growth of ZnO along the (0001) direction and the formation of 1-D ZnO nanostructures such as nanorods, nanowires or nanobelts. One of the most important factors in controlling the morphology involves the inferencing relative surface activities of different growth planes by passivating the corresponding surfaces. Fig. 1.13 shows some of the typical controlled growth crystal morphologies of the 1-D nanostructures of ZnO.

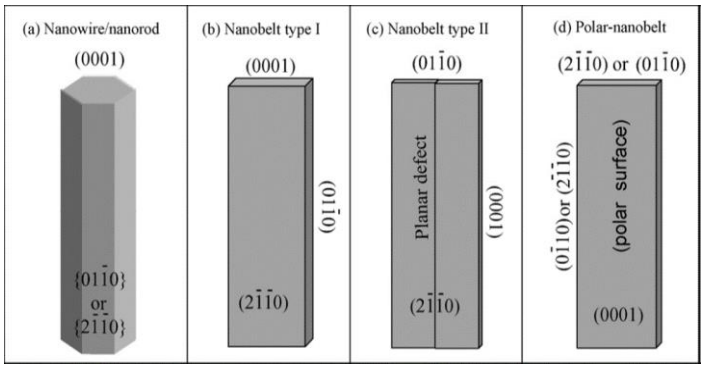

Figure 1.13 Typical growth morphology of one-dimensional ZnO nanostructures with the corresponding planes [159].

1.4.2 Synthesis of ZnO nanostructures

Due to its important physical properties, large efforts have been focused on the synthesis, characterisation and applications of ZnO nanomaterial. It can form 0-D, 1-D and 2-D nanostructures. While ZnO nanoparticles, and nanospheres [160-162] represent the 0-D nanostructures, nanorods [163, 164], nanoneedles [165], nanorings [166], nanotubes [167, 168], nanobelts [169], nanowires [170] and nanocombs [171] represent the 1-D nanostructures. 2-D nanostructures, such as nanoplates/nanosheets and nanopellets, can also be formed [172].

Different synthetic methods are employed to produce ZnO nanostructures, including chemical vapour deposition, sol-gel and hydrothermal synthesis, anodisation, electrospinning and chemical bath deposition.

Chemical vapour deposition (CVD) technique is one of the vapour phase approaches that can produce a variety of high quality, single crystalline ZnO nanostructure at relatively high reaction temperature. The reaction provides high growth rate and precise control of the epitaxial structure. The epitaxial refers to the deposition of a crystalline overlayer on a crystalline substrate. Because the substrate acts as seed crystals, the deposited film may lock into one or more crystallographic orientations with respect to the substrate crystals. However, this technique requires a vacuum system and operates at an elevated temperature. Vaporised zinc compounds are used as Zn source. Usually, two different types of zinc compounds, either zinc powder or a mixture of ZnO and graphite powder, are used as the precursors. The precursor reacts with O_2 to form crystallised ZnO on substrates held at high temperatures. Different ZnO nanostructures can be synthesised by the CVD method, including nanorods [173], nanoflowers [174] and nanocrowns [175] onto different types of substrates. The features of the ZnO nanostructure can be tuned by employing different processing parameters including the substrate temperature, reaction pressures and the catalysts used. For instance, it was found that the diameter of 1-D ZnO nanostructures decreases by increasing the substrate temperature. This was attributed to the change in the growth rate and growth kinetics which results in a faster growth of the ZnO nanostructures along specific crystal axis [176].

Sol-gel synthesis is a simple and low cost method for the production of ZnO colloids and thin films. The chemical composition and doping of the nanostructures can be controlled with relative ease. Large scale fabrication of thin films can be achieved by combining this technique with spin coating, dip coating and hydrothermal techniques.

Sol-gel/spin coating technique involves several steps: the formation of a homogeneous solution by the dissolution of the starting material (zinc chloride or zinc acetate) in a proper solvent (water). A condensation process converts the homogeneous solution into sol of low viscosity [9], which is a colloidal suspension of solid particle in a liquid phase. The hydrolysis and condensation process are affected by several parameters such as the temperature, pH, precursor concentration and type of solvent. A continuous hydrolysis and condensation reactions lead to linking the colloidal particles (sol) together, forming a gel with significant increase in the viscosity of the solution [177]. The precursor concentration and the type of solvent play a key role to determine the time of gelling [178]. The formed sol-gel can be spin coated on a planar substrate with controlled film thickness followed by annealing, sintering and/or calcinations. The thermal treatment modifies the geometry and crystal structure forming stable phase. The annealing temperature and time strongly affect the property of the produced film. High calcination temperature and long thermal treatment time produce material with perfect crystal structure, high crystallinity and large particle size [179].

Hydrothermal technique is a solution phase synthesis method using an autoclave reactor which is widely used in the preparation of ZnO nanostructures. The principle of this method will be discussed in the next chapter. It is a simple, catalyst free and low cost technique which enables a large area deposition at a temperature range of (100-300°C) [151]. Different nanostructured ZnO materials have been synthesised by this method, including nanotubes [180], nanodisks[181] and nanoflowers [182]. A reaction between zinc nitrate or acetate with suitable hydroxide such as NaOH, KOH or NH_4OH, in water yields $Zn(OH)_2.nH_2O$ solution [151]. This solution is the most popular growth solution as a source of Zn and O to synthesis ZnO nanostructure with different morphologies. The nano

morphology and dimension can be controlled by adjusting the seed concentration, reaction temperature, time and precursor concentration.

Electrospinning is a unique approach using electrostatic forces to fabricate fibrous nanostructures. ZnO nanofibers are commonly prepared by this technique. It uses viscous polymer solutions as a carrier which is mixed with zinc precursor and spun into nanofibers within a high electric field (~1 kV/cm). The produced fibre is calcined in air to remove polymer resulting in pure, crystallised ZnO nanofibers. The method can also be used to create most of the metal oxides and their mixture. There are several factors that have significant effects on the morphology of electrospun fibres, such as concentration of the polymer solution, viscosity of the solution, the degree of polymer entanglement and the electrical conductivity of the solution. The processing parameters, such as the electrical field strength, spinning nozzle diameter and the feeding rate for the solution can also affect the size and quality of the nanofibers. For instance, the diameter of the nanofiber increases as the concentration of the solution increases. On the other hand, the diameter of the nanofiber reduced by increasing the conductivity of the solution by adding salts. A high feeding rate for the solution always leads to the formation of thicker nanofibers.

The chemical bath deposition method (CBD) is a self-organised process and the reaction takes place in an aqueous solution where zinc nitrate is used as Zn precursor and hexamethylenetetramine (HMT) as a source of hydroxyl ions. CBD process is operated at a mild temperature of 85°C. Upon heating; HMT decomposes to yield OH^- which will then react with Zn^{2+} to form $Zn(OH)_2$ and then precipitates as ZnO. More details about this process will be discussed in chapter 8. The hydroxyl ions react with Zn ions to form $Zn(OH)_2$. The growth of ZnO nanostructures by CBD method is usually initiated on a seeding layer, which is deposited by several techniques such as spin coating [183]. The reaction operates at a temperature below 100°C, which makes the reaction suitable for

many device fabrication on variety of substrates. Uniformly distributed and vertically aligned 1-D ZnO nanorods are commonly synthesised by this method. The structure and morphology of the ZnO nanorods can be affected by number of parameters, including the density of the seeding layer, pH, growth temperature and growth time [184]. For instance, a thick seeding layer with a uniform ZnO nanoparticles helps to form good quality vertically aligned ZnO nanorods. On the other hand, with a thinner seeding layer, the orientation of the nanorods becomes tilted and the diameter of the nanorods is less uniformly distributed.

A part of this thesis is focused on the use of 1-D ZnO nanorods as semiconductor photoanode materials in photoelectrochemical water splitting. Being mindful of the various ZnO nanorods synthesis methods, the reliable CBD method was used to synthesise these nanostructures.

1.4.3 Applications of zinc oxide nanostructures

1.4.3.1 Photovoltaic and photoelectrochemical cells

Similar to TiO_2 nanomaterials, ZnO nanostructures have been widely used as catalysts in dye sensitised solar cells (DSSCs) and electrochemical photolysis of water. 1-D ZnO nanostructures represent one of the promising materials for efficient solar cell systems. With a large surface area, high carrier mobility and good crystallinity, 1-D ZnO nanostructures offer a good geometry for light absorption and electrolyte transportation. The large surface area of these structures increases the dye loading and light absorption. Therefore, the photoconversion efficiency could be significantly enhanced once the geometry and crystallinity of the ZnO nanorods are optimised.

ZnO nanomaterials have also been used as efficient photocatalyst in electrochemical photolysis of water to generate hydrogen. Different nanostructures of

ZnO have been exploited as photoanode material in the PEC system, including thin films, nanorods NRs, nanowires NWs and nanoparticles NPs. Yet the achieved solar-to-hydrogen efficiency is still limited. This is due to the large band gap energy of ZnO which limits its absorption in the UV light only. In order to enhance the photoconversion efficiency of ZnO, doping processes are used to reduce the band gap energy of ZnO.

Zinc oxide based nanocomposite photocatalysts have also been developed to improve the charge separation. It includes binary nanocomposites of ZnO coupled with another semiconductor. Recent work shows that composite ZnO/TiO_2 nanoparticles was a promising system for producing H_2 through the water splitting process [65, 185]. Nanoparticles of composite ZnO/TiO_2 photocatalysts were prepared by sol-gel method using titanium butoxide and zinc nitrate as precursors. The results show that, the hydrogen production increased by six times when 10 wt% of ZnO was added to TiO_2 photocatalyst in comparison with the pure TiO_2 as the result of the enhanced photogenerated electron-hole separation. The photoexcited electrons from ZnO are transferred to the conduction band of TiO_2, which is less negativity that the conduction band of ZnO.

1.4.3.2 ZnO gas sensors

ZnO nanomaterials have been widely used as active layers in gas sensing devices. The physical and chemical properties of ZnO surfaces can be strongly affected by the adsorption of chemical species. The adsorbed species change the surface charge density, surface electrical conductivity and optical response and vibration properties of the ZnO. The large surface area of nanomaterials offers additional advantage of high sensitivity as more molecules can be adsorbed.

Different types of ZnO nanomaterial based sensors have been developed, including gas, temperature, pressure, humidity and chemical sensors. The mechanism of

gas sensor is based on the conductivity change upon gas exposure, which can be measured by an electrical current passing through the ZnO nanostructure. In this case the oxidation or reduction state of the ZnO will be affected by the adsorbed molecules, therefore the conductivity of ZnO film will be also influenced.

Recently, 1-D ZnO nanorods or nanowires have widely used in the gas ionization sensors devices. In these devices, the gas species are identified by the ionisation discharge voltages while their concentration measured by the discharge currents. Carbon nanotubes were the first nanomaterial used in gas ionization sensor. However, this material has poor chemical stability, which is easily oxidised in oxygen environment and degraded at high current. ZnO nanostructures have been found to have a high electrical stability owing to its high melting point (1975°C) and chemical resistance against oxidation. However, the pure ZnO based gas ionization sensors requires a high discharge voltage to breakdown the targeted gas species. This is due to the intrinsic low conductivity of the ZnO nanorods, which can be improved by doping with Na^{+}, Al^{3+} or Y^{3+} ions

1.4.3.3 Optics and electronics

ZnO nanostructures have shown some key optoelectrical properties. ZnO nanostructures, including nanorods, nanowires and epitaxial layer, have been developed for optical and electron stimulated emission applications, such as light emitting diode and blue lasers. With the high exciton binding energy of ZnO (60 meV), it has been demonstrated that, ZnO nanomaterials can be used as a lasing material to produce intense, monochromatic and coherent light sources. Compared to bulk semiconductor, the nanostructured semiconductor has the additional benefit of being more efficient in stimulated emission and lasing[71]. Meanwhile, the threshold potential for lasing will also decrease with

decreasing in dimension of the materials. Therefore, ZnO nanostructures become an ideal candidate for the development of semiconductor optoelectronic devices.

1.5 Thesis aims

The present study has been undertaken with the aim of developing the synthesis of nanostructured materials based on TiO_2 and ZnO semiconductors in their medical and photocatalytic applications. This thesis consists of ten chapters; the first chapter presents a review about metal oxides nanomaterials. The principles of several synthesis methods, including anodisation, hydrothermal synthesis, chemical bath deposition (CBD), spin and dip coating and molten salt synthesis (MSS), are the experimental objective in this thesis, which will be explained in chapter 2. The growth mechanism of the synthesised nanomaterial has investigated by variety of techniques including, scanning electron microscope (SEM), powder X-ray diffraction (XDR), energy dispersive X-ray spectroscopy (EDX), UV-Vis spectroscopy, UV-Vis refractometer, photoluminescence spectroscopy (PL) and electrochemical impedance spectroscopy (EIS). All these techniques will be described in chapter 3.

Understanding the growth mechanism and precise control of the synthesis conditions are necessary to manipulate the morphology of semiconductor nanomaterials. In Chapter 4, I demonstrate a new method to control the morphology of TiO_2 nanotube. Novel nanotube shape, such as nanobottles, has been created in order to demonstrate the effect of the tube morphology, including shape, diameter and length, and tube coating on the kinetics of drug loading and release.

Several strategies have been followed in order to enhance the photocatalytic performance of the photoanode material in PEC system based on TiO_2 and ZnO. First, in chapter 5, I demonstrate the optimized synthesis of 1-D rutile TiO_2 nanorods structure

through the hydrothermal synthesis method. The effect of the hydrothermal conditions on morphology, crystal orientation and photocatalytic performance of films has systematically investigated. In order to improve the electron-hole separation, in chapter 6, the optimized nanorods were treated through processes of reduction-oxidation cycles. In order to improve the visible light absorption, in chapter 7, Cu doped titanium oxide nanorods TNR_S were also synthesised by one step hydrothermal method. The possible mechanisms of the photocatalytic performance enhancement are discussed.

In Chapter 8, a new design of a 3-D optical waveguided photoanode was created and tested for its PEC performance. The electrode is created based on a transparent conductive glass rod substrates decorated with ZnO nanorods, which allowed the light to be guided through the glass and side emitted to excite the ZnO. Controlling an optimum coating of the ITO conductive layer on such long substrates is a technical challenge. Nevertheless, we proved that it is possible to use such a 3-D photoanode in a PEC system. With further improving the quality of the conductive layer coating, the efficiency of the PEC performance could be enhanced.

In chapter 9, I demonstrate the synthesis and characterisation of copper titanate perovskite material. The influence of the synthesis conditions on the morphology and properties is studied. The thesis conclusions and future work were presented in chapter 10.

Chapter 2 Synthesis of nanostructured metal oxides

2.1 Abstract

This chapter describes the several experimental setups for synthesis of nanomaterials. The principles behind several synthesis methods used to create different nanomaterials in this project are discussed. The details about sample preparation techniques are presented.

2.2 Introduction

Nanotechnology involves the synthesis, design and applications of physical, chemical and biological systems from a scale of individual atoms or molecules to structures of approximately 100 nm. In general, there are two approaches in creating nanostructures and nanomaterials: top-down and bottom-up [118, 186, 187]. The top-down technique sequentially manipulates a bulk material to obtain nanomaterials. The ball milling technique is a typical example of the top-down method of making nanoparticles. The bottom-up approach refers to the build-up of a nanomaterial atom by atom. The hydrothermal technique is one example of a bottom-up synthetic method. Both synthetic routes have importance in nanotechnology. However, the top-down approach relies on the tools used so there are limitations when creating structures smaller than 100 nm. For the bottom-up method, the morphology of the deposited of metal oxide nanostructures can be manipulated by the experimental conditions.

2.2.1 Anodisation method for top-down synthesis of TiO_2 nanotubes

The anodisation process is one the most efficient ways of creating highly quality, well ordered nanotubular arrays. It is an electrochemical process that converts the metal

surface into an anodic oxide. It is simple, reliable and does not require sophisticated synthesis facilities.

The anodisation is an electrochemical oxidation process. A schematic view of the anodisation setup is shown in Fig. 2.1. It is accomplished by immersing the metal plate into a corrosive or oxidative electrolyte bath and passing a DC electric current through the medium with the target plate acting as the anode (thus the process is called anodisation). This method is commonly used for creating thin, densely packed oxide films on metal substrates. This is known as a barrier type film, which acts as a barrier to prevent the flow of ions and electrons. As the oxide film gets thicker, the oxidation electric field strength at the metal surface decreases. It hinders the oxidation process until it ceases, achieving the maximum thickness of the oxide [188]. Aqueous solutions of sulphuric, phosphoric or acetic acid are typical electrolytes capable of forming barrier type TiO_2 films [189].

To synthesis TiO_2 nanotubes (TNTs) *via* the anodisation of a titanium sheet, a fluoride containing solution has been found to be the most effective electrolyte since it can dissolve the TiO_2, resulting in a very thin, porous structure. This dissolution of the metal oxide layer at the solid/liquid interface is directed by the anode bias (positive). It attracts the F^- anions towards the Ti plates, creating the porous structure. The formed array of titanium oxide TNTs is perpendiculair to the Ti substrate. A typical electrolyte uses organic solvent (ethylene glycol) with added F^- anions and small amount of H_2O. The concentrations of F^- anions and H_2O are controlled to balance the kinetics of anodisation and dissolution.

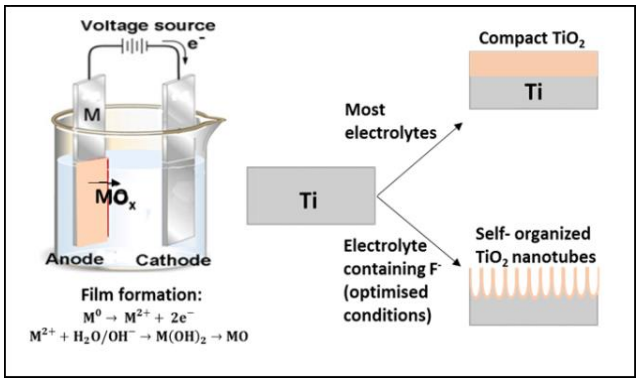

Figure 2.1 Schematic set-up for the anodisation unit consists of two Ti electrodes with applied voltage.

The formation of the anodic oxide layer under an applied electrical field is known as field assisted anodic oxidation (Equation 2.1). In this process, water is used as the source of oxygen to form the metal oxide layer. As the thickness of this oxide layer is increased, the anodic voltage applied at the metal/metal oxide interface will decrease until the oxidation stops. Thus, this oxide layer is named as the passivation layer. The concentration of water in the organic electrolyte together with the oxidation voltage and separation between two electrodes will determine the rate of the oxidation, which can be quantitatively monitored from the anodisation current.

$$Ti + 2H_2O \rightarrow TiO_2 + 2H_2 \qquad \text{(Equation 2.1)}$$

$$TiO_2 + 6F^- + 4H^+ \rightarrow (TiF_6)^{2-} + 2H_2O \qquad \text{(Equation 2.2)}$$

The added fluoride ions will facilitate the dissolution of TiO_2, shown in equation 2.2. The production of the fluorine complex in the electrolyte is assisted by the electric field, which moves the negatively charged F^- ions toward the Ti plate (anode). They will react with the TiO_2 to form soluble TiF_6^{2-} species, causing field assisted corrosion and the formation of porous structure. This will also cause the thinning of the TiO_2 barrier layer

at the centers of the pores which allows a continuous local oxidation. As a result, nanostructured channels are formed through the oxide layer [190]. The concentration of F^- will affect the dissolution rate. If the dissolution is too fast, nanotubes with large diameters, short length and thin walls will be formed. In some extreme cases, the nanotubular structure will collapse if the wall is too thin. The continuous dissolution is competing with the continuous oxidation with their rates to be independently controlled by the concentrations of F^- and H2O together with the applied voltage. When the oxidation rate at the metal/oxide interface is equal to the chemical dissolution rate at the oxide/electrolyte interface, the nanotubes grow at a steady rate.

2.2.1.1 The effect of anodisation parameters on the tube morphology

It is well established that the properties of nanotube arrays depend upon their specific morphology (length, wall thickness, wall roughness, pore diameter and tube-to-tube spacing). The geometric features of nanotube arrays can be controlled by a variety of parameters such as anodisation potential, electrolyte composition as well as anodisation time and temperature.

The chemical composition and the pH of the electrolyte have a significant influence on the resulting nanotubes length [191]. The pH of the solution influences the dissolution rate of the oxide layer, as it can be seen from Equation 2.2. In an aqueous electrolyte, the anodisation and dissolution processes quickly reaches the equilibrium state, therefore short nanotubes are obtained [192]. Extended tube length can be achieved when using an organic electrolyte, owing largely to the suppressed mobility of the fluoride anion, reducing chemical dissolution [193].

The applied voltage strongly affects the electric field across the oxide layer and results in different thickness and tube diameter. Thicker layers and larger diameters can

be obtained by using higher voltages. It has been established that the tube diameter is linearly proportional to the applied voltage, following equation 2.3 [194].

$$OD = 2f_g V \quad \text{(Equation 2.3)}$$

In this equation, *OD* is the outer diameter, *V* is the anodisation voltage and f_g is the growth factor, which is constant for Ti metal and defined as *d/V*, where *d* is the maximum oxide thickness at an applied voltage *V*.

$$f_g = d/V \quad \text{(Equation 2.4)}$$

OD is determined by the inner diameter, *ID*, and the wall thickness, *W*, multiplied by a factor of 2 (Equation 2.5).

$$OD = ID + 2W \quad \text{(Equation 2.5)}$$

Fig. 2.2 illustrates the tube dimensions: the outer and inner diameters, the wall thickness and the barrier layer thickness.

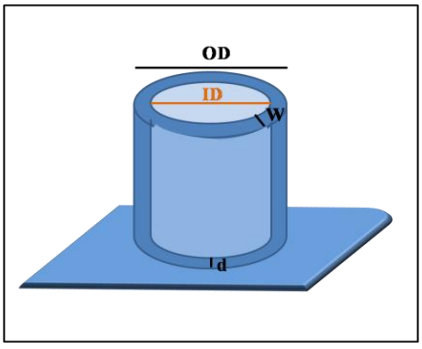

Figure 2.2 Schematic diagram of the nanotube dimensions; OD is the outer diameter, ID is the inner diameter, W is the wall thickness and d the barrier layer thickness.

The linear dependence of the tube's outer diameter as a function of voltage bias allows precise control of the shape and morphology of the nanotubes. The combination of equations 2.3 and 2.4 gives:

$$OD=2d \qquad \text{(Equation 2.6)}$$

The outer diameter of the nanotube equals the double of the maximum thickness of the oxide barrier layer as shown in equation 2.6. Thus, a higher anodisation voltage results in nanotubes with a thicker barrier layer and larger outer diameter.

By fixing the experimental anodisation parameters such as the electrolyte composition, temperature and the applied voltage, the tube length can be controlled with the anodisation time [195]. When the anodisation process is carried out in aqueous solution, where the dissolution rate at the nanotubes top is fast, TNTs of a few micrometers in length are achieved within a short time (up to 2 hours). In contrast, the growth in organic electrolyte, where the growth is much slower and the dissolution is not as significant as in the aqueous solution, long nanotubes up to 100 μm can be grown by extending the anodisation time from several hours up to a day.

2.2.1.2 The development of the anodisation method for creating TiO_2 nanotube

The generation of nanoporous and nanotubular arrays of titania through the anodic oxidation of titanium metal has been developed through further understanding of the growth mechanism. Despite this, measurements of oxidation and dissolution rates are complicated. A qualitative understanding of the mechanism is well established. The development of the synthesis of TiO_2 nanotubes can be summarised in four main stages:

First generation of TiO_2 nanotubes

In 1999, Zwilling and co-workers reported the synthesis of nanoporous anodisation of titania using a diluted solution of HF [196] and the formation of TiO_2 nanotubes was reported in 2001. Due to the aggressive etching action of HF, most of the oxide layer was dissolved, therefore the film thickness obtained was limited to only 0.5 µm.

Second generation of TiO_2 nanotubes

By replacing the acidic electrolyte, HF, with a less aggressive solution with higher pH containing fluoride salts, such as NH_4F, the rapid rate of titania dissolution was reduced. The achieved film thickness was 2-3 µm [100, 197] It was noted that using a water based electrolyte forms nanotubes with irregularities along the wall as the result of fast oxidation.

Macak and colleagues [117] explained that as the oxidation happened at the bottom of the nanotube, the pH at the bottom is expected to be lower than the pH of the electrolyte. They suggested that this pH gradient is responsible for the growth of longer nanotubes and its effects became significant by adding $(NH_4)_2SO_4$ in NH_4F electrolyte. For further increase in the length of the nanotubes, the same authors considered applying a voltage ramp at the beginning of the anodisation process. This would enhance the pH gradient from the bottom to the top of the tubes, which allows the oxidation process to occur for a longer time.

Third generation of TiO_2 nanotubes

The third generation of the TiO_2 nanotube was prepared using organic electrolytes, some of which were nearly water free. The dissolution rate of the oxide formed was minimised. These tubes exhibited smooth walls with no ripples. It is assumed that using viscous

electrolytes would reduce the ionic diffusion and increase the pH gradient between the bottom and top of the tube. The film obtained in this case exhibited a thickness of up to 7 μm. The smoothness and regular morphology of the tube wall are attributed to the lower diffusion coefficient of the electrolyte, suppressing the pH bursts at the bottom of the pore when the anodisation is carried out in aqueous electrolyte.

Fourth generation of TiO_2 nanotubes

In order to investigate the effects of using fluoride-free based electrolyte in the anodisation of Ti on the morphologies and aspect ratios of the nanotubes obtained, Nakayama and co-workers [198] used various electrolytes based on acids (oxalic, formic, hydrochloric and sulfuric). The nanotubes formed by these methods showed disordered nanotubes growing in bundles rather than the regular arrays, with a significant amount of carbon detected in the tube. The formation of these tubes started at the edge of the titanium surface, where there is a higher defect density providing active reaction sites for the growth of the oxide layer.

In this project, TiO_2 nanotubes and nanobottles were created by anodic oxidation of titanium plates targeted for the application of drug release. I used the controlled anodisation voltages to manipulate the diameters of the nanotubes to form the narrow neck and wide body of the nanobottle. In order to preserve the morphology of the bottleneck, an effective hydrophobic coating was applied.

2.2.2 Hydrothermal nanostructure synthesis

The hydrothermal synthesis method is a wet chemical reaction taking place in a closed system with solvent under high pressure at elevated temperature [199]. It has been widely employed in inorganic synthesis for creating crystalline compounds. An understanding of

mineral formation in nature under high temperature and pressure in the presence of water has promoted the development of the hydrothermal technique. Laboratory studies have also helped earth scientists to determine complex geological processes for the formation of rocks, minerals and ore deposits [199, 200].

Hydrothermal reactions occur at temperatures above the boiling point of water and at pressures above 1 bar, raised by the evaporation of solvent and from the gases generated from the synthesis. These conditions come close to, or surpass, the critical point of the water at which its fundamental properties change. The dielectric constant of water decreases significantly as water is heated and approaches that of non-polar solvents. These conditions will affect the solubility of the precursors. Therefore, by tuning the synthesis parameters, specific solvent properties can be obtained to improve the solubility of chemicals that are otherwise insoluble under ordinary conditions.

High reaction pressures can be obtained using a sealed reaction vessel called an autoclave as shown in Fig. 2.3. The autoclave consists of a Teflon cup (with a high corrosion resistance) called a liner (6) covered with Teflon cover (7). The liner is filled with the desired reaction precursors and water. The cup is placed into a stainless steel autoclave (1), which is then sealed by stainless steel top plate (3) and stainless steel lid (2). For maximizing the lid sealing, a stainless steel bolt is a key part attached on the top of the stainless steel lid (5). The system then can be heated to temperatures between 100°C and 250°C, which causes solution expansion inside the vessel. The temperature can be elevated above the boiling point of water, reaching the pressure of vapour saturation. The temperature and the amount of solution added to the autoclave (fill factor) largely determine the internal pressure produced. Although the reaction temperature inside the autoclave cannot be measured directly, it can be assume that the temperature inside the autoclave reach the same temperature as the environment (oven) through the reaction

process, since the normal hydrothermal reaction takes several hours and heating temperature was slowly ramped up.

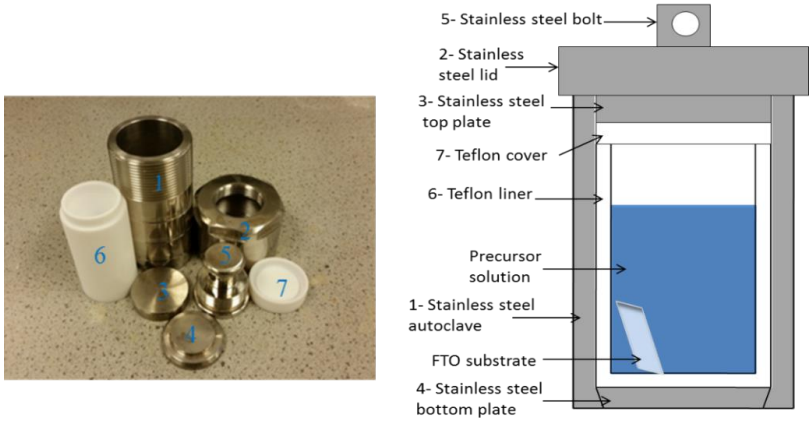

Figure 2.3 Schematic representation of an autoclave used for the hydrothermal synthesis.

Due to the enhanced purity and relative low synthesis temperature associated with hydrothermal synthesis, this technique has found an important place in several areas of material science and technology in recent years. It is used for cystallisation of materials [201], material processing [202] and metal oxide film preparation [203], which is the main interest of this work.

The preparation of metal oxide nanostructured films by the hydrothermal method requires precise control of the rates of nucleation and crystal growth. Nucleation events in solution must be suppressed whilst crystal growth on the substrate should be promoted, allowing for high quality film deposition. This control can be obtained by carefully determining the reaction temperature and duration. Additionally, properties of the substrate remain a key factor that affects the film deposition, for instance fluorine doped tin oxide (FTO) has been found to be the ideal substrate for the growth of 1D TiO_2 nanorod (TNR) films. The FTO crystal acts as a seeding layer to promote heterogeneous crystal growth of TiO_2 on the substrate surface [46]. Therefore, for the target of building

nanostructure arrays with designed morphology, controlling the reaction condition and designing the reaction process is a key to satisfy the needs of different applications. Various structures of nanomaterials can be synthesized with hydrothermal process, including powder, fiber, single crystals and metal oxide film preparation [203].

Different dimensions of metal oxide films such as 1-D nanorods and 2-D nanowalls can be prepared by the one step hydrothermal method. The hydrothermal synthesis can be also performed in multi-step-graded growth, where the previously synthesised arrays are used as template for the growth of secondary structure. It can even synthesize multi-metal oxide nanoarrays by reacting two or more kinds of metal salt together in the hydrothermal process. In such a synthetic strategy, many novel nanoarrays were fabricated [133, 204]. Thus, this hydrothermal synthesis method is expected to be widely used and it also offers new opportunities for the design of new types of highly efficient nanoarrays materials.

In this work, the hydrothermal method was employed for the synthesis of 1-D rutile TNRs structure. The effect of the reaction conditions has been investigated systematically in order to optimize the photocatalytic properties of the grown film. The method was also used for creating Cu doped TNR film in order to enhance the photocatalytic activity of this structure.

2.2.3 Chemical bath deposition nanostructure synthesis (CBD)

Chemical bath deposition (CBD) is an alternative method used for the deposition of metal oxide semiconductor nanostructured films from aqueous solutions. The deposition takes place in a beaker containing a growth solution and a suitable substrate. The reaction is usually carried out at a temperature between 50-95ºC [205]. The film thickness, deposition

rate and crystallite quality can be controlled by varying the seeding concentration, pH of the solution, growth temperature and concentration of the growth solution.

In this study, films of vertically oriented ZnO nanorods were grown via CBD. The deposition of a ZnO seeding layer on the substrate was required when the substrate employed was not a Zn plate. This effect can be explained as two types of nucleation taking place in the solution during CBD, namely homogeneous and heterogeneous nucleation. The homogeneous nucleation occurs in the solution where rapid precipitation forms large particles throughout the solution. In the presence of a substrate, heterogeneous nucleation takes place on the substrate where particles grow slowly to form a thin film. Substrate pre-treatment, such as depositing of ZnO nanoparticles as seeding layer, is a key factor in this process to promote the heterogeneous reaction over the competing homogeneous reaction in the solution.

In this work, the ZnO nanorod films were deposited on different substrates, such as Ti plates, flat glass and conductive glass rods. For the deposition of a ZnO seeding layer on flat substrates, spin coating is a convenient way to apply a thin layer of ZnO particles. In this technique, a polymer solution (PVA solution) containing a zinc precursor (zinc acetate) is used as seeding solution. A drop of the seeding solution is applied on the substrate surface. The spin coating system used in this work provides centrifugal force to spread the film equally and to dry the formed layer immediately. For the glass rode substrates the deposition of the seeding layer was carried out using a dip coating method.

Following the coating step, the seeding layer was annealed (temperature range 350–450ºC) in air to decompose the polymer carrier used in the seeding solution (to increase the viscosity), forming ZnO particle seeds. Zinc acetate dihydrate is commonly used as seed precursor ($Zn(O_2CCH_3)_2(H_2O)_2$). During annealing, zinc acetate will decompose into nanocrystalline ZnO seeds.

The growth solution consists of a mixture of zinc nitrate hexahydrate and hexamethylene tetramine (HMT). HMT decomposes at the temperature at (~85ºC) to form OH^- in water, causing the increase of the solution pH. The details of HMT decomposition process will be discussed in chapter 8. In an alkaline solution, Zn^{2+} ions are readily forming zinc hydroxide ($Zn(OH)_2$, which subsequently forms ZnO crystals at mild temperatures. The selective growth of ZnO crystal facets strongly depends on the density of the seeds and the growth conditions. As the preferential growth direction for ZnO is along the polar face of the (0001) plane, nanorods and nanowire arrays with distinctive hexagonal cross section were typically observed. The (0001) planes of wurzite ZnO crystals are normally terminated by either a plane of Zn^{2+} or a plane of O^{2-}, creating the surface polarisation. This selective growth on the polar crystal plane is due to the preferential adsorption of Zn^{2+} or OH^- alternatively, depending on the termination of the (0001) plane. The growth was normally performed in an oven in air at a fixed temperature of 85ºC.

2.2.4 Dip coating and spin coating procedures

Dip or spin coating techniques are simple and effective for the deposition of thin films on a variety of substrate materials. In the dip coating process shown in Fig. 2.4, the substrate is immersed in precursor solution and then withdrawn at a certain rate, under well-defined temperature and atmospheric conditions. The film thickness obtained is directly affected by the withdrawal speed as well as the viscosity and concentration of the coating solution. The dip coating method can be used for non-planar substrate without restriction on the shape and size of the substrate.

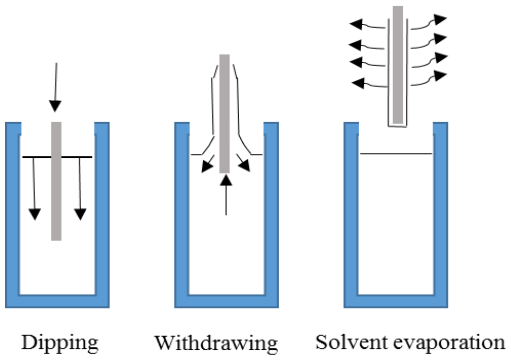

Figure 2.4 Stages of the dip coating process.

The spin coating technique is used for making thin films on small and relatively flat substrates. The precursor reagent is dissolved or dispersed in solvent and then deposited onto the surface of the substrate. The substrate is spun around the axis perpendicular to its surface, allowing the removal of excess coating solution, leaving a uniform layer on the substrate surface. The key stages of the spin coating process are shown in Fig. 2.5. The acceleration and final spin speed, together with the viscosity of the solution determines the quality and thickness of the coated thin film. The film is subsequently converted into nanoparticles by annealing at certain temperatures.

For both dip and spin coating methods, a liquid phase solution is used as coating solution. The vapor pressure of the solvent should be adjusted in order to achieve a uniform coating with required thickness. In the situation that one coating of thick layer could affect the overall morphology (smoothness) of the coated film, repeated coating will need to be applied in order to achieve the required thickness. If preformed nanocrystals (such as quantum dots) are used for coating, a suspension, instead of solution, can also be used. In such cases, the viscosity of the solvent or solution must be carefully managed.

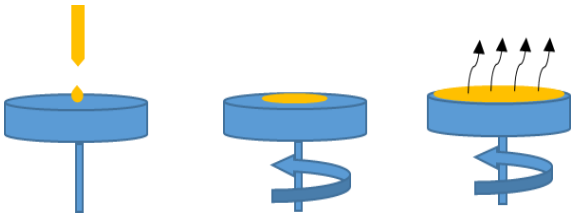

Figure 2.5 Stages of the spin coating process.

2.2.5 Chemical vapour deposition (CVD)

Chemical vapour deposition techniques involve heterogeneous reactions between the precursors in the gas phase and the formation of a thin solid film upon substrates. The simple setup of a CVD for creating nanomaterials is shown in Fig. 2.6. The reaction normally happens at raised temperatures controlled in a tube furnace. Reactive gas is supplied into the reaction tube. A quartz boat is used to hold the precursors and the substrate. At high temperature, the chemical vapor will decompose the precursor to metal oxide. The metal oxide then is deposited on the substrate surface and grows into nanomorphology.

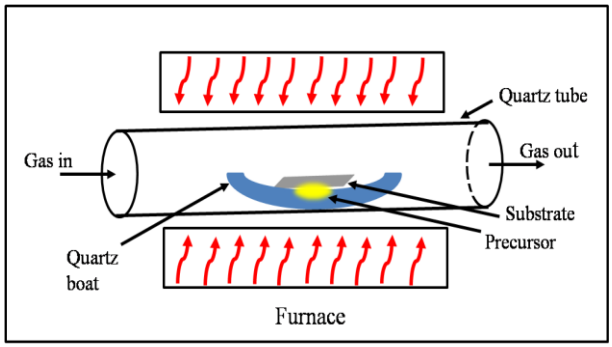

Figure 2.6 Schematic diagram of a CVD deposition furnace.

The rate of the film growth by the CVD technique is determined by the substrate temperature, reactor pressure and the gas phase reaction rate that occurs upon the substrate. At low reaction temperatures, the film growth rate is determined by the kinetics

of the chemical reactions in the gas phase or on the substrate surface. At high temperatures, on the other hand, the film growth rate is determined by the mass transport of the reactants through the boundary layer towards the growth surface and becomes nearly independent of temperature. Meanwhile, the effective growth rate could decrease due to the precursors desorbing from the film surface and/or deposition of reagents on the reactor wall.

2.2.6 Molten Salt Synthesis of Nanomaterials (MSS)

Molten salt synthesis is a unique method for the production of metal oxide powders [206, 207]. During MSS, a low melting point salt is added to the reactants, which are then heated above the melting point of the salt. This allows the salt to act as a solvent to improve the mass transportation required for the synthesis of nanomaterials.

Molten salt synthesis is different from the flux method, which uses a small amount of salt (typically a few percent of the total weight), to enhance the rates of the solid state reactions. Conversely MSS uses a much greater amount of salt as the solvent to control the product size and shape. Chloride and sulphate salts are typically used in MSS due to their suitable melting point and thermal stability. In many cases, a mixture of salts is used to lower the liquid formation temperature [208]. For instance, NaCl and KCl have melting points of 801°C and 770°C respectively. In contrast, a eutectic composition of NaCl and KCl has a lower melting point of 650°C. A low melting temperature is one desired property of the salt, in addition to its chemical stability, ease of removal and, most importantly, low vapor pressure in the heating temperature range. Furthermore, the chosen salt must not react with the reagents, which potentially lead to undesirable side-reactions [207].

In a typical molten salt synthesis process, a complex oxide product is prepared by the following procedure. A mixture of the reactants and the salt is ground to create fine powders and then heated to the temperature above the melting point of the salt. At this point, the salt becomes molten which facilitates the mass transportation and mixing of the reactants in the solution and particles of the product begin to form. The characteristics of the particles synthesised are controlled by adjusting the starting oxides, heating temperature and synthesis time [209]. Products with almost pure phase can be obtained at relatively low temperatures, in comparison to synthesis without the assistance of the molten salt. Increasing the sintering temperature and holding time will increase the particle size with improved crystallinity [210]. Once the reaction is complete, the product mass is cooled to ambient temperature and then washed with deionised water (DI) to remove the salt before being dried. As the MSS reaction is normally operated under ambient condition in air, it becomes widely used for synthesising novel metal oxides.

MSS is also commonly used for growing single crystals. When the reactants are completely dissolved in the molten salt, a uniform liquid is obtained. With controlled cooling process, solid particles nucleate homogeneously in the liquid phase. Large single crystals can be obtained by limiting the nucleation density during the cooling process. Therefore, high solubility of reactant components within the salt is required. Control of the cooling rate is also very important when growing single crystals, since it determines the nucleation density and the final size of the crystals. A slow cooling process encourages sufficient Ostwald's ripening, which allows the coalescence of small crystals (large surface energy) to form large crystals. An increased solubility of reactant (by selecting different types of salt solvent) will also increase the crystal size by delaying precipitating products. On the other hand, if the target products are fine powders, such as nanoparticles,

rapid cooling and less solubility will be required, in order to restrict the Ostwald's ripening during the growth process.

MSS technique was used in this work for the creation of titanate single crystals and nanoparticles. The formed product in this work was copper titanate, $CuTiO_3$. Due to the limited choice of solvent for Ti compound, there is very limited success to synthesis titanate from sol-gel method. With high thermal stability of TiO_2, extreme high temperature (> 1500°C) is normally required for the synthesis of titanate. Thus, we adapted the MSS technique specifically for the produce titanate at relative low temperature (< 1000°C), using NaCl as the molten salt. We expected that titanate would have both the advantage of visible light sensitivity and chemical stability inherited from metal oxide and TiO_2, which could potentially offer a strategy for creating a new class of chemically stable, narrow band gap materials.

Chapter 3 Characterisation Methods and Instrumentations

3.1 Abstract

The material characterisation techniques used for the characterisation of the synthesised nanostructures are presented in this chapter. The morphology of the prepared films was characterised through scanning electron microscope (SEM). Chemical compositions of the samples were characterised by energy dispersive X-ray diffraction (EDX). Crystal structures and their orientation were studied by powder and single crystal X-ray diffraction (XRD). Optical properties were studied with a UV-Vis spectrometer. Photoluminescence (PL) emission spectra were recorded through a photoluminescence spectroscopy. Electronic properties were investigated according to the measurements of the electrochemical impedance of the film. The photocatalytic activity was tested using photocatalytic water splitting in a photoelectrochemical cell.

3.2 Scanning electron microscopy (SEM)

SEM is one of the commonly utilised instruments to investigate the morphologies of nanostructures. SEM is similar to an optical microscope. The main difference between the two techniques resides in the use of photons (visible light with wavelength from 400 to 700 nm) in an optical microscope, whereas SEM uses a high energy electron beam to interact with the sample atoms and to produce signals. These signals contain information about the sample surface topography. The electron beam used in SEM exhibits wave properties. A beam of 30 keV corresponds to a subnanometer wavelength (0.0413 nm) can be used to extend the resolution of an optical microscope to reach 5-20 nm. While, the typical resolution of the optical microscope is limited to 200 nm, which is limited by the light wavelength and its diffraction. Thus SEM is a key technique for characterising

the morphology of nanomaterials. The images obtained though SEM can be used for the measurement of diameter and length of the studied samples.

SEM was developed in 1935 by Max Knoll at the Technical University in Berlin [211]. Knoll used an electron beam of 0.1-1 mm in diameter to scan a sample in a modified cathode ray tube. Nowadays the electron beam used for SEM imaging has very narrow diameter ranging from 3 to 10 nm [212].

3.2.1 Principle of SEM and its signal detection.

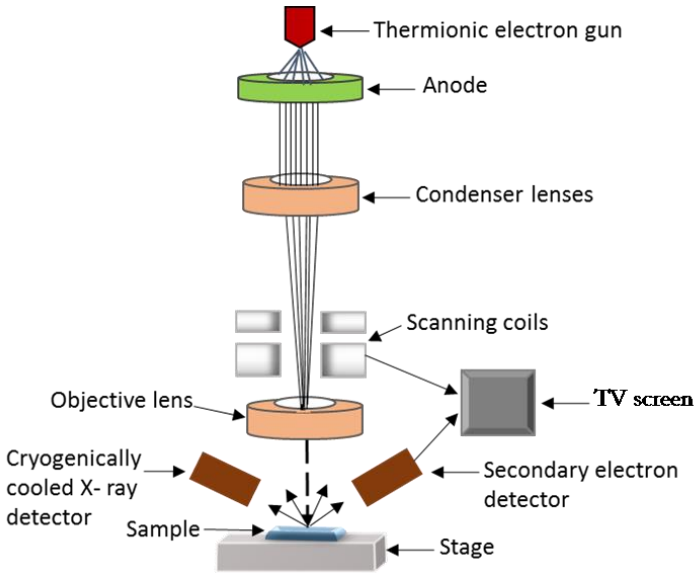

Figure 3.1 The structure of an SEM [213].

Fig. 3.1 displays a schematic view of the SEM instrument. The primary electrons are generated from the thermionic emission from a hot tungsten filament in the electron gun. The emitted free electrons are accelerated by the positive voltage bias on the anode, which are then focused by the condenser lenses. Set of scanning coils are used to drive the scanning of the electron crossing the sample. The objective lens help to project the focused electron beam onto the sample.

When the primary electron beam (10-30 keV) interacts with the sample, electrons either reflect or lose their energy due to the ionisation of the sample. The high kinetic energy of the primary electron beam is required in order to overcome space charge effects resulted from the repulsion between electrons. At lower kinetic energy, the space charge effects will reduce the focusing quality of the electron beam. The reflected electrons, also called back scattering electrons, are elastically scattered with their kinetic energy identical to the primary electron. Meanwhile, the ionised sample subject to the Auger process to generate the secondary electrons with lower kinetic energy (200-500 eV).

The intensity of the backscattered electrons depends on the electron density of the atoms of the sample. Heavy metal elements with higher electron density have higher electron scattering cross section, forming bright images. Therefore, the backscattered electron is used to distinguish the heavy elements in the sample. However, due to the high kinetic energy of the backscattered electrons, the interaction volume within the sample is normally on the scale of 1 μm, defined by the electron mean free path. This large interaction profile limits the spatial resolution of the backscattered electron signal.

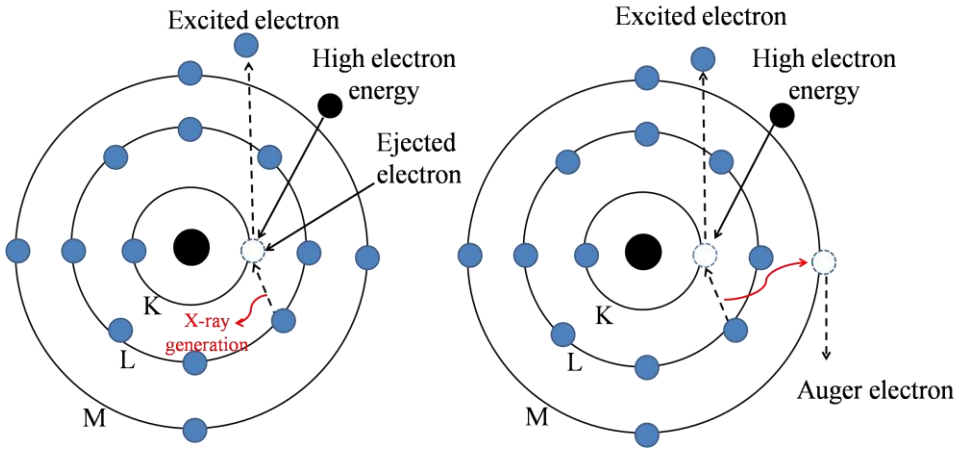

Figure 3.2 Electron excitation, (a) x-ray emission processes and (b) secondary electron generation caused by the impact of the primary electrons.

Secondary electrons are the most common signals observed for high resolution topographic images. The detailed processes for the generation of secondary electrons and X-ray emission from the sample are illustrated in Fig. 3.2. After a core level electron of the sample is excited, an upper level electron will relax to fill in the core level. This will release some energy determined by the energy difference between the corresponding upper level and the core level. This energy can be either used for the release of an electron (Auger electron) from a higher level or as the X-ray fluorescence emission which can be recorded by the energy dispersive X-ray spectroscopy (EDX). In comparison with the primary electron, the secondary electrons have much lower kinetic energy, in the range of 10-300 eV. Based on the characteristic of electron mean free path, such medium energy electrons can only be emitted from a depth of 5-20 nm into the sample, which guarantees the ultimate resolution of the SEM image of the morphology of the sample.

The secondary electron detector is normally mounted horizontally, avoiding in sight with the backscattered electron. The secondary electrons are subjected and collected by the positive voltage bias (500 V) applied at the entrance of the electron detector. They will then be accelerated towards a phosphor screen to convert the electron beam intensity to visible light, which is directly measured by a photomultiplier mounted on the back. The signal from the photomultiplier forms the topography image of the sample.

The energy of the X-ray is quantised due to the quantisation of energy levels, which is determined by the nuclear charge and the electron density. So, it can be used for identifying each element. The intensity of the X-ray fluorescence is proportional to the amount of element in the sample. As such, a combination of information on the energy and intensity of the X-ray emission is used to determine chemical composition.

The heart of an X-ray detector is a solid state Si device. It consists of a p- and n-type semiconductor materials sandwiched between insulating layers, forming a PIN

diode. The detector converts the X-ray energy into voltage signals. The most common detectors are made of Si (Li) crystals which operate at low voltage to improve the sensitivity. The Si (Li) detector is cooled using liquid nitrogen to reduce noise and to increase the sensitivity.

3.2.2 Optimise the resolution of SEM observation.

In order to obtain the best SEM image with ultimate resolution and high signal to noise ratio, it is important to understand the effect of the operation parameters of the SEM in general. The overall resolution of an SEM image is normally limited by the space charge effects, which can be significantly reduced by increasing the beam energy to 20-30 keV and to reduce the beam intensity (probe current) to the level of 10^{-6} A. If the beam profile is distorted from a round profile (stigmatism), the focus cannot be achieved for all directions. This distortion can be corrected by adding an additional electromagnetic field from stigamtor controller [212]. The working distance, defined as the distance between the final condenser lens and the sample, affects the spherical aberration of the imaging system. In the electron beam the electrons travelling in the centre are less refracted that those travelling near the edge. To reduce the spherical aberration, a short working distance and high electron energy should be used for high resolution imaging.

3.3 X-ray diffraction

The crystal structures of nanomaterials can be identified using an X-ray diffractometer (XRD). The X-ray light is generated by bombarding a metal target with high energy electron beam (40 keV), which creates the X-ray fluorescence. Fixed wavelength X-ray passes through a monochrometer before reaching the sample. In a typical Bragg–Brentano theta-2 theta configuration, the sample is attached to a rotating stage and the detector is

attached to another rotating stage with twice the rotating angle of the sample holder, shown in Fig. 3.3.

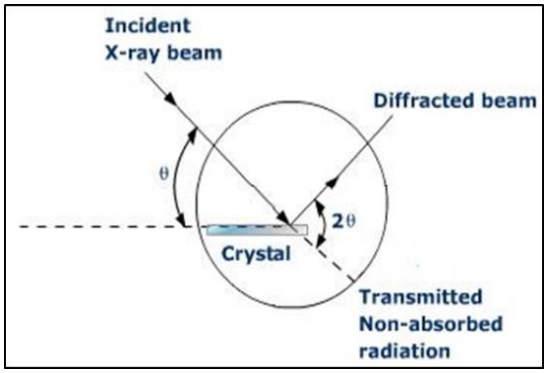

Figure 3.3 Geometry of X-ray diffraction by the crystal lattice with a typical Bragg-Brentano.

As the X-rays reflected by the atoms from crystal lattice, it causes constructive and destructive interference of the reflected waves at certain diffraction angles, according to the crystal lattice spacing, as indicated in Fig. 3.4.

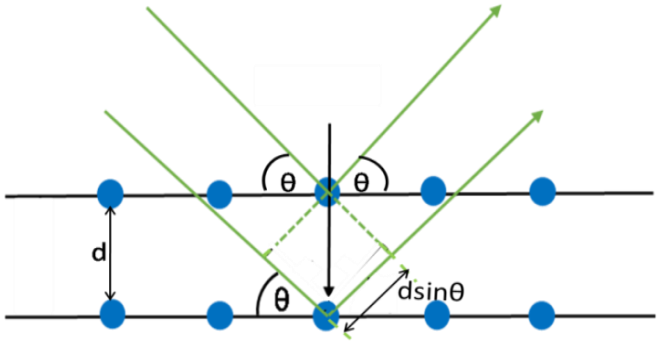

Figure 3.4 Scattering of X-ray from crystal planes.

Under the constructive interference condition, the intensity of the scattered X-ray reaches maximum, which is governed by Bragg's law (Equation 3.1) [214]:

$$n\lambda = 2d \sin\theta \qquad \text{(Equation 3.1)}$$

where *n* is the diffraction order, λ is the wavelength of X-ray, typically about 100 pm (1 pm = 10^{-12} m), *d* is the spacing between the planes in the crystal lattice and θ is the diffraction angle.

In this project, a Siemens D500 powder X-ray diffractometer with Cu-K_α radiation of wavelength 1.54056 Å was used for the characterisation of crystalline samples. The detector angle was measured relative to the incident X-ray beam. The D500 allows a θ/2θ scan, in which both the incident and detector angles relative to the sample plane are changed simultaneously. In a second mode, the incident angle can be fixed while only the detection angle is changed. For the analysis of normal powder samples, the θ/2θ scan was used. For thin film samples, a small incident angle of θ = 4° was fixed while the detector was moved independently. In this case the X-ray beam samples a shallow depth into the material. The 2θ angular range was between 20º to 70º in most measurements and the data was collected with an angular step of 0.02º. The crystal phases of the samples were analysed according to the X'Pert HighScore Plus software (version: 2.0 PANalytical B.V). The program Igor (version: 6.0.5.0) was used for plotting X-ray diffraction graphs.

In addition to the crystal phase, the grain size of the studied sample could be calculated based on the width of the diffraction peaks, according to Scherrer's formula (Equation 3.2):

$$D_{hkl} = \frac{K\lambda}{\beta_{hkl} cos\theta_{hkl}} \qquad \text{(Equation 3.2)}$$

D_{hkl} is the crystal size (nm) perpendicular to the (hkl) crystal plane, $\boldsymbol{\lambda}$ is the wavelength of the X-ray which is 1.5406 Å and K is a constant equal to 0.89 when β_{hkl} takes the half of the diffraction peak boarding. β_{hkl} is related to the diffraction peak width through:

$$\beta = \sqrt{B_M^2 - B_1^2} \qquad \text{(Equation 3.3)}$$

where B_M is the measured full width of half maximum of the diffraction peak (FWHM in radians) and B_I is the instrumental broadening (also in radians). The instrumental broadening is measured from the FWHM of 2θ from standard crystallised particles of size > 200 nm.

3.4 Optical property characterisation instruments

The interaction of the incident light with the material happens through several mechanisms including: Absorption, refraction, reflection, scattering, emission of fluorescence and phosphorescence. Absorption occurs when the incident photons have energy equal or larger than the semiconductor band gap energy. When the photons are absorbed, they transfer their energy to the absorption centre. The absorbed energy generates electron-hole pairs and promotes the excitation of the electrons across the band gap into higher energy levels (conduction band and vacuum). The excited electrons leave an equivalent number of holes in the valance band.

As only specific wavelengths of the incident light are absorbed, the other wavelengths in the incident light could either pass through the sample in a process called refraction or be reflected when they bounce off the surface. In both of these processes, the incident and reflected photons have the same energy.

In the process of fluorescence, the photoexcited electron relaxes to the minimum of the CB generating phonon (lattice vibration), followed by second relaxation to the VB, emitting photon with longer wavelength than the absorbed photon. The energy difference between the emitted photon and the absorbed photon is known as Stoke's shift. It represents the difference in the wavelengths between absorption and emission peaks, which is determined by the difference in the equilibrium bond length of ground and excited states. The above discussion of the fluorescence process is more considered for the gas phase molecules. For the solid lattice, the term phosphorescence is often used in solid state photophysics to indicate a temperature dependent emission process involving recombination of trapped electrons and holes. Photoluminescence in solids arises from transitions involving conduction bands, valence bands, or localized energy levels at impurity or defect sites. Luminescent centres can be introduced into inorganic crystal by the addition of transition metal ion dopants. Emission and absorption bands may be narrow if the transitions involve only the luminescent centre or broad-band if lattice vibrations are involved. In the latter case large Stokes' shifts may be observed as excitation energy is lost to lattice vibrations before emission.

For applications as a photocatalyst, the optical property of the nanomaterial, such as absorption, reflection, transmittance and associated band gap energy, are important factors that could directly affect the overall light harvesting efficiency. For instance, in the application of photocatlytic water splitting process and photovoltaics, the population and energetic power of photogenerated electrons and holes are determined by the alight absorption behaviour. The corss section for the fluorescene is propotional to the rate of charge recombination, which has the reverse effects on the lifetime of the excitons.

3.4.1 UV-Vis spectrophotometer.

UV-Vis spectrophotometer is a convenient tool used to study the optical properties of metal oxide semiconductor films. The measured absorbance and transmittance can be used to calculate the optical band gap energy of the studied films.

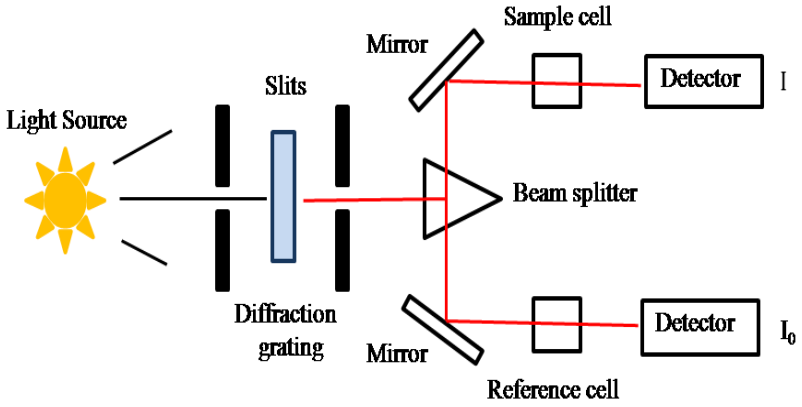

Figure 3.5 A schematic diagram of UV-vis spectrophotometer.

The schematic diagram in Fig. 3.5, presents the principle of a typical double beam UV-vis spectrophotometer. An aligned beam of monochromatic light is divided into two beams of equal intensities when it passes the beam splitter. One of the beams passes through the sample while the other passes through a reference cell. The transmitted light intensities are measured simultaneously as I and I_0 respectively. The detected light intensity from the sample (solution or thin film) will be less than that from the reference (blank). Transmission, T, is expressed as the ratio of I and I_0. This is known is percentage transmission (%T). The transmittance and absorbance, A, of the sample is defined:

$$T = \frac{I}{I_0} \qquad \text{(Equation 3.4)}$$

$$A = -log_{10}\frac{I}{I_0} = -log_{10}T \qquad \text{(Equation 3.5)}$$

The absorbance of the sample is propotional to its molar concentration according to the Beer-Lambert law [215]:

$$\alpha = \frac{A}{bc} \qquad \text{(Equation 3.6)}$$

Where α is the molar absorptivity, *b* is the length of beam in the absorbing medium and *c* is the concentration of the absorbing species.

Since each metal oxide semiconductor has different band gap energy, they exhibit different absorption edges. Therefore, the optical band gap can be related to the absorption coefficient and photon energy according to Tauc expression [216, 217]:

$$(\alpha h\nu)^{1/n} = A(h\nu - E_g) \qquad \text{(Equation3.7)}$$

In which, α is the absorption coefficient, *A* is a constant depending on the electron-hole mobility of the material, *h* is the planck's constant, *v* represents the frequency of the incident photon, *hv* is the photonenergy ($h\nu = \frac{hc}{\lambda(nm)} = \frac{1240}{\lambda(nm)}$ eV), E_g is the band gap energy and *n* is a constant which takes different values depending on the studied electronic transitions. *n* is taken as ½ and 2 depending for direct-allowed and indirect-forbidden transitions, respectively[218].

For a thin film sample, the absorption coefficient can be defined as following:

$$\alpha = \left(\frac{1}{t}\right) ln\left(\frac{1}{T}\right) \qquad \text{(Equation 3.8)}$$

Where *t* represents the film thickness, which can be measured from the cross-sectional SEM image and *T* is the optical transmittance.

In this project, UV-Vis spectrophotometer was used to measure the concentrations of released MB at 663 nm measurements. It was also used to study the transmission of deposited ITO films on normal glass substrates. The spectrometer consists of a radiation source (Tungsten filament), a sample holder, a single monochrometer and a detector. In typical measurements, electromagnetic radiation across the wavelength range of 300-900 nm is scanned over short period of about 20 seconds. Both sample and a reference cell are radiated at the same wavelength and intensity (which was a clean glass substrate for thin film samples). The transmitted radiation is then detected and the spectrometer records the transmittance by comparing light intensities passing through the sample and the reference.

3.4.2 UV-Vis reflectometer

If the substrate is a typical metal sheet or the semiconductor film is too thick, the transmitted light intensity is too low to measure. In such case, the reflection absorption spectroscopy is a vital technique that measures the optical band gap.

Our reflection absorption spectroscopy uses an integrating sphere (Ocean Optics ISP-REF) with an inbuilt tungsten-halogen light source covering wavelengths from 300 to 1000 nm with a beam port diameter of 7 mm and an incidence angle of 10º. A USB UV-Vis spectrometer was directly connected to the measuring port on the integrating sphere by a silica optical fibre, to ensure the UV transmission. With respect to the reflectance data, the absorption coefficient can be found as [219, 220]:

$$2\alpha t = \ln[(R_{max} - R_{min})/(R - R_{min})] \qquad \text{(Equation 3.9)}$$

Where t is the film thickness, R_{max} and R_{min} are the maximum and minimum reflectance in reflection spectra and R is the reflectance as a function of photon energy. From Equation 3.9, the absorption coefficient can be calculated with known film thickness. Band gap energy values then can be determined using the Tauc plot following Equation 3.7.

3.4.3 Photoluminescence Spectrometer (PL)

The photoluminescence is a light emitted by relaxation of the photoexcited atoms or molecules after a finite duration subsequent to the absorption of electromagnetic energy. The optical emission from an excited semiconductor is a direct result of electron-hole recombination, which is the most important energy waste pathway [221]. In the process, the photoexcited electrons lose their excitation energy and relax rapidly to the low energy levels. The relaxation process occurs in two stages; firstly, within the excited state lifetime, electron relaxation to the minimum of the conduction band by losing energy as heat (lattice vibration), within significantly short time (10^{-13} second). Secondly, the excited electrons move from the minimum of the conduction band to the valance band, combining with the previously generated holes. During this latter step, energy is emitted in the form of photons with longer wavelengths, defined as photoluminescence. Fig. 3.6 shows the principle of the photoexcitation and photoluminescence.

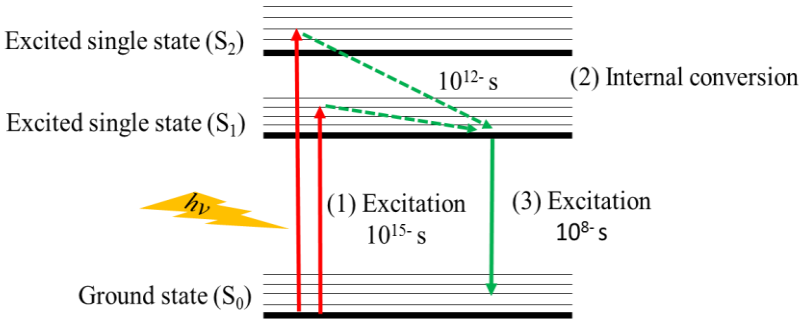

Figure 3.6 Fluorescence Jablonski diagram [56].

The Photoluminescence (PL) spectrum provides information about the electron transition energies. Since the PL excitation spectrum shows a fingerprint of transition energy levels, it can be used to determine the relative position of the electronic energy levels. More important, the luminescence intensity allows evaluation of the recombination rate of the photo-generated charge carriers. The main limitation of this technique is that it cannot give information about the whole electronic structure of the material studied, due to the relaxation to the bottom of the conduction band (heat luminescence) being faster than the radiation recombination process. Another difficulty arises from the effects of environment on the PL signal, which causes difficulty for the proper interpretation of experimental data.

Fig. 3.7 presents PL spectrophotometer setup. In the spectroflurometer, xenon arc lamp is used as source of exiting light (250-800 nm). A monochrometer is used to select both the excitation and emission wavelength. A beam splitter (thin piece of clear quartz) is provided to eliminate the exiting light path which reflects a part of the excitation light to the reference. Polarizers are presented in both excitation and emission light paths. During PL measurements, an excitation light is focused on the centre of the sample. If the energy of the photons is greater than the band gap energy of the semiconductor, this causes photon emission from the sample. The fluorescence is detected with photomultiplier tubes and quantified with appropriate electronic device. The output is presented in graphical form and stored digitally.

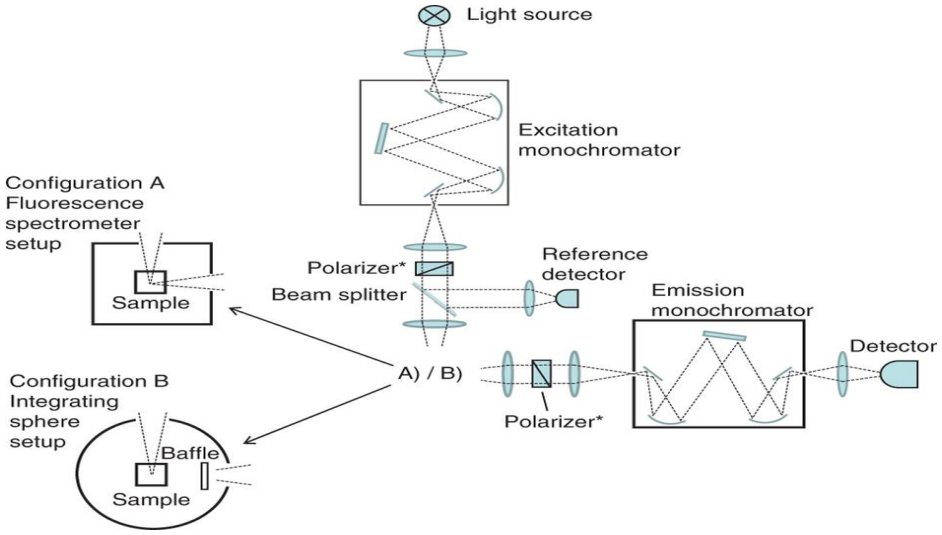

Figure 3.7 PL spectrophotometer setup. It was adopted [72]

In this project, PL analyses were performed to study the effect of Cu-doping on the electronic properties of TiO_2 nanorod films. The study was to evaluate the recombination rate of photo-generated charge carriers when the film used as photocatalysts during the water splitting process. PL emission spectra were recorded at room temperature using an LS45 fluorescence spectrometer. Samples were excited with a xenon arc lamp in the UV region. For the detection, the emission was collected at an angle of 90º and was dispersed by an emission monochrometer.

3.4.4 Electrochemical impedance spectroscopy (EIS)

Impedance spectroscopy is a powerful technique used to investigate the electrical properties of semiconductors and their interface with electrolytes. The electrochemical potential of the electrolyte solution and semiconductor electrode are determined by the redox potential of the electrolyte solution ($E_{F(redox)}$) and the Fermi level (E_F) of the semiconductor respectively. When both electrolyte and semiconductor electrode have the same electrochemical potentials, the two phases are said to be in equilibrium. If these phases do not lie at the same energy, charge movements between them are required in

order to equilibrate the two phases. This can be seen in n-type semiconductors, where the Fermi level is higher than the redox potential of the electrolyte causing electrons to be transferred from the electrode to the electrolyte. This has the effect of charging the semiconductor positively on the surface, forming a depletion region and causing a band bending. The band bending will change depending on the applied voltage. When the applied voltage is such that there is no charge depletion or band bending, the applied voltage corresponds to the flat-band potential of the semiconductor.

Band bending is sensitive to the applied potential. For instance, with positive potential, the majority charge carriers (electrons) of n–type semiconductors will be removed, creating a depletion region. While at negative potential, an excess of majority charge carriers (electrons) will be accumulated in the space charge region.

By exposing the electrode to radiation with sufficient energy, the electrons will be excited to the conduction band and generate an electrical current. However, at the flat band potential, there is no current either in dark conditions or under illumination because there is no field to separate the photogenerated charge carriers.

Impedance is general form of resistance, which includes the contribution from resistors, capacitors and inductors. Since the ohmic resistance represents the direct current circuit resistance, the impedance can be described as the alternating current circuit resistance, which is defined by the electrical capacitance. The behaviour of space charge capacitance can be investigated by EIS. This technique indicates information about the electron-transfer resistance and capacitive behaviour at the electrode-electrolyte interface.

EIS can be used to study any intrinsic property that affects the conductivity of electrode materials under external stimulus. Usually two categories of parameters can be derived from EIS spectrum which are: (i) those related to the materials itself only, for

instance, conductivity, dielectric constant, carrier mobility and bulk generation-recombination rates; and (ii) those pertinent to the interface of electrode and electrolyte, such as rate constants of adsorption reactions, diffuse coefficient of neutral species in the electrode and capacitance of the interface region.

Among several impedance spectroscopy techniques, single-frequency impedance spectroscopy is the most commonly used. A small AC electrical stimulus (10 mV) is applied in addition to a DC voltage to measure the phase shift and capacitance of electrical response. The carrier concentration (donor density) and flat band potential at film/electrolyte interface can be calculated by using the Mott-Schottky (M-S) equation [222]:

$$\frac{1}{C_{SC}^2} = \frac{2\left(V_E - V_{FB} - \frac{KT}{e}\right)}{e\varepsilon\varepsilon_0 N_D A^2} \qquad \text{(Equation 3.10)}$$

Where C_{sc} is the capacitance of the space charge region between the semiconductor and the electrolyte, V_E is the applied DC voltage, V_{FB} is the flat band potential, k is the Boltzman constant, T is the temperature, ε is relative dielectric constant of the semiconductor (for rutile TiO_2 = 170), ε_0 is the dielectric permittivity of free space (8.86 x 10^{-14} F/cm), e is the electron charge (1.06 x 10^{-19} C), N_D is the charge carrier density and A is the area contacted with the electrolyte. The flat band potential can be the estimated from the extrapolation of the linear plot of $1/C^2_{sc}$ vs. V_E to the value of $1/C^2_{sc}$=0. In addition, the slope of the linear plot also indicates whether the studied semiconductor is n- or p-type. The n-type semiconductor shows positive slope, while the p-type semiconductor shows a negative slope.

The charge carrier density can also be calculated from the slope according to equation 3.11:

$$N_D = \left(\frac{2}{e\varepsilon\varepsilon_0 A^2}\right)\left(\frac{d\left(\frac{1}{C^2}\right)}{dV_E}\right)^{-1} \quad \text{(Equation 3.11)}$$

The smaller slope of the liner $1/C^2_{sc}$ vs V_E plot indicates larger carrier concentration [131]. In this project, the electrochemical properties of treated rutile TiO_2 nanorod thin films were compared to those of pristine TiO_2 nanorod films at room temperature in the dark. EIS measurements were performed in order to evaluate the capacitance of doped TiO_2. Donor concentrations and flat band potentials were obtained through Mott-Schottky analysis.

3.4.5 Photoelectrochemical cell (PEC)

The conversion of solar energy to hydrogen by water splitting in the presence of a photocatalyst is one of the important strategies to achieve clean and renewable energy. Semiconductors have been widely used as photocatalytic material in the PEC system. The first TiO_2 photoanode was created over 40 years ago by Fujishiun and Honda for water splitting [58]. Fig. 3.8 shows a schematic diagram of a PEC set up for photocatalytic water splitting reaction takes place in a three electrode configuration. The semiconductor works as a photoanode, a platinum sheet and a KCl saturated Ag/AgCl were used as counter and reference electrodes, respectively.

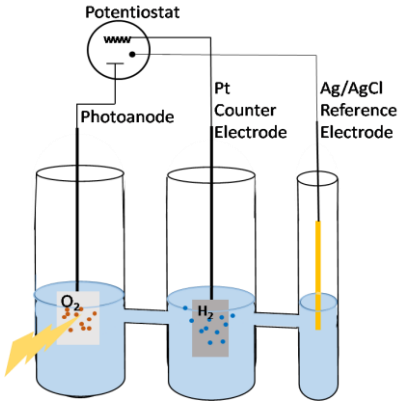

Figure 3.8 Three electrode photo-electrochemical set up.

When the photoanode is immersed in the electrolyte, the charge carriers are transferred to the semiconductor electrode/electrolyte interface until equilibrium is achieved. Upon light radiation, electron-hole pairs are generated and separated in the space charge region where the recombination is prevented. The excited electrons in the conduction band are transferred to the counter electrode through the external circuit while the holes migrate to the anode surface for the water oxidation reaction. The electrons and holes will be accumulated at either the conduction band or the valence band, which will shift the conduction band towards more negative potential and the valence band more positive, until their potentials are sufficient for the reduction of water (on counter electrode) or the oxidation of water (on the anode). Applying an external bias can also shift the band edges of the semiconductor together with the Fermi level of the counter electrode to overcome the reaction barriers, leading to a measurable photocurrent.

In this project a standard three-electrode configuration photoelectrochemical (PEC) cell was used in the photocatalytic water splitting measurements. The photocatalytic performances of different n-type TiO_2 nanorod films were examined by using them as photoanodes in the PEC system. A Platinum sheet and a KCl saturated Ag/AgCl were used as counter and reference electrodes, respectively. In order to simulate

sunlight, a 300 W xenon arc lamp with an AM 1.5 filter was used as the light source. The power intensity of the light was controlled to be 100 mW/cm^2. In this set up all the measurements were performed with the front side illuminated.

The efficiency of the PEC cells are calculated using the following equation [223, 224]:

$$\eta(\%) = \frac{J_P(E^0_{rev} - E_{app})}{I_0} X\ 100\% \quad (3.12)$$

where: η is the photoconversion efficiency, J_P is the photocurrent density (mA/cm^2), E^0_{rev} is the standard reversible potential (1.23 V), E_{app} is the potential between the working electrode and the counter electrode, $Eapp = Emeas - Eoc$ where $Emeas$ is the working electrode potential (versus Ag/AgCl) and Eoc is the working electrode potential (versus Ag/AgCl) under the open circuit condition (J_p= 0 mA cm^{-2}) whilst illuminated and I_0 is the incident light intensity with a typical value of 100 mW/cm^2, in order to simulate the solar radiation on earth.

In order to maximise the light harvesting, 3-D optical waveguided photoanodes were also constructed and their PEC water splitting performance was measured.

Chapter 4 The modification of TiO_2 nanotube structures for their medical applications in controlled drug delivery

4.1 Abstract

This chapter reports an intensive study of a controlled drug release system, using titanium dioxide nanotubular (TNT) arrays as promising candidates for drug delivery applications. This investigation is focused on the examination of the effect of tube morphology, shape, diameter, length and tube coating, on the up-loading and release kinetics. The TNTs were created by anodisation of Ti plates in organic electrolyte containing fluoride. The tube morphology was modified by controlling the anodisation parameters. The TiO_2 nanobottles, TNBs, with small opening and large base volume connected through narrow necks, were created by multiple step anodisation process. A two-step anodisation process with different anodisation temperatures and voltages was used in order to create the bottle neck and base separately. The bottle neck was protected by using covalently bonded organic molecular monolayer coating. The potential application in drug elution was observed through kinetic measurements from TNBs and TNTs. A biocompatible polymer, polyvinyl alcohol, was used to further control the release kinetics in aqueous media. Methylene blue (MB) was used to simulate the drug molecules for the kinetic measurements. It was concluded that the loading and elution of MB can be controlled by adjusting the tube morphology as a result of the control of the anodisation parameters and modified the tube structure.

4.2 Introduction

The ways in which drugs are administered have gained increasing attention in the past two decades. In a conventional drug delivery system, medicines are given in a high dose at specific times; this administration is then repeated regularly over periods of hours or even days. In most cases, this procedure causes problems such as pulsed, unstable exposure to drugs, which can cause temporary overdose and lead to poor bio-distribution, poor targeting and drug efficacy. In the worst case, this could seriously increase the side effects in non-targeted tissues and larger than need quantity of drugs will be needed [225]. Moreover, it is well known that most medical implants such as dental, oral and maxillofacial implants need successive drug therapy over a specified period of time. Therefore, it is important to develop controlled drug delivery techniques.

Controlled drug delivery systems are a technique that aims to deliver the drug locally or systematically at a predetermined rate over specified period as proposed in Fig. 4.1 with zero order kinetics. These systems offer many advantages such as; delivering optimum dose at right time and in the right location, maintaining the drug concentration in the blood within therapeutic effect range, offering predictable controllable release rates and reducing the dosing frequency in order to increase patient compliance.

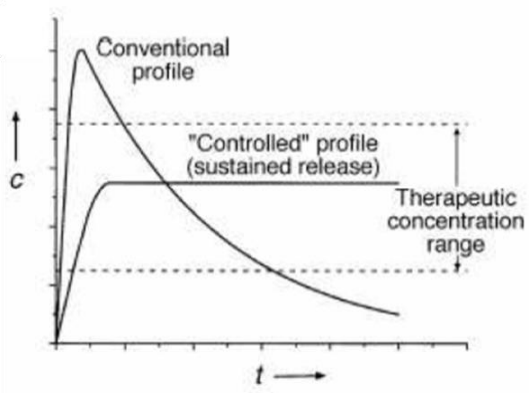

Figure 4.1 Scheme of a comparison between the oral and controlled drug administration systems [138].

The mechanism of this system depends on controlling the diffusion of the drug molecules through adjusted reservoir properties. Porous materials have been established as potential candidates for the design of therapeutic implants [226, 227]. Tissue integrated porous materials also act as exceptional reservoirs for slow drug elution over extended time periods. To date, TNTs are also used for developing controlled drug delivery systems [95, 194, 228]. They offer two key geometrical properties; a high surface-to-volume ratio and a porous structure. Additionally, TiO_2 has a good mechanical strength, excellent thermal and chemical stabilities, high corrosion resistance, non-toxicity and a good biocompatibility [229-231].

The use of TNTs for drug delivery and releasing could facilitate a controlled and sustained drug releasing pattern with delayed drug elution. Two strategies are used to delay the elution of the agent out of the nanotubes; (i) using a polymer to be loaded with the drug into the tube or to coat the top of the loaded TNT and (ii) adjusting the geometrical parameters of the tubes to ensure a slower release of the tube contents.

In the first technique, the nanotubes can be loaded with drug agents, either on their own or mixed into a polymer. Jie & Kerr [232], studied the release behaviour of ibuprofen with a mixture of poly (lactic-co-glycolic acid), PLGA, of different molecular weights, low molecular weight (LMW PLGA) and high molecular weight (HMW PLGA), using defect free TNTs. The results showed that 100% of the agent was released within the first hour without polymer. While, the release is extended to 6 and 9 days for the mixtures of ibuprofen with the LMW-PLGA and HMW PLGA respectively. These results were attributed to a decrease in drug elution rate as a result of the decreased ibuprofen diffusivity with increasing polymer molecular weight and influenced by their large size. Attaching a layer of polymer coating has also been used to adjust drug release kinetics. Aw and co-workers [95] investigated the effect of depositing biocompatible polymer films

over the drug loaded TNTs. The results showed that, depending on polymer layer thickness (the thickness can be controlled by controlling the number of coating times and the concentration of the polymer), a significant improvement in the drug release characteristics was demonstrated, with reduced burst release and extended overall release times. The release kinetics of this system is different from the drug polymer-mixed system. The drug release in this case is mainly controlled by the transport of drug molecules through the polymer coating and by the rate of degradation/dissolution of the polymer film, while for polymer mixed drug, the release was mainly controlled by the degradation and dissolution of the polymer. However, polymer degradation may result an inflammatory response and eventually implant failure. Thus, modifying the geometric parameters of TNTs could be considered as a more appropriate alternative for the development of controlled drug delivery systems.

Various studies have illustrated that the geometric parameters of TNTs, the tube diameter and length, have a considerable effect on their potential for the storage and release of medicinal agents [233]. Moseke and co-workers [228] have used TNTs array as local antibiotics carrier. They studied the effect of varying the morphology of nanotubes on their drug loading and tailored drug release kinetics. According to their results, varying the electrolyte composition, anodisation voltage and time leads to significant difference in the loading and release kinetics. Two types of electrolyte were used in the anodisation of Ti plates. In the first approach, polyethylene glycol was used as the solvent in the electrolyte. The Ti plate was anodised for 18h to form TNTs with diameter and length up to 160 nm and 6.54 µm respectively. The use of the organic solvent could reduce the rate of dissolution of the formed TiO_2. In the second approach, when water is used as the solvent, the anodisation for the same time resulted in tube like pores with diameter and length of 100 nm and 1.45 µm respectively. The increased surface area and pore volume

of the samples anodised in organic solvent enabled them to be loaded with up to 150% more drugs than the smaller TNTs anodised in a water based solvent. The drug release from the longer TNT was significantly retarded over a period of more than 300 days, much slower than from the TNTs formed in water electrolyte. In another study, Song and co-workers [99] synthesised TNTs with a hydrophobic monolayer attachment, forming an amphiphilic nanotubes structure. The attached layer acts as efficient cap prohibiting the release of hydrophilic drug to the environment. The release was effectively controlled by using the photocatalytic ability of the TiO_2 under the UV illumination to promote a precisely controlled oxidation and removal of the cap.

Our strategy of developing a controlled drug release system was to modify the tube shape to form nanobottle morphology for controlled drug release. TiO_2 nanobottles (TNBs) consist of narrow neck attached to a wide bases. Hypothetically, the large base would increase the storage capacity of the formed structure, while the narrow neck could effectively control the drug release kinetic. A sequence of two steps of anodisation with controlled reaction conditions were used to create this shape. A bottle neck with relatively small diameter was prepared at the conditions with the lower temperature and anodisation voltage. The formed layer was then protected, by depositing a layer of hydrophobic monolayer coating, against the second anodisation of forming the bottle base at the higher temperature and anodisation voltage.

In order to study the influence of the tube shape on the release kinetics, TNTs and TNBs films were synthesised and compared for their use in drug delivery. The study further included the quantitative measurements and analysis of the effect of the tube diameter and length on the drug release kinetics. For further release control, the influence of applying a polymer layer to the loaded drug films on the release kinetic was also

investigated. The chosen polymer was PVA due to its biocompatible property and water solubility.

4.3 Materials and methods

4.3.1 Synthesis of TNTs arrays on Ti plates

All chemicals were acquired from Sigma Aldrich. Titanium plates (99.7% purity), with a thickness of about 0.25 mm, were polished until a mirror finish was observed. This is important because the Ti surface to be anodised must be free of impurities and must be planar for creating a good quality of TNTs film without cracks. The polishing process was carried out mechanically using diamond paste of 6, 3 and 1 μm grit sequentially. The titanium was cleaned with ethanol between each step in order to remove residues from the metal surface. After that, the polished samples were cleaned ultrasonically in acetone (15 min) followed by isopropanol (15 min), the samples were finally rinsed with DI water. The repeated use of the same plate required the complete removal of previous nanostructured films through ultrasonic treatment in a mixture of H_3PO_4 (1 wt%), HF (1 wt%) and water, prior to the diamond paste polishing.

Previous work has identified that pre-covering the polished Ti plates with hydroxide layer through acid treatment play a key role on the initial stages of anodic growth of TNTs [234]. The formed hydroxide island catalytically accelerates the anodisation process by forming the initial nanopores on the interface between hydroxide layer and the Ti substrate. It can be formed by immersion polished Ti plates in a mixture of hydrofluoric acid (HF, 0.1 wt%), phosphoric acid (H_3PO_4, 1wt%) and DI water for 3-5 minutes. H_3PO_4 was used for adjusting the pH of the solution to 1.5 and F^- was added to initiate the formation of a hydroxide layer. The dipping time is proportional to the roughness of the

surface. The optimal time to achieve an appropriate density of hydroxide islands was 4 minutes. The samples were then cleaned ultrasonically and dried at room temperature.

The anodisation was carried out in a home-built electrochemical cell. The acid treated samples served as anodes, whilst a pure titanium sheet was used as cathode. The anode and cathode were soaked in an electrolyte composed of ammonium florid (NH_4F, 0.6 wt%), H_2O (2.0 wt%) in ethylene glycol (EG). The electrodes were immersed in the electrolyte 6 cm apart from each other. In order to compare the storage and release of different nanotubes diameters, the anodisation was performed with different applied voltages at 20 V, 40 V and 60 V at room temperature for 1 hour. The current-time profile was recorded using a USB data logger (U12, Labjack). The anodised surfaces morphologies were characterized through SEM (JSM 820M, Jeol operating at 30 keV).

4.3.2 The synthesis of TNBs arrays on Ti plate

TiO_2 nanobottles were created on Ti sheets through a two-step anodisation process. The same anodisation procedure for the synthesis of the TNTs was used with a different electrolyte composition. The electrolyte was prepared by mixing H_3PO_4 (10 ml, 85%), HF (1 ml, 40%) in 100 ml EG. In order to create the narrow neck of the bottle with different lengths, the Ti sheets were initially anodised at temperatures just under 5°C for different time periods ranging from 1 to 2 hours. The inter-electrode distance was set to 2 cm. The applied voltage was fixed at 60 V. After that, the samples were refluxed in an octadecylphosphonic acid (ODPA, 2 mM) in toluene solution at 70°C for at least 10 hours. This was done in order to attach a hydrophobic monolayer of (ODPA) to the surface of the narrow TNTs (neck) created from the low temperature anodisation. The ODPA coating protects the neck from being etched during the second anodisation stage. Contact angle measurement was used to confirm the organic attachment of ODPA. Image

J software was used to measure the angle between the drop of water and the surface of the TNTs film. The phosphate distribution was also monitored by energy dispersive X-ray spectroscopy (EDX).

The second anodisation step was performed at room temperature for 20 min with an inter-electrode distance of 4 cm and an applied voltage of 100 V. Specify the concentrations of the electrolyte. The high temperature and voltage of the second anodisation stage drives the attacking agent, F^- ion, to penetrate through the pores of the neck to reach the underneath Ti film where a wide base of the bottle is formed. The resultant films were also characterised by SEM (JSM 820M, Jeol operated at 30 k eV) and a transmission electron microscope (Hitachi-7100, operated at 100 k eV).

4.3.3 Study the loading kinetics of methylene blue

The influence of TNTs morphologies on their potential drug loading was considered as complementary measurements of the release experiments. In this experiment, anodized plates of TNTs were immersed in methylene blue aqueous solution with a concentration of 2% for 24 hours and then dried under vacuum conditions at room temperature. After that the samples were cleaned gently using DI water and dried again under vacuum. The loaded dye concentration was measured as UV light absorption by using an integration sphere attached to a USB UV spectrometer. The obtained loading curves of absorption against the loading time were fitted as a first order kinetics, according to equation 4.1, in order to measure the loading rate constants [228, 235].

$$I = A_0[1 - exp(-kt)] \qquad \text{(Equation 4.1)}$$

Where I is fraction of drug loaded in time, A_0 is maximum of drug loaded during process, k is the loading kinetic constant [hr^{-1}] and t is the loading time (hour).

4.3.4 Study the release kinetics of methylene blue

The influence of different factors on the release of organic species from TNTs was considered. The studied factors included the tube shape, length, diameter and surface coating. Firstly, in order to compare the release kinetics of different tube shapes, samples of TNTs and TNBs were prepared with controlled morphology. Bottles with different neck length were prepared by adjusting the first anodisation time. In addition, nanotubes with different diameters were created by using different anodisation voltages. For further release control, the study also considered the effect of attaching a layer of a biocompatible polymer, PVA, after MB was loaded. A PVA solution (1 w/v%) was prepared in a mixture of water and ethanol (1:1) and stirred for 4 hours [236]. Ethanol was added in order to improve the drying rate of the film.

The anodised plates were immersed in methylene blue (2% conc.) for 24 hours, in the case of normal tubes, and a week for the bottle shaped films. This was done to ensure that a saturated loading of methylene blue is achieved. Since the nanobottles have narrower neck, a lower loading rate is expected. Methylene blue was used as an organic component to simulate the release of specific drug molecules. The dye loaded plates were then removed from the solution and vacuum dried. This allowed ensuring the complete penetration of dye into the nanotubes array, as well as overcoming the problem of air trapping inside the tubes which would prevent dye penetration. Subsequently, the plates were rinsed gently using deionised water and dried again under vacuum. The loaded samples, nanotubes and nanobottles, can be closed by applying a layer of polymer coating. This layer can act as a cap for the capsule which assists the additional control of

the release kinetics. The drug release will be delayed by the degradation and dissolution of the polymer film. The methylene blue release kinetics were studied by measuring the release concentration in 20 ml deionised water at 22°C. The concentrations of released MB were measured by UV-vis absorption at 663 nm where the MB has maximum absorbance. The obtained release curves of UV-vis absorption against the time of release were fitted with a function following a first order reaction as was presented in equation 4.1.

In order to examine the effects of PVA coating on the release kinetics, the coating layer was dried under vacuum overnight to ensure completed drying.

4.4 Results and discussion

The synthesis of TNTs involved one step anodisation, while the synthesis of TNBs involved three stages: the preparation of the TiO_2 bottle neck, surface modification with an organic passivation and a second anodisation to create the base of the nanobottles. In the following sections, we discuss the technical details of the creation of nanotubes and nanobottles with the parameters that affect their morphology.

4.4.1 Controlling the TiO_2 nanotubes morphology

The morphology of created nanotube structures created at different anodisation voltages was investigated by SEM. Fig. 4.2a-d shows the SEM images of the top view of circular nanotubular arrays and a cross section view of each film (insets). The nanotubes are opened at the top and closed at the bottom. As presented in table 4.1, it was observed that the increase of anodisation potentials from 20 V to 40 V led to the increase of tube inner diameters from 34 to 64 nm and lengths from 0.82 to 1.65 μm respectively (Figs. 4.2a and b). These samples were named as T-1 and T-2. This observation suggests that both

the diameter and length of the nanotubes could increase linearly proportional to the applied voltage. This controlling parameter will be used later to create the narrow neck of TNBs.

Table 4.1 Experimental details for TNTs synthesis.

Tube No	Initial voltage (V)	Anodisation duration(min)	Acid treatment time (min)	Inner diameter (nm)	Length (nm)
T-1	20	60	0	34	820
T-2	40	60	0	64	1650
T-3	60	60	5	80	4000
T-4	60	60	3	80	2650

Figs. 4.2c and d represent the top view of Ti surfaces anodized by applying a voltage of 60 V but different acid treatment times, either 5 minutes (c) or 3 minutes (d). As result of this different acid treatment, the formed nanotubes had the same diameter (80 nm) but different lengths of 4.00 μm (5 min) and 2.65 μm (3 min) respectively (Fig. 4.2c and d). This can be attributed to an increase in the number of catalytic hydroxyl sites of the initial nano-porous layer, with the increase of the acid treatment times. These samples were named as T-3 and T-4 respectively.

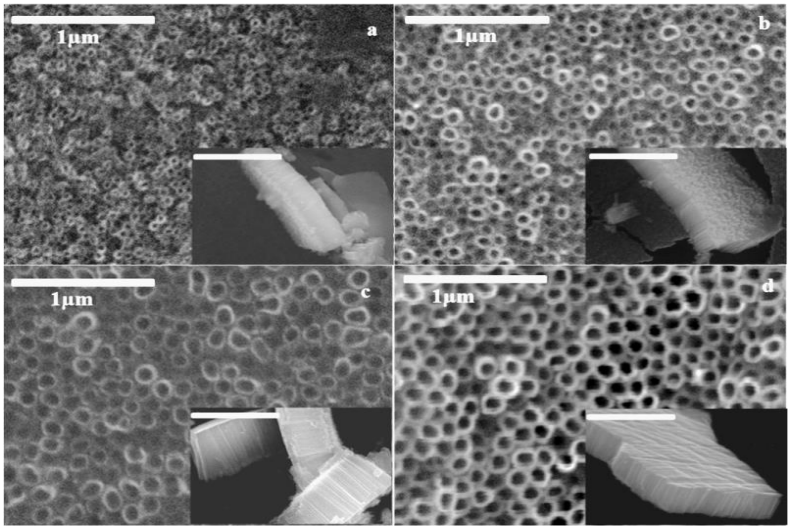

Figure 4.2 Top views of Ti surface anodized at different applied voltages; (a) 20 V (T-1), (b) 40 V (T-2), (c) 60 V (T-3) and (d) 60 V (T-4). The insets represent the corresponding cross sections.

4.4.2 TiO_2 nanobottles morphology

The bottle structure is described as tube shape with small mouths and larger bases connected through a narrow neck. The synthesis procedure of the nanobottles is going through three stages; the preparation of the bottle neck, followed by the attachment of the ODPA protection layer and finally the bottle base formation. The three steps are discussed in detail in the following sections.

4.4.2.1 Synthesis of the TiO_2 nanobottles neck

The bottle neck is characterized as a tube with narrow inner diameter. This part of the bottle is created in the first anodisation stage. In an anodisation process, the metal oxide layers were created by the applied anodic voltage. This oxide layer is thinned by a dissolution process caused by the corrosion with fluoride anion, which was directed by the positive bias on the Ti anode. The oxidation can be accelerated by increasing the bias, while an acidic electrolyte could increase the rate of dissolution. As increase the voltage could also increase the inner diameter of the neck, which should be avoided in order to

achieve a narrow neck. However, with the reduced anodisation voltage, the anodisation process could be too slow. In my experiment, the rate of the anodisation was monitored by the anodisation current. In order to overcome this problem, I used the acidic electrolyte with a mixture of H_3PO_4 and HF in EG. The acidic electrolyte will increase the dissolution rate. To balance this rate with the oxidation rate, anodisation was carried out at a reduced temperature. Fig. 4.3 shows the typical SEM image of an anodised sample, where the anodisation took place within a temperature range of 0-5°C with an applied voltage of 60 V for 1 hour.

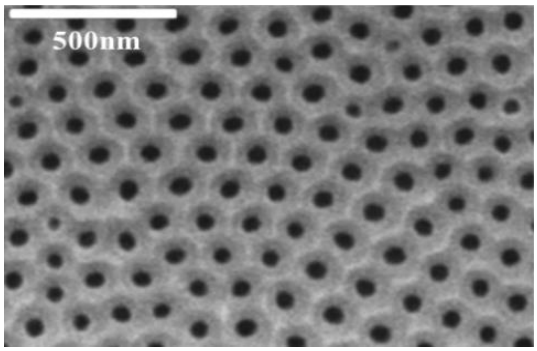

Figure 4.3 SEM image of TiO_2 nanopores with (ID= 40 nm, OD= 200 nm) prepared via an anodisation of Ti sheets in an acidic electrolyte at temperature range of (0-5ºC) using an applied voltage of 60 V for 1 hour.

The achieved porous structure has an inner diameter of 40 nm and an outer diameter of 200 nm. The overall thickness is about 350 nm. If this sample is directly anodised in a second step anodisation at room temperature, the pore diameter will be opened up and resulting in nanotubes. In order to maintain the morphology of the bottle neck created at the low temperature in the first step, we developed surface coating method using organic monolayer as a protecting layer. Below, I present the details of the surface coating method.

4.4.2.2 Modification of the TiO_2 porous layer with octadecylphosphonic acid (ODPA)

In order to protect the inner diameter and the length of the formed neck from the etching through the second anodisation stage, a monolayer of ODPA was applied on the surface. The ODPA molecules are self-assembled via covalently bonding the phosphate head group to the hydroxide-terminated metal oxide surface sites. On the other hand, the long hydrocarbon chain is left free giving the surface hydrophobic property. The ODPA treatment is carried out by refluxing the sample in ODPA solution (10 mM in Toluene) for 10 hours at 70°C.

While the anodised Ti surface shows good hydrophilic properties, this behaviour changes after applying a layer of ODPA, presenting a gradual decrease in the water wetting feature with an increase in refluxing time. This phenomenon was examined by measuring the contact angle between a drop of water and the porous TiO_2 surface. Generally, if the contact angle value is more than 90 degree that means the surface is non-wet. On the other hand, if the contact angle closes to 0 degree, the surface is total wetting with water. In between these two values, the liquid is said to wet the solid [99]. Fig. 4.4 represents the contact angle measurements of the TiO_2 arrays at different times of reflux treatment. The contact angle (red curve) increased sharply in the first hour followed by a gradual increase, reaching saturation after 10 hours. Meanwhile, the associated phosphorus concentrations with respect to Ti were monitored using EDX (blue curve). The measurements were done in order to understand the change of the surface wetting behaviours and quality of the surface coating as a function of the refluxing time.

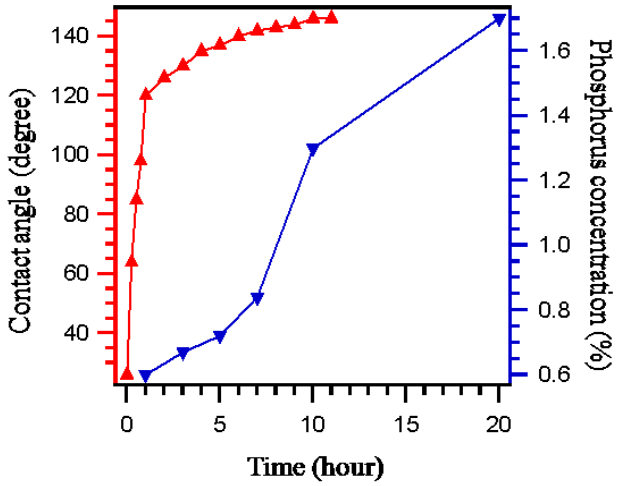

Figure 4.4 The contact angle measurements (red line) and EDX analysis of P% relative to Ti (blue line) at different refluxing times.

The EDX measurements in Fig. 4.4 show a steady increase in the phosphorus concentration as a function of reflux time. The behaviour of the contact angle and EDX measurements is quite different. The contact angle increases much faster than the surface phosphorus concentrations. From this observation, it can be suggested that, in the first hour of the refluxing, a monolayer of ODPA was formed on the top of the nanotubes. This process was linked with a rapid increase in the contact angle value. After forming a monolayer on the surface, the ODPA will penetrate through the porous structure to form an organic monolayer covering the inside walls of the TNTs. This explains the saturation behaviour in contact angle at later stage of reflux. The EDX measurements also support this mechanism as the electron beam can effectively penetrate through the pores of the sample under the surface. This means that both the phosphorous signals from the top and the inside wall surface of the pores were detected at the same time. The measurements show a rapid rise in the phosphorous concentration until 10 hours of reflux. From here, the nanopores were covered with the ODPA both inside and on the top. As such, there was no further increase in the contact angle and relatively slow increase in the ODPA concentration.

As mentioned above, the ODPA layer was deposited on the porous film as protection layer. This layer allows protecting the bottle neck from being etched during the second anodisation stage. In this step the demanding conditions of temperature and voltage, will guide the etching agent to penetrate through the protected pores, until they reach the unprotected part of the film, forming the wide base of the bottle structures.

4.4.3. Controlling the tube morphology by adjusting the anodisation parameters

The anodisation conditions have a strong effect on the formed nanotubes morphology. In order to create nanotubes with a bottle shape, the effect of varied anodisation parameters has to be controlled; in particular, the electrolyte temperature, the applied voltage and the anodisation time need to be precisely defined.

4.4.3.1 Varying the electrolyte temperature

Since the electrolyte temperature has a strong influence on the inner diameter of the formed tubes, anodisation at different temperatures was studied during this work in order to control the tube size. Fig. 4.5 shows the current-time behaviour of performing the anodisation at low (0-5°C) and high (22±2°C) temperatures. When the process is performed at low temperatures, overall anodisation current is lower than at room temperature. This is because, at low temperature, the movement of fluoride ions and surface reaction rate is restricted, which results a reduction in the tube etching speed. The initial increase in the anodisation current is due to the oxidation of water, which is observed at both low temperature and room temperature.

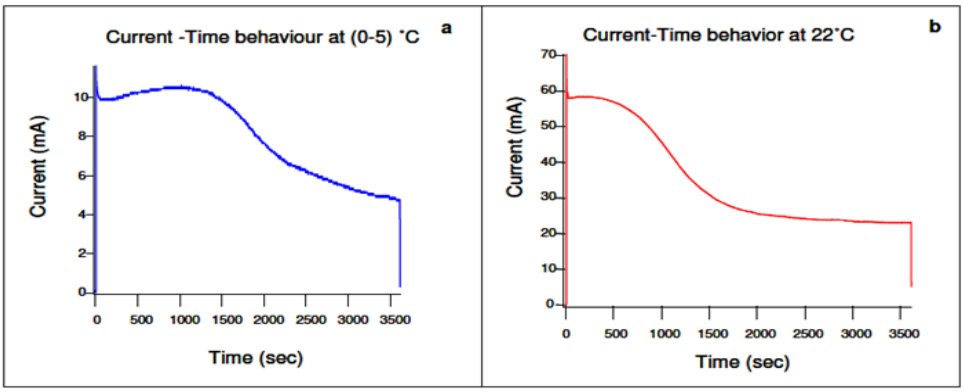

Figure 4.5 The current-time behavior at an electrolyte temperature of (a) 0-5°C and (b) room temperature, with anodisation voltage of 60 V.

At low temperature, the inner diameter of the created tubes was observed to remain below 40 nm. In contrast, the anodisation at room temperature shows much higher anodisation current. The resulting porous layer shows relatively large inner pore diameters of 120 nm. This is attributed to an increase in the mobility of the fluoride ion and surface reaction rate at an increase in electrolyte temperature. It was thus found that anodisation at low temperatures is an essential condition to form a narrow bottle neck.

4.4.3.2 Varying the applied voltage

In this study, in order to modify the tube structure and form bottle shape, the anodisation conditions of both stages were adjusted. The procedures and parameters for creating nanobottles are summarized in the table 4.2.

Table 4.2 Experimental details for TNBs development stages.

Exp. No.	Ini. Voltage (V)	Ini. T (°C)	Duration (min)	Voltage at 2nd st(V)	Final T. (°C)	Duration (min)	The final tube shape
1	100	< 5	60	100	25	60	Tube with neck
2	100	< 5	90	120	25	20	Conical shape
3	60	< 5	60	120	25	20	Nanobottles
4	60	< 5	90	120	25	20	Nanobottles

To study the effect of the temperature only, the applied voltage was kept at 100 V in both stages of Exp. 1 in Table 4.2. The electrolyte temperature was < 5°C for the first step anodisation and at room temperature for the second steps anodisation. The resultant shape can be described as a tube with neck as can be seen in Fig. 4.6a. The top of the tubes has a narrow neck compared to the relatively wide base. Nevertheless, the diameter difference between the neck and the base was observed to be relatively minimal (Fig. 4.6b).

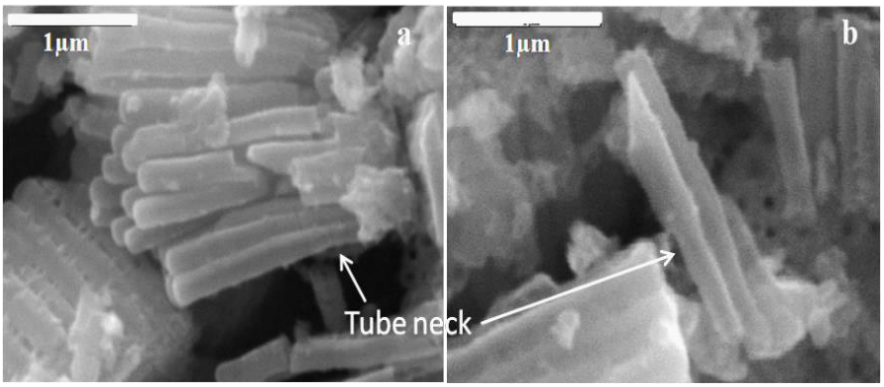

Figure 4.6 SEM images of TNTs, a cross section of nanotubes with neck of narrow diameter.

In order to achieve the bottle morphology, the time of the first step anodisation was extended and the anodisation voltage of the second step was increased as well. As shown in Fig. 4.7a nanotubes with conical shape can be formed as result of (Exp. 2). The increase in the second anodisation voltage allows assisting in expansion of the bottle base. Fig. 4.7b shows an individual tube with wide base shape.

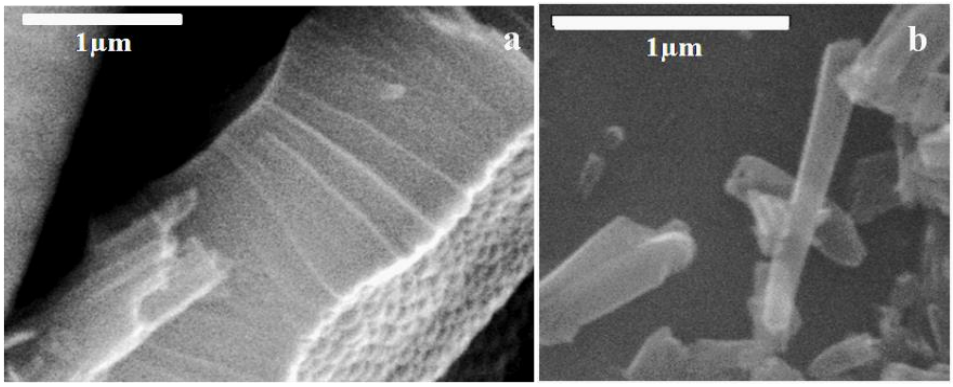

Figure 4.7 SEM images of TNTs with conical shape (a) cross section and (b) individual tube with wide base-shape.

According to these observations, reducing the applied voltage in the first step anodisation combined with a low electrolyte temperature will help to create a narrow bottle neck. On, the other hand, a wide bottle base can be formed by increasing the temperature and voltage. The conditions of the second step of anodisation drive the fluoride ions to penetrate through the protected neck to the unprotected part of the titanium oxide layer, forming a wide base.

In (Exp. 3 and 4), the voltage of the first anodisation was reduced to 60 V; while in the second step, the voltage was increased to 120 V. The difference between the Exp. 3 and 4 is on the duration of the first step anodisation. Exp. 3 has a shorter anodisation time of 60 min, while Exp. 4 has a longer anodisation time of 90 min. Fig. 4.8 shows the achieved nanobottles with different neck lengths, which were achieved under these conditions. Therefore, the length of the neck can be effectively controlled by adjusting the first anodisation time. Compared with the bottle shapes obtained from Exp. 1 and 2, it is clear that the anodisation voltage for the first anodisation (forming bottle neck) need to be controlled at smaller value, in order to get good shape of the bottle neck.

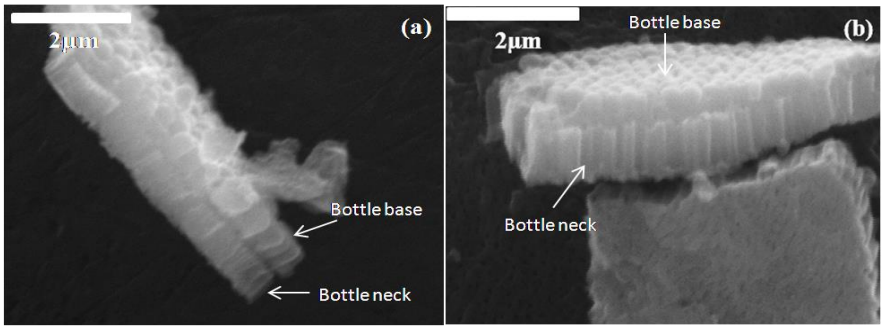

Figure 4.8 A cross sectional sample of TNBs with different neck lengths. These shapes were formed by anodisation of Ti samples at low condition of voltage of 60 V and temperature of < 5ºC for different times in the first step. (a) TNBs with short neck formed after 60 minutes of anodisation (B-1), (b) TNBs with long neck formed after 120 minutes of first anodisation (B-2). The second anodisation was performed at 22°C, 120 V for 20 minutes.

The duration of the first anodisation stage plays a key role in determining the neck length of the bottle. It can be seen that one hour of anodisation leads to create bottles with a neck length (L_N) of 350 nm (named as B-1), whilst anodisation procedures carried out for 2 hours resulted in bottles with a neck length (L_N) of 700 nm (named as B-2). Both of these samples displayed equal pore diameter (30 nm) as the same applied voltage (60 V) was used during both first step anodisation**.**

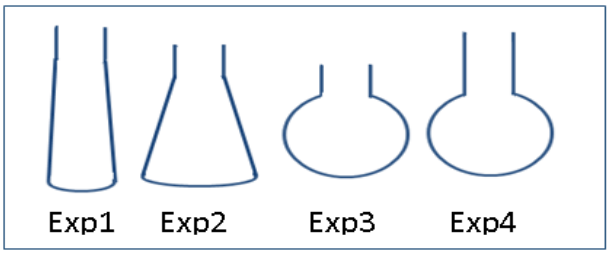

Figure 4.9 Scheme of the formed shapes of TNTs through the different anodisation conditions listed in table 4.1.

Fig. 4.9 represents a schematic of created tube morphologies as result of varying anodisation conditions presented in table 4.1. Nanotubes with conical shape were produced when the difference between the applied voltages in the two step anodisation

was not high enough (Exp. 1). On the other hand, the appropriate bottle shape can be generated by adjusting the anodisation conditions; temperature, voltage and time, between the two steps whilst maintaining a layer of ODPA protection in between. The first anodisation time has a direct effect on the neck length of the nanobottles.

The particular dimensions of good nanobottles were measured using SEM images of single bottles. As shown in Fig. 4.10, the bottle neck has a length of 221 nm, ID and OD of the neck are 30 and 124 nm respectively. Furthermore, the base has a width of 330 nm and length of 410 nm. It was noted that, the measured neck length of the single bottle is less than the neck length measured from the cross section of images in Fig. 4.10a. That could be explained as the break of the neck when the nanobottles are separated from the film. The dimension of the nanobottles was confirmed by TEM as shown in Fig. 4.10b.

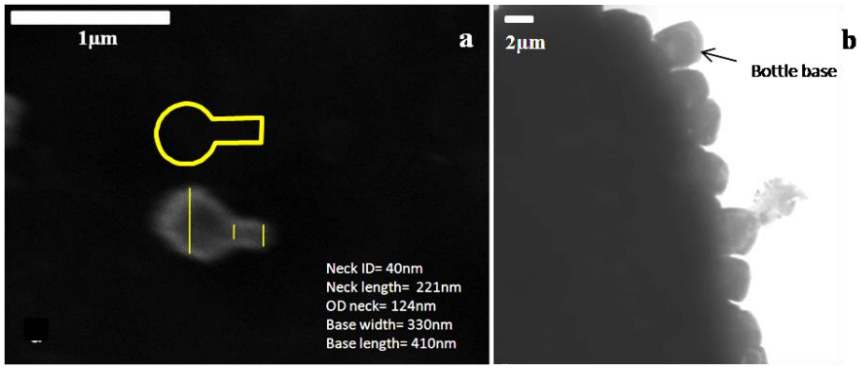

Figure 4.10 Shows the morphology of TNBs; (a) SEM image of single bottle, (b) the typical TEM images of the side view.

To confirm the key role of the ODPA coating, the two stage anodisation was run without applying a layer of ODPA. The resulting structures can be seen in Fig. 4.11. It is clear that, nanobottles almost with no neck were formed as shown in Fig. 4.11a. Additionally, the cross section shown in Fig. 4.11b shows some bottles with broken neck. That happened as a result of the dramatic dissolution in the second anodisation stage at

higher temperature and voltage. This result shows the importance of the neck protection by the ODPA coating in the creation of nanobottles morphologies.

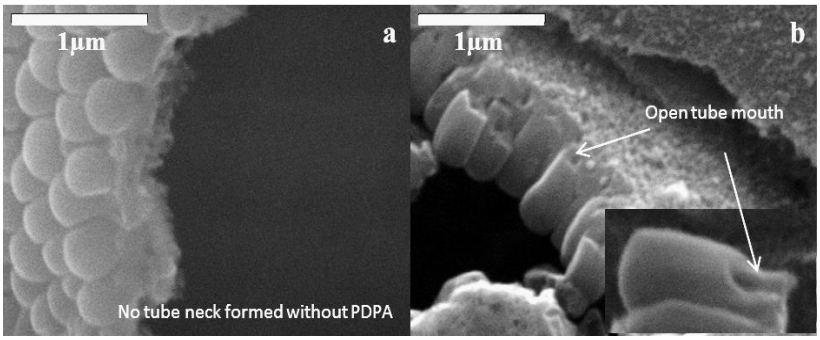

Figure 4.11 SEM images (a and b) of the TNBs with broken neck formed through two step anodisation without using ODPA coating.

4.4.4 Application of the prepared films in drug delivery

Since the goal of this study was to achieve a controlled drug release system, the effect of several factors on the loading and release kinetics was extensively studied. The studied morphological factors included the tube/neck diameter and length and the effect of polymer coating deposition.

4.4.4.1 Methylene blue loading in TNTs

In the typical application of the TNTs in the drug release system, standard nanotubes with one end opened shape are used as porous reservoirs filled with medicine. One of the goals of creating the bottle shape was to increase the tube capacity for higher drug loading by using the wide base. In addition, the narrow neck assists to control the release rate over extended time period. These properties give the bottle shape great importance in the clinical applications.

In this investigation, methylene blue (MB) was used to simulate general drug agent. MB is a precursor compound for the synthesis of chlorpromazine and other

antipsychotics [237], because it has a similar molecular structure. Different techniques have been applied to load the drug agents into the nanotubes. For instance, the sample is dipped in a solution of drug agents for certain time. The process can be performed under vacuum to remove penetrated air and encourage a larger chemical loading. Recently, Shokuhfar and co-workers [238] used a self-sustained diffusion process to load sodium naproxen, as drug model, into TNTs. In this technique the tubular film is detached from the Ti foil and suspended in ethanol with the dug agent. Loaded tubes could then be obtained after ethanol evaporation.

In this work, TNTs samples with different diameters and lengths were dipped in MB for 24 hr. Due to an expected low loading rate through the narrow neck, TNBs samples were submerged for a week to ensure complete loading. Because of the huge difference in the loading time of the TNBs compared to TNTs, only TNTs were employed as drug carriers to investigate the loading kinetics. At the same time, the result of this study could be effectively applied on the bottle neck with similar shape to the standard tubes. The study considered the effect of the tube diameter and length on the loading kinetics. The tubes were created by anodisation in NH_4F/EG solution with different biases of 20 V (T-1), 40 V (T-2) and 60V (T-3) at room temperature. The difference between T-3 and T-4 TNTs relies on the duration for the acid pre-treatment. The details are summarised in Table 4.1. The loading was measured by absorption from an integration sphere. The MB loading kinetics on TNTs with different lengths and diameters are displayed in Fig. 4.12.

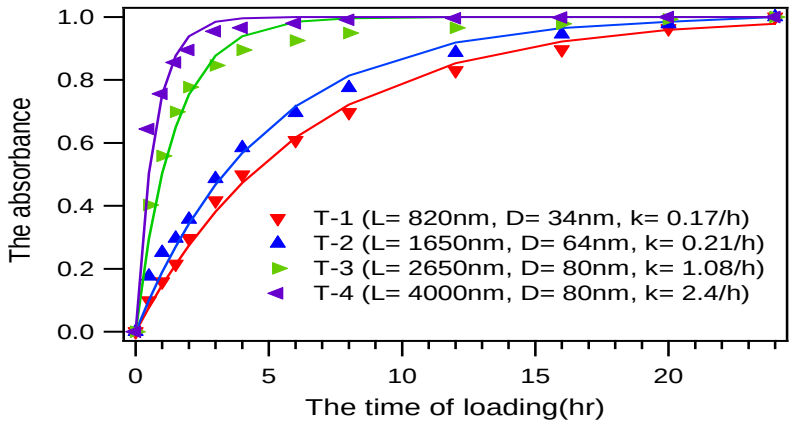

Figure 4.12 Normalised methylene blue loading into Ti surface anodized at; 20 V (T-1), 40 V (T-2), 60 V (T-3) and 60 V (T-4) with different times of acid treatment.

It can be clearly seen from Fig. 4.12 that the drug loading rate is dramatically affected by the morphology of the nanotubes. With the nanotubes of small diameters (T-1, red curve) and (T-2, blue curve), the drug was loaded slowly and reached the maximum loading only after 20 to 24 hours, respectively. In comparison, the loading rate of the larger nanotubes diameters, which were prepared by applying a higher anodisation potential (T-3, green curve), was much higher and saturation was observed after 8 hours. The large tubes diameter allows larger amount of dye molecules to penetrate through them in short period of time. On the other hand, the smaller diameter of the anodised tube at lower voltage impedes the penetration of large amount of dye molecular into them in short time. Therefore, the tube loading speed in this case is relatively slower. It is also evident from the graph that the rate constant of the tubes loading, k, is significantly influenced by the tube morphology. Here k is the loading rate constant using a first order kinetics. These results could be effectively applied on the bottle neck with similar shape to the standard tubes.

Furthermore, the drug loading kinetics from nanotubes with the same diameter but different lengths, were also different (T-4, purple curve compared to T-3, green curve). The drug molecules go a longer distance through the longer tube; therefore, longer

time is required for complete tube loading. Therefore, the length of the nanotubes can also affect the loading kinetics.

These results can be effectively applied on the drug loading kinetics from nanobottles, due to their similar neck shape compared to the tube morphology. Based on that, the drug loading rate from the nanobottle films (B-1 and B-2) would be slower than that from the normal tubes, since the bottle neck in both films has narrower diameter. Furthermore, by taking the effect of the tube length into account on the loading speed, the loading rate into B-2 film would decrease much further due to its longer bottle neck compared to B-1 film.

4.4.4.2 A comparison between MB releases of different nanotube structures

The drug release from tubes of different diameters and lengths are presented in Fig. 4.13. These tubes were created by controlling the anodisation conditions. The nanotubes were created by anodisation in NH_4F/EG solution with applying different biases of 20V and 60 V at room temperature for 1 hour. The formed nanotubes have inner diameter of 34 nm (T-1) and 80 nm (T-3) and length of 0.82 and 4 µm respectively. T-4 has equal diameters to T-3 and different lengths of 2.65 µm due to the difference in the acid treatment time (5 min and 3 min respectively).

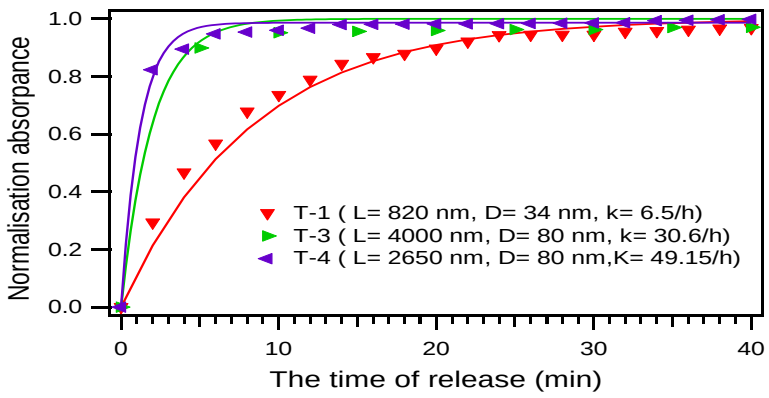

Figure 4.13 The dye release from TNTs with different diameters and lengths.

The MB loaded TNTs and TNBs were submerged in the DI water to allow the release of MB. The concentrations of released MB were measured by UV-Vis spectrometry at 663 nm where the MB has maximum absorbance. Under controlled conditions, MB elution was measured at various times up to 5 hours, after which the MB concentration reached a plateau and release finished. The MB was released quickly during the first hour.

As the release follows a diffusion mechanism which is proportional to the concentration of the loaded drug, it is reasonable to assume that the MB release follows first order kinetics. Under such conditions, the release kinetics can also be fitted by Equation 4.1. The drug concentration can be normalised against the maximum drug release.

From Fig. 4.13, it clear that, the tube diameter and length have a significant influence on the dye release. The rate constant decreases with decreasing the tube diameter and increasing the tube length. Therefore, the dye elution from tube with smaller diameter (T-1) is much slower compared with that from the tube of wider diameter (T-3). On the other hand, the dye release from T-3 is slower than the release from T-4 although both samples have the same diameter of 80nm. This observation confirms the role of the tube length of controlling its release kinetic. The tubes T-3 sample show longer length than that is sample T-4. The dye molecules in this case require diffusing longer distance compared to their diffusion through shorter tube length.

4.4.4.3 A comparison of MB releases from nanotubes and nanobottles

The MB elution profiles from different tube morphologies: nanotubes and nanobottles with different neck lengths are presented in Fig. 4.14. The nanobottles were formed in two stages anodisation as mentioned previously. The formed nanobottles films have

different neck length, of 0.35 µm (B-1) and 0.7 µm (B-2), as result of varying the first anodisation time (60 and 120 min respectively).

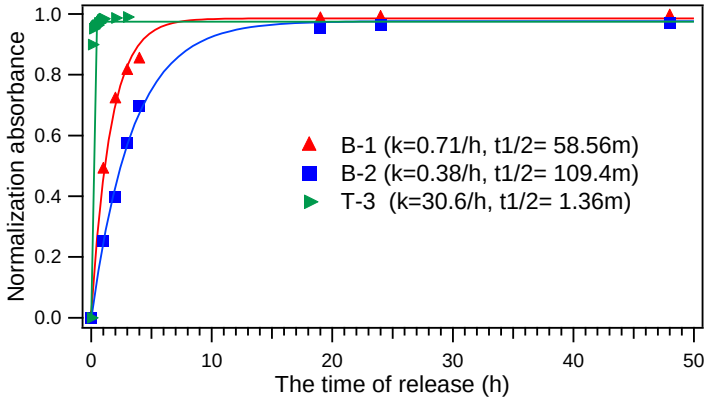

Figure 4.14 The dye release from different tube shapes; normal tubes (T-3), short necked bottles (B-1) and bottles with a long neck (B-2).

It is clear from the graph that; the tube shape has a considerable effect on the release rate. By measuring the rate constant, *k*, value, it is clear that the MB release from the tubes is much faster than the release from the bottles. This is further confirmed by the difference between the half-life times of elution of the bottle with the short neck length (B-1, red curve) and the tube (T-3, green curve). They were calculated to be at 58.56 and 1.36 min respectively. The small diameter of the bottle neck (30 nm) plays a key role in restricting the diffusion of drug molecules from being eluted in short time.

4.4.4.4 A comparison between the releases of nanobottles of different neck lengths

From Fig. 4.14, it can also be seen that the dye release from the bottle structures, was significantly affected by the length of the bottle neck. The rate constant decreases with increasing neck length. As result of this, the dye release from long-necked bottles is significantly slower than that of the shorter necked bottles. That is because the dye molecules require diffusing longer distance compared to their diffusion through shorter

neck. Therefore, the elution half-life of the long necked bottle structures (B-2, blue curve) is doubled compared to that observed in short-necked bottles (B-1, red curve).

4.4.4.5 A comparison between the releases of different tube with polymer coating

Fig. 4.15 shows a comparison between the elution behavior of synthesised bottles and tubes with a layer of PVA coating. The purpose of the PVA coating is to further reduce the drug release rate constant.

As we can see from the graph, the release rate of the tubes and bottles was significantly influenced by the presence of a coating layer. The *k* values of MB release with coating are much smaller than those without coating, this is linked with an increase of the half life time required to release the half amount of the loaded drug. With the geometrical properties of the used platform, the presence of the polymer layer provides additional control on the drug elution. The drug release in this case is controlled by the dissolution of the polymer coating and by the transport of drug molecules through the polymer film.

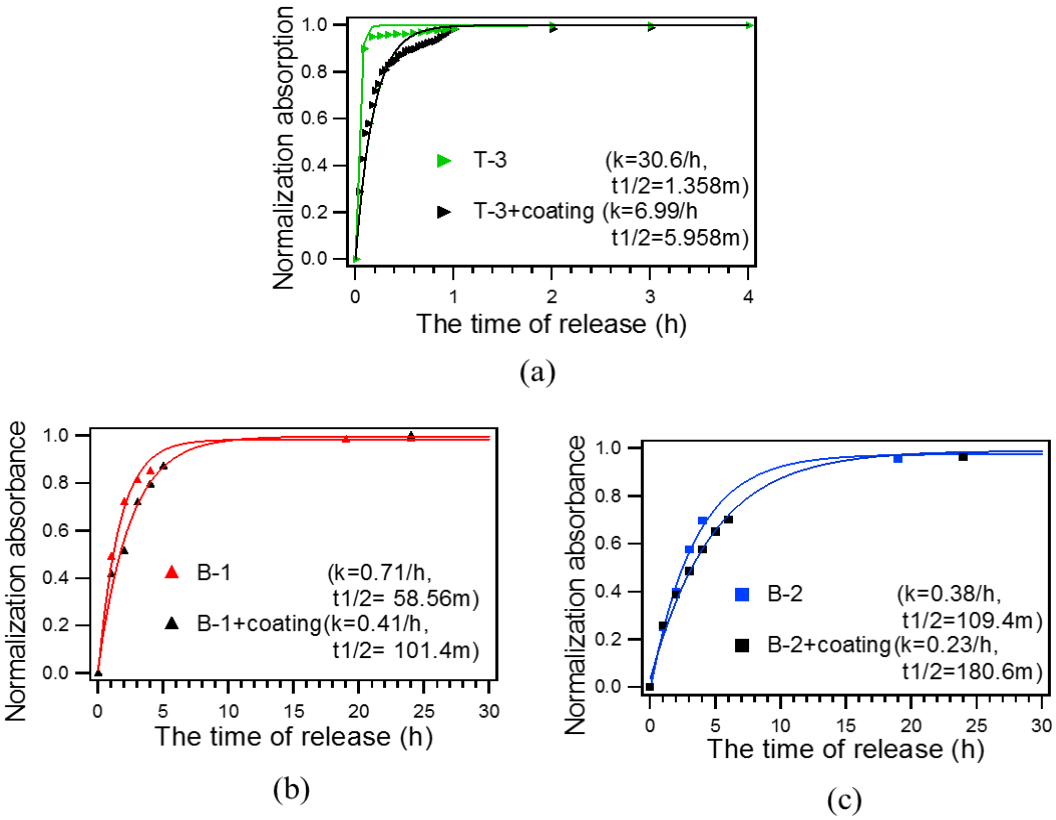

Figure 4.15 The release of different TNTs shape, with and without coating; (a) normal tubes (T-3), (b) short necked bottles (B-1) and (c) bottles with a long neck (B-2).

Table 4.3 summarizes the release kinetic constants *k* and the half-life time $t_{1/2}$ of the drug elution from different tube morphologies. These values were obtained by applying a liner fitting to the logarithmic of MB release curves as a function of time. The table also includes the measured tubes and the bottles neck dimensions, neck diameter (d) and neck length (L_N).

It can be clearly seen from the experimental data that, the release kinetic constants and the half life time of the TiO_2 anodised surfaces are strongly affected by their morphology and the polymer coating. The delay time of the TiO_2 nanobottles increases with an increase in neck length for the nanobottles morphology. The effect of polymer coating is less obvious than for nanobottles than for nanotubes. The fast release of MB from TNTs can be efficiently reduced with a polymer coating. For nanobottles, since the

release kinetics is already dominated by the neck dimension, the effects of the polymer coating became less effective. In conclusion, the drug elution kinetics has been successfully controlled by controlling the tube morphology and polymer coating.

Table 4.3 Release kinetic constants *k* and the half life time $t_{1/2}$, obtained from liner fits of MB elution curves for different tube morphology.

TiO_2 nanostructure	B-1	B-1+ coating	B-2	B-2+ coating	T-3	T-3+ coating
k (h^{-1})	0.71	0.41	0.38	0.23	30.6	6.99
$t_{1/2}$ (min)	58.56	101.4	109.4	180.6	1.358	5.958
d (nm)	30	30	30	30	80	80
L (nm)	350 (L_N)	350 (L_N)	700 (L_N)	700 (L_N)	4000	4000

4.4.4.6 The quantitative relationship between the release kinetic (*k*) constant and tube geometry factor (P)

Based on the surface spread phenomenon, diffusion is accepted to be the main mechanism driving the drug molecules from a region of higher concentration (loaded nanotubes) to the lower concentration region until equilibrium is attained. Moreover, according to the experimental data analysis presented in this work, the tube geometry (diameter and length) plays a key role in controlling the release rate. To confirm the effect of the nanotubes geometry on the release rate, a model of the relationship between the release kinetic constant and tube geometry of the anodized surfaces (P) was established. We assume that the drug release rate constant is proportional to the tube cross section and inverse proportional to the length of the nanotube.

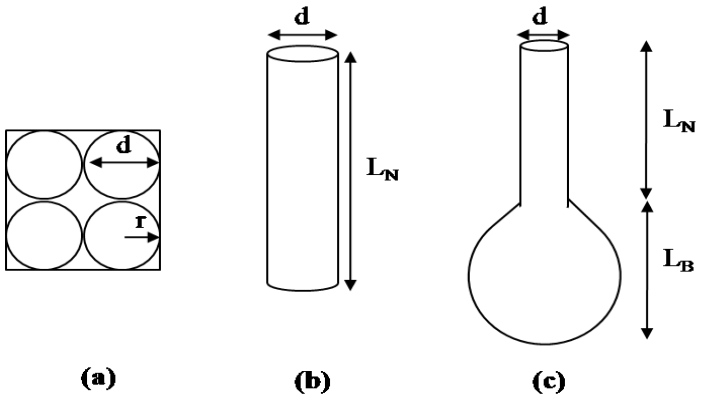

Figure 4.16 The dimensions of nanotubes with different shapes (a) unit pore volume, (b) normal TNTs and (c) TNBs.

Based on this assumption, the cross section area (S), as shown in Fig. 4.16a, can be defined as equation 4.3.

$$S = \frac{\pi d^2}{4} = \pi r^2 \qquad \text{(Equation 4.2)}$$

Where *d* is the inner diameter of the tube and *r* is the tube radius. The release rate constant is directly proportional to S and inversely proportional to the tube length (L). The nanotube geometry factor in this case can be written as following:

$$P = \frac{S}{L} = \frac{\pi d^2}{4L} \qquad \text{(Equation 4.3)}$$

The geometry of the normal nanotubes (Fig. 4.16b) can be defined in the following equation:

$$P = \pi \frac{d^2}{4L_B} \qquad \text{(Equation 4.4)}$$

Where, L, is equal to the length of the tube, $L_{B.}$ The geometry factor of the nanobottles shown in Fig. 4.16c can be written as following:

$$P = \pi \frac{d^2}{4(L_N + L_B)} \quad \text{(Equation 4.5)}$$

Where the tube length, L, is equal to the total length of tube neck, $L_{N,}$ and the tube base $L_{B.}$ the geometry factor of the prepared nanotubes and nanobottles were calculated according to equations 4.4 and 4.5 and presented in table 4.4 together with the release kinetic constant and tubes dimensions.

Table 4.4 A summary of the release kinetic constant *k* and the half life time, $t_{1/2}$, of different tube morphologies.

TiO_2 nanostructure	B-1	B-2	T-1	T-3	T-4
k (h^{-1})	0.71	0.38	6.9	30.6	49.15
d (nm)	30	30	34	80	80
L (nm)	350 (L_N) + 410 (L_B)	700 (L_N) + 410 (L_B)	820	4000	2650
P (nm)	0.92	0.64	1.11	1.44	1.9

In table 4.4, B-1 and B-2 are the TNBs created by different times of the first step anodisation (1 and 2 hours respectively). T-1 is the TNTs prepared by an applied voltage of 20 V for 1hr. T-3 and T-4 tubes were formed by using a 60 V anodisation voltage but varying the time of the acid treatment on each sample. The release kinetic constant as a function of the calculated tube geometry factor were plotted in Fig. 4.17.

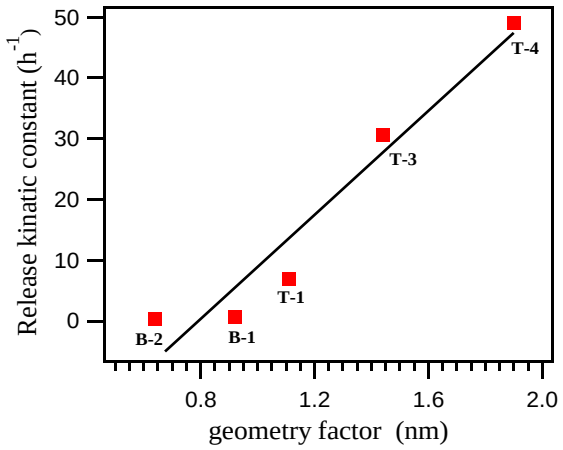

Figure 4.17 A model of the release of different tube shape.

As shown in Fig. 4.17, a good liner relationship exists between the film geometry factor and the release constant, where the straight line is a fit to the measured data. The concept behind this model confirms the proposed mechanism for elution behaviour of different tube morphologies. The tube morphology, diameter and length, play a key role in controlling the diffusion rate. While the drug molecules release rate increases rapidly whenever the tube diameter is increased. On the other hand, the release rate decreases with increasing the tube length or neck length for nanotubes or nanobottles. Here, we are not able to distinguish the effect of L_N and L_B for a nanobottle, limited by the simplicity of our model. This could affect the linearity of the plot in Fig. 4.17 for the nanobottles. For disentangling the contributions from L_N and L_B, different experiments can be proposed that, for synthesising TNBs with the same L_N and different L_B. Investigating the effect of that on the release kinetics could be an effective way for demonstrating the effect of the base properties on the release kinetics. These structures can be obtained through controlling the anodisation time. By fixing the second anodisation time (control the L_B) and changing the first anodisation time (control L_N), the length of the neck can be adjusted while maintaining the length of the base. However, to some extent, this will also

affect the diameter of the neck, which will become difficult to achieve accurate quantitative results.

4.5 Conclusion

This chapter has outlined the effects of different factors on the drug elution from TNTs and TNBs. These factors included; the tube shape, diameter, length and polymer coating. The tube shape plays a key role in the control of release kinetics of the drug elution. The drug agent can be eluted at slower rates by using TiO_2 nanostructures with specialised morphology, nanobottles, compared to the normally used nanotubes. Moreover, the release kinetic constants were seen to increase sharply with an increase in tube diameter, while they decreased considerably with increasing tube lengths. For further release control, a PVA coating is a key factor to reduce the tube elution rate constant. A geometry model has been established quantitatively between the release rate constant and the geometry for nanotubes and nanobottles.

Chapter 5 Optimisation the structure of TiO_2 nanorod films for photoelectrochemical water splitting

5.1 Abstract

This chapter optimises the structures of the synthesised TiO_2 nanorod (TNR) films for improved photoelectrochemical (PEC) water splitting activity. One-dimensional (1-D) rutile TNR films have been synthesised on Fluorine doped tin oxide (FTO) using a one-step hydrothermal method. The effect of the reaction conditions on the morphology, crystal orientation and photocatalytic activity of the grown films were systematically investigated. The experimental results showed that the morphology of the grown film could be controlled by several parameters, including temperature, reaction time and the titanium precursor concentration. With lower titanium precursor concentration, short reaction time and lower reaction temperature, shorter TNRs with lower density, smaller diameter and less alignment with the substrate were formed. By increasing the reaction time, temperature and the precursor concentration, greater density, larger rods diameter and film thickness were achieved, in addition to the superior vertical alignment perpendicular to FTO substrate. The PEC measurements revealed that the tilted TNRs film at the density of 14 μm^{-2} and thickness of 2.2 μm exhibited the highest photocatalytic efficiency.

5.2 Introduction

The storage of solar energy in the form of H_2 has been considered to be one of the ideal routes for developing a versatile clean and sustainable energy source in future. When the solar energy is captured and stored as the chemical energy in the form of hydrogen gas,

it can be used as fuel either in combustion engine or in a fuel cell day and night. Cost-effective and high efficiency PEC splitting of water is essential for the competitiveness of green hydrogen production technology. As an effective PEC photoanode material for water splitting, TiO_2 has been most intensively studied. [58, 239, 240]. The low cost TiO_2 [63] has a favourable band-edge positions [65], chemical stability, photocorrosion resistance and controllable nano-morphology [81].

One-dimensional (1-D) TiO_2 nanostructures, including nanorods (TNRs) [46, 82], nanowires (TNWs) [80, 81] and nanotubes (TNTs) [53, 84], have been considered as ideal morphologies of photoanode for water splitting application. As 1D nanomaterial, most of these structures have their longer axis perpendicular to the conductive substrates with good crystallinity. This provides good pathways for the photogenerated electron transportation, which could increase the electrons separation and reduces their recombination rate with the hole [131, 241]. This in turn may improve the performance of photoanode in the PEC system. The larger surface area of the 1-D nanostructure is another important character for high efficient PEC, since it offers better contact between the nanomaterials and the electrolytes with higher volume density of surface reaction centre.

Among different polymorphs of TiO_2, anatase and rutile crystallites are known as superior photocatalysts and it is also accepted that anatase exhibits a higher photocatalytic activity compared to rutile. Possible explanations could be included in the following: (i) since anatase has a larger band gap of (3.2 eV) than rutile (3.0 eV) that could increase the top edge of its valance band to higher energy levels in respect to the redox potential of the adsorbed molecular. This increases the oxidation power of the holes and facilitates the electron transition from the adsorbed molecules to the TiO_2. (ii) The difference in the surface properties between two TiO_2 polymorphs may affect the adsorption of the molecular and the charge transition. These properties could have chemical effect in terms

of coordination structure of the surface and or could have electronic effect such as surface defects which provide states to act as charge trapping and separation at surface. (iii) Anatase exhibits an indirect band gap while rutile exhibits both direct and indirect band gaps. In rutile both band gaps are very similar. Generally, due to the different characters of atomic orbitals and their specific arrangements in crystal lattice, semiconductors can have several band gaps and in many cases, both direct and indirect band gaps can be observed. Normally, only one band gap has the smallest energy and it determines either direct or indirect character. In the case of rutile, there is two band gaps are accidentally degenerate with almost identical band gap energy. One is a direct band gap (Γ-Γ transition), while the other is an indirect band gap (Γ-X transition), although the direct band gap energy is slightly smaller than the indirect band gap. This is due to the distortion of the TiO_6 octahedron. Thus, strictly, speaking, rutile is a direct band gap semiconductor. For anatase, only an indirect band gap (Γ-X transition) has the smallest energy, hence it is a clearly indirect semiconductor.

In general, the photogenerated charge carriers in semiconductor with indirect band gap have longer lifetime compared to those in the direct band gap. Charge carriers of longer lifetime in anatase are likely to be involved in photocatalytic reaction at the surface [115]. For rutile, although the rate for charge recombination is higher, if the charge mobility within the material can be improved, the recombination can be effectively reduced. (iv) For the photogenerated electron-hole pairs, to be involved in the photocatalytic reaction, they must have efficient mobility to reach the surface within their lifetime. The exciton mobility along certain crystallographic direction has been proposed to be important factor in the dependence of their oxidation/reduction behaviour on the surface orientation [242]. Since higher effective mass was reported in rutile than in anatase [68], it implied lower charge mobility in rutile. Resent study demonstrated that, the bulk transport of excitons

to the surface is a key factor that has to be taken into account to explain the photocatalytic differences between anatase and rutile [115]. They evaluate the photocatalytic activity of TiO_2 films of the two polymorphs as a function to the film thickness. The investigation showed that in anatase the charge carriers excited deeper in the bulk contribute to surface reactions compared to rutile film. This confirms that charge mobility in rutile is poorer. As such only thinner film of rutile can reduce the charge recombination. Alternatively, a nanostructured material, such as nanorods, might also help to overcome the mobility problem in rutile. With improved crystal quality or introducing dopants could affect the charge mobility along the nanorod long axis. A smaller diameter is also essential for improving the utilisation of holes to oxidise chemical species in the electrolyte.

The synthesis of single crystal TNRs films was first reported in 2009, by the bottom up hydrothermal method [46]. The method is cost-effective with high reproducibility for the synthesising large quantities of TNRs. The electrical and photocatalytic properties of this nanostructure need to be optimised, although previous works have been focused on improving the visible light absorption, reducing the band gap and the charge carrier recombination rate for PEC. However, there is still limited knowledge about the effect of the hydrothermal synthesis conditions on the structures and performance of TNRs.

In the present work I report on the detailed study of the structure and photocatalytic activity of the rutile at different hydrothermal synthesis conditions. The studied conditions include the titanium precursor concentration, growth time and reaction temperatures. The obtained TNRs film with optimal performance could be used as template for other applications such as DSSCs, as well as for developing composite nanomaterials for further photocatalytic performance enhancement by depositing different materials on the TNRs.

5.3 Experiments

5.3.1 Fabrication of TNRs arrays

All the chemicals were used as received, including concentrated hydrochloric acid (Fisher Scientific, 32 wt%), titanium (IV) n-butoxide (Alfa Aesar, 99+ %). Fluorine doped tin oxide (FTO) coated glass (Sigma Aldrich, 7Ω/sq) was used as the substrate.

Films of TNRs were prepared by the hydrothermal synthesis, with the method illustrated in detail in chapter 2 (Section 2.2.2). In a typical synthesis, DI water (10 ml) was mixed with concentrated hydrochloric acid (14 ml). The mixture was magnetically stirred at room temperature for 5 minutes after which titanium butoxide (TBO, 0.2~0.6 ml) was slowly added. The solution went from colourless to cloudy upon the addition of TBO. Once the solution turned clear again, usually after further 5 minutes of stirring, it was transferred to a Teflon-lined stainless steel autoclave (50 ml). Two pieces of cleaned FTO glass substrate (1×2 cm^2) were placed at an angle against the wall of the Teflon liner with the conducting side face down. In order to study the effect of the growth conditions on the film morphology and photocatalytic efficiency, the reaction temperature and time were varied from 140~200°C and 3~20 hours respectively. The autoclave was then taken out and left to cool to ambient temperature. The coated FTO pieces were washed with deionised water and left to dry in air. After confirming the growth of nanorod structures of TiO_2 by X-ray diffraction and SEM, the samples were annealed in air for 3 hours at 550°C. This step improves the adhesion of the nanorods to the substrate and also enhances the crystalline structure. The structure was then checked with XRD and SEM again. No observation of any degrading of the nanomorphology, although the crystallinity was significantly improved.

5.3.2 Structure characterisations and PEC measurements

The crystal structures of the annealed TNRs films were characterized by X-ray diffraction (Siemens D500). Scanning electron microscope (SEM) images were collected, over the as grown samples, (SEM, JSM 820M, JEOL, operating at 30 keV) and used to measure the film thickness, using Image J (National Institutes of Health, USA) software. The optical band gaps of the optimised TiO_2 film were evaluated based on the reflection absorbance spectra. These spectra were collected using an integrating sphere (Ocean Optics ISP-REF) with a built-in tungsten-halogen light source, covering wavelengths from 300 to 1000 nm, at room temperature. The PEC measurements were performed at room temperature using a standard three-electrode configuration. The TNRs samples were used as a working electrode (photoanode), a KCl saturated Ag/AgCl was used as a reference electrode and a platinum sheet was used as a counter electrode. 1 M KOH aqueous solution (with measured pH of 13.6) was used as the electrolyte. A USB potentiostat (eDAQ) was used to control and record the photocurrent as a function of electrochemical potential. Sunlight was simulated with a 300 W xenon arc lamp with an AM1.5 G filter and the output light power density was adjusted to 100 mW cm^{-2}.

5.4 Results and discussion

5.4.1 Controlling the growth parameters for optimising the growth of TNRs film

In this section, a comparison between the effects of the hydrothermal growth conditions on the morphology, crystal structure and photocatalytic efficiency of produced films was illustrated. The parameters studied included the concentration of titanium source, growth time, reaction temperature, substrate materials and substrate positions in autoclave. The growth mechanism of the TNRs crystals on FTO was also proposed. Finally, the PEC performances of the grown films were discussed.

5.4.1.1 Effect of initial titanium concentration

In order to study the effects of TBO concentrations, the growth temperature and time were fixed at 150ºC and 4 hours. The volumes of added TBO were varied from 0.3 ml, 0.4 ml, 0.5 ml to 0.6 ml which forms the volume concentrations of 1.23 v%, 1.63 v%, 2.04 v% and 2.44 v% respectively. When 0.3 ml TBO was used, no film was formed on the FTO sample while at higher concentrations, homogeneous TNRs were successfully formed indicated by a white film on the FTO. Fig. 5.1 displays top and side views SEM images of TNRs films grown at different TBO concentrations. All images reveal nanorod structure with smooth side surfaces and square cross sections. It also can be seen that, the density of the nanorods can be varied by changing the initial titanium precursor concentration in the growth solution. Increasing the initial TBO concentration causes an increase in the film density with better orientation of the rods along the longer axis. This observation can be attributed to the variation of nucleation density formed at the beginning of the hydrothermal synthesis. When the titanium precursor concentration is low, which give low nucleation density, nanorods start and continue to grow at an angle to the substrate, since there are no neighbouring rods to hinder their growth. Subsequently, the obtained TNRs film exhibits low density of regularly tilted nanorods with a tilt angle of about 60º to the substrate as shown in Figs. 5.1a and b. At high concentrations, when the nucleation density is high, the growth of the angled rods is hindered by neighbouring rods and more vertically aligned TNRs were achieved (Fig. 5.1c and f). That was associated with obvious increase in the grown nanorods density.

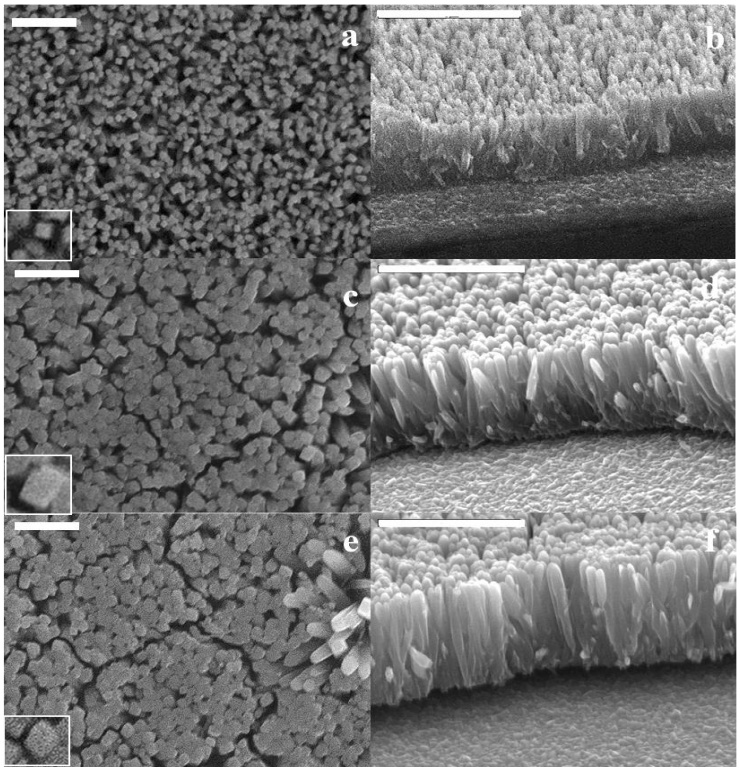

Figure 5.1 SEM images of the top view and cross section of TNR arrays grown at different titanium butoxide volumes. (a and b) 0.4 ml, (c and d) 0.5 ml and (e and f) 0.6 ml. The scale bars of the top views and cross section views are 2 µm and 5 µm respectively.

Fig. 5.2a shows the measured diameter distribution of the TNRs. The TNRs have a good mono-dispersed diameter at different TBO concentrations, although the average rods diameter was significantly affected by the initial TBO concentration (Fig. 5.2b). Reacting 0.4 ml of the TBO for 4 hours produced TNRs with an average diameter of 187 nm and full width of half maximum (FWHM) of 30 nm. Increase the volume of to 0.5 ml leads to sharp increase in the average rod diameter to about 360 nm with a greater variation in rod diameter distribution (FWHM reached 60 nm). By further increase the TBO volume to 0.6 ml, the diameter of the nanorods increased to 380 nm while the diameter distribution was actually narrowed. This observation indicates that increasing the TBO concentration causes its rapid hydrolysis as soon as it is added to the growth solution. Therefore, the condensed nuclei will have wide average diameter and large size distribution. The top views SEM images also show that with increased TBO

concentration, there is some coalescence of the nanorods resulting in larger diameters with less space between the adjacent rods. This also has some contribution to a wider diameter distribution. The growth mechanism of TNRs will be discussed later.

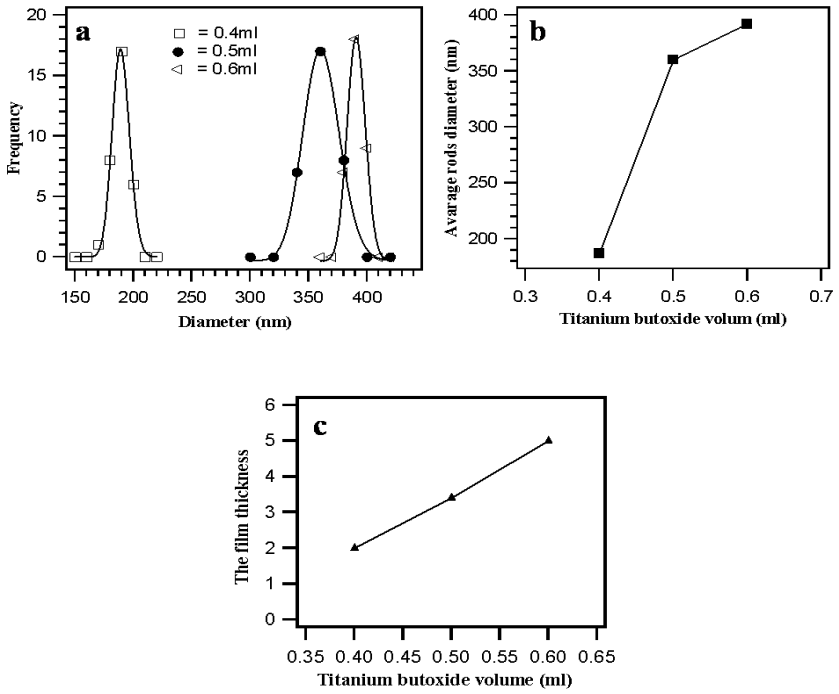

Figure 5.2 (a) Diameter distribution of TNRs arrays prepared on FTO substrate with varied TBO volume of 0.4 ml, 0.5 ml and 0.6 ml. (b) Average rods diameter as function to the titanium precursor volume. (c) The measured film thickness as a function of the TBO volume.

It was also observed that, there is a proportional relationship between the TBO concentration and the TNR film thickness as presented in Fig. 5.2c. In addition, as the TNRs become thicker, the film becomes fragile and the adhesion strength is reduced. XRD studies were undertaken to confirm the crystalline phase of the as prepared TNRs films. XRD patterns of annealed TNRs films prepared using different initial titanium volumes were collected and presented in Fig. 5.3

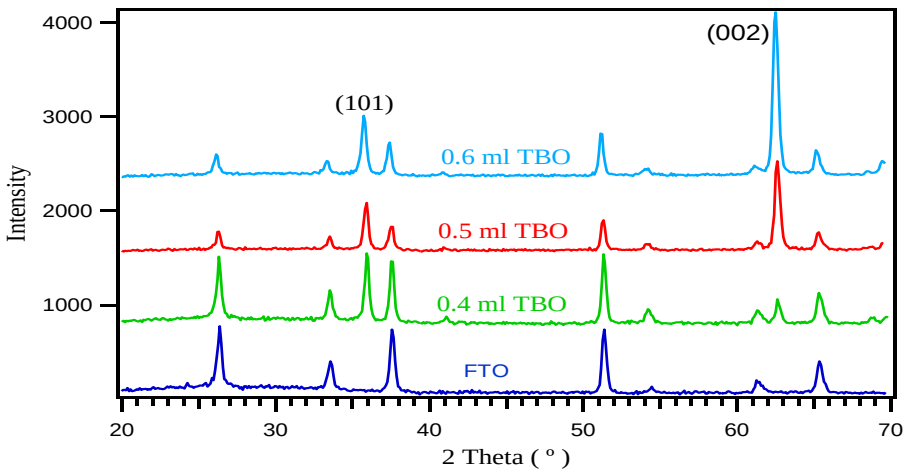

Figure 5.3 XRD patterns of the rutile TNRs films on FTO substrates. These films were synthesised using different titanium butoxide volumes, 0.4 ml, 0.5 ml and 0.6 ml and then calcined at 550°C for 3 hours.

In comparison with the clean FTO glass, two additional diffraction peaks located at 2θ angles of 36.3° and 63.2° were observed on TNR samples. These two peaks are indexed to the tetragonal rutile TiO_2 crystal structure (JCPDS No. 88-1175) [131] and correspond to the (101) and (002) planes respectively. Furthermore, the absence of the other diffraction peaks of rutile TiO_2, which normally occur in polycrystalline or powder samples, suggests that the nanorods are aligned vertically with the rod cross section dominated by the (002) plane. It can be seen clearly that, in the tilted TNRs film, which was grown using low TBO volume of 0.4 ml (green pattern), the peak centred at 36.3° corresponds to (101) diffraction is dominant over the (002) peak. Conversely, the peak intensity of the (002) plane was higher for thicker TNRs films that were prepared at higher TBO concentrations of 0.5, 0.6 ml (red and blue pattern respectively). These results could suggest that the plane of the tilted TNRs crystals exposed to the XRD is (101) (the side view of the rod crystal), while the (002) plane is for the top of the perpendicularly aligned TNRs (which is again the exposed side of the crystal). Fig. 5.4 shows a schematic diagram of the rutile unit cell with highlighting (101) and (002) planes.

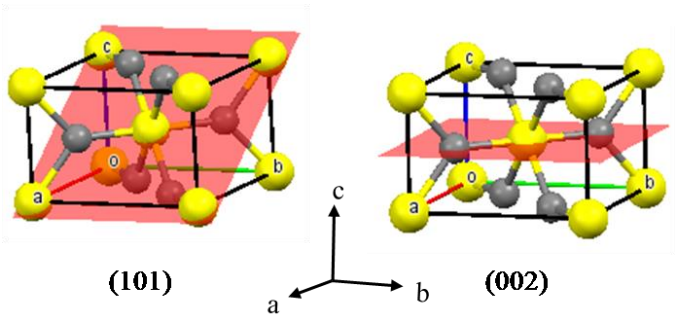

Figure 5.4 Schematic diagram of rutile unit cell shows (101) and (002) planes (in red colour).

Interestingly it has been reported that the (101) surface is the most photocatalytically active surface of all rutile surface orientations studied, (110), (001), (100) and (002).[243] This surface shows more abundant of four fold coordinated Ti structural features.[243] This special geometry might increase the reactivity either by altering the efficiency with which carriers are trapped at the surface or by altering the rate at which photogenerated carriers are transferred across the solid-liquid interface. For example, it is possible that the relatively electron-rich surface O surrounding the four coordinate Ti are more effective hole traps than those surrounding five-coordinate metal sites [244]. Similarly, a surface Ti with four O neighbours might bind adsorbed species from the solution more effectively and this could promote charge transfer from the crystal to the adsorbent.

For oriented nanostructures, nanorods or nanowires, the peak height will be intense at the Bragg angle corresponding to the preferred orientation. Based on the diffraction peak intensities of the grown TNR films, the degree of crystal orientation, *p*, can be determined by the diffraction intensity of (002) plane, which is the favoured growth direction, according to equation 5.1 [245]:

$$p = I(002)/\sum I(hkl) \qquad \text{(Equation 5.1)}$$

In which $I(002)$ is the intensity of (002) diffraction peak and $\sum I(hkl)$ is the intensity of all other diffraction peaks of the sample. The degree of orientation for the TNRs and the peak width of the 002 plane (measured by the FWHM) at different TBO volumes were calculated from the XRD patterns and plotted in Fig. 5.5a. Since the FWHM of the diffraction peak is inversely proportional to the averaged crystal size of the materials according to Scherrer's equation (Equation 3.2, chapter 3):

$$D_{hkl} = \frac{K\lambda}{\beta_{hkl} cos\theta_{hkl}}$$

D_{hkl} is the crystal size (nm) perpendicular to the (hkl) crystal plane, $\boldsymbol{\lambda}$ is the wavelength of the X-ray which is 1.5406 Å and K is a constant equal to 0.89 when β_{hkl} takes the half of the diffraction peak boarding. β_{hkl} is related to the diffraction peak width. The crystal domain, D, of the TNRs with different initial titanium volumes were calculated and plotted against the different TBO volumes as presented in Fig. 5.5b. That was performed in order to confirm the correlation between p and FWHM.

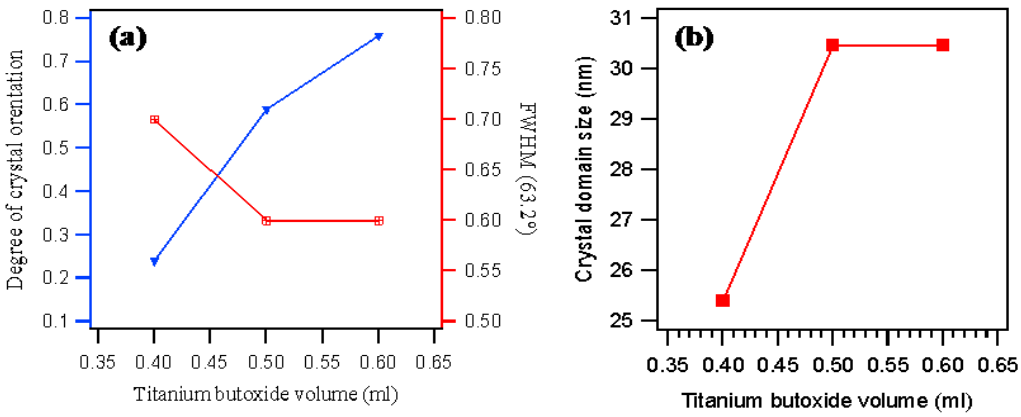

Figure 5.5 Effect of TBO concentration on the degree of TNRs crystal orientation and the FWHM of (002) plane.

The orientation degree of TNRs nanorods increased sharply with increasing initial titanium concentration in the growth solution. This indicates that the growth in a solution containing higher titanium processor concentration yields nanorods film with a preferred orientation along (001) direction (Fig. 5.5a). While the degree of orientation is increased, so are the crystal domain sizes, shown in Fig. 5.5b. This suggests that with increased growth solution, the overall quality of the TNRs was improved.

5.4.1.2 Effect of growth time

In order to study the effects of the growth time on the morphology of the TNRs, the initial titanium precursor concentration and growth temperature were kept constant at 0.4 ml and 150°C respectively. The growth duration was controlled at 3, 4, 5, 6, 7 and 16 hours. The SEM images of the grown uniform white films are shown in Fig. 5.6. These images reveal well-defined vertically oriented nanorod structures with smooth sides and rough square tops. For 3 hours' growth, low density TNRs are formed on the FTO substrate. The orientation of the nanorods is not well aligned perpendicular to the substrate due to the low density (Fig. 5.6a and b). The alignment of the TNRs was improved significantly as the growth time was increased. After five hours the nanorods were much better perpendicularly aligned to the substrate with increased TNR density (Fig. 5.6e and f). This is attributed to the constraint of tilted rod formation by densely packed adjacent TNRs.

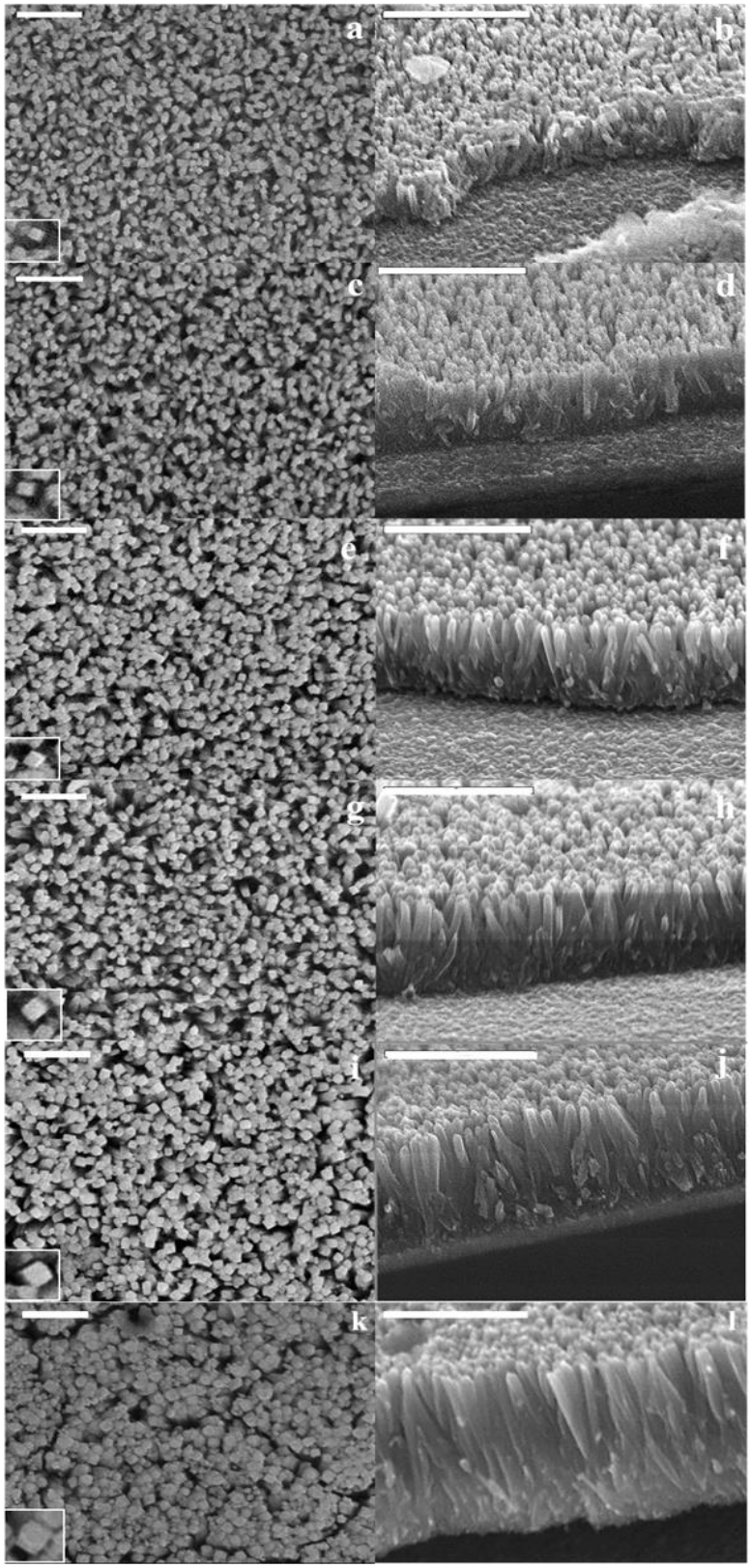

Figure 5.6 SEM images of top views and side views of TNR arrays grown for different periods on FTO glass substrates. (a and b) 3 hours, (c and d) 4 hours, (e and f) 5 hours, (g and h) 6 hours, (I and j) 7 hours and (k and l) 16 hours. The scale bars of the top views and cross section views are 2 µm and 5 µm respectively.

The growth behaviour of the nanorods exhibited a gradual increase in the density, diameter and length with increasing the reaction duration. The average diameter and film thickness of the TNRs measured at different reaction times are plotted in Fig. 5.7.

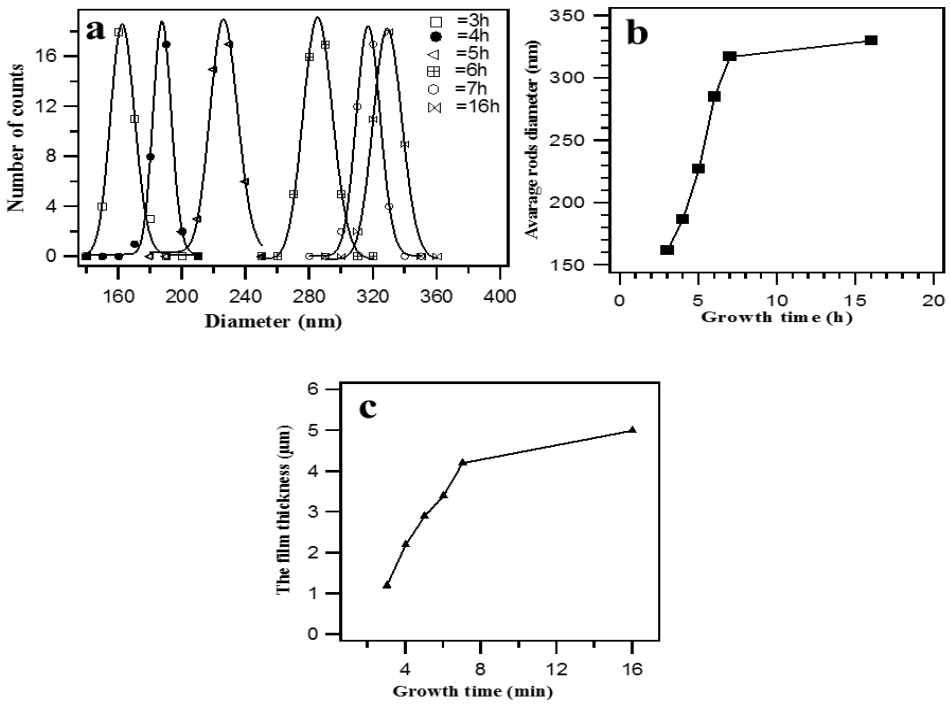

Figure 5.7 (a) Diameter distributions of TiO_2 nanorods arrays synthesised on FTO substrate at different growth times of 3 hours, 4 hours, 5 hours, 6 hours, 7 hours and 16 hours. (b) The effect of the growth time on the average diameter of the grown rods. (c) The effect of the growth time on the film thickness.

As shown in Fig. 5.7a the TNRs obtained after different reaction times have a mono-dispersed diameter. The FWHM of the diameter distribution is varied slightly for the nanorods synthesised at different growth times, due to the limited accuracy for sampling of the diameters and some coalescence of the TNRs at high density.

Moreover, the growth time has a noticeable effect on the average rod diameter (Fig. 5.7b). A steady increase in rod diameter, from 162 nm to over 300 nm was observed by increasing the growth time from 3 hours to 7 hours. Further increase in the growth time (16 hours) shows less effect of the rod diameter (350 nm) as the TNRs were very

densely packed after 7hours growth, leaving no space for horizontal growth. This can be observed from both the top- and side-view of SEM images in Fig. 5.6(i-l).

The growth time has similar effect on the film thickness (Fig. 5.7c). It was also increased steadily from 1.2 μm to 5.0 μm by increasing the time from 3 hours to 16 hours. Fig. 5.6c also shows that between 7 hours and 16 hours, the increase of the film thickness slows down. This is due to the depletion of Ti precursor in the solution. After 20 hours' growth, some parts of the film started to detach from the FTO substrate. That is attributed to the increased stress at the interface between the densely packed crystallised thin film and FTO glass. This leaves no space between the TNRs to release the stress and the film became fragile. Post washing and annealing process could easily damage the integrity of the thick film.

Fig. 5.8 displays the XRD patterns of FTO and TNRs samples, annealed at 500°C for 3 hours in air, as a function of growth duration. The two dominant diffraction peaks from the tetragonal rutile TiO_2 crystal structure (JCPDS No. 88-1175) [10] corresponding to (101) and (002) planes were observed at 36.3° and 63.2° respectively. All the other peaks are related to the FTO substrate. The XRD patterns show gradual increase in intensity as the growth time increases. This phenomenon is in agreement with the morphologies observed in SEM images in Fig. 5.6.

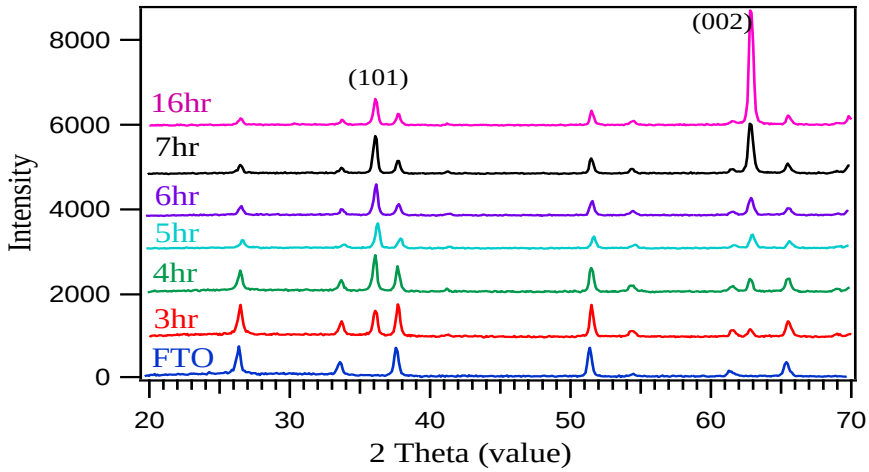

Figure 5.8 XRD patterns of the TNRs films on an FTO substrate. These films were grown for various periods and annealed at 550°C for 3 hours.

After 3-4 hours of growth, the (101) peak dominants over the (002) peak. At this stage, the rods are tilted with angles of approximately 28° and 24° respectively to the surface normal. As was mentioned previously, this structure led to exposure of the side of the rod crystal that was detected by XRD, which seems to be the (101) plane. The subsequent grown TNRs show increased diffraction intensities from (002), while the intensities from the (101) peak maintains constant. Therefore, the orientation of the TNRs became more perpendicular to the substrate with increasing growth time, as observed from the SEM images. The grown nanorods have angles to the surface normal which were calculated to be 19.3°, 16.17°, 6.7°and 1.26° at grown time of 5, 6, 7 and 16 hours. Moreover, some diffraction peaks from (110) and (111) planes, which are normally present in polycrystalline TiO_2 or powder samples, are absent. This indicates that the individual nanorods are single crystals throughout their composition and the (110) and (111) planes are perpendicular to the substrate.

The degree of crystal orientation of the obtained TNRs can be confirmed by analysing the XRD data as shown in Fig. 5.9 as complementary analysis to the SEM characterization.

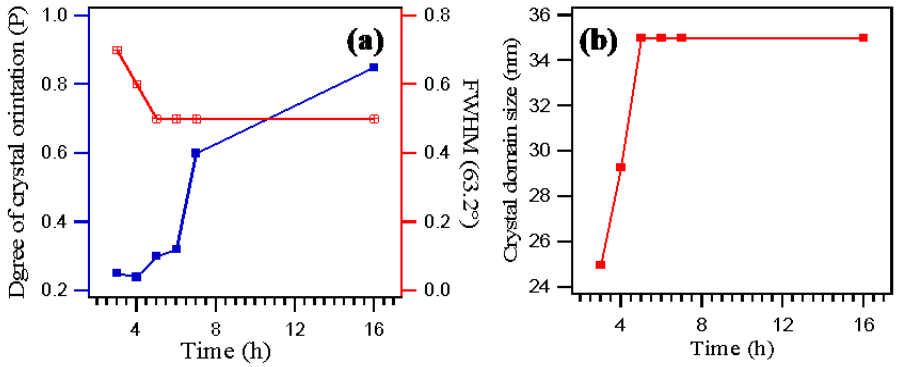

Figure 5.9 Effect of the TBO concentration on the degree of TNRs orientation and the FWHM of (002) plane.

It is clear from Fig. 5.9, the orientation of the nanorods along the (002) plane improved gradually in the first six hours, followed by a sharp increase indicating greater perpendicular character with respect to the substrate. In addition, a narrower FWHM with increasing growth time shows the improvement in their crystallinity.

5.4.1.3 Effect of the growth temperature

The synthesis of TNRs was also carried out at different reaction temperature (140, 150 and 160ºC) at fixed initial titanium volume of 0.4 ml TBO and a fixed growth time of 4 hours. The growth temperature was found to be another important factor affecting the morphology of the nanorods film as shown in SEM images in Fig. 5.10. The diameter of the rods is directly proportional to the growth temperature. Films of small, particle-like nanorods were formed at 140ºC, as shown in Fig. 5.10a and b. Increasing the temperature to 160ºC leads to nanorods with greater diameter and density (Fig. 5.10e and f). That could be due to the increasing in nucleation and growth rate at high temperature.

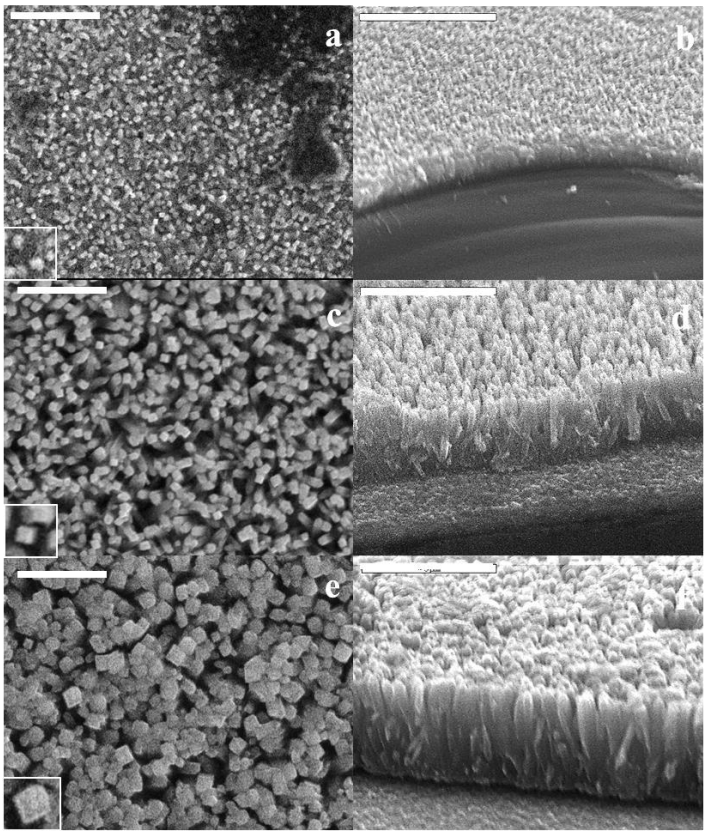

Figure 5.10 Typical top view and side view SEM images of TiO_2 NRs prepared using varied temperatures. (a and b) 140ºC, (c and d) 150ºC and (e and f) 160ºC. The scale bars of the top views and cross section views are 2 µm and 5 µm respectively.

Fig. 5.11 shows the measured morphological parameters as a function of growth temperature. The diameter distribution at different temperature in Fig. 5.11a confirms that the rods are monodispersed, although the distribution becomes wider at higher temperature. Nanorods with an average diameter of 110 nm and FWHM of 20 nm were formed at 140ºC. Increasing the hydrothermal temperature to 160ºC saw the average diameter rise significantly to 180 nm with the broadening of the FWHM to more than 60 nm, which indicate the large difference in the size of the rods formed at high temperature. That can be attributed to rapid increasing in the nucleation density and the formation of nucleation sites with different particles sizes as result of increasing the reaction temperature. More explanation will be presented in the following sections.

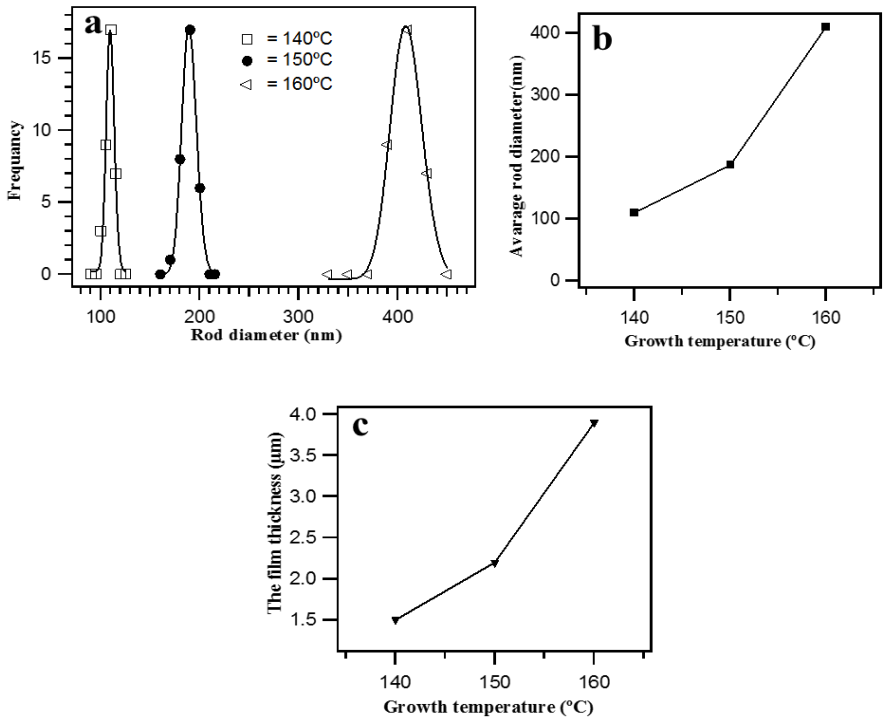

Figure 5.11 Effect of the growth temperature on the properties of grown TNRs arrays. (a) Diameter distributions of TNRs arrays synthesised on FTO substrate at different growth temperatures, (b) the average rods diameter and (c) the film thickness.

Moreover, increasing the reaction temperature leads to a proportional increase in the obtained film thickness (Fig. 5.11c). The growth at 140ºC leads to a TNRs film with the thickness of 1.5 µm. By increasing the growth temperature to 160ºC, the thickness of the nanorods film was increased to 4 µm. This can also be attributed to the increasing of the reaction rate at higher temperatures.

5.4.1.4 Effects of different type of substrates

Based on our experimental conditions, the growth of TNRs arrays was examined on three different types of substrates: FTO glass, normal flat glass substrate and titanium sheet. Oriented TNRs film only grew successfully on the FTO glass substrate. By using FTO as substrate, an epitaxial interface is formed between the SnO_2 and the deposited rutile TiO_2 layer. The epitaxial growth refers to the deposition of a crystalline over-layer on a

crystalline substrate, which acts as a seed crystal. Therefore, the deposited film may lock into one or more crystallographic orientations with respect to the substrate crystal. In this case, the FTO crystals behaves as the seeding centre for the epitaxial growth which can help to initialise the deposition of TiO_2 with improved alignment of the rutile TNRs. This is due to the similarity between the crystal structure of SnO_2 crystals and rutile TiO_2. Both crystals has a tetragonal structure and more important, there is only 2% difference in their lattice constant [246]. The FTO crystal layer in this case acts as seeding layer to promote the heterogeneous nucleation of TiO_2 nanoparticles on the substrate from being disrupted by the homogeneous nucleation in the solution. Slow growth of the rutile nanoparticles at low precursor concentrations and low temperature could help to form uniform vertical arrays of TiO_2 nanorods with tetragonal crystal structure on the FTO. On glass and titanium plate, there is no such interface layer and the attachment of TiO_2 particles becomes difficult.

Compared to Kumar and co-workers results [247], who also investigated the hydrothermal growth of TNRs on different substrates, such as ITO glass, normal glass and Ti plate. Their results showed that, nanorods with dandelion-like morphology were formed on glass. The difference in the experimental conditions between their work and the current work could be the main reason for promoting the TiO_2 nanostructure growth with dandelion-like morphology on glass substrate. They used higher concentration of different titanium source ($TiCl_4$) and higher reaction temperature of 180°C. We expect $TiCl_4$ to be more reactive and it helps to form seeding layer on glass, which is assisted by the higher concentration. Additionally, the growth process was carried out in smaller autoclave (23 ml) with using filling factor of more than 90% of its capacity. However, as the formation of the seeding layer is not properly controlled, only sparse, low density seeds were formed, which leaves large space for the growth of dandelion morphology.

This hierarchical structure was formed by simultaneously growth of nanorods from the same seeding centre into a radially growth orientation. This implies that high density of seeds on the substrate is important for increasing the growth rate and for achieving well oriented TNRs.

5.4.2 TNRs growth mechanism in hydrothermal synthesis

The growth mechanism of the TNRs crystals can be proposed as following: generally, the growth of TiO_2 crystals in aqueous solution results from the formation of growth units which are incorporated into the crystal lattice. The nature of these units depends on the acidity of the growth solution and the presented legends [247, 248]. The reaction takes place in three stages: a hydrolysis stage, a nucleation stage and crystal growth stage. Since TBO has high reactivity towards water [249-251], the formation of TiO_2 begins with the hydrolysis of TBO according to the equation 5.2:

$$Ti(OBu)_4 + 4\,H_2O \xrightarrow{\text{hydrolysis}} Ti(OH)_{4\,\text{complex}} + 4BuOH \qquad \text{(Equation 5.2)}$$

In a strong acid environment, $Ti(OH)_4$ becomes soluble and stabilised in the solvent. At this stage, the solution is clear. TiO_2 is subsequently formed by the condensation of the hydrolysed species at raised temperature as shown in equation 5.3

$$2Ti(OH)_{4\,\text{complex}} \xrightarrow{\text{condensation}} TiO_2 + 2H_2O \qquad \text{(Equation 5.3)}$$

In the nucleation stage, TiO_2 nuclei are formed as a product of the condensation of the hydrolysed titanium species. To avoid the problems related to the high solubility of small particles and also to promote the formation of stable nucleation sites, a certain

number of hydrolysed molecules are required in the oversaturated solution. It has been reported that both the hydrolysis and condensation stages are sensitive to the pH of the solution [247] and titanium precursor concentration [46]. Highly acidic conditions significantly restrict the supply of the growth units. In contrast, increasing the titanium precursor concentration leads to increase its hydrolysis and nucleation rate, which need to be balanced by the growth rate.

Finally, the crystal growth stage occurs as the deposition of the TiO_2 particles on the substrate. Alternatively, the crystal growth could also happen with the condensation of hydroxides directly on the substrates. We believe, at the initial stage of the growth, TiO_2 particles were formed and suspended in the solution since there is limited number of nucleation centres (seeds) on the substrate. These particles precipitate initially on the surface of the substrate as seeds. Once there is some TiO_2 crystals formed on the substrate, the growth of TNRs will be carried out. However, this is difficult to be proved experimentally in the hydrothermal synthesis environment.

The growth stage of TNRs can be affected by many factors. The experimental parameters, such as substrate orientation, titanium precursor concentration, pH, temperature and the growth time can directly influence the growth rate. Fig. 5.12 shows a scheme summarising the effects of growth conditions on the morphology of the rutile TNRs based on the SEM images. At low titanium precursor concentration and/or low temperature and short reaction times, in which both hydrolysis and nucleation rates are slow, the growth is anisotropic. The crystal orientation is restricted by the lattice mismatch between SnO_2 and TiO_2. Subsequently, the nanorods will have a tilted appearance with low density (Fig. 5.12a). In contrast, by increasing the growth temperature, time and/or initial titanium concentration, the hydrolysis and nucleation rates will increase, thus a high density of vertically aligned nanorods with larger diameter

and longer length are obtained Fig. 5.12c. Under intermediate conditions, shown in Fig. 5.12b, a mixed crystal orientation is formed.

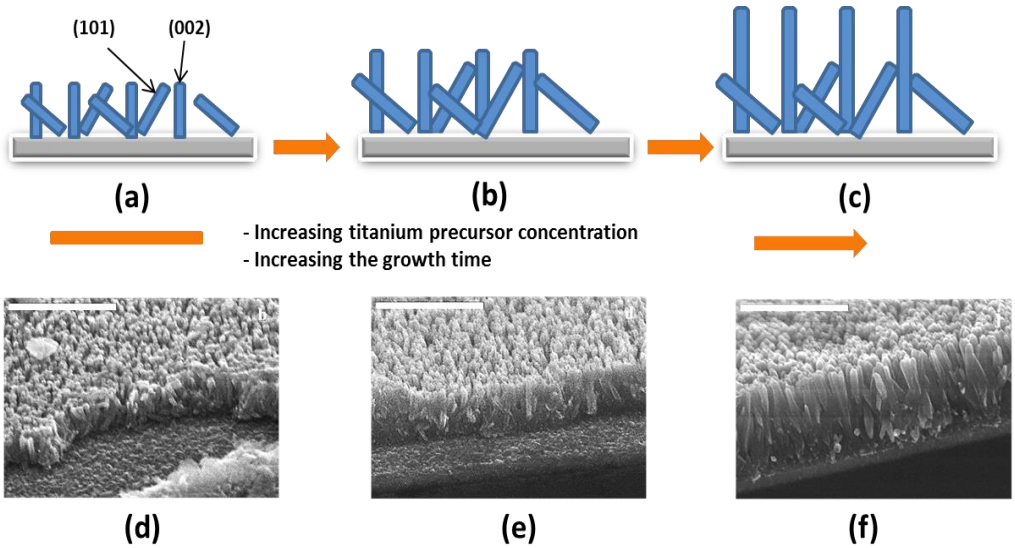

Figure 5.12 Schematic diagram of rutile TNRs films grown on FTO substrate using 0.4 ml of TBO at 150°C for different growth times with the associated SEM images. (a and d) 3 hours, (b and e) 4 hours and (c and f) 16 hours.

5.4.3 The effect of morphology on the photocatalytic performance of TNRs films

To examine the effect of the nanorods structures on the photocatalytic activity of prepared TNRs films, photoelectrochemical water splitting experiments were undertaken on the films, which were used as the photoanode. Fig. 5.13 shows the PEC performance of the TNRs films annealed films at 550°C for 3 hours, prepared under different conditions. The PEC measurements were carried out in an electrolyte of 1 M KOH under illumination of a 100 mW cm^{-2} solar simulator with an AM 1.5 G filter. In the potential range from -0.6 V to 0.7 V vs Ag/AgCl, the dark currents were almost zero in all measurements, which is typical for an n-type semiconductor.

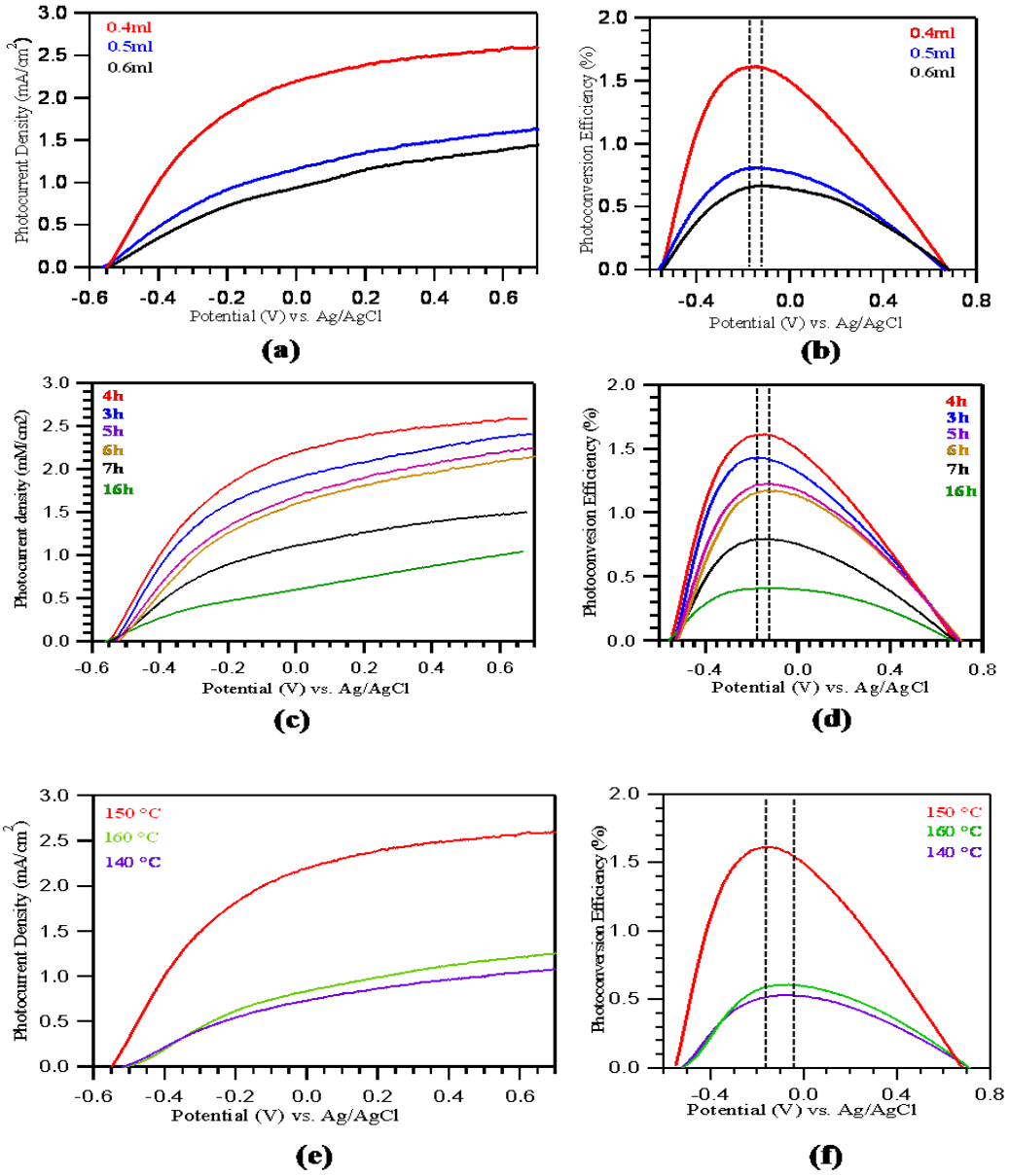

Figure 5.13 I-V curve in darkness and under simulated AM 1.5 irradiation of TNR films which were prepared under different hydrothermal conditions, with calculated photo conversion efficiency. (a and b) show the effect of the initial titanium volume. (c and d) show the effect of the growth time. (e and f) show the effect of the growth temperature.

The effect of the hydrothermal conditions on the photocatalytic performance of these films can be summarized in three parts. Firstly, with respect to the effect of the initial titanium concentration (different TBO volumes of 0.4, 0.5 and 0.6 ml), samples prepared using 0.5 ml (blue curve) and 0.6 ml (black curve) of TBO generate a photocurrent density of only 1.2 mA cm^{-1} and 0.8 mA cm^{-1} at 0 V vs. Ag/AgCl potential

respectively. In contrast, almost double of the photocurrent density, 2.34 mA cm^{-1}, was achieved from the sample synthesised in a mixture containing 0.4 ml (red curve) Fig. 5.13a. This sample also showed lower photocurrent saturation potential of the generated photocurrent, which is vital since it indicates a better charge carrier separation and transportation. Subsequently, the highest photoconversion efficiency of 1.6% at low bias of -0.18 V was achieved by this sample (Fig. 5.13b). The possible reasons will be discussed in the end of this section.

Secondly, to investigate the role of the growth time on the PEC performance of the TNRs films, the TBO volume and hydrothermal temperature were fixed at 0.4 ml and 150ºC, while the growth time was ranged from 3 to 16 hours. Fig. 5.13c and d display a set of linear-sweep voltammograms and the photoconversion efficiency for these samples. At short reaction time of 3 hours (blue curve), the sample generated a photocurrent density of 2 mA cm^{-2} at 0 V vs. Ag/AgCl and exhibited a photoconversion efficiency of 1.4% at -0.18 V. Increasing the time to 4 hours showed a photocurrent increase to the maximum of 2.34 mA cm^{-2} at 0 V vs. Ag/AgCl. This value was corresponding to the highest photoefficiency of 1.6% at -0.18 V. However, when the growth time was increased further, the films showed gradual lowering in PEC performance (0.4% at -0.12 V for the 16-hour sample).

Finally, when fixing the initial titanium concentration and the growth time at 0.4 ml and 4 hours, the hydrothermal synthesis temperature was varied (140, 150 and 160 ºC), which plays an important role in determining the photocatalytic activity of the grown TNRs film. Fig. 4.13e and f show 150ºC (red curve) to be the best temperature to generate TNRs films, since they show the best PEC performance.

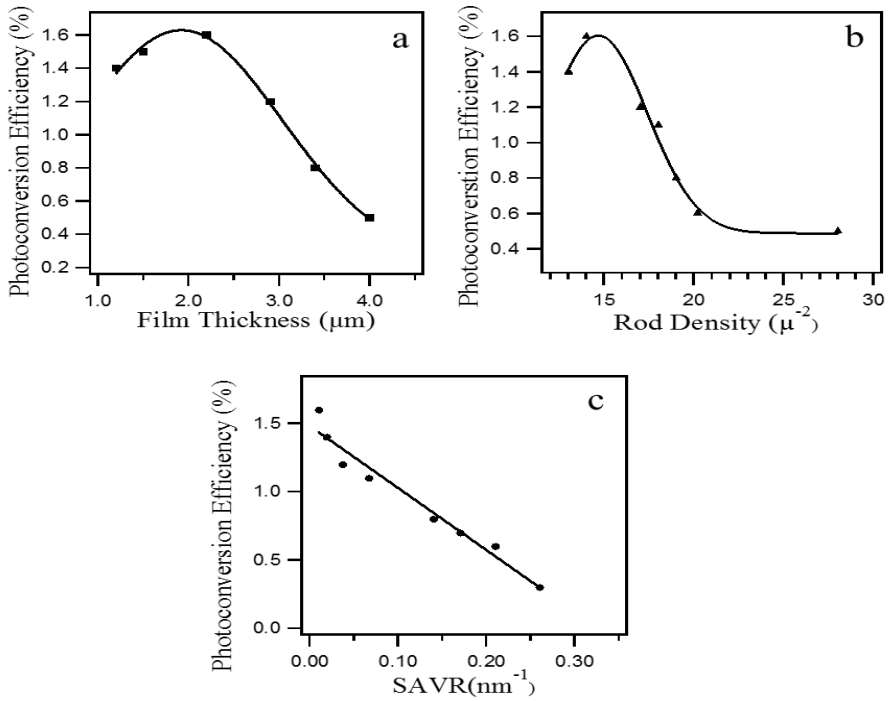

Figure 5.14 The relationship between the photoconversion efficiency of the TNRs films and their morphology. (a) Film thickness, (b) rod density and (c) SAVR.

Based on the water splitting data analysis shown in Fig. 5.14, the photocatalytic performance of the TNRs films is mainly affected by their morphology, film thickness and nanorods density. Both factors are directly influenced by the hydrothermal synthesis conditions. At low initial titanium concentrations, growth temperature and reaction time, nanorods arrays with low density, small diameter and low thickness are formed. In contrast, wider nanorods diameter and density with longer length are obtained by increasing the growth conditions (concentration, temperature and time). Fig. 5.14 summarises the correlation between the photoefficiency and sample morphological parameters, including film thickness, rods density and surface area to volume ratio (SAVR). The definition of SAVR will be discussed later through equation 5.4.

As shown in Fig. 5.14a, the highest photoconversion efficiency of 1.6% was achieved from shorter TNRs with a thickness of 2.2 μm. The small film thickness allows the illuminated light to radiate through the whole nanorods layer. This offers a good

electron conductivity through the rods, which is important for reducing the electron-hole recombination. On the other hand, the efficiency showed a sharply decrease by increasing the film thickness up to 4 μm. Generally porous material with high film thickness enhances the light absorption efficiency. However, if the bottom part of the TNRs is not effectively illuminated, the electron conductivity is reduced and the recombination of the photogenerated charge carrier are increased. Normally, a thicker TNR film is also packed in higher density. The effects of the TNR density will be discussed below.

The nanorods density was also observed to play a key role in determining the photoconversion efficiency of the grown film. The density of the nanorods is referred to the number of single rods per μm^2. The TNRs density in this work was calculated by counting the number of TNRs using Image J software, averaged from 20 μm^2 area. Fig. 5.14b, shows the maximum efficiency of 1.6% was obtained over TNRs film with relatively low density of only 14 μm^{-2}. Low nanorods density is important because it offers high surface area of the TNRs crystals with large number of reaction sites to be in contact with the electrolyte, which leads to enhance photocatalytic reactions. In contrast, increasing the film density as result of increasing the growth conditions will restrict the ion mobility within the TNRs film. This effectively reduces the surface area and accessible reaction sites on TNR crystals.

The volume density of surface area of nanomaterials can be evaluated by the surface area to volume ratio (*SAVR*). This is a critical morphological parameter for 1D nanomaterials, such as TNRs, in which the conventional weight averaged surface area for particulate materials becomes difficult to assess. Assuming it is proportional to the available reaction centre volume density, it determines the reaction kinetics for gas or liquid at solid surface. The *SAVR* for the square nanorods arrays can be calculated according to equation 5.4

$$SAVR = \frac{D(4+\frac{D}{T})}{l^2} \quad \text{(Equation 5.4)}$$

where *D* is the width of the square rods, *T* is the nanorods length and *l* is the average distance between the centres of adjacent nanorods.

Highly porous nanomaterial with large *SAVR* offers a large number of reaction sites and leads to increase the reaction rate. Therefore, as the *SAVR* increases, the photoconversion efficiency should enhance. Based on that, the *SAVR* of the grown TNRs film at different hydrothermal conditions were calculated according to equation 5.4 from associated SEM images and plotted as a function to their efficiency in Fig. 5.14c. The plot is in contrast with the above prediction. It shows a gradual decrease in the photoconversion efficiency with increasing the calculated *SAVR* values of the TNRs films. The reason behind that is related to the morphology of the grown films. The obtained nanorods arrays at high reaction conditions show wide nanorods diameter, high density and large film thickness and therefore the high *SAVR* values. However, the nanorods in this stage tend to coalescence with each other leaving very little gap in between the nanorods. This structure prevents the illuminated light and the penetration of electrolyte through the whole layer. Thus the effective reaction sites for water splitting reaction are reduced. Moreover, as the diameter of the nanorods increases, the PEC activity could be significantly limited by hole diffusion length. When this becomes dominant factor, the separation of electron-hole pair in the depth deeper than the hole diffusion length will be difficult and result in increased charge recombination. This observation confirms that lowering the film density and film thickness could enhance the photocatalytic efficiency.

As presented above, out of all the TNRs films prepared by hydrothermal method in this research, the optimal PEC water splitting efficiency was obtained when the film of

average rods diameter of 187 nm, thickness of 2.2 μm and rods density of 14 μm^{-2} is used as photoanode. This film was prepared by reacting 0.4 ml of TBO at 150ºC grown for 4 hours. Fig. 5.15 summarises the photocatalytic properties of this film.

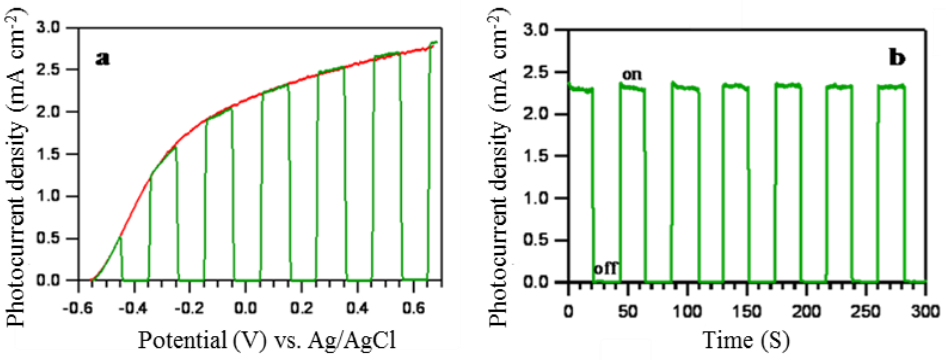

Figure 5.15 Photocatalytic properties of the optimised TNR thin film. (a) Line sweep voltammograms measured in 1 M KOH at 100 Mw cm^{-2}. (b) Time-dependence of photocurrent density of the sample during repeated on/off cycles of illumination from the solar simulator at fixed voltage of 0 V.

Compared with all other films, prepared under different conditions, this film shows a sharp increase in the photocurrent density at very low onset potential at -0.55 V vs. Ag/AgCl and approaching saturation points from -0.1 V vs. Ag/AgCl respectively as shown in Fig. 5.15a. All other samples yielded photocurrent at higher onset potential ranged from -0.53~ -0.50 V vs. Ag/AgCl. This indicates that the higher photoefficiency is related to the improved charge separation and transportation at appropriate film thickness and relatively small nanorods diameter and film density. Subsequently, a maximum photoconversion efficiency of 1.6% at -0.18 V vs. Ag/AgCl is achieved. To the best of our knowledge this is the highest photocatalytic performance reported for rutile TNR structure to date. The efficiency of this film is higher than that reported by Liu and co-workers [46]. Their photocurrent was only 0.6 mA cm^{-2} at 0 V vs. Ag/AgCl with maximum photoconversion efficiency of 0.2% [131]. This could be due to their high nanorod

density and large nanorod diameter. Fig. 5.15b shows that with illumination on and off, the promoted photocurrent was observed and remained in a steady photocurrent, which reflects the stability of the photocatalytic property of my TNRs.

5.5 Conclusion

This work reports on the synthesis of 1-D TNRs films with high photocatalytic activity, when used as photoanode material for a PEC system. For the first time, the effect of hydrothermal conditions on the photocatalytic performance was studied in depth. The results show that a low initial titanium concentration and short reaction time, with suitable growth temperature produces TNRs film with optimal photocatalytic performance. This is attributed to the low nanorods density, which offers a high surface area to react with the electrolyte. The short film thickness allows the incident UV light to penetrate through the entire film. Using 0.4 ml of TBO and using a well-defined growth time (4 hours) and temperature (150^{o}C) were found to be the ideal conditions to obtain optimised TNRs films, with their associated superior PEC performance. This film yields a high photocurrent of 2.34 mA/cm^2 at 0 V vs. Ag/AgCl, which corresponds to a photoconversion efficiency of 1.6%.

Chapter 6 Reduction and re-oxidation treatments of TiO_2 nanorod arrays for photoelectrochemical water splitting enhancement

6.1 Abstract

This chapter demonstrates a surface treatment of TiO_2 nanorod (TNR) arrays as a simple and effective method to improve its photocatalytic performance for the photoelectrochemical (PEC) water splitting. Rutile TNR films grown by the hydrothermal method were reduced by annealing in hydrogen atmosphere and re-oxidised in air. The effects of the annealing temperature and time of both processes on the morphology, crystal structure, conductivity and photocatalytic performance were investigated. Compared to the pristine film, sample was annealed in hydrogen at 350°C for 30 minutes and re-oxidised in air at 300°C for 90 minutes exhibits substantially enhanced photocatalytic performance. The electrochemical impedance analysis showed that, hydrogen treatment increases the donor density of the outer shell of the TNRs crystals. This can be attributed to generating sufficient density of surface defects and oxygen vacancies, which acts as electron donor. The layer thickness is proportional to the extent of reduction. In the re-oxidation step, the addition of the oxidised layer creates a sandwiched structure with a reduced rutile in the centre, which is assumed to improve the electron mobility and inhibit the electron-hole recombination. It was proposed that, photogenerated electrons travel through the reduced layer, with higher conductivity, to the core of the NRs and the hole remains on the surface.

6.2 Introduction

Despite the high photocatalytic activity of TiO_2 as photoanode material for hydrogen generation through the water splitting process, the solar to hydrogen conversion (STH) efficiency over pure TiO_2 is relatively low. Although the theoretical maximum photoconversion efficiency of 2.25% for rutile TiO_2 at 100 mW/cm^2 Am 1.5 was predicted [131, 252] based on the rutile TiO_2 band gap and the UV energy percentage in the solar radiation. The reported photoconversion efficiencies over rutile at present are significantly below 1%. This is mainly due to low charge mobility and fast recombination rate of photogenerated electron/hole pairs in the direct band gap rutile semiconductor. [131, 133, 253]. Among various methods have been established to overcome these drawbacks, discussed in chapter 1 Section 1.1.1, the surface treatment of TiO_2 nanomaterials is considered as simple and effective strategy to enhance their photocatalytic performance.

The surface treatment of TiO_2 refers to the formation of titanium surface defects (TSDs), such as oxygen vacancies, Ti^{3+} and surface disorder. Self-doped TiO_2 or the TSDs can be produced by various routes including; UV irradiation, heating under vacuum, thermal annealing to high temperature, plasma treating and annealing in reduction atmosphere such as hydrogen [79]. Hydrogenation of TiO_2 at controlled temperature and time is a simple approach for creating TSDs. The oxygen vacancies are known to be electron donors for the rutile TiO_2 with relatively low formation energy. They can improve the electrical conductivity of TiO_2, In addition, the energy levels of the oxygen vacancies in hydrogenated rutile TiO_2 are reported to locate at 0.75 and 1.18 eV below the conduction band (CB) [131]. The presence of these levels can promote the electronic excitation and transition from these levels to the CB in response to the visible light. Therefore, the efficiency of the solar light absorption could also be enhanced by extending the absorption spectrum range. Ti^{3+} is formed in accompanying the oxygen

vacancies. In addition, the formation of the surface disorder is linked with the surface treatment at high temperature for long time. Ti^{3+} and surface disorder can act as trapping sites for the holes to decrease the recombination rate of the photogenerated charge carriers [130].

Our strategy of enhancing the PEC performance is to develop TiO_2 nanostructure with enhanced charges separation. 1-D TNRs film, which is synthesised hydrothermally as discussed in chapter 5, was chosen as photoanode material. The nanorods structure provides appropriate geometric configurations, which can effectively trap photons with energy larger than the band gap. In addition, the small dimension in the cross section helps the diffusion of minor charge carriers (holes) to the surface with short pathways. The film is reduced in hydrogen atmosphere at adjusted temperature and time, following by oxidation in air. Hypothetically, the reduction step will increase the donor density with increased annealing temperature and time. During the oxidation step (annealing in air at controlled temperature and time), the outside of the reduced layer would be oxidised, leaving a thin reduced layer between the rutile-TiO_2 core and the oxidised shell. In this case, the efficiency of the rods could be enhanced as the outer shell with high surface disorder act as sites for trapping the generated holes. While the thin reduced layer as an electron donor will assess to improve the electron conductivity of the rods and transferring the photogenerated electrons to the TiO_2 core.

6.3 Experiments

6.3.1 Fabrication of TiO_2 nanorods arrays

In this experiment, the film of vertically aligned TNRs with optimized properties was prepared by the hydrothermal synthesis method as illustrated in last chapter. Fluorine

doped tin oxide (FTO) glass (Sigma-Aldrich, 7Ω/sq.) was used as a substrate for all the prepared films.

In a typical synthesis, 10 ml of DI water was mixed with 14 ml of concentrated hydrochloric acid (32 wt %). The mixture was stirred at room temperature for 5 minutes before the addition of 0.4 ml of titanium but oxide (TBO). After further 5 minutes of stirring, it was transferred to a Teflon-lined stainless steel autoclave (50 ml). Two pieces of clean FTO glass substrate (1×2 cm^2) were placed at an angle against the wall of the Teflon liner with the conducting side facing down. The autoclave was sealed and placed in a 150°C pre-heated oven for 4 hours. The autoclave then was taken out and left to be cool down naturally to room temperature. The glass pieces were washed with deionised water and left to dry in ambient air. After confirming the growth of nanorods structured TiO_2 by XRD and SEM analysis, the samples were then annealed in air for 3 hours at 550°C in order to improve the contact of the rods to the substrate and to increase the crystallinity of the structure.

6.3.2 Reduction and oxidation of the nanorods arrays

Once TNRs samples had been annealed, they were then put forward to the reduction and oxidation stages. In the reduction process, the samples were annealed in hydrogen atmosphere at 350°C, using hydrogen gas at a flow rate of 270 ml/min for the duration from 15 to 60 minutes. To ensure maximum contact between TNR film and hydrogen gas, the samples were placed with the TNRs facing the gas flow. The effects of the annealing time on the crystal quality, bang gap energy, carrier densities and photocatalytic performance of the treated nanorods films were investigated. After the samples had been reduced for the desired temperature and time, they were then removed for the oxidation.

In the oxidation stage, the reduced TNR films were calcined in air. The effects of the oxidation temperature and duration on the crystal structure and PEC performance were studied. Range of temperatures was investigated (200, 300 and 400°C) for 30 minutes. After optimizing the oxidation temperature, the effects of the duration of oxidation at the optimal oxidation temperature were studied at 30, 60, 90 and 120 minutes.

6.3.3 Material characterisations and PEC measurements

The crystal structures of the TNRs films were characterized by the X-ray diffraction (Siemens Powder X-500). The surface morphologies were studied by SEM (JSM 820M, JEOL, operated at 30 kV). The average diameter and film thickness were scaled from the SEM images using Image J (National Institutes of Health, USA). The optical band gaps of the untreated and treated TNRs films were determined from their reflection absorption spectra, collected with an integrating sphere (Ocean Optics ISP-REF) with a built-in tungsten-halogen light source covering wavelengths from 300 to 1000 nm. PEC water splitting was measured using a standard three-electrode configuration in a 1.0 M KOH electrolyte. A platinum foil was used as counter electrode and a KCl saturated Ag/AgCl electrode was used as a reference. A USB potentiostat (eDAQ) was used to control and record the photocurrent as a function of electrochemical potential. Sunlight was simulated with a 300W xenon arc lamp with an AM1.5 G filter and the output light power density was adjusted to 100 mW cm^{-2}. Electrochemical impedance spectroscopy (EIS; Palmsens 3.0) measurements were carried out on the as prepared, reduced and oxidized TNRs films in the dark, using a 1M KOH electrolyte (pH 13.6). The amplitude of the sinusoidal wave was set at 10 mV at a fixed frequency of 1 kHz. The measurements help to understand the mechanism behind the enhancement of photoelectrochemical efficiency.

6.4 Results and discussions

6.4.1 Controlling the reduction conditions for optimizing the photocatalytic performance of TNR arrays

The nature and density of surface defects has a vital effect on the photocatalytic performance of TiO_2. Ti^{3+} defects and oxygen vacancies have been reported as dominant defects in the TiO_2 surface [254, 255]. An annealing of TiO_2 material in reduction gas is easy and effective way to generate TSDs. During the annealing process, Ti^{4+} is reduced to Ti^{3+} by losing O^{2-} from the surface lattice. This process occurs in three steps; firstly, at low reaction temperature, hydrogen interacts physically with the adsorbed oxygen on the surface of TiO_2. At higher temperature (higher than 300ºC) [254], electrons are transferred from H atoms to O atoms in the TiO_2 lattice, forming surface hydroxyl group. The combination of 2 hydroxyl groups will form H_2O molecules which desorbs from the surface, generating oxygen vacancy and reduced Ti^{3+} in the TiO_2 structure. Since oxygen vacancies are known as electron donors, Ti^{4+} ions are effectively reduced to Ti^{3+} by receiving electrons from the adjacent oxygen vacancies or through the instruction of reductive gas, such as hydrogen.

Changing the annealing conditions in the reducing atmosphere changes the reduction kinetics. The reaction temperature plays a key role in controlling the defects density. At higher annealing temperature, the more Ti^{3+} ions are more rapidly produced [254]. The reduction time also determines the reduced layer thickness. The longer the reaction time, the deeper the defects penetrate. It is worth noting that heavily reducing the TNR films will increase the number of defects to the extent destroying the nanorod morphology. Therefore, the reduction temperature and duration must be controlled. In this section, the effect of the reduction conditions on the crystal structure, band gap energy and PEC performance were studied.

6.4.1.1 The effect of reduction temperature

In order to study the effect of the hydrogen reduction temperature on the PEC performance of TNR films, varied annealing temperatures were attempted (300, 350, 400 and 450°C) for 30 minutes. To determine the crystal structure and possible phase changes during the hydrogen annealing, XRD spectra were collected from the untreated and reduced TNRs in different annealing temperatures (Fig. 6.1).

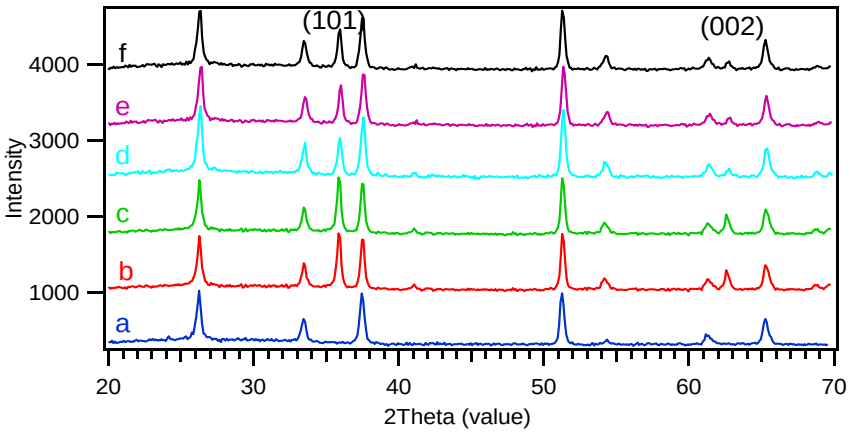

Figure 6.1 XRD patterns of the rutile TNRs films (b) on FTO substrates (a) reduced in hydrogen atmosphere for 30 minutes at different temperatures, (c) 300°C, (d) 350°C, (e) 400°C and (f) 450°C.

In comparison with the clean FTO glass, two main diffraction peaks located at 2θ angle of 36.3° and 63.2° were indexed to the tetragonal rutile TiO_2 crystal structure (JCPDS No. 88-1175) [131] and corresponding to the (101) and (002) planes respectively. Furthermore, the absence of the other diffraction pecks of rutile TiO_2, which normally occurs in polycrystalline or powder samples, suggests that the nanorods have their crystal plane aligned throughout their structure. As shown in the Fig. 6.1, in comparison with the untreated sample, there is no major phase change after the hydrogen treatment, although there is a gradual decrease in the TiO_2 peaks intensities when the reduction temperature was increased. This observation indicates the formation of TSDs on the grain boundary

and on the outer layer of the rod crystal, converting the rod crystals to rod structure with core of pure TiO_2 and a shell of amorphous, defected and reduced structure. The density of these defects increases with increasing the reduction temperature.

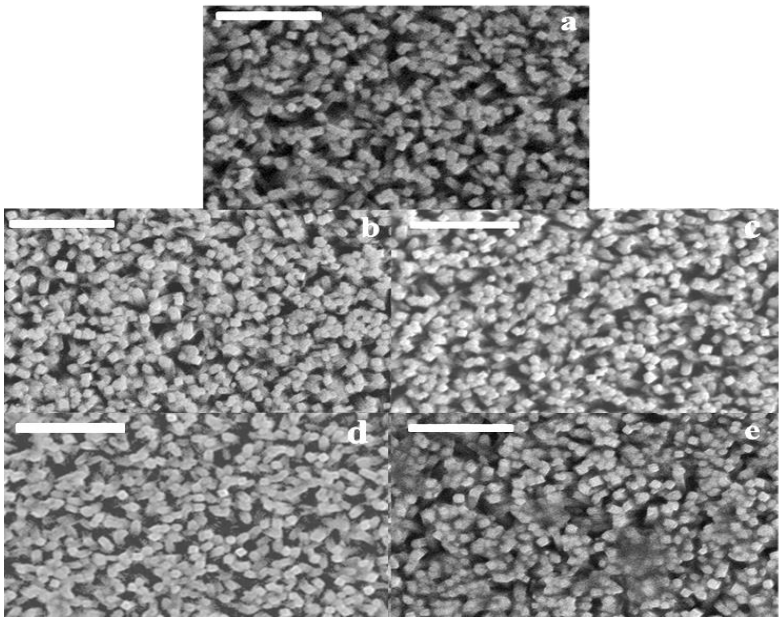

Figure 6.2 SEM images of the untreated and reduced TNRs at different temperatures. (a) as prepared, (b) 300°C, (c) 350°C, (d) 400°C and (e) 450°C.

To understand the influence of the annealing temperature in hydrogen atmosphere on the morphological properties, SEM measurements were performed on the untreated and reduced samples at different temperatures and presented in Fig. 6.2. There is also no significant change in the rod morphology after the reduction treatment. The average nanorod diameter was slightly increased by increasing the reduction temperature. It was measured to be 187, 190, 197, 202 and 212 nm with FWHM of 30, 28, 25, 22 and 20 nm for the pristine and reduced TNRs at 300, 350, 400 and 450°C respectively. The increase in the average diameter could be attributed to disordering of the crystal structures within the nanorods through the annealing in hydrogen or the Oswald ripening during the thermal treatment. Increasing the annealing temperature increases the vaporisation of small TiO_2

nanoparticles and TNRs with larger diameter can be formed. That can be evidenced in Fig. 6.2d and e where the TiO_2 started to build up within the gaps between the nanorods after reduction at 400 and 450 °C. Some degree of coalescence between adjacent nanorods was also observed.

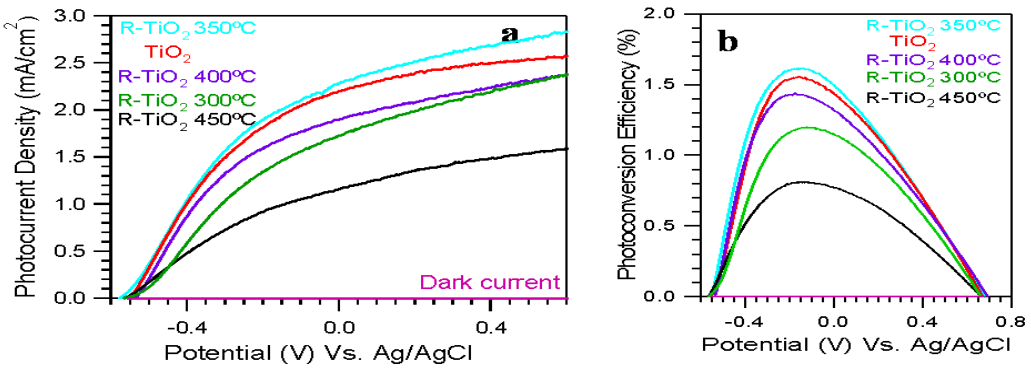

Figure 6.3 (a) *I-V* curve in darkness and under simulated AM 1.5 irradiation of untreated and reduced TNR films at under different temperatures (b) the calculated photo conversion efficiency.

The PEC performance of the reduced TNR films at different temperatures is shown in Fig. 6.3. It was found that, treating the film at 350°C in a hydrogen atmosphere increases the photocurrent and photoefficiency slightly in comparison with the as prepared TNRs. Thus, slightly introducing surface defects help to improve the charge separation. However, further increase the reduction temperature decreases the photocurrent and photoefficiency progressively. This suggests that when the surface defect density and crystal disordering is too high, such defects immobilise the holes, while the electron conductivity is increased. Thus, the electron-hole recombination will increase. Therefore, a fine control of the surface defect density is necessary for optimise the photocatalytic performance. The PEC measurement from the sample reduced at 300°C gives an odd, inconsistent reading which could due to the experimental error and thin film flaked off for that particular sample. These results are comparable to the results of similar

study that was reported by Wang and his workers [131], therefore reduction at 350°C was used in further studies.

6.4.1.2 The effect of reduction time

By fixing the reduction temperature at 350°C, the reaction time is proportional to the extent of reduction [79]. By increasing the reduction time, the formation of oxygen vacancies takes place deeper into the nanorods. TNRs were treated in a hydrogen reducing atmosphere for 15, 30, 45 and 60 minutes. XRD patterns of the reduced rutile TNR films at 350°C for different times compared to the pristine film are presented in Fig. 6.4.

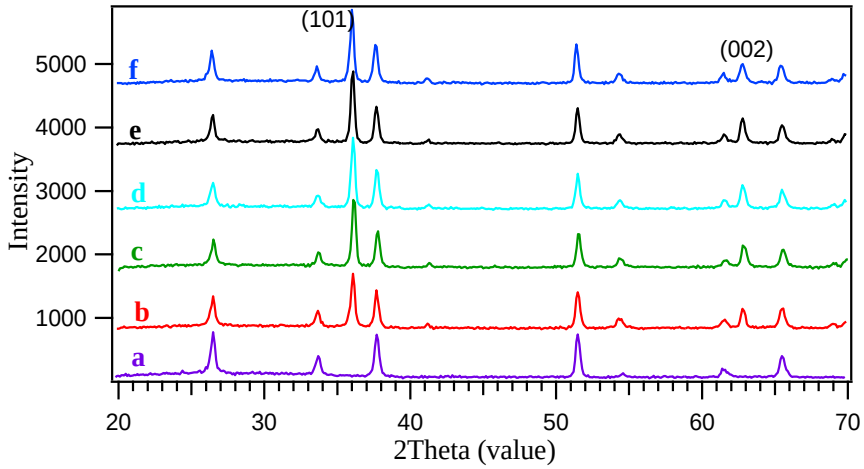

Figure 6.4 XRD patterns of the rutile TNR films grown on FTO substrates (a) and reduced in hydrogen at 350°C for different times: (b) 0 minutes, (c) 15 minutes, (d) 30 minutes, (e) 45 minutes and (f) 60 minutes.

As shown in the XRD patterns there are also no phase change after the hydrogen reduction for different times, although the peak intensities of TiO_2 slightly decreased and broadened after (45 min). This is due to the increase in thickness of defect layer and density of defects. It has been reported that hydrogen treatment disorders the outermost surface of the structure, penetrating a few nanometres into the crystal structure, depending

on the extent of the treatment, observed by high resolution transmission electron microscope (HRTEM) [256].

Band gap energies of the pristine and reduced films were calculated according to Tauc relation (Equation 3.7, Section 3.4), where the absorption coefficient is written in terms of reflection (Equation 3.9, Section 3.4). The band gaps measurements were plotted and presented in Fig. 6.5a (wide range) and Fig. 6.5b (small range). The plots show a gradual reduction of band gap energy during the reduction. The reduced sample for 30 and 60 min exhibits band gaps of 2.98 and 2.93 eV respectively in respect to that of the pristine TiO_2 (3.02 eV). The reduction in the optical band gaps can be resulted from the formation of new energy levels in the band gap related to the formed oxygen vacancies.

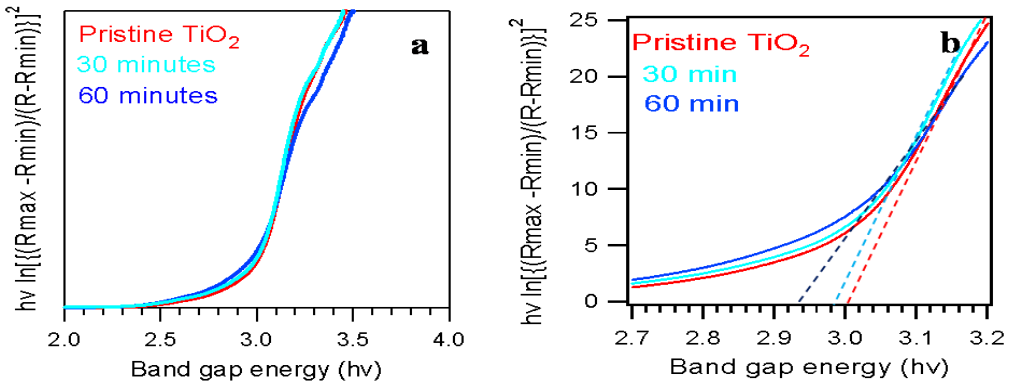

Figure 6.5 Band gap energy of unreduced and reduced TiO_2 nanorods films at 350°C for 30 and 60 minutes. (a) Low magnification of the plot and (b) high magnification of the plot.

Fig. 6.6a and b show the I-V curves and the corresponded calculated photoconversion efficiency plots of reduced TNRs films in hydrogen atmosphere at 350°C for different times. After 15 minutes of the reduction, the produced photocurrent density decreased in respect to the pristine film (from 2.34 mA to 2.22 mA cm^{-2} at 0 V vs. Ag/AgCl). That corresponded to a decrease in the maximum achieved photoconversion efficiency (PE) from 1.55 to 1.52%. Doubling the reduction time to 30

minutes showed a photocurrent increase to the maximum of 2.43 mA cm^{-2} at 0 V vs. Ag/AgCl with an increase in the maximum PE. With additional reduction time, the achieved PE decreased to below that of the pristine TNRs film. This result could be attributed to the fact that initially, only the surface defects are formed. By further reduce the TiO_2, defects were formed deep into the nanorods. While the surface defects can help to trap the holes on the surface and enhance the photoefficiency, the deeper defects could also trap the holes inside the crystals which will then became the recombination centres, leading to a reduction of photoefficiency.

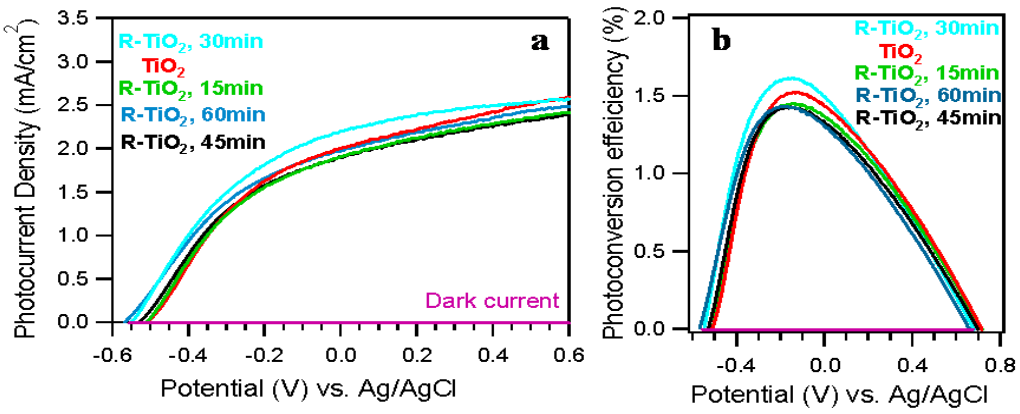

Figure 6.6 The PEC performance of untreated and treated TNRs films. (a) I-V curves of the pristine TNRs film reduced at 350°C for different times. (b) Calculated photoconversion efficiency of the re-oxidized TNRs films in air as a function of the oxidation time.

The EIS measurements were performed to study the intrinsic properties of the samples in 1 M KOH electrolyte in dark at a fixed frequency of 1 kHz. Fig. 6.7 shows The Mott-Schottky plots of the untreated and reduced TNR films at 350°C for 30 and 60 minutes. The samples exhibit positive slope which confirm the typical n-type semiconductor behaviour.

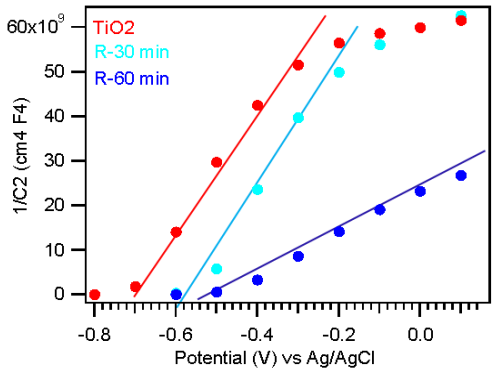

Figure 6.7 M-S plots of unreduced and reduced TNR arrays at 350°C for 30 and 60 minutes measured in 1 M KOH solution (pH 13.6) in the dark. The amplitude of the sinusoidal wave was set at 10 mV at a fixed frequency of 1 kHz.

For the pristine TNRs, the flat band potential (V_{FB}) was estimated to be -0.72 V Ag/AgCl whereas the V_{FB} for the reduced samples for 30 and 60 minutes showed a gradually increasing positive shift to be -0.6 and -0.55 V Ag/AgCl respectively. That means the band bending at the interface between the electrode and electrolyte is reduced for reduced TNRs, as well as the width of the space charge region. This could be the result of formation of hydroxyl groups on the reduced TiO_2 surface. Meanwhile, the charge carrier densities can be evaluated from the slope of the Mott-Schottky plots. It is important to note that the slopes of the reduced samples are much smaller than that of the untreated film indicating higher carrier densities of the reduced films. The Mott Schottky equation (Equation 3.11, Chapter 3), which is restated in the following was used to calculate charge carrier densities:

$$N_D = \left(\frac{2}{e\varepsilon\varepsilon_0 A^2}\right)\left(\frac{d\left(\frac{1}{C^2}\right)}{dV_E}\right)^{-1}$$

Where N_D is the charge carrier density, e is the electron charge (-1.602 x 10^{-19} C), ε is relative dielectric constant of the semiconductor (for rutile TiO_2 = 170), ε_0 is the dielectric permittivity of free space (8.86 x 10^{-14} F/cm), C is the capacitance of the space charge region

between the semiconductor and the electrolyte and A is the area contacted with the electrolyte and V_E is the applied voltage. The calculate charge carrier densities are 6×10^{18}, 8×10^{18} and 16×10^{18} cm^{-3} for the untreated, reduced samples for 30 and 60 min respectively. This confirms that as the reduction time is increased, the charge charrier densities were also increased. The formation of these vacancies is not restricted on the surface; they penetrate through the crystal, forming a bulk defects with a thickness proportions to the reduction time.

Increasing the TSDs could either enhance or decrease the photocatalytic efficiency, depending on the location of the defects. Although both surface and bulk defects could extend the photoresponse of TiO_2 from UV to visible light region, discussed in Section 6.2, only the surface defects can help to trap the holes. And prevent electron-hole recombined. However, with significant reduction of TNRs, the defects will penetrate to the bulk of nanorods, which will trap the holes in the bulk and prohibit them reaching the surface for the oxidation of water. Meanwhile, the increased charge carrier density will increase the electron mobility. Under both situations, the electron-hole recombination will increase and the overall PEC performance will decrease. In the next section, I will try to re-oxidise the reduced TNRs to recover the surface and to form a sandwiched structure of TiO_2/reduced TiO_2/TiO_2.

6.4.2 Controlling the oxidation conditions for optimizing the photocatalytic performance of TNR arrays

The reduction of TNRs increases both the charge carrier density and the electron-hole recombination (as shown by EIS measurements in Fig. 6.7). By increasing the charge separation to an extent above the diffusion length, the probability of recombination is reduced. The diffusion length is the separation between the excited electron and hole that

still allows recombination [257]. This length varies for different materials and also changes in material structure. For rutile TiO_2 the diffusion length is ≈ 10 nm which is an order of magnitude less than anatase [130, 258]. With the reduced layer giving increased charge carrier density and electrical conductivity, the oxidative conversion of the outer layer by a thickness approaching the diffusion length, will lower recombination. The photogenerated electrons will diffuse into the higher conductive reduced layer and flow around the electrical circuit, rather than remain at the surface to recombine with the holes.

The original aim of reduction and oxidation of TNRs was aimed to create anatase TiO_2 TNRs through the recrystallisation during the thermal treatment process, as anatase was expected to have better photocatalytic performance. However, our experiment shows that only very little anatase phase was formed after re-oxidation. Nevertheless, the re-oxidation restores oxygen atoms in the oxygen vacancies where the density of these vacancies decreases with increasing the annealing temperature. Here, we will study the correlation between the re-oxidation conditions and the PEC performances.

6.4.2.1 The effect of the oxidation temperature

First, the effects of re-oxidation temperature were investigated. XRD spectra were collected from the pristine TNRs, reduced samples at 350°C for 30 minutes and re-oxidised in air for 30 minutes at different temperatures of 200, 300 and 400°C as shown in Fig. 6.8. There is a gradual increase in the diffraction peak intensities of TiO_2 associated with the rutile phase as the annealing temperature increases. This indicates an improvement in the crystallinity by restoring oxygen in the oxygen vacancies. It is noted that although after annealing the sample in air, the diffraction peak intensities from the TNRs are still lower than those from the pristine film. This indicates that the defects in reduced TNRs were not completely removed even at 400°C. Those residual defects would

be expected to be located in the centre of the TNRs. Meanwhile, there is a new diffraction peak appears at 25.3° with relative low intensity. This peak can be assigned to the (101) plane of TiO_2 anatase. For powder anatase, this is the dominant diffraction peak. The low diffraction intensity suggests that either only a small portion of the reduced TNR is subject to the phase transition or the (101) plane is perpendicular to the substrate. Here, we expect that anatase is formed on the surface of the TNRs, while the bulk of the TNR maintain the rutile phase.

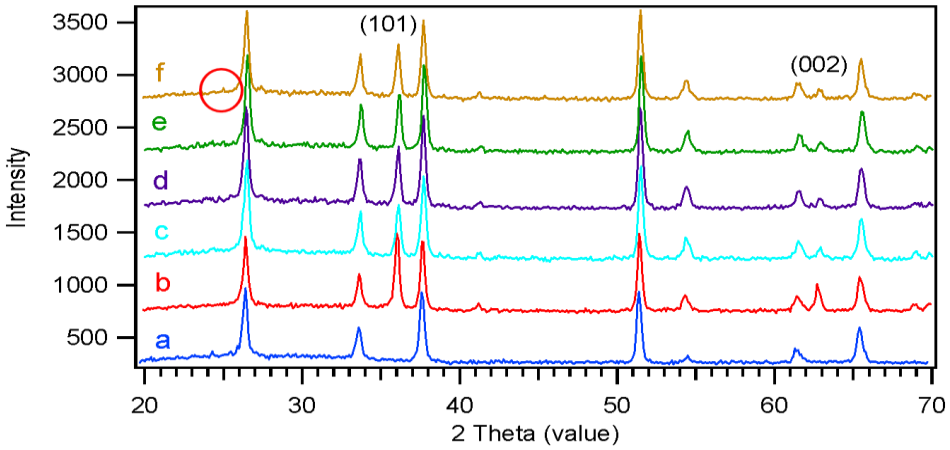

Figure 6.8 XRD patterns of the rutile TNR films on FTO substrates which were annealed in air (for adhesion improvement), reduced in hydrogen at 350°C for 30 minutes and re-oxidised in air for 30 minutes at different temperatures. (a) FTO, (b) untreated TiO_2 (c) reduced rutile TiO_2 for 30 minutes at 350°C (d) 200°C oxidation (e) 300°C oxidation, (f) 400°C oxidation. The red circle shows the position of anatase peak.

To investigate the role of the oxidation temperature on the photocatalyst performance of the oxidised samples, PEC performance was examined and the results are plotted in Fig. 6.9. We labelled the spectra in the form of TiO_2 R 350°C-Oxxx, where R indicates the reduced film at specific temperature and xxx represents the different re-oxidation temperatures. It was found that the re-oxidised film at 300°C in air gives the best PEC performance.

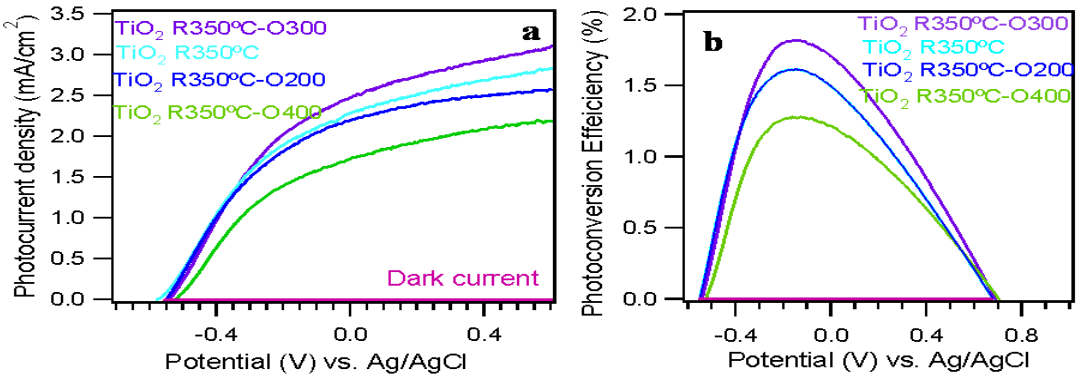

Figure 6.9 The PEC performance of reduced sample in hydrogen at 350°C for 30 minutes and re-oxidised in air for 30 minutes at different temperatures. (b) Calculated photoconversion efficiency.

6.4.2.2 The effect of the oxidation time

Similar to reduction, the duration of the sample oxidisation changes the thickness of the reoxidised TiO_2 layer. With a sandwiched structure, the photogenerated electrons can travel through the reduced layer to the base of the electrode, while the holes stay in the outside layer for the oxidation of water. This arrangement can facilitate effective charge separation and the decreasing of electron-hole recombination. Fig. 6.10 shows the TNRs reduction, re-oxidation process and the sandwiched structure formation.

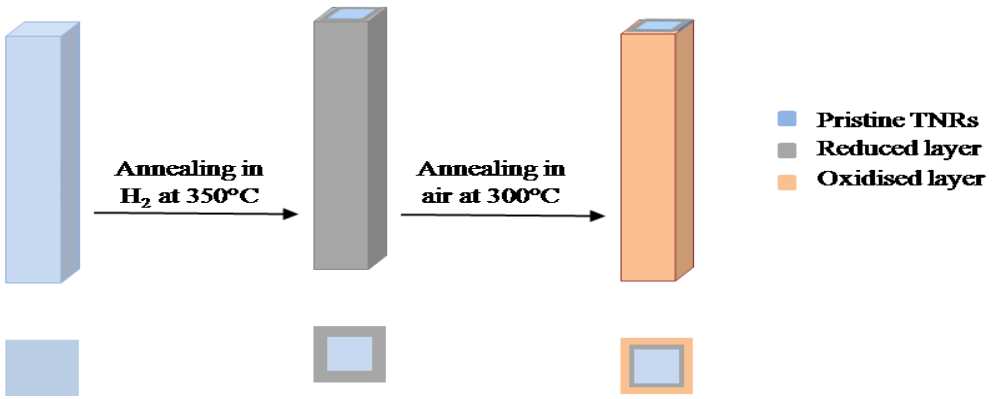

Figure 6.10 A schematic diagram shows a single TNR with the reduction and re-oxidation process.

To study the crystal structure phase changes during the oxidation treatment, XRD spectra were collected from the pristine TNRs and reduced samples at 350°C for 30 minutes and re-oxidised in air at 300°C for different time periods are shown in Fig. 6.11.

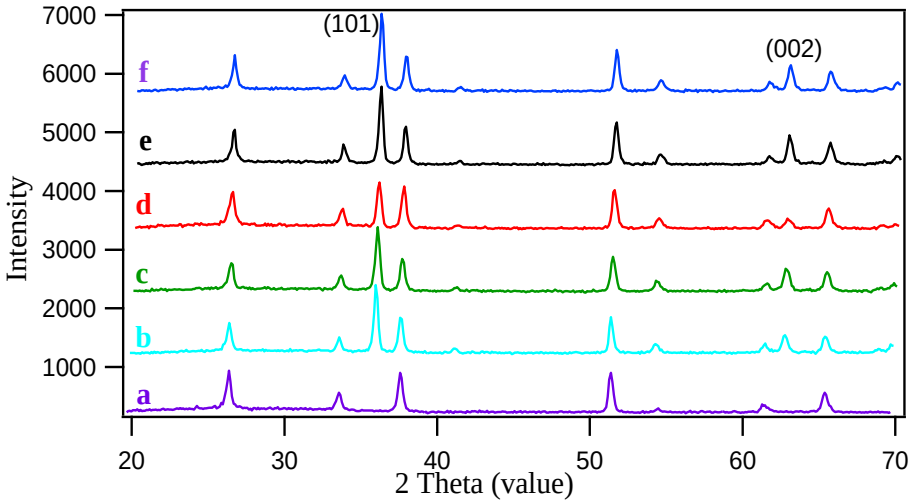

Figure 6.11 XRD patterns of the rutile TNR films on FTO substrates which were annealed in air (for adhesion improvement), reduced in hydrogen at 350°C for 30 minutes and re-oxidised in air at 300°C for different times. (a) FTO, (b) reduced rutile TiO_2(c) 30 minutes oxidation (d) 60 minutes oxidation (e) 90 minutes oxidation and (f) 120 minutes oxidation.

There is no obvious phase transition observed in the diffraction patterns, since the oxidation temperature is too low. However, intensities of the rutile peaks are enhanced slightly through the oxidation stages and peaks are narrowed slightly, which is related to improvement in film crystallisation with increasing the oxidation time. The sample re-oxidised for 60 minutes showed different trend which can be referred to the bad film quality.

The corresponding morphology of the TNRs after re-oxidation at 300°C for different durations is presented in the SEM images in Fig. 6.12.

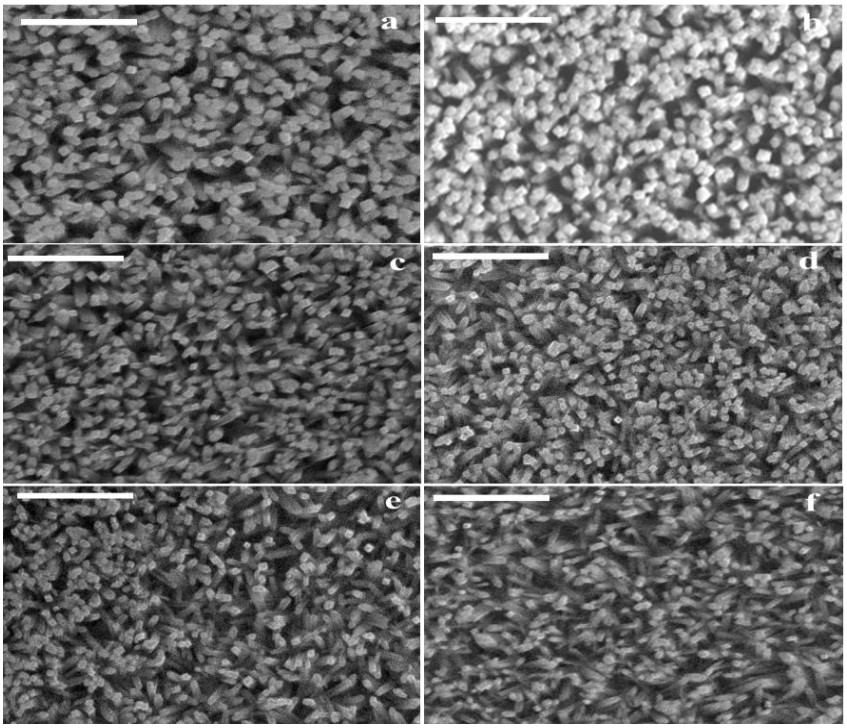

Figure 6.12 Typical SEM images of top views of rutile-TNR films grown on FTO which were annealed in air at 550°C for 3 hours (for adhesion improvement), reduced in hydrogen at 350°C for 30 minutes and re-oxidised in air at 300°C for different times. (a) Pristine (b) 30 minutes reduction followed by (c) 30 minutes oxidation (d) 60 minutes oxidation (e) 90 minutes oxidation and (f) 120 minutes oxidation. The scale bar is 2 µm.

Compared to the pristine sample (Fig. 6.12a), the SEM images show a slight increase in the nanorod diameter after annealing in hydrogen at 350°C for 30 minutes (Fig. 6.12b). The average nanorod diameters of the pristine and reduced samples were 187 and 197 nm with FWHM of 30 and 25 nm respectively. This can be due to the increase in the defects density in TiO_2 structure. A diminishing in the nanorod diameter is occurred by oxidising the reduced sample for different annealing times in air. The average rods diameter for the re-oxidised samples at 300°C for 30, 60, 90 and 120 minutes were 170, 150, 115, 97 and 70 nm with FWHM of 30, 35, 42, 50 and 64 nm respectively. This suggests that there is an evaporation of outer shell of disordered TNRs during the re-oxidation process. That is could be attributed to two factors; since the tip of the nanorods structure are separated while the bottom is more packed and directly attached

to the substrate, a temperature gradient from the bottom to the top will occur. In addition, the difference in the density between the top and the bottom of the nanorods allows the tips to be more exposed to the environment than the bottom, therefore the evaporation more likely to occur from the top part of the rods. The decrease in the rod diameter was also associated with decrease in the film density. Based on the SEM images, The TNRs density in this work was calculated by counting the number of TNRs using Image J software, averaged from 20 μm^2 areas. The densities of the pristine, reduced samples at 350°C for 30 minutes and re-oxidised at 300°C for 30, 60, 90 and 120 minutes were roughly estimated to be 17, 16, 14, 13, 12, 11 rods/μm^2. This observation confirms the evaporation of disordered TNRs at the tips.

The photocatalytic performance of the re-oxidised samples was also tested in a standard PEC water splitting device. The reduced film with the highest efficiency, reduced at 350°C for 30 minutes, was used for the re-oxidation procedure. Fig. 6.13a displays the I-V measurements of the untreated and reduced sample. Re-oxidation for 60 and 90 minutes increases the produced photocurrent from 2.2 mA cm^{-2} to 2.84 mA cm^{-2} at 0 V vs Ag/AgCl. The PE plot Fig. 6.13b shows the increase of PEC efficiency, with a maximum value of 1.89 %. Further increasing the oxidation time to 120 minutes, both the photocurrent and PEC efficiency decrease. This observation suggests that for 60 and 90 minutes' calcination in air, the surface of the reduced TNRs was re-oxidised. There is a residual reduced layer sandwiched between the surface and core low defects TiO_2. Such a structure is important for improved charge separation as the photoexcited electrons can be easily diffused to the reduced layer and effectively separated from the surface oxide, where the hole will oxidise the water. Further increase the re-oxidisation time will destroy the reduced layer and resulting reduced electron conductivity. This is responsible for the decrease of photocurrent and PEC efficiency.

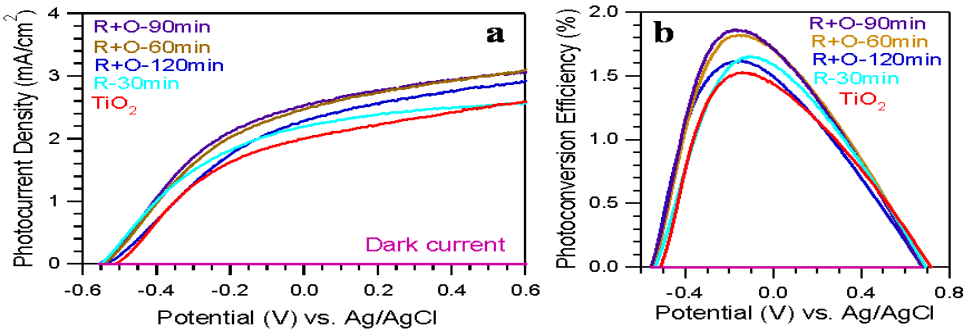

Figure 6.13 The PEC performance of untreated and treated TNR films. (a) I-V curves of the reduced TNR film at 350°C for 30 minutes and oxidised TNR films at 300°C for different times. (b) Calculated photoconversion efficiency of the re-oxidized TNR films in air as a function of the oxidation time.

The EIS measurements were carried out to estimate flatband potentials, V_{FB} and charge carrier concentrations of the re-oxidised samples in 1 M KOH electrolyte in dark at a fixed frequency of 1 kHz. Fig. 6.14 shows The Mott-Schottky plots of the reduced sample at 350°C for 30 minutes and re-oxidised at 300°C for 60, 90 and 120 minutes. The re-oxidised samples for 60, 90 and 120 minutes exhibited V_{FB} of -0.66, -0.67 and -0.72 V. The shift of the V_{FB} towards high negative values for the n-type semiconductor suggests an increasing of band bending and width of space charge region. The direct consequence of this would reduce the charge recombination ratio, since the space charge field strength is increased. This could result in an increase of photocurrent and photoefficiency. We believe that our unique sandwiched TNR structure is important which overcomes the reduced charge separation due to the reduced band bending.

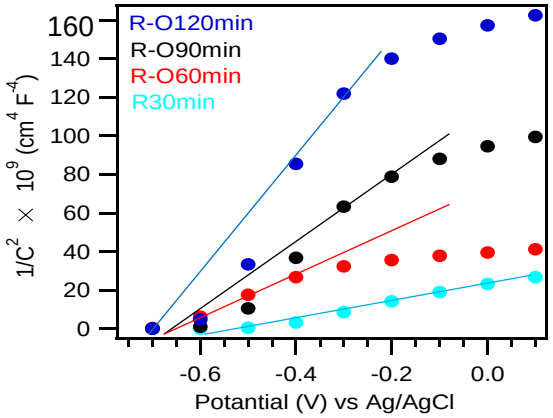

Figure 6.14 M-S plots of reduced TNR arrays at 350°C for 30 minutes and re-oxidised for different times, measured in 1 M KOH solution (pH 13.6) in the dark. The amplitude of the sinusoidal wave was set at 10 mV at a fixed frequency of 1 kHz.

The charge carrier densities of the reduced sample at 350°C for 30 minutes before and after being oxidised at 300°C for 60, 90 and 120 minutes were 8.0×10^{18}, 7.6×10^{18}, 6.2×10^{18} and 6.0×10^{18} cm^{-3} respectively. When the film has undergone reduction only, the resulting carrier density is at a maximum. This quantity decreases with increasing exposure time to the oxidising atmosphere. By increasing the oxidation time, the relative thickness of the reduced layer decreases which lowers the oxygen vacancy concentration. This is the reason for the decrease in charge carrier density during re-oxidation. After re-oxidation for 120 min, the charge carrier density is very close to the value of the pristine sample. Thus, by then, we could expect that reduced TNRs were fully oxidised. Therefore, it confirms that the sandwiched reduced layer disappeared after 120 min oxidation, which results in the reduction in apparent electron conductivity.

6.5 Conclusion

This chapter reports a simple and effective method for enhancing the performance of TNRs arrays as photoanode material in PEC water splitting. This study considered the surface treatment of TiO_2 crystals through a reduction in hydrogen atmosphere and then

re-oxidation in air. The reducing hydrogen atmosphere creates oxygen vacancies and the Ti^{4+} reduced into Ti^{3+}. By fixing the temperature that the hydrogen atmosphere is exposed to, at 350°C, the reduction time is proportional to the extent of reduction. The resulting Ti^{3+} atoms are thermally unstable and the oxidation treatment in air at 300°C restores the Ti^{4+} atoms. The longer oxidation time results in a higher proportion of the Ti^{4+} being restored. In comparison to the untreated TNRs which generates photocurrent of 2.34 mA/cm^2 at 0V vs. Ag/AgCl and a photoconversion efficiency of 1.5%, the reduced TNR film at 350°C for 30 minutes yields a photocurrent density of 2.43 mA/cm^2 at 0V vs. Ag/AgCl which corresponds to a photoconversion efficiency of 1.6%. Based on the EIS measurements, charge carrier density increases as the reduction time increases but decreases as the oxidation time increases. As longer reduction times lead to a higher charge carrier density and lower photoconversion efficiency. Oxidation acts to decrease the charge carrier density by decreasing the concentration of the oxygen vacancies. With mild oxidation conditions (300°C, 90 min), only the surface of the reduced TNRs is recovered, which results in the formation of a sandwiched, three layered structure. In this structure, the residual reduced layer was left in the middle layer which serves as the electron conductor. With the band bending and charge separation are being increased after re-oxidation, the photoconversion efficiency is increased to 1.89% due to the unique three layered structure with the electron passing through the reduced layer to the substrate, while the holes are trapped into the surface. A sequence of reduction and oxidation helps to achieve maximum photoconversion efficiency.

Chapter 7 Enhancing water splitting performance of TiO_2 nanorods photoanode by controlled Cu doping

7.1 Abstract

In this chapter, I report, for the first time, the synthesis of Cu doped TiO_2 nanorod (TNR) films for enhancing their photoelectrochemical (PEC) water splitting performance when they are used as photoanode material. Cu ions were directly incorporated into TNRs with Cu:TiO_2 molar ratios ranging from 0.4 to 1.2 mol%, via a one-step hydrothermal method. The obtained Cu doped TNRs are single crystals with the rutile structure. The effect of Cu doping on the morphology, crystal structure, optical band gap and PEC performance of TNRs films were studied. The diameter and density of the doped nanorods were decreased with increasing Cu doping concentration up to 0.8 mol%. When doped nanorods were illuminated by a solar simulator (intensity 100 mW/cm^2), the photocurrent intensity increased gradually with increasing Cu doping concentration reaching a maximum photocurrent of 3.25 mA/cm^2 at 0 V vs Ag/AgCl using a film of 0.8 mol% Cu doped TiO_2. This performance corresponds to a maximum photoconversion efficiency of 2.1%. This value is almost three times higher than that of the non-doped TNRs film.

7.2 Introduction

As discussed in the previous chapters, the solar to hydrogen conversion efficiency over pure TiO_2 photocatalyst is limited by its lack of visible light absorption and the fast recombination rate of the photogenerated charge carriers. To overcome these issues, doping with metal ions has been established as another popular method to improve the photocatalytic activity of TiO_2. The doping process of the semiconductor refers to

modifying its band gap structure by introducing controlled impurities states. Upon the doping with metallic ions, the cationic dopants replace the Ti cations and introduce energy levels below the conduction band. These levels can act as electron donor or acceptor and allow absorbing the visible light. Moreover, the doping process could be also associated with increasing the density of oxygen vacancies in TiO_2. Oxygen vacancies are generated if the cation has less ionic charges than Ti^{4+} ions in order to preserve the neutrality. The doping in this case also leads to a distortion in the octahedral of TiO_6 unit. Thus the formation of oxygen vacancies is more likely to occur. These defects form impurity levels near the CB [259], which can act as electrons donor and can also act as hole trapping sites, facilitating the electron separation and transportation.

Many studies have reported enhancements in the photocatalytic efficiency of TiO_2 nanomaterials by doping with noble metals and cations, including Ag [260], Pt[261] or transition metals such as V [262], Cr [263], Mn [264], Fe [253] and Pd [265]. Most of these materials were prepared through a sol-gel synthesis method, which is difficult to control the morphology of the obtained film.

Based on the literatures [266, 267], the incorporation of Cu species into TiO_2 nanostructures would be an attractive proposition to improve their photocatalytic activity and stability. The Cu doping would effectively extend the absorption of the doped film to the visible light region, enhancing the photocatalytic activity of the TiO_2 nanostructure [268]. The doping with Cu species can efficiently avoid the charge recombination by trapping both electrons and holes into formed energy levels in the band gap of the Cu-doped TiO_2 structure, which leads to a longer interfacial charge transfer lifetime [267, 269]. To our knowledge, direct Cu doping into 1D TiO_2 nanostructures, nanorods and nanowires, have not been reported for PEC water splitting. The only study was published recently [267], that reported the modification of TNRs films with Cu^{2+} ions in two steps; the

hydrothermal synthesis of TNRs film followed by the adsorption of Cu^{2+} via an ultrasonic-assisted surface deposition process. Nevertheless, the doped TNRs showed a photocurrent density about 26 times higher than the untreated sample. The authors attributed this to the combination of lowered band gap energy, reduced rates of electron-hole recombination and higher donor density. Therefore, it was interesting to investigate the direct Cu-doping into TNR arrays via a one-step hydrothermal synthesis method. The one step hydrothermal method offers a precise control in the created TNRs morphology with high reproducibility, cost effective and capable of large quantities synthesis. In the present work, the effects of Cu-doping upon the morphology, optical band gap and the PEC performance of 1D TNRs were investigated. The doping could improve the conductivity of the TNRs films by promoting the charge carrier density, enhancing the visible light absorption or by reduce carrier recombination through creating defects to act as active trap centres of electrons.

7.3 Experimental

All the chemicals were used as received. Hydrochloric acid (Fisher Scientific, 32 wt %, d= 1.16), titanium (IV) n-butoxide (Alfa Aesar, 99+ %), copper nitrate tri-hydrate ($Cu(NO_3)_2.3H_2O$) and conductive fluorine doped tin oxide (FTO) coated glass (Sigma Aldrich, 7Ω/sq.) was used as the substrate.

7.3.1 Fabrication of un-doped the TNRs film

Films of TNRs were prepared by a hydrothermal synthesis method reported in chapter 5. In a typical synthesis, DI water (10 ml) was mixed with concentrated hydrochloric acid (10 ml). The mixture was stirred magnetically at room temperature for 5 minutes before the addition of titanium butoxide, TBO, (0.4 ml). After another 5 minutes of stirring, the

mixture was transferred to a Teflon-lined stainless steel autoclave (50 ml). Two pieces of clean FTO glass substrate (1 ×1.5 cm^2) were placed at an angle against the wall of the Teflon liner, with the conducting side facing up. The reaction temperature was fixed at 150°C for 16 hours, which gives high quality TNRs. The autoclave was then left to cool down naturally to ambient temperature. The samples were washed with deionised water and left to dry in air. After confirming the growth of nanorods structured TiO_2 by SEM and XRD, the samples were annealed in air for 3 hours at 550°C. This was done to improve the contact of the nanorods to the substrate and also to enhance their crystalline structure.

7.3.2 Production of Cu doped TNRs films

To prepare the Cu doped samples, $Cu(NO_3)_{2.}3H_2O$ was added as copper source to the growth solution containing DI water, concentrated HCl and TBO. The copper source was added as a range of ratios (0.4, 0.6, 0.8, 1, 1.2 mol %) with respect to the TiO_2. The obtained films were washed with deionised water and left to dry in air. After confirming the growth of nanorods structured TiO_2 by SEM and XRD studies, the samples were annealed in air for 3 hours at 550°C.

7.3.3 Material characterisation

The crystal structures of the TiO_2 films were characterised by X-ray diffraction (XRD) (Siemens Powder X-500). The surface morphologies were studied by Scanning electron microscope (JSM 820M, JEOL). The average diameter and film thickness were measured from the SEM images using Image J (National Institutes of Health, USA). Photoluminescence (PL) emission spectra were recorded at room temperature on (LS 45 fluorescence spectrometer) for the Cu doped TiO_2 in respect to the untreated sample.

Since it was difficult to measure the absorption or transmission spectra of the obtained films because of their low transparency, the optical band gaps of the non-doped and doped TiO_2 films were measured from reflection absorption spectra using an integrating sphere (Ocean Optics, ISP-REF) with a UBS UV-Vis spectrometer (S/N: LR1-900) in the wavelength ranging from 200 to 800 nm at room temperature. The PEC water splitting was measured at room temperature using a standard three-electrode configuration. The TiO_2 samples were used as a working electrode, a KCl saturated Ag/AgCl was used as the reference electrode and a platinum electrode was used as the counter electrode. KOH aqueous solution at a concentration of 1 M (pH= 13.6) was used as electrolyte. In order to obtain simulated sunlight, a 300 W xenon lamp with AM 1.5 filters was used as the source. The power intensity of the light was 100 mW cm^{-2}.

7.4 Results and discussions

7.4.1 Morphology analysis of undoped and Cu doped TiO_2 nanostructure

All samples of non-doped and Cu doped TNRs were synthesised on FTO substrates. Fig. 7.1 shows top view SEM images of pure TiO_2 and Cu doped TNRs grown at 150°C for 16 hours with different copper doping concentrations. These images reveal the homogenous morphologies of deposited TiO_2 nanostructures with no detectable micro-cracks. With the copper incorporated, the samples maintained a similar TNRs structure with square top, while significant effects on the average rod diameter, size distribution and density were observed.

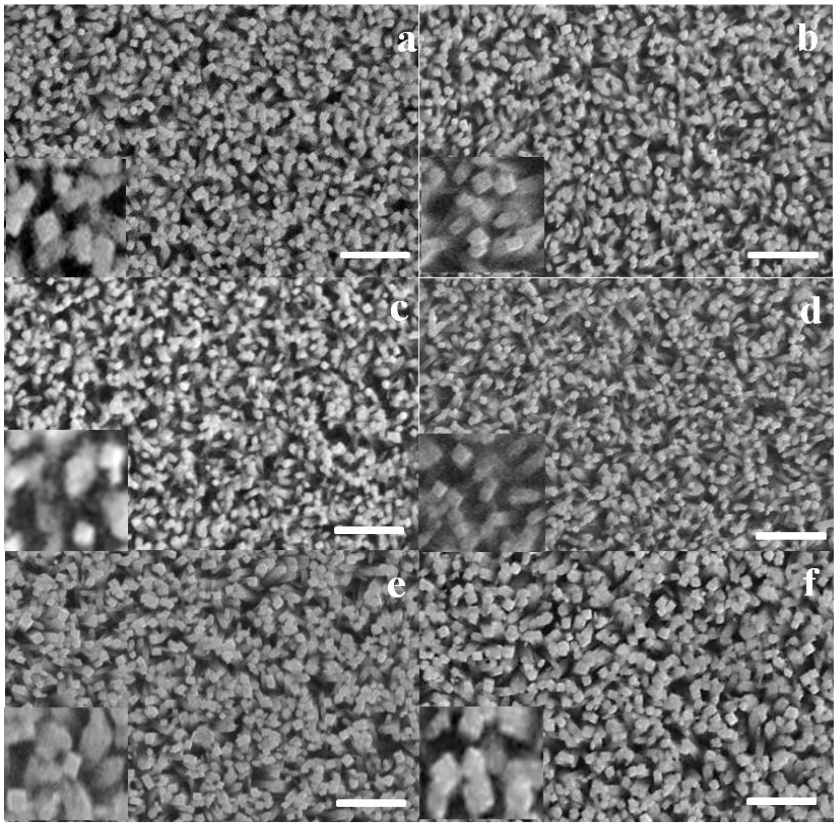

Figure 7.1 Typical SEM images of top views of Cu doped TNR films grown on FTO using DI water (10 ml), HCl (14 ml, 32%) and TBO (0.4 ml) at 150°C for 16 hours with different Cu doping concentrations. (a) 0 mol%, (b) 0.4 mol%, (c) 0.6 mol %, (d) 0.8 mol %, (e) 1.0 mol % and (f) 1.2 mol %. The scale bar of the main images is set at 2 µm. The onsets have magnification three times higher than the main images.

As shown in Fig. 7.2, the un-doped TNRs film shows an average rod diameter and full width of half maximum, FWHM, value of 190 nm and 30 nm respectively. An increase in the Cu doping concentration decreases the average rod diameter and increases the FWHM. The measured TNRs diameters of the samples doped with 0.4, 0.6 mol% are 160 and 150 nm, with FWHM of 65 and 70 respectively. The minimum average rod diameter was observed for the sample with 0.8 mol% Cu doped TNRs (140 nm). These rods exhibit the largest FWHM of 100 nm. Further increase in the doping concentration to 1.2% leads to an increase in the average rod diameter to 250 nm and the narrowing of the FWHM to 60 nm.

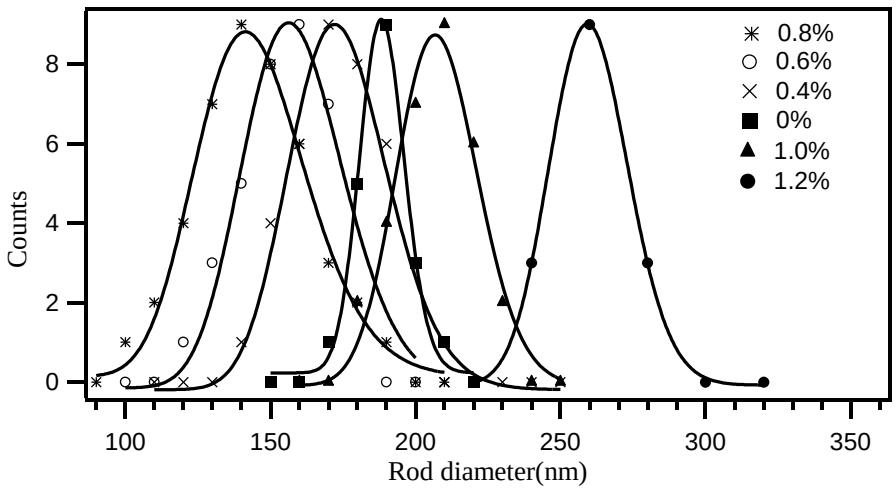

Figure 7.2 Size distribution of TiO_2/FTO nanorod samples with different concentrations of Cu doping.

The introduction of Cu dopant has less effect of the grown film thickness compared to the undoped TiO_2 film. Fig. 7.3 shows typical SEM images from the cross section of TNRs with and without Cu doping. The images reveal that with respect to the undoped TNRs film of 2.2 µm in thickness, there is small reduction in the length of the nanorods after the incorporation different concentrations of Cu. This phenomenon can be attributed to the reduction in the reaction rate as result of pH effect upon the hydrolysis and nucleation stages of crystal formation. This effect will be discussed in the next section. The measured thicknesses are 2.0, 1.94, 1.93, 2.0 and 2.1 µm for films doped with 0.4, 0.6, 0.8, 1.0 and 1.2 mol% Cu respectively.

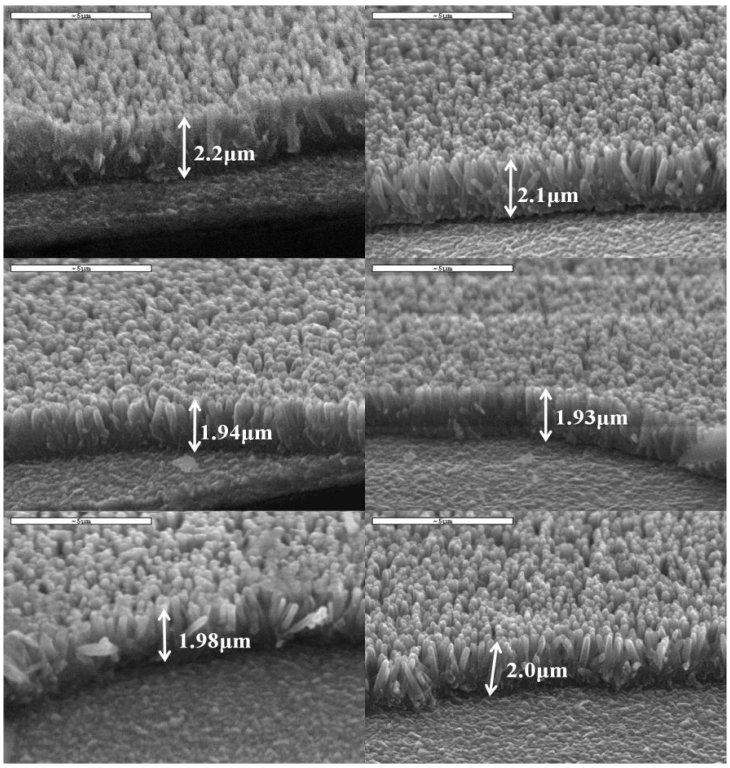

Figure 7.3 Cross section views of non-doped and Cu doped TiO_2/FTO nanorods with different doping precursor solution concentration. (a) 0 mol%, (b) 0.4 mol%, (c) 0.6 mol%, (d) 0.8 mol%, (e) 1.0 mol%, (f) 1.2 mol%.

7.4.2 Effect of Cu doping on the morphology of TNRs

The SEM observations of the Cu doping TNRs films in Figs. 7.1 and 7.3 confirm the proposed growth mechanism of the TNRs crystals presented in chapter 5, Section 5.4.2. It was mentioned that, the growth of un-doped TiO_2 crystals in aqueous solution results from the formation of growth units, which are incorporated into the crystal lattice. The creation of these units depends on the acidity of the growth solution and the presented legends. The reaction takes place in three stages: a hydrolysis stage, a nucleation stage and a crystal growth stage. Both the hydrolysis and condensation stages are sensitive to the pH of the solution. Highly acidic conditions significantly restrict the supply of the growth units.

In the doping process, copper nitrate is added into the growth solution as a copper source. The incorporation of Cu species into the Ti (IV) units in the form of $Ti(OH)_4$ and

the formation CuO increased growth solution acidity. Lowering the pH of the growth solution slows the hydrolysis of TBO, which reduces the availability of Ti (IV) units. As result, the obtained crystals are smaller and have larger size distributions. On the other hand, Zhang and co-workers [270] reported a hydrothermal synthesis of TiO_2 nanoparticles and found that very low or very high acidity of the growth solution induces aggregation in the nucleation stage, which supported the formation of large crystals. Another work has also investigated the preparation of TiO_2 nanoparticles by the hydrothermal method and confirmed that larger rutile crystals are formed in concentrated HNO_3 [271]. These observations support the increase in the Cu doped TNRs diameter after adding 1 mol% and 1.2 mol% of the copper nitrate to the growth solution.

The hydrothermal growth process is governed by the balance of three kinetic factors: 1) the rate for the formation of $Ti(OH)_4$, R_1, 2) the rate for Oswald ripening, R_2 and 3) the rate of deposited $Ti(OH)_4$ on the existing nanorods, R_3. While R_1 determines the rate of R_3, R_2 will determine the morphology of the nanorods. By increasing the acidity of the solution, R_1 will decrease, which reduces R_3. Thus the growth becomes slower and the achieved TNR diameter is also reduced. Increasing the acidity further, $Ti(OH)_4$ is stabilised in the solution. Meanwhile, significant increase in R_2 will result TNR with larger diameter at broader width distribution. Therefore, the overall morphology is determined by the Oswald ripening kinetics.

7.4.3 Crystal structure properties of the Cu doped TNRs

The crystal structures and crystal orientation of the non-doped and Cu doped TiO_2 NRs grown on FTO were characterised by powder XRD. The obtained XRD patterns were compared with standard XRD database for tetragonal rutile TiO_2 (JCPDS No. 88-1175) and FTO, plotted in Fig. 7.4. All samples show sharp and narrow peaks, which indicate a high quality crystalline structure. The diffraction spectra of each sample correspond to

the tetragonal rutile TiO_2 crystal structure. Two diffraction peaks locate at 2θ angle of 36.3° and 63.1°, which were indexed to the (101) and (002) planes of the tetragonal rutile TiO_2 phase were observed in all patterns. The remaining diffraction peaks are consistent with the FTO substrate. No CuO diffraction peaks were detected in the XRD pattern of doped samples. This observation confirms that either Cu dopant is homogenously distributed into the TiO_2 or the CuO crystals are too small and the total amount of the CuO dopant is too little. There are no significant changes of the diffraction intensity ratio between TiO_2 and FTO. Therefore, it is expected that the film thickness is not affected by the Cu doping.

It can be also seen that in all samples the diffraction (101) peak is dominant over the (002) peak, which suggests that the (101) plane is parallel to the FTO substrate. In comparison to pure sample, the diffraction peak intensities of doped samples show a gradual decrease with slight broadening when the copper doping is increased up to 0.8 mol% (green curve), before rising again as the doping concentration is further increased.

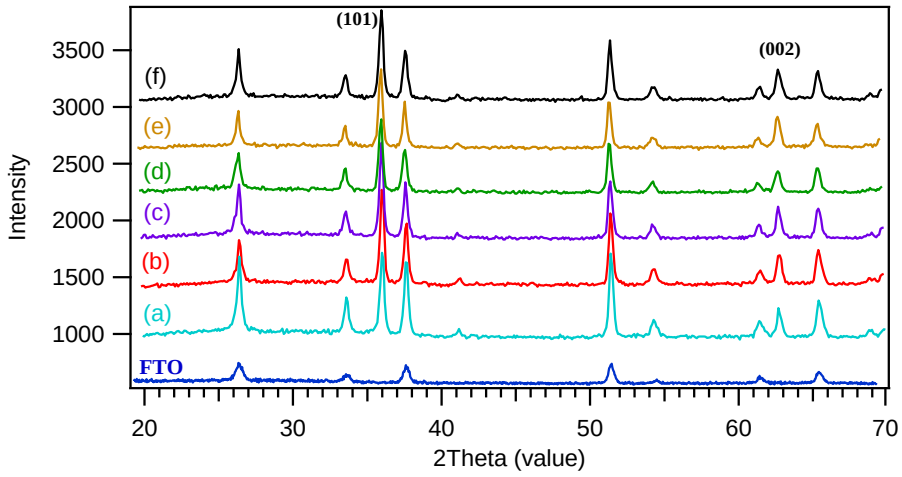

Figure 7.4 XRD patterns of the pure and Cu doped TNR films with varying doping concentration grown on FTO substrate. (a) 0 mol %, (b) 0.4 mol %, (c) 0.6 mol%, (d) 0.8 mol%, e) 1.0 mol% and (f) 1.2 mol%. All films were grown for 16 hours and subsequently annealed at 550°C for 3 hours.

The XRD peak broadening of doped samples suggests a significant reduction in the nanorods crystal domain size, which is consistent with the reduction of nanorod diameters and densities observed in SEM images in Fig. 7.1.

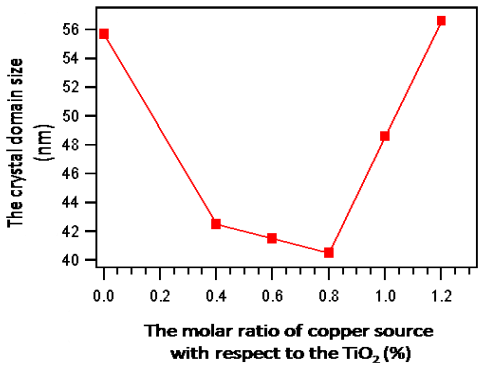

Figure 7.5 The calculated crystal domain size of the undoped and Cu-doped TNRs as a function molar ratio of the copper source.

The crystal domain sizes shown in Fig. 7.5, were calculated used the pervious mentioned equation (Equation 3.2, Section 3.4), which is restated as following:

$$D_{hkl} = \frac{K\lambda}{\beta_{hkl} cos\theta_{hkl}}$$

D_{hkl} is the crystal size (nm) perpendicular to the (hkl) crystal plane, $\boldsymbol{\lambda}$ is the wavelength of the X-ray which is 1.5406 Å and K is a constant equal to 0.89 when β_{hkl} takes the half of the diffraction peak boarding. The crystal domain sizes of the pristine and the Cu doped TNRs with 0.4, 0.6, 0.8, 1.0 and 1.2 mol% were found to be 55.7, 42.5, 41.5, 40.5, 48.6 and 56.6 nm respectively. Lowering the pH of the growth solution affects the nucleation and condensation of the growth stages.

In addition to the peak broadening, the reduction in the diffraction peak intensities with increasing the doping concentration indicates the reduction of crystalline quality due

to the formation of surface defects on the grain boundary and on the lattice of TiO_2. In TiO_2, Ti^{4+} is formally surrounded by six oxygen anions, to form octahedral units. The difference in ionic charge and size between Ti^{4+} (0.069 nm) and the copper ions, Cu^{2+} (0.073 nm) and Cu^{+}(0.096 nm), means that the substitution of these dopants on lattice sites of TiO_2 leads to a distortion in the octahedral units. This leads to the formation of oxygen vacancy defects, in order to preserve the charge neutrality. The presence of oxygen defects will induce stress in the TiO_2 lattice structure and restrict the growth of TiO_2 crystal. Both interstitial and substitional Cu^{2+} could happen in the doping, however, it is difficult to distinguish them experimentally.

7.4.4 Optical properties of un-doped and Cu doped TNRs

The effects of the doping on the optical band gap energy of TiO_2 were studied based on its reflection absorption spectra using an integrating sphere couple with UV-vis spectrometer. All samples were prepared on FTO substrates. The band gap energies were determined according to Tauc equation. Fig. 7.6a displays plots of $[h\nu \ln (R_{max}-R_{min})/(R-R_{min})]^2$ vs $h\nu$ for the un-doped and Cu doped TNRs at different Cu concentrations. The linear curvature at the absorption edges of the Tauc plots indicates that both un-doped and Cu doped TNRs have indirect band gaps. The extrapolation gives the reading on the band gap energies, which are plotted in Fig. 7.6b as a function of dopant concentration, shows a gradual reduction in the band gap energies of the Cu doped films with increasing Cu concentration.

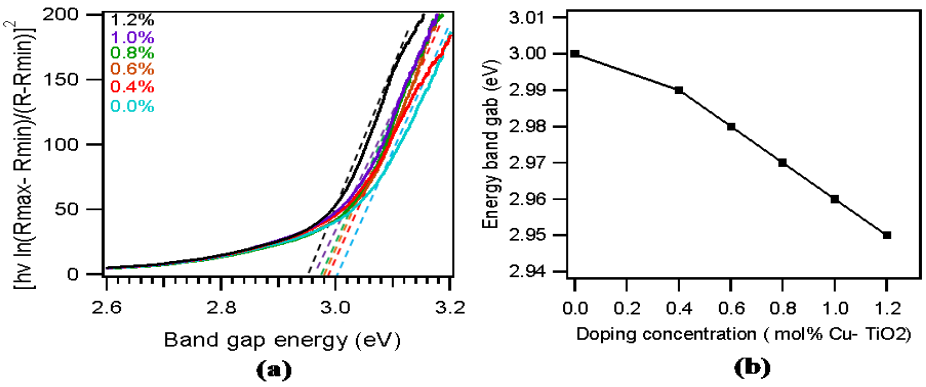

Figure 7.6 Band gap energy calculations of the un-doped and Cu doped TNR films.

The calculated band gaps of the pure and doped TNRs films with 0.4, 0.6, 0.8, 1.0 and 1.2 mol% Cu were 3, 2.99, 2.98, 2.97, 2.96 and 2.95 eV respectively. The measurements indicate that the Cu doping narrows the optical band gaps with increasing the concentration. The doping process forms new energy levels within the rutile band gap structure.

7.4.5 Photoluminescence (PL) properties

Following the photoexcitation process, the excited electrons and hole can be recombined in competition with the PEC process. During the charge recombination, energy will be released either as thermal energy or as photoluminescence. Therefore, the extent of the recombination of the photogenerated charge carriers can be effectively measured by the PL intensity. High PL intensity means that more photo-induced electron-hole pairs are recombining within the measurement timescale, while lower PL intensity indicates that more photo-generated charge carriers are involved in either non-irradiative recombination or transferred to the surface to incorporate in the photocatalytic reaction [267, 272]. In this study, PL measurements on un-doped TiO_2 and Cu doped TNR arrays were recorded to investigate the effect of the doping process on the electron-hole recombination efficiency.

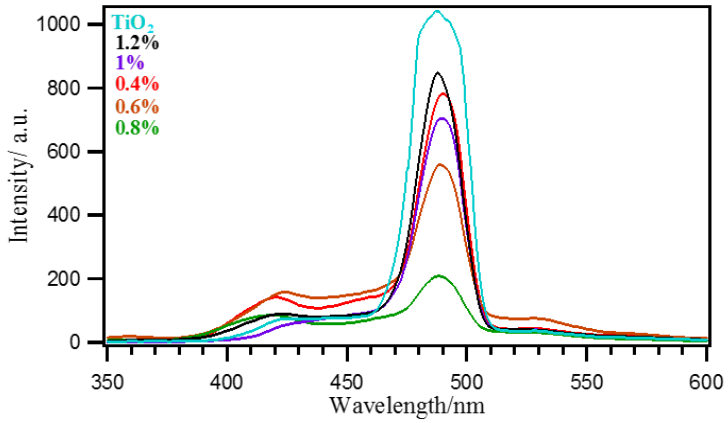

Figure 7.7 PL spectra of TiO_2 and Cu doped TNRs on FTO. The excitation wavelength 240 nm.

Fig. 7.7 shows that non-doped and Cu doped TNR films with different doping concentrations exhibit similar PL emission profiles. There are two PL signals in all the samples. The first emission band centred at 413 nm (3.02 eV) is attributed to the self-trapped exciton within the octahedral rutile structure [273]. The other emission band located at 487 nm (2.55 eV) is associated with the defects, Cu dopants and oxygen vacancies. These defects support the charge transfer transition from Ti^{3+} to oxygen anion in TiO_6 [274]. The electrons are excited upon photon absorption and are transferred to the conduction band. Due to the short lifetime of the excited state (of the order of 10^{-9} s), the excited electrons fall back to the oxygen vacancy defect sites before relaxing down fully into the valance band, where they recombine with the holes to yield PL emission. Therefore, the intensity of PL emission reflects the recombination efficiency.

Compared to the pure TiO_2, (light blue), Cu doped TNRs showed decrease in the defects PL intensities (at 487 nm) with increasing doping concentrations up to 0.8 mol% (green curve). This represents the decrease of recombination rate, indicating optimised photocatalytic activity. Increasing the copper doping concentration above 0.8 mol% increases the PL signal intensity. The reduction of PL signal at lower doping concentrations suggests effective trapping of excited holes with improved charge

separations. However, at higher doping concentrations, both electrons and holes were immobilised and the charge recombination are increased.

7.4.6 Photoelectrochemical (PEC) properties of the pure and Cu doped TNR films

The photocatalytic activities of the Cu-TNRs with varying Cu doping levels in PEC water splitting are shown in Fig. 7.8a. The linear sweep voltammograms measured from TNRs samples with varying Cu doping concentrations of 0.4 mol%, 0.6 mol%, 0.8 mol%, 1 mol% and 1.2 mol % in comparison with pure TiO_2 film. The measurements were done throughout the potential range of -0.9 to 0.5 V vs Ag/AgCl. The dark current for all the samples are too small to be measured. Whiles under illumination, the pure rutile TNRs film shows a low photocurrent density of 1.0 mA cm-2 at 0V vs Ag/AgCl. The photogenerated current density shown from Cu doped TNRs samples were significantly higher, except the 1.2 mol% doped sample.

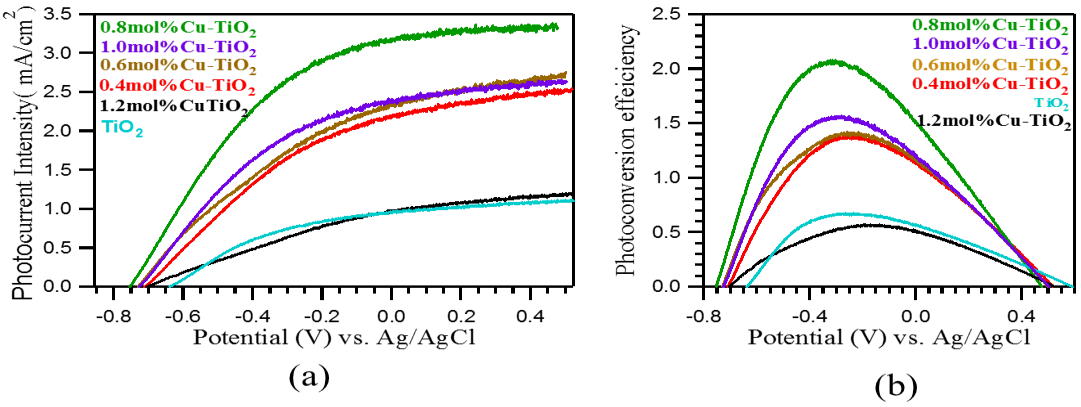

Figure 7.8 (a) Linear sweep *voltammograms* collected from pure TNRs and Cu doped samples with concentrations of 0.4 mol%, 0.6 mol%, 0.8 mol%, 1 mol% and 1.2 mol%. All samples grown at 150°C for 16 hours (b) calculated photoconversion efficiency for the non-doped and Cu doped TNRs as a function of applied potential (vs. Ag/AgCl).

Cu doped TNRs samples of 0.4, 0.6 and 1 mol %, yielded photocurrent densities at least two times higher than that of the pristine film. The maximum photocurrent density

of 3.25 mA at typical potential of 0VAg/AgCl was achieved using the sample of 0.8 mol% Cu doped TNRs film. Increasing the copper doping above 0.8 mol% leads to decrease the generated photocurrent.

Additionally, it is worth to note that, all the Cu doped photoanode exhibited more negative onset and saturation potentials compared to the pristine TNRs. The onset potential of pure and Cu doped TNRs with 0.4, 0.6, 0.8, 1 and 1.2 mol% were -0.62, -0.65, -0.66, -0.68, -0.66 and -0.65 V vs Ag/AgCl respectively. In general, the onset potential is related to the water oxidation kinetic at the anode surface, where four holes are used to oxidise two water molecules and form one molecule of oxygen. In order to promote this process and prevent the recombination between the photogenerated electron-hole pairs that accumulate at the anode surface, positive potential requires to be applied between the electrodes. Shifting the onset potential to lower value (more negative value) over the doped samples reflects the high efficiency of the charge separation and transportation of the photogenerated charge carriers. This can be attributed to the formation of surface defects such as oxygen vacancies as result of the doping treatment. These defects act as trapping sites for the holes in addition to their role as electron donors. Therefore, the charge carrier separation with the electrode conductivity will increase. These results confirm that copper doping of 1-D TNRs through the one-step hydrothermal method is an effective technique to enhance the photocatalytic performance of 1-D TNRs films.

The corresponding photoconversion efficiencies of the samples were calculated and plotted as a function of the applied potential according to (Equation 3.12, Section 3.4), shown in Fig. 7.8b. The pure TiO_2 nanorods film gives a maximum photoconversion efficiency of 0.6 % at -0.2 V vs Ag/AgCl. The highest photoconversion efficiency was

achieved by the 0.8 mol% Cu doped sample which was 2.1 % at a lower bias of -0.35 V vs Ag/AgCl.

The significant enhancement in photocatalytic performance observed for the Cu doped TNRs samples can be rationalised by two factors: firstly, the significant reduction in the recombination rate by introducing energy levels of Cu doping according to the PL measurements. In pure TiO_2, the electronic excitation occurs directly from the valance band (VB) to the conduction band (CB), where the recombination rate is high. In the doped samples, with their unoccupied Cu^{2+} *s-d* states and oxygen vacancies, the electrons are not directly excited to the conduction band. The sub-band states may capture electrons and prevent them from the recombination with holes. Subsequently, the lifetime of the exited electrons is increased and their initial excitation into the conduction band is supported, which increases their availability for involvement in photocatalytic reactions. A precise level of the doping is a key factor; a high doping concentration creates high levels of defects, which act as charge carrier recombination centres. This leads to the reduction in the photocatalytic activity.

Additionally, the clear reduction in the rod density and rod diameter after adding concentrations of copper doping (0.4, 0.6, 0.8 mol % which was determined to be 12, 10, 9 μm^{-2} compared to 14 μm^{-2} for the un-doped sample) offered as another factor responsible for their enhanced photocatalytic performance. Low rod density and small diameter TNRs allow high portion of the illuminated UV light to penetrate through the nanorods film, therefore the irradiated light is effectively used. In contrast, increasing the doping concentration to 1.2 mol% leads to a significant increase in the rod diameter and density (16 μm^{-2}), as confirmed by the SEM image. The increased void between the nanorods offers an easier diffusion of electrolyte in and out of the film framework, which helps to maintain the local pH value near the TNRs.

The another possible factor that play a role for enhancing the PEC water splitting is the reduction in the optical band gap of the TiO_2 upon doping with Cu ions. The smaller band gap will extend the absorption region of the doped samples to the visible region, leading to increasing the solar exited electrons and holes.

7.5 Conclusion

In this work, Cu doped TNRs were successfully synthesised for the first time through one-step hydrothermal method. According to XRD analysis, Cu doped TNRs show a similar crystal structure and morphology as the non-doped film, with a gradual reduction in the main diffraction peak intensity as a function of increasing the doping concentration up to 0.8 mol%. This is attributed to the suppression of crystal growth as result of the incorporation of Cu^{2+}, which has large ionic radius, inducing stress in the TiO_2 lattice structure. The reduction in the Cu doped TNRs crystal size is in agreement with SEM characterisation. The optical band gap of the doped samples reduced with increasing dopant concentration. The PEC measurements reveal that the achieved photocurrent density reached 3.25 mA cm^{-2} at 0V vs Ag/AgCl for 0.8 mol% Cu-TiO_2, which is almost three times higher than that of the non-doped film. This performance corresponded to the maximum photoefficiency of 2.1%. The improvement in the photoactivity of PEC water splitting of this sample may be attributed to the improved charge separation and transportation with reduced band gap energy and reduced nanorod density and diameter. The efficiency reduced significantly by increasing the doping concentration above 0.8 mol%. Increasing the doping concentration further forms a greater density of doping level states, which act as recombination centres. This leads to a decrease in the photocatalytic performance.

Chapter 8 Synthesis of ZnO nanorods on transparent conducting glass rod substrate for high efficient photo electrochemical water splitting

8.1 Abstract

This chapter highlights the design and fabrication of a three dimensional photoanode for a PEC device in order to enhance the photocatalytic performance. Clear conductive glass rods decorated with a zinc oxide thin film were fixed to a copper disc, forming a three dimensional photoanode. The conductive glass rods ware fabricated by depositing conductive layers of an Indium Tin Oxide (ITO) by the sol-gel synthesis method. A thin film of vertically aligned zinc oxide nanorods was grown on conductive glass rod substrates, using chemical bath deposition. The electrical and optical properties, structure and morphology of the 3-D photoanode were investigated. 3-D photo electrodes with different lengths, 5 cm and 15 cm, were assembled and tested in prototype PEC systems. The photocurrent densities from both electrodes ware measured. It was observed that, high photocurrent can be achieved by using this 3-D photoanode configuration. In addition, the electrode of longer rods length yielded lower photocurrent density than the shorter rods length. This is due to the limited charge transportation through the ITO film as a result of difficult to deposit a homogeneous ITO film on large surfaces of the longer glass rods. The efficiency of the electrodes can be enhanced further by improving the conductivity of the ITO film and the light leakage from the side of the glass rods (with increased roughness of the glass surface). In addition, by adding organic compounds to the PEC system, the photocurrent density could be further enhanced.

8.2 Introduction

Photoelectrochemical (PEC) process of splitting the water into hydrogen and oxygen is not an easy target, as it requires an effective catalyst that can absorb the solar light and convert the photoenergy into chemical energy. The performance of the photocatalyst is significantly influenced by its morphology and electronic properties such as high crystallinity, low defect density, charge-transfer pathways, chemical and mechanical stability, band gap positions, band gap energy and surface area [65, 133]. These factors affect energy absorption and charge re-combination; therefore, the selection and design of the photoanode in PEC systems is crucial.

The surface area of the anode material is considered as one of the key factors affecting the PEC performance. The photoelectrode should have a high contact area with the electrolyte in order to provide large amounts of interfacial reaction sites for the PEC reaction. More important, the light absorption/reflection can also affect the over efficiency of the PEC process. Most of the photoanodes are made of thin films of semiconductors. For such devices, the efficient light absorption requires to increase the film thickness, which will hinder the charge transportation. To overcome such restriction, we designed an innovative 3-D electrode, in contrast to the conventional 2-D thin film electrode. Fig. 8.1 shows a schematic diagram of the 3-D design. In many 2-D electrodes, a large amount of sunlight is reflected back. With a 3-D transparent electrode, made of glass, quartz or PMMA, the rod structure forms a wave guide which will guide the light through the transparent substrate. Normally, the light will be trapped within the glass, since its refractive index is higher than water. However, once it is coated with metal oxide, a small amount of light will leak through the side of the glass (side-emission) and excite the metal oxide. This is because that the refractive index of the metal oxide is usually higher (almost double) than the glass or quartz, which reduces the total reflection incident

angle. This side-emission could be further improved if the surface of the glass rod is roughened to some degree. The conductive ITO coating will further assist the charge collection and transportation along the glass rods.

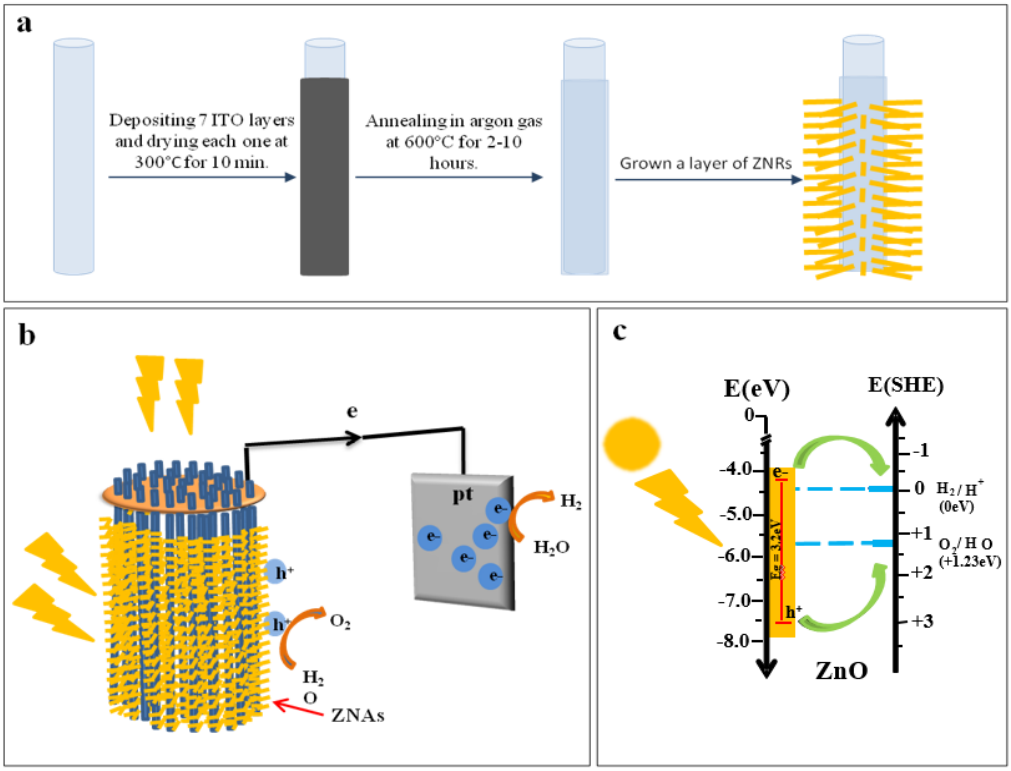

Figure 8.1 A scheme of the 3D electrode; (a) is the coating process of a single glass rod with 7 layers of ITO conductive film, (b) conductive glass rods decorated with zinc oxide nanorods and attached to copper disc with charge transfer mechanism in PEC system and (c) the excitation process of the ZnO nanorods in response to the UV absorption.

The surface area of the photoanode material can also be extended by controlling the morphology and grain size of semiconductor nanostructure. For instance, a 1-D nanorod semiconductor has the key advantages of providing high surface area with more interfacial reaction sites. It also offers a direct electrical pathway, leading to the increased carrier transport rate and reduced recombination rate between the photogenerated electrons and holes. Therefore, many studies are focused on processing the

semiconductors into 1-D nanostructures for enhanced photocatalytic performance, when used as photoanode materials in a PEC system [46, 272].

It was decided to use vertically aligned (1-D) ZnO nanorods, ZNRs, as the active semiconductor materials to decorate the glass rod in the 3-D electrode. ZnO has a direct band gap energy similar to that of TiO_2, large exciton binding (60 meV) [275], high electron mobility when exposed to UV radiation [276] and has also been reported as an effective photocatalyst [157].

In this work, the design and fabrication of a novel photoanode for PEC devices was investigated as shown in Fig. 8.1. Conductive glass rods were prepared by coating normal glass rods with 7 layers of indium tin oxide (ITO) (Fig 8.1a). The preparation process will be discussed in details in the experimental section. Thin films of well aligned ZnO nanorods, were deposited on conductive glass rod substrates by the CBD method. Installation of a number of these rods to a copper sheet forms a three-dimension electrode (Fig 8.1b). Illuminated either from the top of the electrode (back-side illumination) or from the side of the electrode (front-side illumination) gives different photoefficiency and the mechanism is explained (Fig 8.1c). The excitation process of ZnO in response to the UV light and the electron-hole generation process is shown in Fig. 8.1c. The structure of the 3-D electrode provides large surface area, increases the number of interfacial reaction sites, enhances light absorption and improves photoefficiency in the water oxidation process and hydrogen generation.

Indium oxide, In_2O_3, is a transparent conductive oxide (TCO) that is commonly used to produce transparent conductive films. This is due to its superior electrical properties, combined with high transparency and infrared reflectivity, which can be attributed to its high band gap of 3.75 eV. It is a poor conductive material when it is stoichiometric, the conductivity is increased substantially by doping the lattice with an

appropriate dopant, such as tin [277]. In this process, the dopant (Sn) replaces the In^{3+} in the crystal structure of indium oxide of cubic bixbyite [277, 278], forming an interstitial bond with the oxygen forming SnO or SnO_2. The low valence state (Sn^{2+}) traps the charge carriers, causing the electrical conductivity to reduce. In contrast, the higher oxidation state of Sn^{4+} acts as an n-type donor that donates one electron to the conduction band and contributes with the oxygen vacancies to increase the conductivity[279].

In this work, ITO film was synthesised and deposited on glass rods to obtain optical transparent conductive glass rod substrates. Since conductive glass rod is not commercially available, part of my project is to develop a coating procedure. Fortunately, the conductive layer of ITO can be deposited using solution dip coating methods and the preparation of this material becomes technically straightforward. Meanwhile, the FTO coating will need CVD deposition facility which is not available in the lab. ITO generally has better conductivity than FTO. However, due to the limited global supply of Indium, FTO is normally commercially available, that is why we used FTO glass as a flat substrate in earlier work. Among different methods of preparing transparent conductive films of ITO, the sol-gel was favoured. This is due to the high degree of control over the chemical composition of the resulting metal oxide, the good quality of the coated films on desired shape and area, without any expensive and complex equipment.

In the following sections, the preparation of ITO thin films by the sol-gel method is described. Metal salts were used as starting material with organic solvents. The resistivity of the formed films was measured as a function of the annealing temperature in different atmospheres. In addition, the optical and structural characteristics were studied. Moreover, the growth of ZNR films on the conductive glass substrates, by CBD method is discussed. The photoelectrochemical (PEC) measurements of the designed electrodes are also presented.

8.3 Experiments

8.3.1 Preparation of ITO films

All chemicals were used as received. Indium chloride ($InCl_3$, 99.99%, Across Organics), tin chloride ($SnCl_4$, 99.99%, Across Organic) with acetyl acetone and ethanol as solvents. A flat glass substrate (2×2 cm^2) was used for studying the ITO film properties. Pyrex glass rods was chosen as the substrate materials since it is UV transparent down to wavelength of 340 nm, which is sufficient shorter than the ZnO band gap energy. Thus Pyrex rods with 2 mm in diameter and of different lengths, 5 and 15 cm were coated with ITO film and used as substrate for the 3-D electrode. In the later experiment, Pyrex rods with 3 mm in diameter and 10 cm in length were used. The end of these Pyrex rods was grounded to a slant tip to improve the light reflection.

8.3.1.1 Preparation of ITO solution

1.11 g of $InCl_3$ was dissolved in 50 ml of acetyl acetone and the solution was heated at 70°C for 1 hour to increase the solubility of $InCl_3$. 0.05 ml of $SnCl_4$ was dissolved in 50 ml of ethanol and the solutions were mixed at room temperature and aged for 24 hours before use.

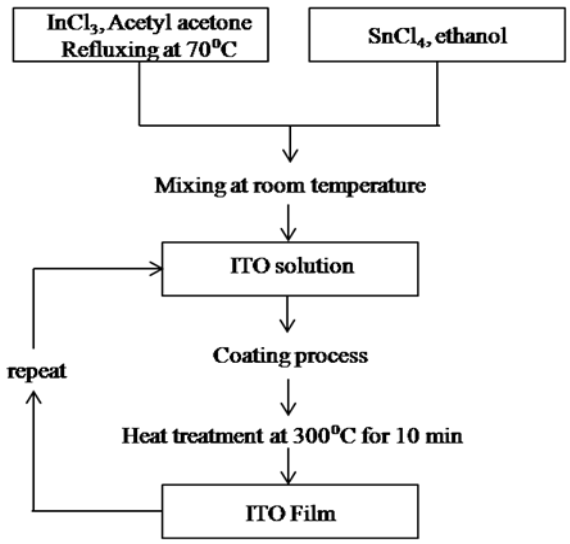

Figure 8.2 Preparing procedure of ITO thin film by sol-gel.

Fig. 8.2 represents a schematic diagram of various steps required for procedure preparation ITO thin film. In the experiments, the glass substrate was cleaned using KOH solution, soap, DI water and isopropyl alcohol sequentially. It was then coated with an ITO layer and preheated at 300°C for 10 minutes. As increasing the film thickness will increase the charge carriers concentration and the conductivity [280, 281], the coating process was repeated multiple times until desired film properties, thickness, homogeneity and conductivity, were obtained.

8.3.1.2 Deposition of coating onto glass substrates

In order to examine the efficiency of the prepared ITO solution, it was deposited on conventionally cleaned flat glass substrates by a home-made spin coater in air. About 50 µm of the solution was dropped onto the substrate and rotated with different speeds (1000, 1500 and 2000 rpm) for 1 minute. The substrate then was dried at 300°C for 10 minutes. To increase the film thickness, the above process was repeated nine times. The obtained ITO thin films were further annealed in either air or argon gas at different temperatures, 400°C, 500°C and 600°C with a heating and cooling ramping of 50°C/min and 10°C/min respectively for 2 hours. This process was to study the effect of the annealing environment and temperature on the film conductivity.

To deposit the ITO conductive film on glass rods, a dip coating method was employed. The glass rods substrates were dipped in the ITO solution then dried before annealed at 300°C for 10 minutes. The process was repeated to increase the film thickness. Finally, the coated samples were annealed at 600°C for 2-10 hours in argon gas atmosphere. The film thickness as a function of its conductivity was investigated.

8.3.2 Growth of well-aligned ZNRs on the conductive glass substrates by two-steps chemical bath deposition (CBD)

All chemicals were used as purchased from Sigma-Aldrich without further refining. Titanium/flat glass substrates (2×2 cm^2) and glass rods were used as substrates, which were cleaned by isopropanol (IPA) and dried in air before the deposition of a seeding layer. The synthesis process of zinc oxide nanorods, ZNRs, was carried out in two steps: the substrate seeding followed by the growth step.

Seeding solution of 0.1 M of zinc acetate was prepared by dissolving 2.195 g of zinc acetate in aqueous PVA solution (3% ww) and magnetically stirred for 3 hours. A spin coating technique was applied to deposit one layer of the seeds on the titanium/flat glass substrates. These samples were used for characterizing the grown film. The conductive glass rod substrates were dip coated once in the seeding solution and allowed to dry at room temperature (about 90% in length of the rod was coated by the seeding solution and 10% left as a contact point). The coated substrates were then annealed at 400°C in air for 1 hour.

For the CBD growth process, zinc nitrate (99.9%, Fisher Scientific) and hexamethylenetetramine (99.9%, Fisher Scientific) were first dissolved individually in DI water at a concentration of 20 mM each, then mixed together to be used as growth solution. The seeded part of the substrates was immersed into the growth solution in a glass beaker containing 100 ml of the growth solution, which then was placed into an oven for 20 hours at a constant temperature of 84°C. The substrates were taken out from the solution, rinsed with DI water and dried at room temperature.

8.4 Characterization techniques

The crystal structures of the ITO thin films and the ZNRs were characterized by the X-ray diffraction (Siemens Powder X-500) at room temperature, over an angular range of $20° \leq 2\theta \leq 70°$ at a step of 0.02° using Cu Kα radiation. Scanning electron microscope (JSM 820M, JEOL, operating at 30 kV) imaging was performed to check the morphology of the surfaces. The average diameters and film thickness were scaled from the SEM images using Image J (National Institutes of Health, USA). The electrical resistance of the ITO films was investigated by a four-point probe method. The conductivity of the sample can be calculated using equations 8.1, 8.2 [282, 283]:

$$\rho = R \times t \qquad \text{(Equation 8.1)}$$

$$\sigma = \frac{1}{\rho} \qquad \text{(Equation 8.2)}$$

Where ρ is the electrical resistivity (Ω cm), R is the film resistance (Ω), t is the film thickness (cm) and σ is the conductivity (S cm^{-1}). The optical transmittance of the ITO thin films was studied by a UV-Vis spectrometer (UV300). For the glass rod substrate, the intensity of the penetrated light through different rod length was measured by UV light meter (YK-35UV).

A three-dimension electrode was assembled by attaching a number of the conductive glass rods of the same length, either 5 or 15 cm, to a copper disc fixed with conductive silver loaded epoxy adhesive (RS Components). Another disc was attached at the end of the electrodes to protect the glass substrates during the assembling and drying processes. By using the three dimensional electrode as a photoanode in the PEC system, the photocurrent was measured in a special experiment set up. The three dimensional reactor was used as a working electrode and a platinum electrode was used as a counter

electrode. Aqueous KCl solution at a concentration of 1M (measured pH of 6.7) was used as electrolyte. A USB potentiostat (eDAQ) was used to control and record the photocurrent as a function of electrochemical potential. The reactor was illuminated from different angles, top and side illumination, using compact illuminator 6000CI Xenon lamp as a light source. Full spectrum with no AM 1.5 filter (not available yet) was used in this PEC setup, which is considered as primary examination of this electrode. This step would be optimised in the future work.

8.5 Results and discussions

In this section, the crystal structural, electrical properties, optical properties and morphology of ITO thin films deposited on flat glass and glass rod substrates are discussed. The growth of ZNRs on conductive substrates was studied. Finally, the PEC performances of the formed 3-D electrodes are investigated.

8.5.1 Study the properties of the ITO thin films

8.5.1.1 Study the properties of the ITO thin films deposited on flat glass substrates

To study the effect of the annealing conditions on the formation and properties of the formed ITO films, nine ITO layers were deposited on cleaned flat glass substrates. The films then were annealed at different temperatures (400, 500 and 600°C) in two different atmospheres (air and argon gas) for two hours. To study the crystal structure of the formed ITO films, which consist of 10% SnO_2, XRD patterns were collected as shown in Fig. 8.3. The XRD patterns of the films annealed at different temperatures in air are presented in Fig. 8.3A. First of all, the rolling baseline shown in all the PXRDs are contributed from the Pyrex substrate with small degree of crystallinity.

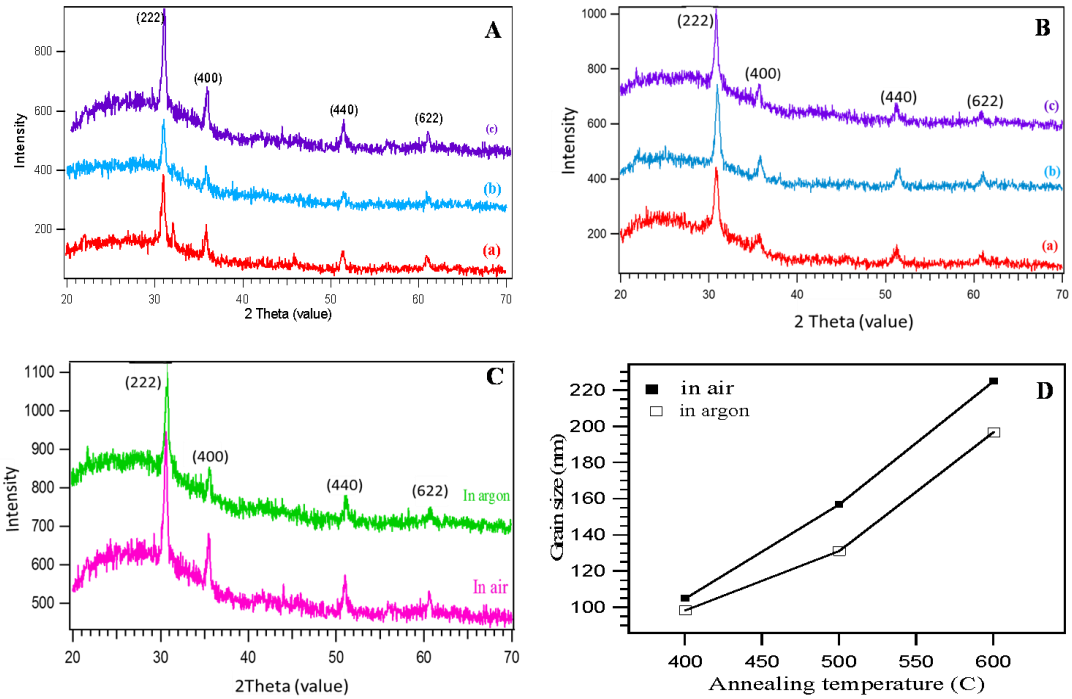

Figure 8.3 XRD patterns of the ITO films formed by annealing for 2 hours in different atmospheres; (A) air and (B) argon gas, at different annealing temperatures; (a) 400°C, (b) 500°C and (c) 600°C. (C) XRD patterns of the ITO films formed at 600°C in different atmospheres. (D) The calculated grain size of ITO films annealed at different temperature in different atmospheres.

By annealing at 400°C, the pattern of ITO exhibits diffraction peaks at 2θ of 30.7°, 35.6°, 51.2° and 61°; corresponding to (222), (400), (440) and (622) plans respectively. These peaks were indexed to the indium tin oxide with cubic crystal structure (JCPDS:71-2194) [284]. The (222) peak is the most prominent for all films, suggesting that the films have a strong (222) preferential orientation. Intensity of all peaks increased gradually by rising the annealing temperature up to 600°C, indicating an improvement of the crystalline structure. At low annealing temperature of 400°C, the observed peak at 32.5° was indexed to In_2SnO_5. This product may be formed as an intermediate compound at a low annealing temperature. Since there are no peaks that can be indexed to Sn, SnO or SnO_2 observed in the spectra, it can be concluded that all Sn atoms have arranged into the In_2O_3 crystal lattice.

Fig. 8.3B, displays the XRD pattrens of ITO films annealed in argon gas atmosphere at 400°C, 500°C and 600°C for 2 hours. The results confirm the formation of ITO film with cubic crystal structure. The films show similar XRD pattrens to those annealed in air where (222) peak is the most prominent.

To compare the effect of the annealing atmosphere on the crystal formation of ITO films, Fig. 8.3C shows the XRD pattrens of two ITO films annealed at 600°C for 2 hours in different atmospheres. When annealing in argon gas, film crystallization occurred, but the intensities of the peaks were weaker than those of the films annealed in air. That could be attributed to the removing of oxygen interstitials from the lattice, forming oxygen vacancies. The formation of the oxygen vacancies, which is known as electron donor, leads to increase the film conductivity. Meanwhile, the presence of these defects in the crystal could reduce the crystal size of the resulted film. On the other hand, by anealing in air, the available atmospheric oxygen may react with the substrate, resulting in an increase in sample crystallinity.

To confirm that, the crystal size of formed ITO can be calculated based on the XRD patterns by using the Scherrer's equation, which was presented in chapter 3, section 3.4 as the following:

$$D_{hkl} = \frac{K\lambda}{\beta_{hkl} cos\theta_{hkl}}$$

where D_{hkl} is the crystal size (nm) perpendicular to the (*hkl*) crystal plane, $\boldsymbol{\lambda}$ is the wavelength of the X-ray which is 1.5406 Å and K is a constant equal to 0.89 when β_{hkl} takes the half of the diffraction peak boarding. The grain size was calculated based on the (222), (400), (440) and (622) diffraction peaks. The average grain sizes of ITO films as a function of the annealing temperature were plotted in Fig. 8.3D. According to the

calculated results, the crystallite size in the ITO films becomes larger as the annealing temperature increases. The increase in grain size is primarily due to the Oswald ripening promoted by the higher temperature. However, there are obvious reductions in the crystal size of ITO films when the calcinations are performed in the argon compared to those formed by annealing in air. These differences increase with raising the annealing temperature. These results can be attributed to the removal of oxygen interstitials from the lattice by annealing in argon, which could reduce the crystal size of the resulted film, as discussed above.

SEM imaging was performed to study the morphology of the ITO surfaces. Fig. 8.4 shows the SEM images of the films prepared by depositing nine layers of the ITO and annealed in argon gas for 2 hours at different temperatures.

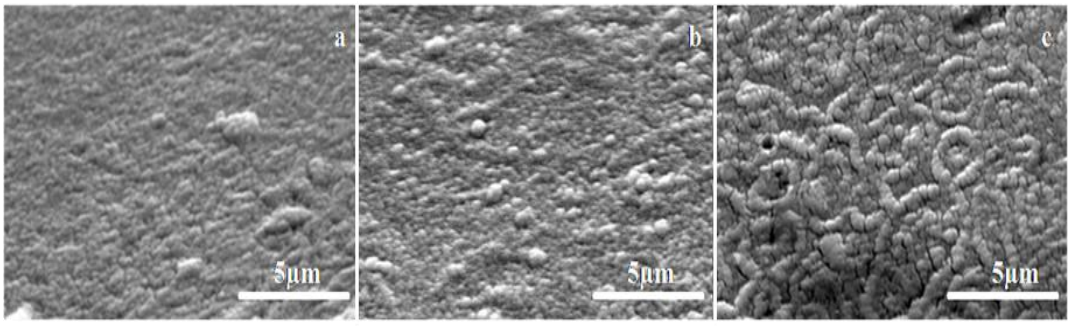

Figure 8.4 SEM images of the ITO films centred for two hours in argon gas at different temperatures, (a) 400°C, (b) 500°C, (c) 600°C.

It can be seen that all the films have a uniform surface morphology consisting of small particles without any voids and cracks. The grain size of the ITO films increased gradually with increasing annealing temperature, confirming the calculated results from the XRD patterns. The film thickness shows gradual increase with increasing number of deposited layers, approximately 55 nm for each layer. On the other hand, varying the annealing temperature from 400°C, 500°C to 600°C leads to slight decrease in the total

film thickness, 517 nm, 510 nm and 500 nm respectively. This phenomenon can be attributed to shrinkage of the film within the sintering process. This means increasing the annealing temperature enhances the crystallinity of the film and induces grain growth, which limits the grain boundary scattering of the charge carriers.

Energy dispersive X-ray spectroscopy (EDX) analysis was carried out to confirm the chemical composition of the films. Fig. 8.5 shows that the formed film is exclusively composed of In and Sn as a dopant. The silicon signal is related to the substrate (Pyrex glass). Boron signal, on the other hand, is impossible to be detected. That is because our EDX has a Be window which will only detect elements heavier than Na. Due to the significant overlapping of the EDX signals from In and Sn, quantitative analysis is difficult using EDX.

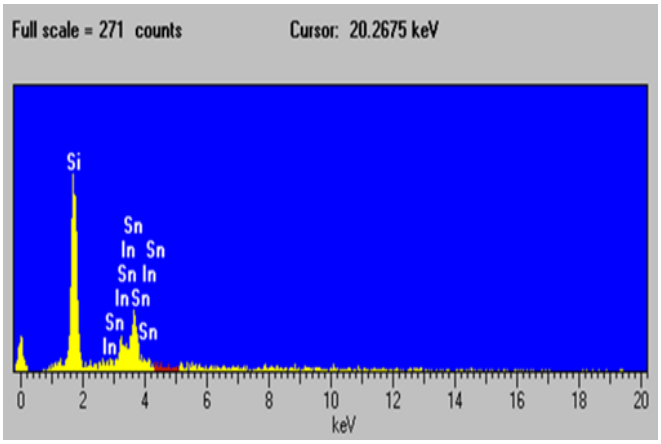

Figure 8.5 Shows the EDX spectra of the sample of ITO film annealed at 400°C for 2 hours in argon gas.

The overall effect of sample annealing at high temperature is to increase the electrical conductivity of the ITO sheet. Fig. 8.6 shows the effect of the annealing temperature and environment as a function of the film resistivity.

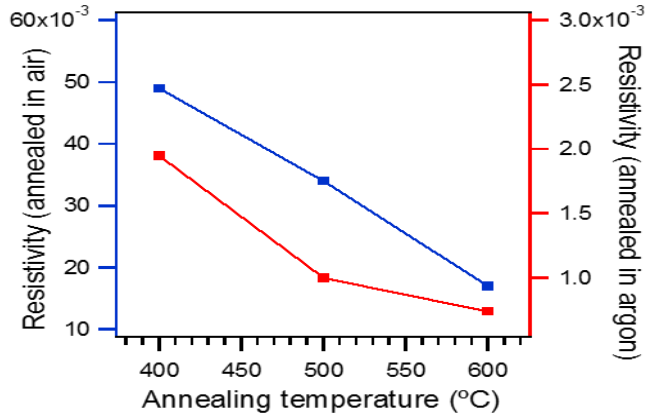

Figure 8.6 Electric resistivity of the ITO films for various annealing temperatures and atmospheres

It can be seen that the resistivity of ITO films is greatly influenced by the annealing temperature and annealing atmosphere. The resistivity decreased dramatically with increasing temperature. According to the experimental results, the annealing atmosphere has also a key role to reduce the film resistivity. A minimum film resistivity of about 7.4×10^{-4} Ω.cm was achieved by heating the prepared film at 600°C in argon gas, while post annealed films in air show higher electric resistivity of 1.7×10^{-2} Ω.cm at the same temperature. This is attributed to removal of the oxygen interstitials in the lattice, forming a high density of oxygen vacancies. These vacancies act with the tin atoms as donor sites to increase electrons densities, therefore improving the film conductivity. The density of these defects increases with increasing the annealing temperature.

The optical transmittance spectra of various ITO films, annealed in different environments at varied annealing temperatures, are presented in Fig. 8.7. The annealing enhances the optical transmission of the films within the visible region (400-700 nm), where the colour was converted from dark brown to transparent. The average transmittances of ITO films annealed in air at 400°C, 500°C and 600°C are 55%, 58% and 70% respectively. As mentioned above the crystallinity of ITO films greatly depends

on the annealing temperature, therefore the increase in the optical transmittance could be relate to the enhancement in the crystallinity.

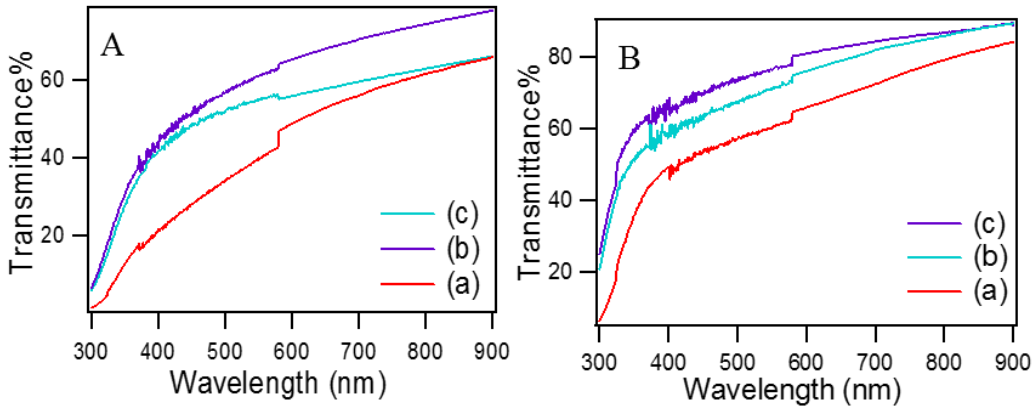

Figure 8.7 Transmission spectra of the of ITO films annealed in different atmospheres, (A) in air and (B) in argon, with varied annealing temperatures, (a) 400°C, (b) 500°C, (c) 600°C.

Moreover, films annealed in argon atmosphere show higher optical transmission compared to those annealed in air. The maximum transmittance of 85% was obtained at 600°C. These results could be assigned to the increase of structure homogeneity and film crystallinity at high temperatures.

The stability of the ITO solution was also studied by compare the film conductivity from aged stock solutions in order to establish the lifetime of the solution. It was found that the precursor solutions are stable up to a maximum two months. Fig. 8.8 displays the XRD patterns of the two films annealed in argon gas at 600°C for 2 hours.

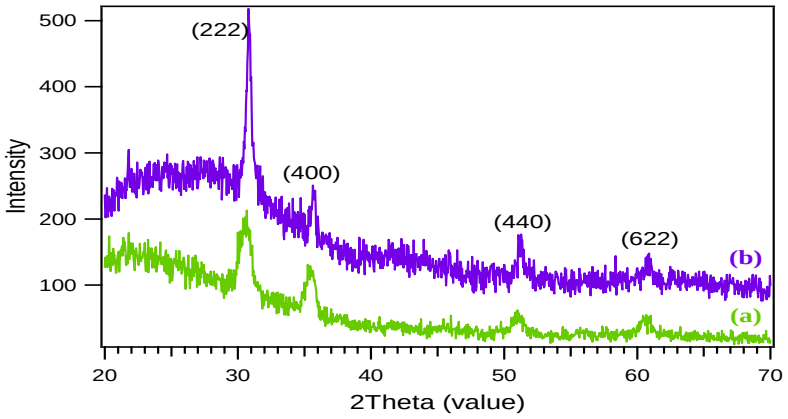

Figure 8.8 XRD patterns of ITO films formed; (a) after two months and (b) before two months of preparing the ITO coating solution.

The intensity of the ITO diffraction peaks significantly decreased after 2 months of preparing the starting solution. That was associated with an increase in the resistivity of the formed film, from 7.4×10^{-4} Ω.cm to 4×10^{-3} Ω.cm. This result could be attributed to the chemical decomposition of the ITO precursor solution after 2 months under air at 25°C.

8.5.1.2 Study the properties of ITO thin films deposited on glass rod substrate

Before the deposition of ITO film on the glass rod for preparing conductive glass rods substrate, the length of the rod should be chosen carefully. By using the three dimensional electrode as a photoanode in the PEC system, the photocurrent is measured in a special experiment set up. By directing the light towards the top of the electrode, the light will travel through the glass rods while emitting sideway to excite coated semiconductors. In order to optimize the length of the glass rods and provide more light to be absorbed by the film, residual light intensity was measured (using YK-35UV light power meter) at the end of rods with different lengths, I_m, (table 8.2). The side-emitted light intensity, I_c, can be evaluated from equation 8.3:

$$I_c = I_0 - I_m \quad \text{(Equation 8.3)}$$

where I_0 is the light intensity of the light source. Equation 8.4 gives residual light intensity percentage, P_m:

$$P_m(\%) = 100 \times I_m/I_0 \quad \text{(Equation 8.4)}$$

As shown in table 8.1, the residual light intensity through the glass rod substrate decreases with increasing rod length. In other words, by increasing the length of the glass rod, more light is side emitted. In the experiment, rods of 5 cm in length were initially used to form the electrode. At this length, 55.5% of the light is side emitted and can be absorbed by the coated film. With the glass rod length increases to 45 cm, 98.7% of the light is side emitted. There many factors affect the percentage of the residual light intensity travelling through the glass rods. The quality of the glass, such as high purity and less defects, can improve the light travelling. The initial intensity of the light source can also affect the travelling distance. Finally, the side emitting is strongly affected by the roughness of the glass rod wall. By increasing the roughness, the light travelling distance could be significantly reduced. In addition, by depositing a layer of metal oxide semiconductor, which normally has higher refractive index than the glass, the side emitted light will be increased. Overall, the ZnO nanorods film thickness and light absorption characteristics should match up with the side-emitting light intensity and length of the glass rods. The measurements reported in Table 8.1 are valid under my experimental conditions. The results form a practical guidance on the selection of glass rods dimension.

Table 8.1 Light intensity measurements through the glass rods substrate

Rod length (cm)	I_m (mw/cm^2)	P_m (%)
5	8.29	44.5
10	5.85	31.7
15	3.62	19.9
20	1.76	9.5
25	1.28	6.95
30	0.912	4.9
35	0.505	2.7
40	0.392	2.1
45	0.241	1.3

In order to make conductive glass rods to be used as substrate for the 3D electrode, a number of glass rods of 5 and 15 cm in length were dip coated with multiple ITO layers and preheated at 300°C for 10 minutes after each dipping. After that, the coated glass rods were annealed at 600°C for 2-10 hours, depending on the rod length. The relationship between the number of coatings of ITO solution and the resulted film resistivity and thickness is shown in Fig. 8.8. The resistivity of the ITO coated glass rods was measured from two point contacts with separation of *L*. The equation that used to calculate the resistivity is:

$$\rho = {}^{R2\pi rt}/_{L} \qquad \text{(Equation 8.5)}$$

Where *R* is the measured resistance, *r* is the radius of the glass rod and *t* is the ITO film thickness. Factor $2\pi rt$ gives the cross section area of the ITO. The measured resistivity ρ as a function of number of coatings is plotted in Fig. 8.9.

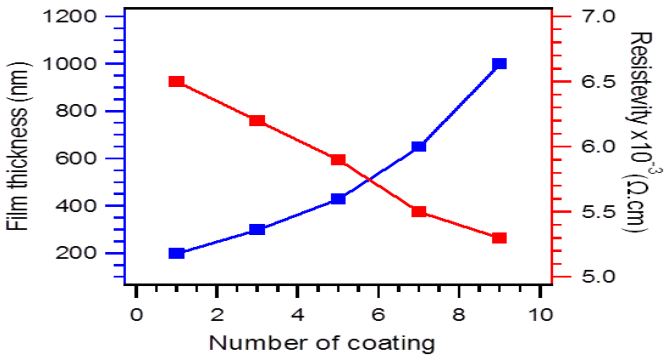

Figure 8.9 The number of the ITO coated layers as a function to the film thickness and resistivity.

It can be seen that the film thickness increases gradually with increasing the number of coatings, which is connected with the gradual enhancement in the electrical conductivity of the resulted film. The dip coating with 7 ITO layers results a film with comparable thickness to the film of nine layers deposited by spine coating technique. More important, the final achieved resistivity on the glass rods is similar to those achieved by spin coating on flat substrates. The coated glass rods show the dark brown colour, which requires long time, high temperature annealing to improve the optical transparency.

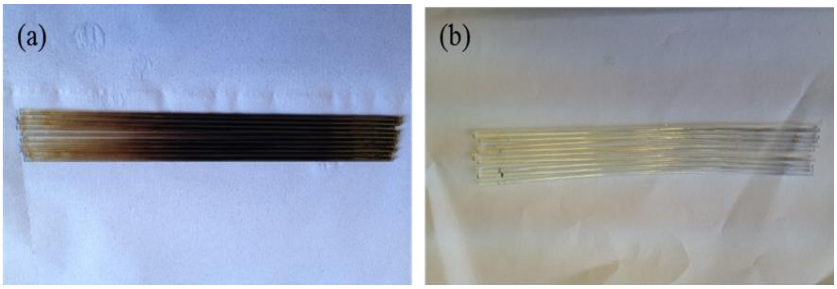

Figure 8.10 Glass rod of 15 cm coated with 7 layers of the ITO, (a) before annealing, (b) after annealing in argon at 600°C for 10 hours.

Photographs of dip coated glass rods, 15 cm in length, with 7 layers of the ITO are presented in Fig 8.10. Each layer dried at 300^{0}C for 10 minutes (Fig 8.10a). After that the film was post annealed at 600°C for 10 hours in argon gas (Fig 8.10b). These rods

became optical transparent and were used as substrates to grow ZnO nanorods film by the CBD method to form the 3-D electrode.

8.5.2 Study the growth of ZNRs on the conductive substrates

In order to obtain a homogenous dispersion of the seeding layer, the substrate cleanness is a crucial factor. The thermal treatment of the coated layer at 400°C is performed to remove PVA and convert the zinc acetate into ZnO nanocrystal seeds. The growth process of ZNRs is more facile when it is carried out on a nanoparticle-seeded substrate. The growth solution consists of an aqueous solution of equal molar zinc nitrate and hexmethylene tetramine (HMT). The growth reactions of the ZNRs are listed below:

$$(CH_2)_6N_4 + 6\,H_2O \rightleftharpoons 4NH_3 + 6\,HCHO \qquad \text{(Equation 8.6)}$$

$$NH_3 + H_2O \rightleftharpoons NH_3.H_2O \qquad \text{(Equation 8.7)}$$

$$NH_3.H_2O \rightleftharpoons NH_4^+ + OH^- \qquad \text{(Equation 8.8)}$$

$$Zn^{2+} + 2OH^- \rightleftharpoons Zn(OH)_2 \qquad \text{(Equation 8.9)}$$

$$Zn(OH)_2 \rightarrow ZnO + H_2O \qquad \text{(Equation 8.10)}$$

The HMT acts as a weak base to produce OH^- and NH_4^+ ions, through the thermal reaction with water (Equations 8.6 to 8.8). At high pH, Zn^{2+} will be hydrolysed into $Zn(OH)_2$ which will be then deposited onto the nucleation sites, building up the ZNRs (Equations 8.9 and 8.10). The balance between the precipitation rate and the growth rate is the key for the formation of good quality of ZnO crystals. Thus, the decomposition of HMT plays an important role in the growth of ZNRs. The properties of the formed film can be controlled by adjusting the reaction parameters, such as the concentration of the growth solution, temperature and time. While the precursor concentration defines the film

density, rod diameter and film thickness are affected by temperature and time variables. The SEM images in Fig. 8.11 show successful growth of ZNRs film through CBD on seeded glass rod substrate. The film grown in 100 ml of the growth solution at 84°C for 20 hours.

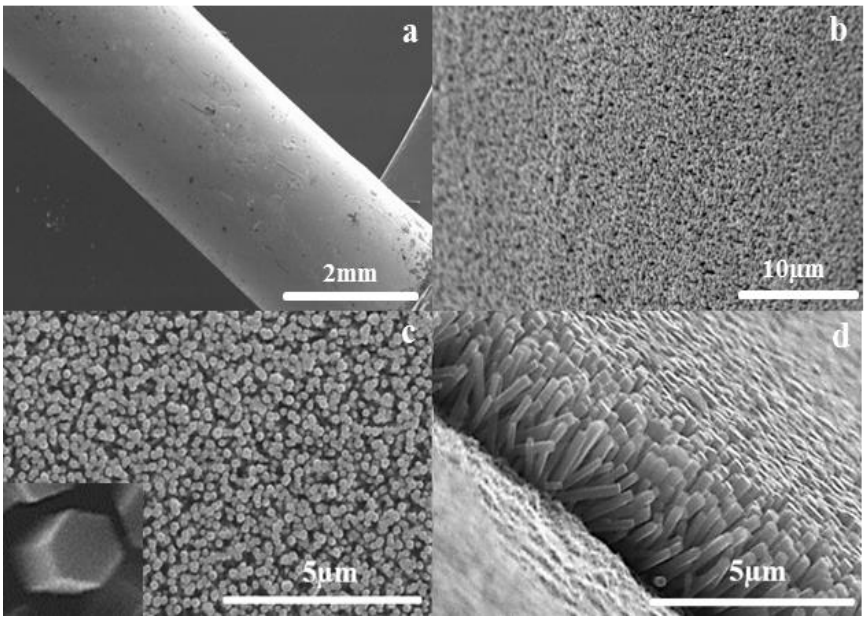

Figure 8.11 SEM images of zinc oxide nanorods grown on glass rod substrate; (a) low magnification of the coated glass rod with ZNRs film, (b and c) top views of ZNRs with different magnifications and (d) the cross section.

The glass rod substrate was covered with a homogeneous layer of ZNRs with an average diameter of 250 nm and a length of 3.5 μm (Fig. 8.11a and b). The nanorods are hexagonal shaped and vertically aligned on the surface of the glass rod substrate (Fig. 8.11c). The vertical growth of the ZnO crystal is related to the high reactivity of the (002) face. This face allows the 1-D growth along the c-axis. Fig. 8.11d shows the cross section. The crystal structure and orientation of the as-grown ZNRs were studied by powder XRD on a flat Ti and glass rod substrates, shown in Fig. 8.12.

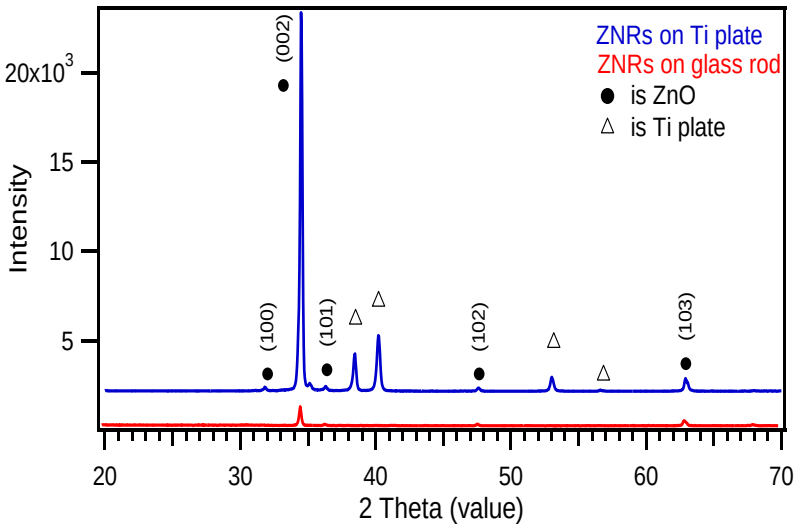

Figure 8.12 The XRD pattern of the zinc oxide nanorods synthesis by CBD method on Ti plate and glass rod substrates.

From the pattern it can be demonstrated that a crystalline zinc oxide phase is formed. After subtracting the diffraction peaks from the titanium substrate, which are located at 38.6° , 53.35° and 40.27°, another five XRD peaks were observed and indexed to the wurtzite hexagonal ZnO (JCPDS #36-1451) [275]. The diffraction peaks of the hexagonal ZnO are centred at 2θ of 31.94°,34.51°, 36.36°, 47.67° and 63.21°. These peaks are corresponding to crystal planes of (100), (002), (101), (102) and (103) respectively. The peak centred at 34.51° corresponding to the (002) plane dominates the spectrum, indicating that the ZnO nanorods are highly oriented along the c-axis perpendicular to the substrate with the [0001] being the most favoured growth direction for the 1-D ZnO nanocrystal. The glass rod substrate showed the same XRD pattern, however, the peaks intensity is significantly lower than that of the film grown Ti plate. That could be related to the less surface of the glass rod is available to be detected by the XRD beam.

8.5.3 The application of 3-D electrode in the water splitting process

Vertically aligned ZNR films, of 3.5 μm in thickness, were grown on conductive glass rods substrates. As shown in Fig. 8.13, two of 3-D electrodes were assembled by installing 30 glass rods with lengths of either 5 cm (Fig. 8.13a) or 15 cm (Fig. 8.13b). The number of the glass rods was determined by considering the diameter of the glass rods, the illumination light source projection area and the relative easy for assembly. The photocurrent measurements of the three dimension photoanodes were studied with the 3-D photoanodes immersed in the electrolyte. To avoid the photo-oxidation of copper plates, the upper plate was positioned above the electrolyte, while the bottom supporting copper plate was removed together with the metal fixing. As the silver epoxy was cured, the 3-D electrode structure is rigid enough to be self-supported on the top copper plate.

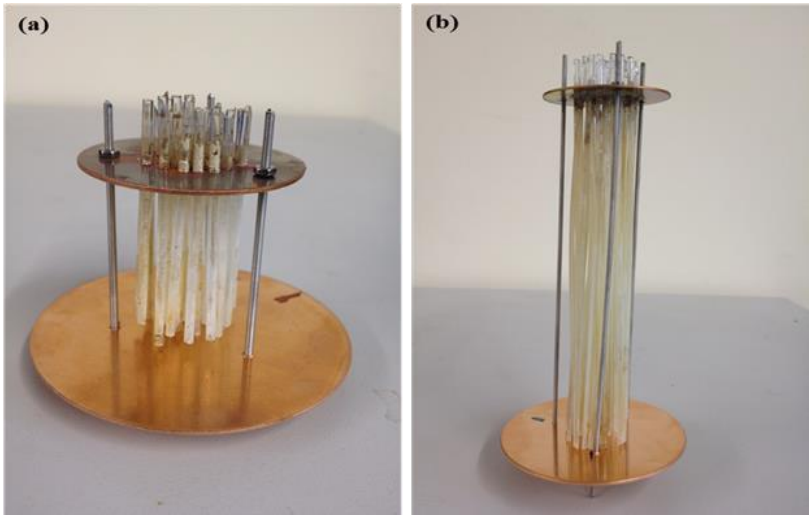

Figure 8.13 Pictures of three dimension electrodes for PCE system using glass rod substrates with different length. (a) 5 cm and (b) 15 cm.

The photocurrent measurements were performed at room temperature using a home built cell in two configurations. The measurements were taken by illuminating the electrodes from different angles, top and side illuminations. That was carried out in order to study the effect of side illumination on the photocurrent generation.

8.5.3.1 The effect of the side illumination of the photoelectrode on the photocurrent density

Fig. 8.14 shows the generated photocurrent from the side illumination of the electrode, which is made of assembling 30 glass rods of 5 cm and decorated with zinc oxide nanorods of 3.5 µm in thickness. A Pt foil was used as the counter electrode and KCl saturated Ag/AgCl electrode was used as the reference electrode.

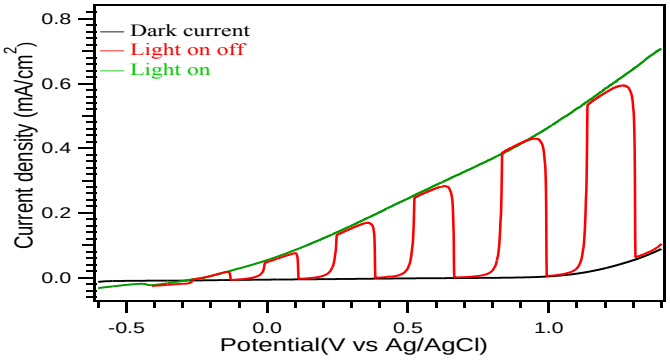

Figure 8.14 I-V curve for the side illumination of the electrode, made of assembling 30 glass rod of 5 cm in 1M KCl pH = 6.7.

The black curve represents the dark current and the green curve represents photocurrent measured as a function of the electrochemical potential in 1M KCl (pH = 6.7). The photocurrent with illumination alternating on and off is shown in the red curve. Without light, the detected current between the electrochemical potential of -0.4 and 1.2 is almost zero. Conversely, the side illumination of the three dimensional electrode produces photocurrent density increases gradually to reach maximum of 0.42 mA/cm^2 at 1.0 V vs Ag/AgCl. The electrochemical potential was linear ramping up from -0.6 V to 1.4 V vs Ag/AgCl at a rate 0.2 V/s. By switching the light on, as well switching the light off, photocurrent shows a slow increase or decrease in time. This is due to the limited charge transportation through the ITO film as a result of difficult to deposit a homogeneous ITO film on large surfaces (long glass rods). Thus there forms a charge

capacitance between ZNRs and the copper collector. Such behaviour was more obvious for longer glass rod. This technical challenge could be overcome with improvement on the quality of ITO coating and on the contact between ITO and copper collector. Such capacitance could accumulate charges and therefore increase the charge recombination.

8.5.3.2 The effect of the top illumination of the photoelectrode on the photocurrent measurements

The photocurrent density yielded by illuminating the reactor from the top is presented in Fig. 8.15, in comparison with that produced by the side illumination of the same electrode.

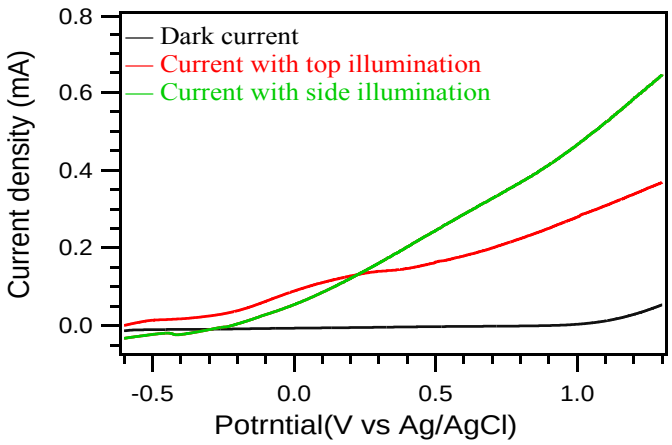

Figure 8.15 Photocurrent measurement of the top and side illuminated electrode that made of assembling 30 glass rods of 5 cm.

It was assumed that, by illuminating the top side of the 3-D electrode, the light travels through the glass rod substrate and is side emitted to ZNRs with massive surface area in contact with the electrolyte. Therefore, the total absorbed light was expected to increase and so was the photocurrent efficiency. However, according to Fig. 8.15, shining light from the top of the electrode yields lower photocurrent density compared to the side illuminated electrode. Similar behaviour was shown by the second electrode that was

assembled by accumulating 30 glass rods of length 15 cm. This could be attributed to two reasons: Firstly, the top illumination of the 3-D electrode provides a back side illumination for the ZNR film coated on the glass rods surface. The back side illumination always results in lower photocurrent density than the front illumination [285]. This is due to the defects in the block layer underneath the ZNR films, where the electron hole recombination rate is relatively fast and increases by increasing the layer thickness. Secondly, the detected UV light from the outer side of the uncoated glass rod was very low. This indicates side emission is less effective than expected, although the situation might change once the glass is coated with metal oxide. Also, for short glass rods (5 cm), significant amount of light intensity (55.5%) will travel through along the longer axis of the rod. This situation can be improved by either roughening the surface of the glass rods to create multiple surfaces scattering, or by increase the length of the glass rods. However, simply increase the rod length will suffer the limitation of the charge transportation along the glass rods.

Thus, two strategies were chosen to improve the light side emission: by roughing the surface of the glass rods and by creating a slant, cone shaped termination. The surface of the rods was roughened using wet and dry paper (P800 grit). The cone shaped rod tip was also created by ground the glass at an angle of about 45°. This shape could help to reflect most of the illuminated light back along the glass rod for a second pass, rather than travelling through the flat end and exiting the glass rod. The modification steps on the glass rod substrates and their assembly into 3-D electrodes without the semiconductor thin film are shown in Fig. 8.16.

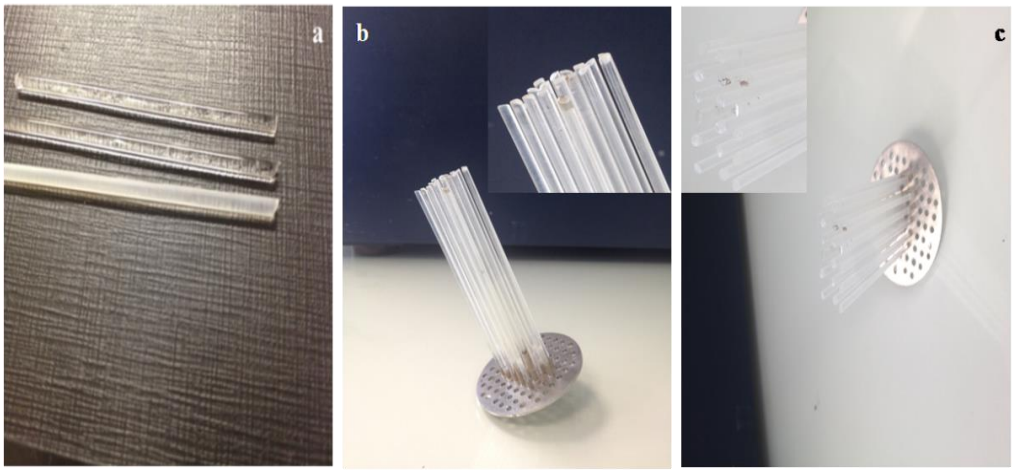

Figure 8.16 Pictures of the glass rod substrates with different modification stages. (a) Flat tip with smooth wall (upper), slant tip with smooth wall (middle), slant tip with rough wall (lower). (b and c) three dimension electrode for PCE system using 18 modified glass rod substrates with 10 cm length before the deposition of ZNR film. Insets in (b and c) show high magnification of the electrodes tops.

To examine the effect of the electrode modifications on the water splitting performance under top illumination, three electrodes were assembled by accumulating 18 glass rod substrates of 10 cm in length with different modification steps. Here, the glass rods have a larger diameter of 3 mm. This is because we found that previous 2 mm diameter glass rods are too fragile for the mechanical process to roughen the surface and to ground into a slant tip. Then the total number of the glass rods was consequentially reduced to 18. Three different electrodes were tested in their PEC performance. Electrode A was made of 18 glass rods with smooth wall and flat ends, while electrode B was made of 18 glass rods with smooth wall but slant ends and electrode C was made of 18 glass rods with rough wall and slant ends. The length of the glass rods was all 10 cm, which has 31.7% light travels to the end. Their water splitting abilities were carried out under the same conditions with top illumination and the results are shown in Fig. 8.17.

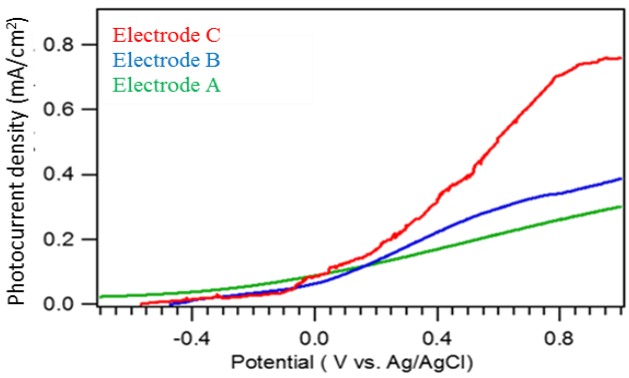

Figure 8.17 Photocurrent measurement of the top illuminated electrodes that were made of assembling 18 glass rods of 10 cm with different modification steps (Electrode A, B and C).

Fig 8.17 shows the photocatalytic performance of the three electrodes under top light illumination. Electrode A generated a maximum photocurrent of 0.3 mA/cm^2 at 1V vs Ag/AgCl. The achieved photocurrent increased to 0.4 mA/cm^2 by using electrode B, which has the slant tip to create the light reflection at the end. The reflected light could increase the overall absorbed light by the thin film. More importantly, the generated photocurrent (0.75 mA/cm^2) was doubled by using electrode C, which has a roughened surface and slant tip. The roughness of the glass wall allows more light to be scattered and emitted from the glass wall, providing more light for the thin film to absorb. The results suggest that the control of the light side emission is essential for improving the PEC efficiency from a 3-D electrode, although the current design is not fully optimised.

8.5.3.3 The use of organic compounds to enhance photocurrent response

Organic molecules can often be used as hole scavengers to improve the hydrogen generation. In the photocatalytic hydrogen generation process, the oxidation of water into O_2 is usually the rate limiting step, since each O_2 molecule will need 4 electrons. Thus the reaction normally requires activation energy to overcome the reaction barrier. By using organic molecules as the hole scavenger will reduce such energy barrier and

improve the generation of hydrogen. Here, the experiment was carried out to investigate the effect of adding an alcohol to the electrolyte in the PEC system. Methanol was used as an organic additive into the electrolyte and electrode C was used as the anode. The addition of methanol (0.5, 1.0 or 1.5 ml) to 300 ml of aqueous KCl (1 M) drives a gradual enhancement in the measured photocurrent density, as shown in Fig. 8.18. Without the addition of methanol, the photocurrent density was 0.75 mA/cm2 at 1V vs Ag/AgCl. By adding 0.5, 1.0 and 1.5 ml of methanol, the photocurrent densities were obtained for 0.85, 1.2 and 1.8 mA/cm^2 at 1V vs. Ag/AgCl, respectively.

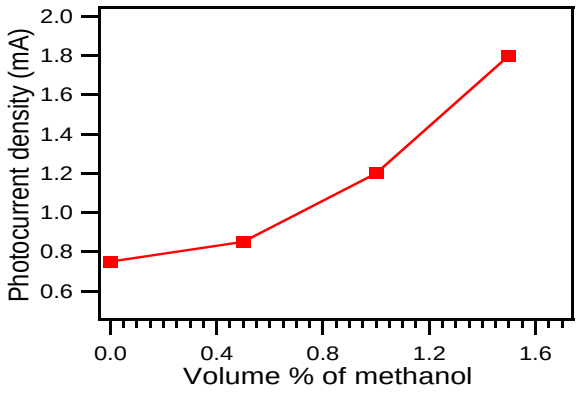

Figure 8.18 The effect of the addition of methanol on the photocurrent density using a reactor of 30 glass rods, each 10 cm in length.

As a hole scavenger in water splitting reactions, when methanol was added to the reaction, holes can be consumed more efficiently at the anode, producing H^+ ions by oxidising the organic compound and water molecules, as presented in equations 8.11 and 8.12:

$$CH_3OH + H_2O + 6h^+ \rightarrow CO_2\,(g) + 6H^+\,(aq) \qquad \text{(Equation 8.11)}$$

$$6H^+ + 6e^- \rightarrow 3H_2\,(g) \qquad \text{(Equation 8.12)}$$

This process contributes to reducing the electron-hole recombination phenomenon. Subsequently, the hydrogen productivity at the cathode will increase. The use of methanol as the hole scavenger is a relatively efficient process compared with direct oxidise H_2O. This is due to that the oxidation of methanol requires less electrochemical potential for the holes and therefore will require less over potential. The direct oxidation of water in the photolysis process is always the rate limiting process, which requires 4 electrons to complete. When the holes in the VB in contact with water and methanol, it will always oxidise methanol first. The oxidation of methanol will follow a multistep process forming intermediates like formaldehyde and formic acid, then decomposed into CO_2 and H_2O. Such oxidation process requires less energy from the holes and therefore is more kinetically favourable.

8.6 Conclusion

In this chapter, the design, fabrication and application of a three dimensional photoelectrode for water-splitting systems was introduced. The electrode was made by assembling conductive glass rod substrates with lengths of 5, 10 and 15 cm to a copper or a stainless steel disc. The conductive rods were prepared by depositing a film of Indium tin oxide (ITO) by the sol-gel method onto standard glass rods. The sheet resistivity was found to be influenced by the film thickness, annealing temperature and annealing atmosphere. A minimum resistivity of 7.4×10^{-4} Ω.cm, with transmittance of 85%, was achieved by forming an ITO film with the thickness of 500 nm calcined at 600°C in argon gas for 2 hours. The conductive glass rods were then decorated with a thin film of ZnO nanorods, 3.5 μm thick, and used as a photoanode in a PEC system. The photocurrent density was influenced by the direction of the light illumination. For top illumination, the shape of the glass rod tip and the wall roughness will significantly affect the PEC

performance. By shinning the light from the top of electrode, the photocurrent is almost half the measured current from illuminating the side of the electrode. However, this was improved by increasing the roughness of the glass wall and cutting an angle at the end of the glass rod. It was also found that the obtained photocurrent, whilst illuminating the top of the electrode, could be further increased from 0.75 mA/cm^2 to 1.8 mA/cm^2 when 1.5 ml of methanol was added into 300 ml the electrolyte.

Chapter 9 Synthesis and Characterization of Copper Titanate Single Crystal

9.1 Abstract

This chapter investigates the preparation and characterisation of crystallised copper titanate. Copper titanate was synthesised for the first time by molten salt synthesis method (MSS). The effect of the synthesis conditions on the morphologies, structures and properties of the formed products was investigated. The products were characterized by Powder X-ray Diffraction (XRD), Scanning Electron Microscope (SEM) and Energy Dispersive X-ray spectroscopy (EDX). High yield of large perovskite copper titanate $CuTiO_3$ crystals with cubic morphology were prepared by heating a mixture of equal molar ratio of CuO and TiO_2 using NaCl salt as flux at the temperature above 805°C.

9.2 Introduction

TiO_2 powders, including anatase, rutile and their mixture (P25), are considered as excellent photocatalysts for photocatalytic reactions [118]. They have been attracted a great attention due to their promising applications in photocatalytic degradation of pollutants and solar energy conversion. However, due to their large band gap, their photoexcitation is restricted in the ultra-violate region, which represents less than 5% of the solar radiation [286]. In order to improve the photoreactivity of TiO_2 and to extend its absorption edge into the visible-light region, doping of various transition metal cations has been intensively investigated. The doping of cation will form band gap states near the conduction band. Alternatively, anions, such as C, N and S can also be doped into TiO_2, which creates band gap states above the valence band. Both cation and anion doping, or the combination of them, can effectively reduce the band gap. However, the doping will also generate defects

and reduce the crystallinity, when the dopant concentration is increased significantly. This could cause the reduction of charge mobility and increase in charge recombination.

On the other hand, many transition metal oxides have small band gaps and capable to absorb visible lights. For photocatalytic water splitting, the water reduction equilibrium potential is about 0 V vs NHE and the water oxidation equilibrium potential is about 1.23 V vs NHE. Thus a band gap 1.23 eV would be needed. With consideration of reaction energy barrier and internal energy lost, an ideal band gap should be around 2.0 eV, as far as the conduction band minimum is more negative than 0V vs NHE and the valence maximum is more positive than 1.23 V. Many transition metal oxides have suitable small band gaps allowing visible light excitations, however they also suffer from chemical instability. Corrosion and dissolution can easily happen to destroy the nano morphology.

Copper oxide exists in two stable forms namely, CuO and Cu_2O with a direct band gap in each case. The band gap can be tuned between 1.6 eV (CuO) to 2.3 eV (Cu_2O) [287]. To overcome the chemical stability problem, it can be used as dopant for TiO_2, although the dopant concentration will be limited. Alternatively, binary metal oxide system consisting of CuO and TiO_2 can be synthesised. The advantage of using binary metal oxide, such as titanate, is that it can have the small band gap determined by the CuO, while maintaining the chemical stability inherited from TiO_2. The surface of the titanate nanomaterials might decompose under acidic or alkaline conditions. But the resulting TiO_2 will form a layer of coating which protects the morphology of the nanomaterials.

Some copper titanate species have been synthesised at high temperature. Hexagonal crystal structure of Cu_3TiO_4 were synthesised by heating the mixture of Cu_2O, CuO and TiO_2 (mole ratio 1:1:1) at 1050°C in air. The Cu_3TiO_4 contains 2 of Cu^+ and 1 of Cu^{2+} cations. Since Cu_3TiO_4 can decompose to CuO and TiO_2 in the temperature range

600～900℃, the reaction product needs to be rapidly cooled. On the other hand, $CuTiO_3$ has not been successfully synthesised even at higher temperature.

Various methods have been developed to prepare the titanate ceramic powder, such as high-energy ball milling [288], chemical co-precipitation [289], hydrothermal [290], solid state synthesis [291] and sol-gel [292]. The molten salt synthesis (MSS) method is a well-established low temperature synthesis technique that has recently attracted increasing interest for the preparation of titanate ceramic powders [293, 294], in which the molten salt is used as ionic solvent (flux) to assist the dissolution and precipitation of reactants and products. The features of this synthesis method are related to the surface and interface energies between the constituents and the salt, resulting in a tendency to minimize the energies by forming a specific morphology. The resulted powder morphology and characteristics are affected by the preparation conditions, such as the type of salt, the precursor composition, the initial particle size and the solubility of the constituents in the salt. Because of the MSS method is versatile, reliable, and cost effective and requires relative low temperature, it is attractive for commercial production of nanostructured complex oxides.

In the present work, copper titanate crystals $CuTiO_3$ (CTO) with cubic morphology was prepared for the first time, by using MSS method. With conventional solid state synthesis method, heating the reactant mixture ($CuO+TiO_2$) directly at high temperature, $CuTiO_3$ was failed to form even with temperature higher than 1000°C. Therefore, we developed the MSS to assist the formation of $CuTiO_3$. The reaction was carried out in an alumina crucible. Alumina was chosen for its high thermal and chemical stability. NaCl salt with a melting point of 801ºC was used as reaction media. Other salt, such as KCl was also tested for the MSS synthesis of $CuTiO_3$. The reactions were

performed in a laboratory furnace with a temperature ramping system in order to control the heating and cooling processes.

9.3 The experimental procedure

9.3.1 Synthesis

The starting materials were simple oxides. TiO_2 (Sigma Aldrich, 99.98% anatase) and CuO (Sigma Aldrich, 99.9%) were selected as the reactants while NaCl (Sigma Aldrich, 99.9%) was selected as the flux due to its low melting point (MP) of 801°C. In order to exam the effects of stoichiometry ratio on the structure and morphology of the product, different molar ratio of 0.5, 0.6, 0.8, 0.9 and 1 of CuO to the TiO_2 were mixed for 20 min in a pestle mortar with drops of acetone. The salt was ground separately until smoother finish. Oxides mixture and NaCl were mixed before were introduced into aluminium crucible. The crucible was then covered and annealed at 960°C for 10 hours. Subsequently, the molten mixture was slowly cooled down to room temperature inside the furnace in order to increase the obtained crystal size. The residual NaCl salt was removed by washing using (DI) water several times until no Cl^- ion remained in the washing solution. The Cl^- content of the solution was detected by the use of silver nitrate of 0.1M. Finally, the obtained powder was dried at 85°C. The effects of different factors, such as the annealing temperature (805, 850 and 960°C) and time (from 6 hours up to 5 days), on the crystallinity and morphology of copper titanate were investigated.

Appropriate amount of salt is required which determined by the need to fill the interstices of reactant particles and coat their surface to prevent the particle aggregation. Lower amount of salt leads to decrease the dissolution of the reactants due to the lack of solvent, that would be associated with reduce the reactant motilities, therefore the reaction and growth rates are decreased. On the other hand, higher amount of salt causes high

separation of the reactant participles subsequently, the growth rate is decreased. In this work, high yield of copper titanate was obtained by using (1:1 w %) of oxides: NaCl in all the experiments.

9.3.2 Structure characterization

The resulting powders were characterized by X-ray diffraction (Siemens D500). The morphology of the powder was observed by scanning electron microscope (SEM-Jeol JSM 820M, operating at 30 keV). The chemical compositions of the samples were detected by an energy dispersive X-ray spectrometer (EDX).

9.4 Results and discussions

9.4.1 Study the effect of preparation factors on the copper titanate productivity

The effects of MSS synthesis conditions on the formation and purity of $CuTiO_3$ will be investigated in order to understand and optimise the growth process. In the following sections, the role of the molar ratio of the oxides mixture, reaction temperature, reaction time, the product stability and the salt composition were discussed.

9.4.1.1 The effect of the molar ratio of the oxides mixture

As compounds with higher molar ratio between Cu and Ti, such as Cu_3TiO_4 and Cu_3TiO_5, is thermodynamically stable and can be readily synthesised, we try to reduce the Cu contents to see whether it is possible to obtain pure $CuTiO_3$ phase. Different amount of CuO were reacted with 1 molar ratio of TiO_2 at controlled molar ratio from 0.5 to 1. The X-ray diffraction patterns of CuO and TiO_2 powder mixtures calcined at 960ºC for 10 hours with NaCl as flux are shown in Fig. 9.1.

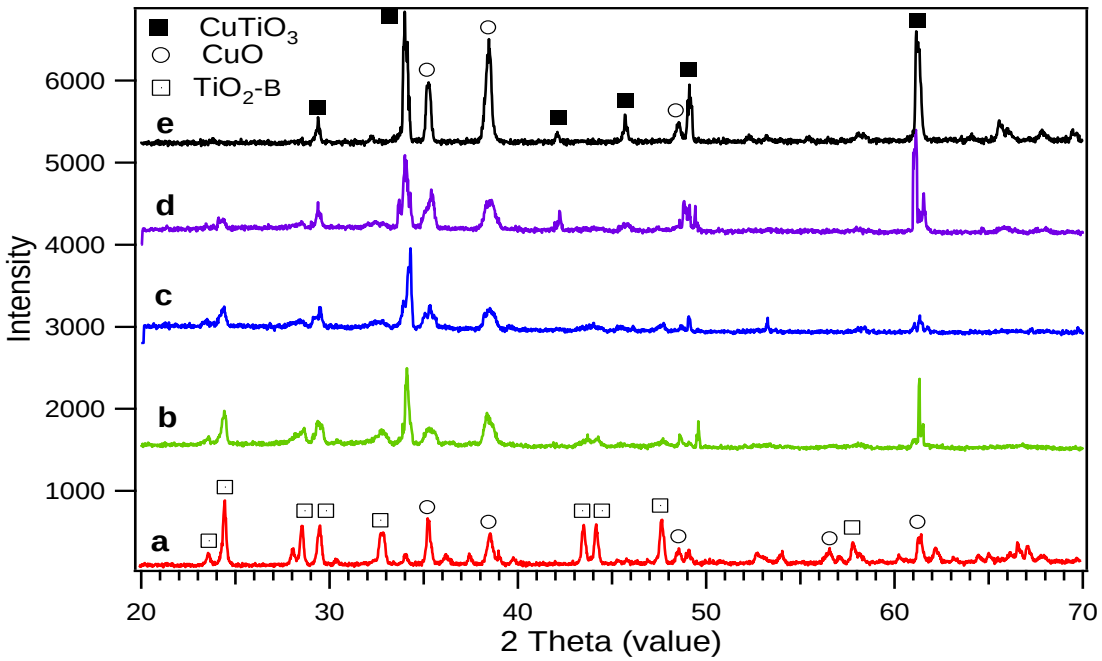

Figure 9.1 X-ray patterns of the samples annealed at 960^{0}C for 10 hours and synthesised with NaCl salt in weight ratio of (1:1) using different oxides molar ratio mixed of CuO:TiO_2. (a) (0.5:1), (b) (0.6:1), (c) (0.8:1), (d) (0.9:1) and (e) (1:1).

As shown in Fig. 9.1, at different CuO: TiO_2 molar ratio, there were some residual un-reacted materials. Five diffraction peaks located at 2θ of 35.49, 38.68, 48.65, 56.64 and 61.45° were observed in this sample (red curve). These peaks are indexed to the monoclinic CuO crystal structure (JCPDS No 080-1916) and correspond to the (-111), (111), (-202), (021) and (-113) planes respectively. Other eight diffraction peaks cantered at 2θ of 23.75, 24.98, 28.59, 29.79, 33.24, 43.49, 44.61 and 57.39°. All these peaks were indexed to monoclinic titanium oxide in the form of TiO_2-B with main diffraction peak at 24.3° (JCPDS No 074-1940). These peaks correspond to (201), (110), (002), (-401), (310), (003), (-601) and (022) crystal planes respectively. The TiO_2-B is a less known metastable phase of TiO_2. It could be formed as result of the reaction between the excess of anatase with the NaCl forming sodium titanate (Na_2TiO_3). The sodium titanate converts to (H_2TiO_3) then TiO_2-B through washing and drying (dehydration) processes respectively. With increasing the CuO contents, new diffraction peaks were observed at

2θ of 29.55, 34.32, 45.89, 49.33 and 61.3°, which could be related to the copper titanate product. These peaks cannot be indexed to any structure of TiO_2 or CuO according to JCPDS standard spectrum. As this is first time to synthesise $CuTiO_3$, there is no standard spectrum in the JPCD database (Joint Committee on Powder Diffraction Standards) for direct comparison and the quantitative phase analysis became difficulty. The XRD reading of the diffraction peaks observed in all patterns of the samples at different reactants compositions are summarised in table 9.1.

It can be seen that, the main component of the sample prepared by mixing (0.5:1) is the TiO_2-B with high percentage of un-reacted CuO (red coloured column of the table). By increasing the copper oxide in the mixture, the residual TiO_2 was decreased and disappeared while the yielded copper titanate was increased (green coloured column of the table). The only impurity presented is the unreacted copper oxide. With (1:1) Cu: Ti molar ratio, the final product always gives higher Cu contents with residual CuO. It was found that Al_2O_3 can also react with TiO_2 to form Al_2TiO_5 ceramic. As we are using alumina crucible, this reaction can also happen on the surface of the crucible, the formed Al_2TiO_3 could be firmly attached to the crucible, which could explain the loss of Ti.

Table 9.1 The diffraction peak position and relative intensities of the product at different oxides molar ratio mixed of CuO:TiO_2.

TiO_2-B					
standard	Sample (0.5:1)	Sample (0.6:1)	Sample (0.8:1)	Sample (0.9:1)	Sample (1:1)
24.98 (100%)	24.52 (100%)	24.41 (48.7%)	24.39 (26.5%)	24.09 (13%)	24.3 (7.5%)
28.59 (50.6%)	28.64 (60.0%)	28.64 (19.3%)	28.34 (6.71%)	28.51 (4.4%)	-
29.79 (34.7%)	29.61 (57.8%)	29.61 (24.5%)	29.49 (23.2%)	29.35 (18%)	-
33.24 (15.6%)	32.99 (43.9%)	32.80 (15.6%)	32.65 (7.01%)	32.23 (3.8%)	32.21 (4%)
43.49 (27.9%)	43.61 (59.2%)	43.53 (7.63%)	43.94 (6.44%)	-	-
44.61 (23.4%)	44.2 (56.8%)	44.2 3(10.8%)	-	-	-

CuO					
standard	Sample (0.5:1)	Sample (0.6:1)	Sample (0.8:1)	Sample (0.9:1)	Sample (1:1)
35.49 (95.5%)	35.3 (65.88%)	35.21 (20.0%)	35.33 (19.5%)	35.44(34.5)	35.29(30.6)
38.68 (100%)	38.64 (47.9%)	38.3(42.42%)	38.58 (23.1%)	38.64(26.9)	38.5(23.4)
48.66 (28%)	48.67 (20.1%)	48.6 (14.76%)	47.7 (8.40%)	-	-
56.64 (0.8%)	56.66 (19.4%)	-	-	-	-
61.46 (18.2%)	61.51 (43.3%)	61.51 (34.5%)	-	-	-
New peaks					
	Sample (0.5:1)	Sample (0.6:1)	Sample (0.8:1)	Sample (0.9:1)	Sample (1:1)
	-	29.6(24.48)	29.49(26.2)	29.35(18.6)	29.55(17.9)
	34.13(65.88)	34.11(100)	34.31(100)	34.28(35.5)	34.3(100)
	-	-	45.4(4.62)	45.8(5.64)	45.7(21.02)
	49.3(18.33)	49.6(25.44)	49.06(18.1)	49.11(26.5)	49.5(25.37)
	61.35(36.6)	61.3(94.03)	61.33(20.8)	61.15(100	61.35(69.1)

The Cu:Ti ratio in the product was analysed by EDX. The EDX analysis of the crystals synthesised using (1:1) molar ratio of CuO to TiO_2 is shown in Fig. 9.2. It confirms that, the chemical composition of the crystal is exclusively composed of Cu and Ti with average molar percentage of (50.76%) and (49.24%) respectively, which is almost in the 1:1 ratio and there is no evidence of Na^+. Therefore, the formed product could be $CuTiO_3$. Oxygen cannot be detected by our EDX analysis, since a Be window was attached to the EDX. Elements light than Na cannot be detected unless the Be film is replaced with thin polymer window.

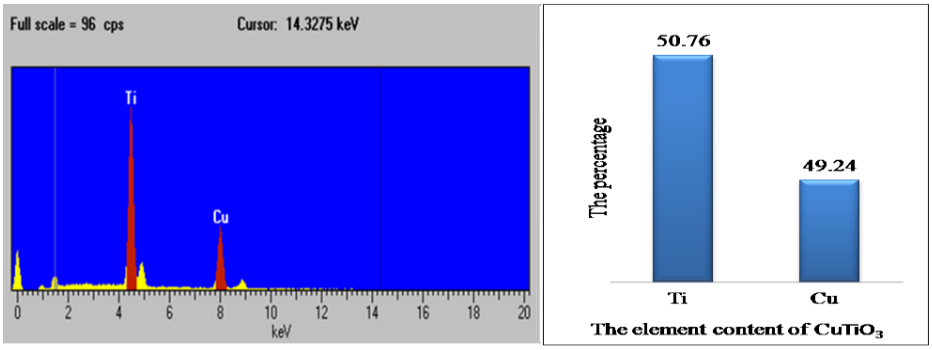

Figure 9.2 The EDX analysis of the crystals synthesised using (1:1) molar ratio of CuO to TiO_2 mixed with NaCl salt in weight ratio of (1:1)and heated at 960ºC for 10 hours .

$CuTiO_3$ has a typical perovskite structure with the general chemical formula of ABX_3, where A and B are two cations of different sizes. If cation A is larger than cation B and X is an anion that bonds to both, the typical crystal structure of cubic ABX_3 consists of corner sharing $[BX_6]$ octahedral with the A cation occupying the 12-fold coordination site formed in the middle of the cube surrounded by eight octahedral in the corners. This structural family of perovskites is related to the mineral $CaTiO_3$. The proposed crystal structure of the perovskite copper titanate $CuTiO_3$ is presented in Fig. 9.3, where the Ti^{4+} occupies the octahedral corner, while the Cu^{2+} sits in the middle of the unit cell. Normally, cations in the octahedral are much smaller than the cation in the middle of the cubic. However, for $CuTiO_3$, the radius of Cu^{2+} (0.073 nm) is similar to that Ti^{4+} (0.069 nm).

Therefore, the structure of $CuTiO_3$ is expected to be thermodynamically unstable and is difficult to be formed by conventional synthesis methods, such as sole-gel or solid state synthesis.

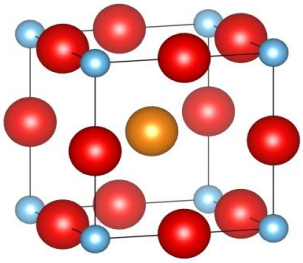

Figure 9.3 Proposed crystal structure of the produced copper titanate $CuTiO_3$. Ti (blue), Cu (yellow) and O (red).

In principle, the PXRD spectrum can be analysed to confirm the proposed perovskite structure, using Rietveld refinement analysis. However, currently, the fitting software is not available in the group and we are looking for external collaboration to resolve the crystal structure of the $CuTiO_3$.

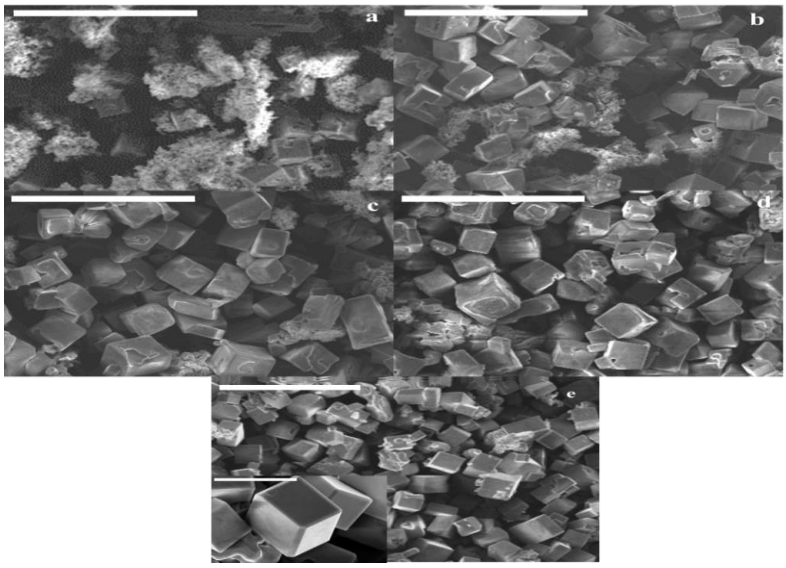

Figure 9.4 SEM images of the copper titanate derived by mixing different molar ratio of the CuO, (a) 0.5, (b) 0.6, (c) 0.8, (d) 0.9 and (e) 1 with 1 molar ratio of TiO_2 respectively. Scale bar in the main images is 200 µm and inset 50 µm.

The morphologies of the synthesised product as a function of initial CuO contents are shown in SEM images in Fig. 9.4.

It is obvious from these images that; the cubic crystals were clearly formed with increasing the copper oxide's molar ratio. At lower CuO contents, many powder and particular materials were observed, which are the mixture of TiO_2 and CuO, possibly dominated by the TiO_2-B. As this product could be formed in the washing process, the powder morphology was expected. For the large cubic crystals, there were many surface defects and irregularity observed on the surface facets at medium Cu contents. Meanwhile, the size of the cubic crystal was not affected by the change of the molar ratio of the starting chemicals. The average size is about 47-50 μm. At high Cu:Ti ratio, only small amount of particular materials is left, which is formed by CuO, as indicated from XRD study.

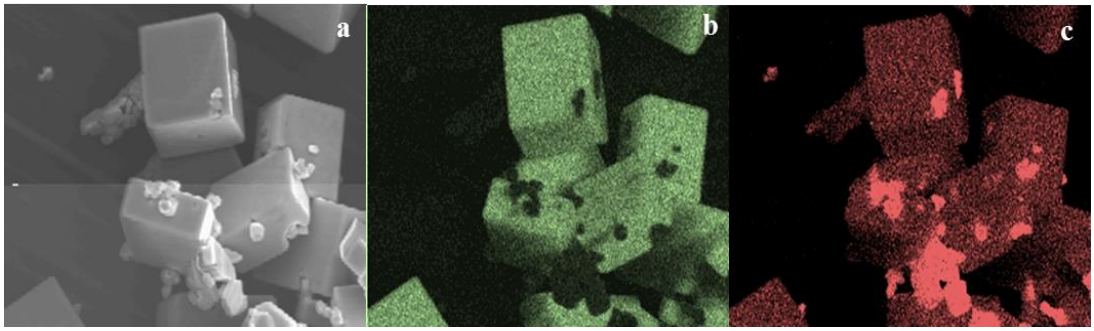

Figure 9.5 Mapping scan images of the $CuTiO_3$ product; (a) the normal SEM scan, (b) the Ti Constance in the cubic body and (c) the Cu Constance in the cubic body and in the uncreated CuO.

The atom components of the cubic crystal were further identified by EDX mapping in SEM. Fig. 9.5a shows a zoomed topography image of the cubic crystal with some small particles. The Ti mapping is shown in Fig. 9.5b. It shows that the Ti cations are evenly distributed in the cubic crystal and the small particles contain no Ti at all. Meanwhile, the Cu cation mapping is shown in Fig. 9.5c, which shows an even

distribution in the cubic crystal and highly concentrated on the particles. Therefore, it confirms that the small particles were formed by CuO while the cubic crystals were formed by $CuTiO_3$, which is consistent with our XRD observation. The stoichiometric ratio of the Cu and Ti in the product was confirmed by the EDX analysis presented in Fig. 9.2. It was shown that, the chemical composition of the product is exclusively composed of Cu and Ti with almost 1:1 ratio.

Efforts have been made to reduce the residual CuO and to achieve pure $CuTiO_3$. In the following sections, I will present different tried approaches, including control the reaction temperature, duration and change of the salt compositions.

9.4.1.2 The effect of reaction temperature

Generally, the reaction temperature and duration determine the final product characteristics. The material transportation rate increase with increasing the temperature. Equal molar ratio samples were reacted at two different reaction temperatures of 805 and 850ºC with duration of 4 days. The X-ray diffraction (XRD) patterns of the CTO products are shown in Fig. 9.6.

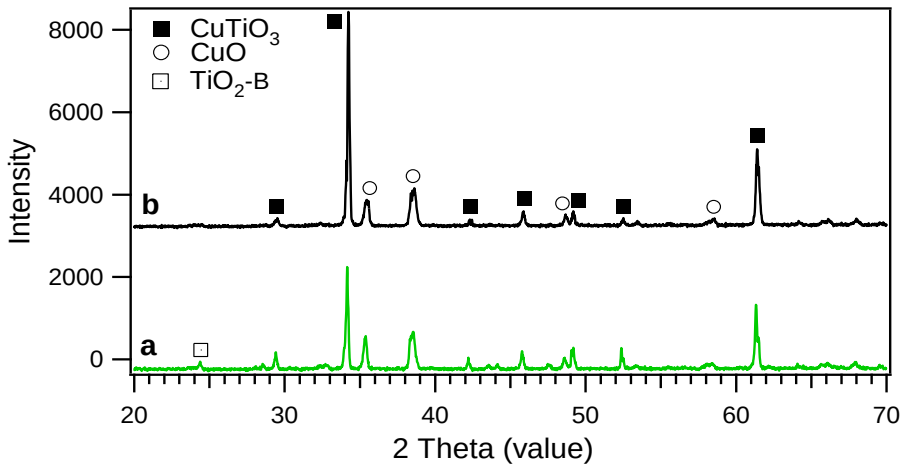

Figure 9.6 XRD pattern of the copper titanate prepared at different annealing temperature. (a) 805ºC and (b) 850ºC for 4 days.

For a low reaction temperature, 805ºC, small amount of TiO_2-B phase together with some residual CuO were detected as impurities. At 805ºC which is just over the melting point of the NaCl, the nobilities and mixing of reactants (TiO_2 and CuO) are lower than that at the higher temperature,850ºC. Therefore, the productivity of the copper titanate is limited. At 850ºC, it is clear that the impurity concentrations decrease. Although there is still some CuO left, no TiO_2 related phase can be observed. Therefore, the reaction is assumed to be complete. The residual CuO could be the result of reaction of TiO_2 with Al_2O_3 of the crucible. Meanwhile the diffraction intensities from CTO also increased significantly relative to the background noise level, which suggests the increased formation of CTO at higher temperature.

Based on the XRD results, the average crystal sizes of the $CuTiO_3$ products was determined according to the Scherrer's equation (Equation 3.2, chapter 3). The measured FWHM of diffraction peak of the copper titanate located at 34.3° related to the samples annealed at 805 and 850ºC are 0.098 and 0.096 respectively. The calculated crystal domain size increased with increasing the reaction temperature, which ranging from 97 nm to 103 nm respectively. These results indicate the increase in the crystal domain size at higher reaction temperature.

9.4.1.3 The effect of the reaction time

The heating duration has also strong effect on the growth products. To investigate the effect of the reaction time on the properties of the product, three copper titanate samples were prepared by combining an equal molar ratio of the starting materials and reacted at 805ºC for different reaction times (ranged from 1 day to 5 days).

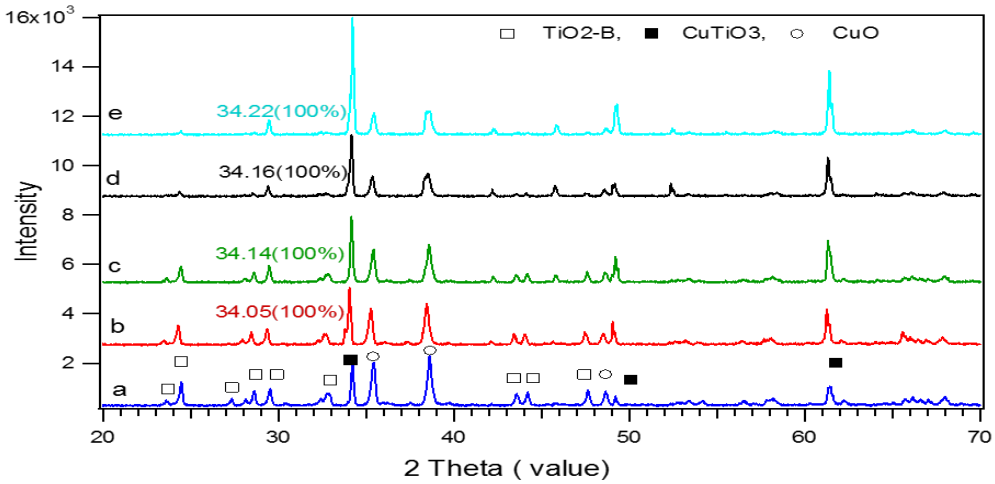

Figure 9.7 The XRD pattern of the copper titanate prepared at 805ºC, different reaction time. (a) 1day, (b) 2days, (c) 3 days, (d) 4 days and (e) 5 days.

The observed XRD spectra of the products are displayed in Fig. 9.7. The diffraction intensities from TiO_2, CTO and CuO were sampled from the diffraction peaks at 24.52, 34.21 and 35.42º, normalised against the background noise level. The measured diffraction intensities are plotted in Fig. 9.8. It is clear that the decreasing of TiO_2 is accompanied by the decrease of CuO and the increase of CTO. However, at low temperature (805ºC), even after 6 days of reaction, residual TiO_2 can still be observed. Therefore, it could be expected that the reaction temperature of 805ºC might be too low for the completion of the reaction.

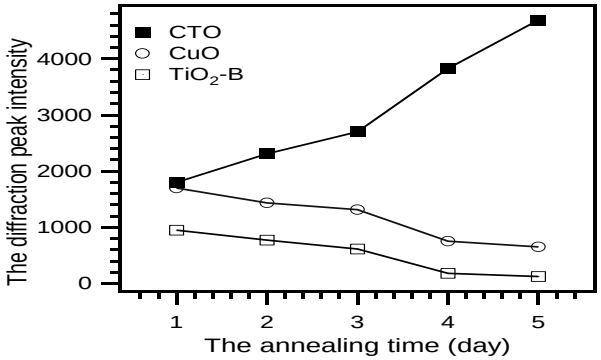

Figure. 9.8 The measured intensities of the diffraction peaks located at 24.52, 34.21 and 35.42º from the TiO_2, CTO and CuO in the samples prepared at 805ºC for different times and as presented in Fig. 9.7.

By increase the reaction temperature, the reaction rate could be increased significantly. Fig. 9.9 shows the XRD spectra of the products reacted at 850ºC as a function of reaction time.

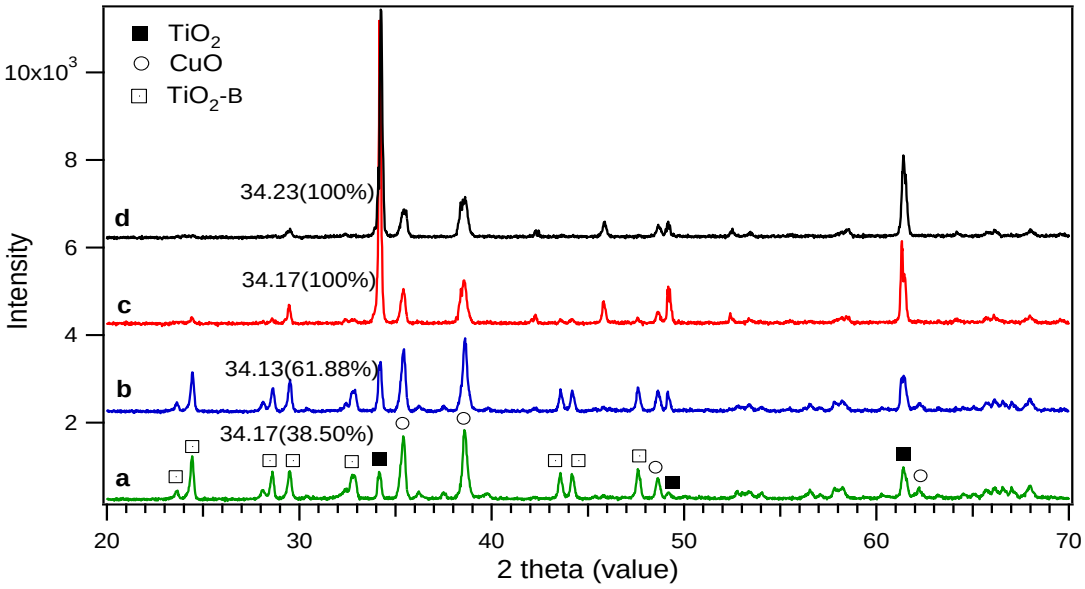

Figure 9.9 The XRD pattern of the copper titanate, at 850ºC, different reaction time. (a) 6 hours, (b) 12 hours, (c) 24 hours and (d) 4 days.

While Fig. 9.10 shows the measured the intensities of the diffraction peaks at 24.52, 34.21 and 35.42º representing TiO_2, CTO and CuO. It seems the reaction is completed within 24 hour of heating as the TiO_2 almost disappeared by then while the CuO reached its minimum. However, after 24 hours, by continuing the reaction for 4 days, the diffraction intensity from the CTO increases slightly, which suggests the improvement in the crystal quality.

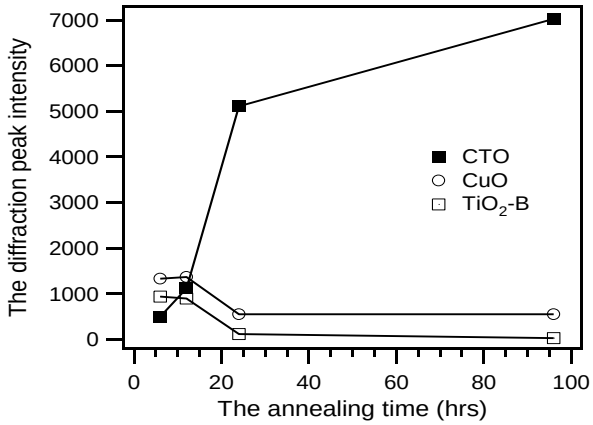

Figure. 9.10 The measured intensities of the diffraction peaks located at 24.52, 34.21 and 35.42º from the TiO_2, CTO and CuO in the samples prepared at 850ºC for different times and as presented in Fig. 9.9.

In summary, copper titanate can be obtained at lower reaction temperature with longer time. At the end of the reaction, TiO_2 disappeared while residual CuO remained.

9.4.1.4 The effect of the salt composition

The melting point of molten salt can affect the composition of the products. The role of the molten salt is used as a flux to facilitate the mass transportation of the reactants by dissolution and precipitation. It helps to increase the contact between the reactant particles and therefore, to increase the reaction rate at reduced reaction temperature.

The effect of the type of salt on the crystal structure, morphology and composition of the product was investigated. Two types of molten salts have been examined, KCl and NaCl with melting points of 770ºC and 801ºC respectively. Equal weight ratio between the reactant mixture and flux salts were used in the MSS. The mixture was heated at 960ºC for 10 hours. The XRD patterns of the products were collected and presented in Fig. 9.11.

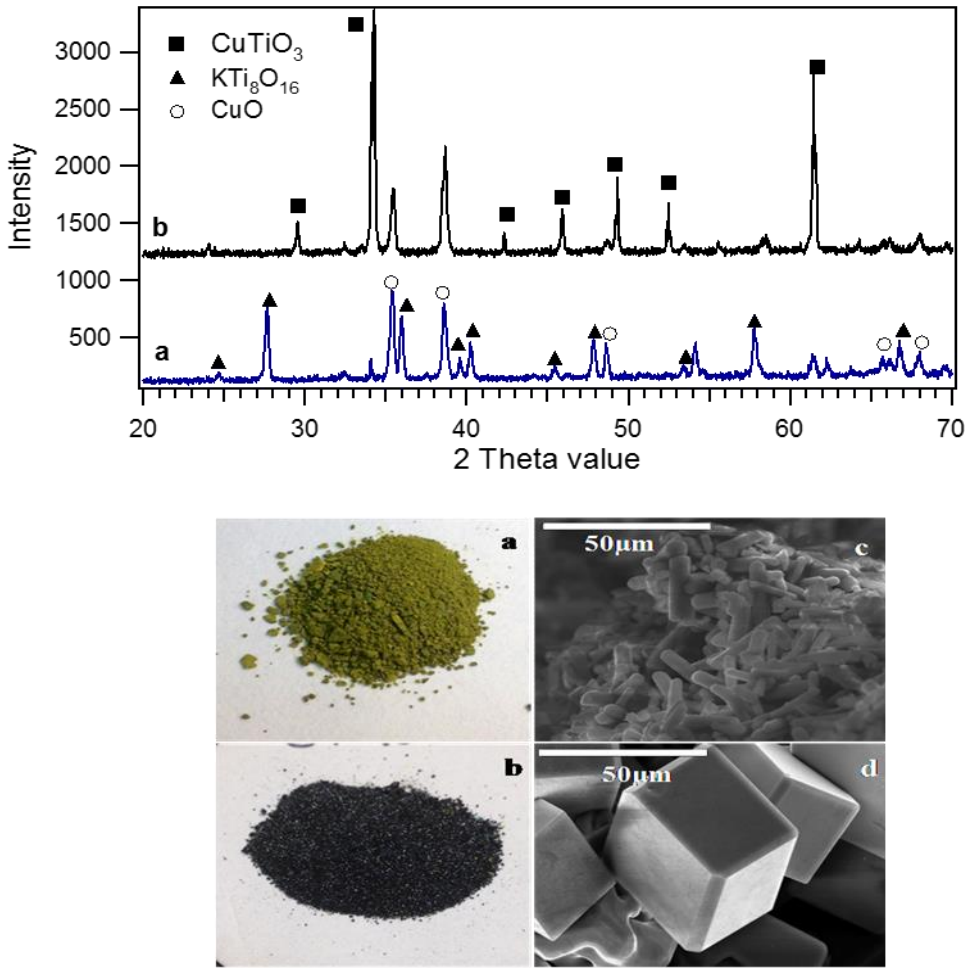

Figure 9.11 The XRD pattern of the copper titanate prepared in different salts, at 960ºC, 10hours. (a) KCl and (b) NaCl. Photographic picture with the typical SEM images of the different products morphology as result of using different molten salt medium, (a and c) KTi_8O_{16} formed in KCl salt and (b and d) $CuTiO_3$ resulted in NaCl salt.

As shown in Fig. 9.11, the type of molten salt has a significant influence on the product composition. Using KCl as the flux salt, the dominant product is the potassium titanate, KTi_8O_{16}, leaving high percentage of CuO as impurity. The XRD peaks positions with the related indexed crystal planes of KTi_8O_{16} are tableted in table 9.2. This is different to the reaction using NaCl as the salt, where the majority of the product is $CuTiO_3$.

Table 9.2 The diffraction peak position and relative intensities of the KTi_8O_{16} product.

Index	2θ (REF)	2θ (EXP)
(220)	24.63 (9.0%)	24.51 (3.6%)
(310)	27.61 (100%)	27.55 (100%)
(211)	36.08 (56.0%)	35.8 (87.0%)
(420)	39.49 (12.0%)	39.42 (20.4%)
(301)	40.32 (35.0%)	40.04 (46.1%)
(510)	45.33 (10.0%)	45.26 (13.33%)
(411)	47.86 (39.0%)	47.63 (51.19%)
(600)	53.96 (24.0%)	53.96 (35.63%)
(521)	57.75 (40.0%)	57.62 (63.53%)
(002)	62.63(8.0%)	62.12 (12.65%)
(611)	63.78 (3.0%)	63.65 (6.9%)
(541)	66.66 (29.0%)	66.6 (43.13%

Photographic pictures with the corresponded SEM images are also presented in Fig. 9.11. The potassium titanate shows a yellow-greenish colour (Fig. 9.11a) and the copper titanite has a dark green colour (Fig. 9.11b). This indicates the role of binary metal oxide in narrowing the band gap of product to almost (2-2.5 eV) and (1-1.2 eV) respectively in comparison with TiO_2 (3~3.2 eV). The SEM images of these products show rod like morphology for the potassium titanate (Fig. 9.11c) in contrast to the typical cubic shape for the copper titante (Fig. 9.11d).

This observation indicates that care must be taken when choose the flux salt. Not only its melting point is the critical factor determines the reaction temperature, but also the ion components of the salt should be relative inert to the reactants and products involved in the MSS synthesis. It is essential to avoid side reactions which lead to by-products.

We have also tried to deposit the $CuTiO_3$ on a metal substrate to form a thin film. It was experimentally tested by using $CuTiO_3$ in interface with TiO_2 nanoparticles film in a DSSCs system. The electrode showed a small cathodic photocurrent. This suggests that the $CuTiO_3$ is a p-type semiconductor. The poor performance of the DSSC could be due

to the difficulty of forming a mechanical stable homogenous thin film, since the crystal size is too large for this purpose. Further experiment will be carried out to overcome this problem.

9.5 Conclusion

An important titanate compound, perovskite single crystal copper titanate, was successfully prepared for the first time with facile molten salt synthesis method. The reaction conditions have a remarkable effect on the product composition, size and morphology. The best conditions for the forming of $CuTiO_3$ with highly defined cubic crystallinity were found to be (1:1) molar ratio of the CuO and TiO_2 with NaCl as a salt. The reaction temperature and time can affect the completion of the synthesis. On the other hand, using KCl as the molten salt, only potassium titanate, $KTi_8O_{16,}$ was formed. The future work will focus on preparing smaller crystal size which could be managed by controlling the cooling process.

Chapter 10 Thesis conclusions and future work

In this thesis, the synthesis and modification of metal oxide nanomaterials with different morphologies, optical and electrical properties were performed for enhancing their applications in the drug delivery and PEC water splitting.

For the first time, TiO_2 nanotubes with unique shape, nanobottles, were created and used as a platform for developing controlled drug delivery system. The bottle shaped nanotube were synthesised through controlling the anodisation parameters and surface passivation with organic thin films. The release kinetic studies indicate that the release kinetic constant is strongly affected by the bottle neck shape, including diameter, length and the polymer coating. The drug agent can be eluted at slower rates by using TiO_2 nanobottles, compared to the nanotubes. Moreover, the release kinetic constants decreased sharply with a decrease in tube diameter and increase in tube lengths. For further release control, a PVA coating is also an important factor to reduce the elution rate constant. The lowest release kinetic constant of 0.23 h^{-1} was achieved by applying a layer of PVA coating on the nanobottles, in contrast to 6.5 h^{-1} from nanotubes. A geometry model was established to quantify the correlation between the release rate constant and the structures of nanotubes and nanobottles.

Rutile TiO_2 nanorods were synthesised and modified for the application in photocatalytic water splitting. The PEC water splitting measurements revealed that the photocatalytic water splitting performances could be significantly influenced by the morphology, electrical and optical properties of the metal oxide films. The efficiency of the pristine TNRs film has optimised through studding the effect of the hydrothermal synthesis conditions. The results indicated that, the photocatalytic performance of the TNRs is mainly affected by their morphology, film thickness and nanorods density. The

highest photoconversion efficiency of 1.6% was achieved by the pristine film with low nanorods density. On the other hand, it was found that with increased film thickness, the density of the nanorods will increase. This leads to the decrease of photoefficiency as the charge recombination was increased.

The reduction and re-oxidation of TNRs could improve the photoconversion efficiency up to 1.9%. In this film, pristine TNRs film was reduced in hydrogen atmosphere at 350°C for 30 minutes and re-oxidised in air at 300°C for 90 minutes. This treatment process results the formation of a sandwiched, three layered structure. In this structure, the residual reduced layer was left in the middle layer between the untreated TiO_2 core and the re-oxidised shell. The reduced layer serves as the electron conductor.

The highest photoconversion efficiency of 2.1% was achieved by copper doped TNRs photoanode. This sample was prepared by doping TNRs with copper species with molar ratio of 0.8 mol% Cu to TiO_2 through one step-hydrothermal method. The high PEC performance of this sample may be attributed to the improved charge separation and transportation, reduced band gap, low nanorods density and reduced nanorod diameter.

To improve the PEC performance, high quality glass rods, which could be considered as a light wave guided, were used to design a 3-D electrode with ZnO nanorods as the photocatalyst deposited on the conductive ITO layer. The optical quality of the glass rods is important to minimise the internal light loss and leave most of the light side emitted to excite the coated ZnO semiconductor. This design is aimed to improve the photon trapping, light absorption and charge transportation. The termination of the glass rod substrate and surface treatment was also investigated, which shows a significant increase in photocurrent with rough surface.

For developing visible light sensitive semiconductors, perovskite copper titanate was synthesised with molten salt synthesis. The synthesis conditions were optimised by

controlling the duration and temperature of the reaction. At mild temperature, a TiO_2-B phase was also formed through the hydroxylation and decomposition of Na_2TiO_3. With higher reaction temperature and longer reaction time, large cubic $CuTiO_3$ was successfully synthesised, in addition to some residual CuO. However, by replace the salt from NaCl to KCl, only KTi_8O_{16}, instead of $CuTiO_3$ was formed.

The future work will be focused on studying the in vivo application of nanobottles in drug delivery. Antibiotics will be loaded into the nanobottles with the outside coated with proteins to recognise the bacteria. More intelligent encapsulating materials, such as metal and magnetic loaded polymers, will be developed. Such composite materials can be heated through coupling with external electromagnetic field to decompose or dissolute the polymer cap and achieving a better controlled drug release.

TNRs and 3-D photoelectrode can also be used for solar cells. For further increase in the photoconversion efficiency, the TNRs film will be used as template for developing porous composite nanomaterials with small band gaps. The created heterojunctions at interfaces, which will increase the charge separation, reduce electron-hole recombination rate and also enhance the photon absorption. Different shapes of the glass rods will be tested as the substrates for 3-D electrodes. Sheet glass, cone shaped rods or even spiral rods will be tested with potential of improving the light travelling pathways. Doped ZnO or TiO_2 will be deposited on the 3-D electrode to improving the visible light absorption. Variety of transition metal titanate will be synthesised and their photoelectrochemical performance will be investigated. Although such materials might not have the correct band edge positions for water splitting, their performance in solar cell will not be restricted. It is also expected that $CuTiO_3$ will be a p-type semiconductor. This was demonstrated experimentally by using $CuTiO_3$ in interface with TiO_2 nanoparticles film in DSSCs system. The electrode showed cathodic photocurrent, although it was not

presented in this thesis because the photocurrent was very small. Therefore, a p-n junction could be formed by depositing $CuTiO_3$ on TiO_2 nanorods. The formation of such junction will help to facilitate the charge separation due to the electrical field at the interface. Meanwhile such junction will help for broadening the absorption of light in a wider wavelength.

References

1. J. L. G. Fierro, *Metal Oxides Chemistry and Applications*, CRC Press, Florida, 2005.
2. V. E. Henrich and P. A. Cox, *The Surface Science of Metal Oxides*, University Press, Cambridge, 1994.
3. M. Ohkubo, K. Fukai, M. Kohji, N. Iwata and H. Yamamoto, *Supercond. Sci. Technol.*, 2002, **15**, 1778-1780.
4. B. G. Yacobi, *Semiconductor Materials: An Introduction to Basic Principles*, Kluwer, New York, 2003.
5. L. Manchanda, M. L. Green, v. Dover, M. D. Morris, A. Kerber, Y. Hu, J.-P. Han, P. J. Silverman, T. W. Sorsch, G. Weber, V. Donnelly, K. Pelhos, F. Klemens, N. A. Ciampa, A. Kornblit, Y. O. Kim, J. E. Bower, D. Barr, E. Ferry, D. Jacobson, H. Schulte, *IEDM Tech*, 2000, 23- 26.
6. S. W. Cheong, *Nat. Mat.*, 2007, **6**, 927-928.
7. J. Meyer, S. Hamwi, M. Kroger, W. Kowalsky, T. Riedl and A. Kahn, *Adv. Mater.*, 2012, **24**, 5408-5427.
8. C. X. Wang, L. W. Yin, L. Y. Zhang, D. Xiang and R. Gao, *Sensors*, 2010, **10**, 2088-2106.
9. J. B. Cao and J. Q. Wu, *Mat. Sci. Eng. R.*, 2011, **71**, 35-52.
10. D. Wang and G. R. Bierwagen, *Prog. Org. Coat.*, 2009, **64**, 327-338.
11. A. Clark, *Ind. Eng. Chem*, 1953, **45**, 1476–1480.
12. M. E. Ali, M. M. Rahman, S. M. Sarkar and S. B. Abd Hamid, *J. Nanomat.*, 2014, 192038.
13. S. Colodrero, A. Mihi, L. Haggman, M. Ocana, G. Boschloo, A. Hagfeldt and H. Miguez, *Adv. Mater.*, 2009, **21**, 764–770.
14. L. M. Chen, Z. R. Hong, G. Li and Y. Yang, *Adv. Mater.*, 2009, **21**, 1434-1449.
15. P. Prene, E. Lancelle-Beltran, C. Boscher, P. Belleville, P. Buvat and C. Sanchez, *Adv. Mater.*, 2006, **18**, 2579–2582.
16. H. J. Snaith and L. Schmidt-Mende, *Adv. Mater.*, 2007, **19**, 3187–3200.
17. M. K. Nazeeruddin, P. Pechy, T. Renouard, S. M. Zakeeruddin, R. Humphry-Baker, P. Comte, P. Liska, L. Cevey, E. Costa, V. Shklover, L. Spiccia, G. B. Deacon, C. A. Bignozzi and M. Gratzel, *J. Am. Chem. Soc.*, 2001, **123**, 1613-1624.
18. M. Gratzel, *J. Photochem. Photobio. C*, 2003, **4**, 145–153.
19. Y. F. Gao, M. Nagai, T. C. Chang and J. J. Shyue, **,.Cryst. Growth Des**2007, **7**, 2467–2471.
20. W. J. E. Beek, M. M. Wienk, M. Kemerink, X. N. Yang and R. A. J. Janssen, *J. Phys. Chem. B*, 2005, **109**, 9505-9516.
21. J. Tornow and K. Schwarzburg, *J. Phys. Chem. C*, 2007, **111**, 8692-8698.

22. D. C. Olson, Y. J. Lee, M. S. White, N. Kopidakis, S. E. Shaheen, D. S. Ginley, J. A. Voigt and J. W. P. Hsu, *J. Phys. Chem. C*, 2008, **112**, 9544-9547.

23. E. Galoppini, J. Rochford, H. H. Chen, G. Saraf, Y. C. Lu, A. Hagfeldt and G. Boschloo, *J. Phys. Chem. B,*, 2006, **110**, 16159-16161.

24. C. W. Huang, C. H. Liao and J. C. S. Wu, *JOCET*, 2013, 1.

25. D. Chauhan, V. R. Satsangi, S. Dass and R. Shrivastav, *Bull. Mater. Sci.*, 2006, **29**, 709–716.

26. K. Sun, K. Madsen, P. Andersen, W. N. Bao, Z. L. Sun and D. L. Wang, *Nanotech.*, 2012, **23**, 194013-194013.

27. K. Maeda, D. Lu and K. Domen, *Chem. Eur. J.*, 2013, **19**, 4986 – 4991.

28. R. Dom, L. R. Baby, H. G. Kim and P. H. Borse, *Int. J. Photoenergy*, 2013, 928321.

29. P. Poizot, S. Laruelle, S. Grugeon, L. Dupont and J. M. Tarascon, *Nature*, 2000, **407**, 496-499.

30. J. S. Im, S. J. Park, T. Kim and Y. S. Lee, *Int. J. Hydrogen Energy*, 2009, **34**, 3382 – 3388.

31. Z. P. Guo, L. Yuan, K. Konstantinov, Z. G. Huang and H. K. Liu, *Mater. Lett.*, 2006, **60**, 3891–3894.

32. S. Ramachandran, J. H. Ha and D. K. Kim, *Catal. Commun.*, 2007, **8**, 1934–1938.

33. P. Poizot, S. Laruelle, S. Grugeon, L. Dupont and J. M. Tarascon, *Nature*, 2000, **407**, 496-499.

34. H. M. Chen, R. C. MacDonald, S. Y. Li, N. L. Krett, S. T. Rosen and T. V. O'Halloran, *J. Am. Chem. Soc.*, 2006, **128**, 13348-13349.

35. S. I. Stoeva, J. S. Lee, J. E. Smith, S. T. Rosen and C. A. Mirkin, *J. Am. Chem. Soc.*, 2006, **128**, 8378-8379.

36. S. Bae, S. W. Lee and Y. Takemura, *Appl. Phys. Lett.*, 2006, **89**, 2525031-2525033.

37. K. Y. Cheong, J. H. Moon, D. Eom, H. J. Kim, W. Bahng and N. K. Kim, *Electrochem. Solid-State Lett.*, 2007, **10**, H69-H71.

38. A. J. Bard and L. R. Faulkner, *Electrochemical Methods Fundamentals and Applications*, Wiley, New York, 2001.

39. X. Lu, S. Xie, H. Yang, Y. Tong and H. Ji, *Chem. Soc. Rev.*, 2014, **43**, 7581-7593.

40. S. R. Morrison, *Electrochemistry at Semiconductor and Oxidized Metal Electrodes*, Plenum Press, New York, 1980.

41. L. Z. Majjad, PhD Thesis, An-Najah National University, 2005.

42. C. H. Hsu and H. C. Chen, *Nanotechnology*, 2010, **21**, 285603- 285611.

43. N. Al-Dahoudi and M. A. Aegerter, *Thin Solid Films*, 2006, **502**, 193-197.

44. D. Beydoun, R. Amal, G. Low and S. McEvoy, *J. Nanopart. Res.*, 1999, **1**, 439–458.

45. I. S. Cho, Z. Chen, A. Forman, D. R. Kim, P. M. Rao, T. F. Jaramillo and X. Zheng, *Nano Lett.*, 2011, **11**, 4978–4984.

46. B. Liu and E. S. Aydil, *J. Am. Chem. Soc.*, 2009, **131**, 3985–3990.

47. P. R. Solanki, M. K. Patel, A. Kaushik, M. K. Pandey, R. K. Kotnala and B. D. Malhotra, *Electroanalysis*, 2011, **23**, 2699–2708.

48. J. N. Tiwari, R. N. Tiwari and K. S. Kim a, *Prog. Mater Sci.*, 2012, **57**, 724–803.

49. H. K. Yu and J. L. Lee, *Scientific Reports*, 2014, **4**, 6589.

50. S. Rackauskas, A. G. Nasibulin, H. Jiang, Y. Tian, V. I. Kleshch, J. Sainio, E. D. Obraztsova, S. N. Bokova, A. N. Obraztsov and E. I. Kauppinen, *Nanotech.*, 2009, **20**, 165603- 165611.

51. R. Zou, Z. H. Zhang, L. Yu, Q. Tian, Z. Chen and J. Hu, *Chem. Eur. J.*, 2011, **17**, 13912 – 13917.

52. C. Jiang, Y. Han, S. Liu and Z. Zhang, *CrystEngComm*, 2014, **16**, 952-958.

53. A. Elsanousi, N. Elamin, S. Elhouria and A. Abdallaha, *JAIS, ,* 2013, **1**, 39-42.

54. H. L. Cao, X. F. Zhou, C. Zheng and Z. P. Liu, *Appl. Mater. Inter.*, 2015, **7**, 11984-11990.

55. Z. Sun, T. Liao, Y. Dou, S. M. Hwang, M.-S. Park, L. Jiang, J. H. Kim and S. X. Dou, *Nat. Commun.*, 2014, 5.

56. R. M. Hazen, E. S. Grew, R. T. Downs, J. Golden and G. Hystad, *Can. Mineral.*, 2015, **1**, 1-29.

57. A. Fujishima and X. T. Zhang, *Comptes. Rendus. Chimie.*, 2006, **9**, 750–760.

58. A. Fujishima and K. Honda, *Nature*, 1972, **37**, 37-38.

59. A. Linsebigler, G. Lu and T. Y. Yates, *Chem. Rev.*, 1995, **95**, 735-758

60. W. Li, C. Ni, H. Lin, C. P. Huang and S. I. Shah, *J. Appl. Phys.*, 2004, **96**, 6663-6668.

61. S. Sangeetha, S. R. Kathyayini, P. D. Raj, P. Dhivya and M. Sridharan, *International Conference on Advanced Nanomaterials & Emerging Engineering Technologies*, 2013.

62. H. J. Johnston, G. R. Hutchison, F. M. Christensen, S. Peters, S. Hankin and V. Stone, *Part. Fibre Toxicol.*, 2009, **6**, 33.

63. G. Mital, S. and T. Manoj *Phys. Chem.*, 2011, **56**, 1639–1657

64. U. Diebold, *Surf. Sci. Rep.*, 2003, **48**, 53- 229.

65. Y. Ma, X. Wang, Y. Jia, X. B. Chen, H. Han and C. Li, *Chem. Rev.*, 2014, **114**, 9987−10043.

66. C. Shang, W. N. Zhao and Z. P. Liu, *J. Phys.: Condens. Matter*, 2015, **27**, 134203-134211.

67. D. S. Mo and W. Y. Ching, *Phys. Rev. B*, 1995, **51**, 13023

68. H. Tang, K. Prasad, R. Sanjinbs, P. E. Schmid and F. Levy, *J. Appl. Phys.*, 1994, **75**, 2042-2046

69. A. Di Paola, M. Bellardita and L. Palmisano, *Catalysts*, 2013, **3**, 36-73.

70. J. G. Li, T. Ishigaki and X. D. Sun, *J. Phys. Chem. C*, 2007, **111**, 4969-4976.

71. K. Nomenyo, A.-S. Gadallah, S. Kostcheev, D. J. Rogers and G. Lérondel, *Appl. Phys. Lett.*, 2014, **104**, 181104.

72. C. Wurth, M. Grabolle, J. Pauli, M. Spieles and U. Resch-Genger, *Nat. Protocols*, 2013, **8**, 1535-1550.

73. X. Rocquefelte, F. Goubin, H. J. Koo, M. H. Whangbo and S. Jobic, *Inorg. Chem.*, 2004, **43**, 2246-2251.

74. J. Zhang, M. Li, Z. Feng, J. Chen and C. Li, *J. Phys. Chem. B*, 2006, **110**, 927-935.

75. A. K. See and R. A. Bartynski, *J. Vac. Sci. Technol., A*, 1992, 10**,** 2591-2596.

76. M. Scrocco, *Chem. Phys. Lett*, 1979, **61**, 453-456.

77. P. Roy, S. Berger and P. Schmuki, *Angew. Chem. Int. Ed.*, 2011, **50**, 2904 – 2939.

78. Z. Wang, B. Wen, Q. Hao, L. M. Liu, C. Zhou, X. Mao, X. Lang, W. J. Yin, D. Dai, A. Selloni and X. Yang, *J. Am. Chem. Soc*, 2015, **137**, 9146-9152.

79. L. B. Xiong, J. L. Li, B. Yang and Y. Yu, *J. Nanomat.*, 2012, **2012**, 831524.

80. H. Lee, S. Dregia, S. Akbar and M. Alhoshan, *J. Nanomat.*, 2010, **2010**, 503186.

81. W. W. Liu, H. Lu, M. Zhang and M. Guo, *Appl. Surf. Sci.*, 2015, **347**, 214-223.

82. J. J. Wu and C. C. Yu, *J. Phys. Chem. B*, 2004, **108**, 3377-3379.

83. Z. Zhao, J. Tian, Y. Sang, A. Cabot and H. K. Liu, *Adv. Mater*, 2015, **27**, 2557–2582.

84. M. Adachi, Y. Murata, I. Okada and S. Yoshikawa, *J. Electrochem. Soc.*, 2003, **150**, G488-G493.

85. J. Li, H. Qiao, Y. Du, C. Chen, X. Li, J. Cui, D. Kumar and Q. F. Wei, *Scientific World*, 2010, **2012**, 154939.

86. M. I. Dar, A. K. Chandiran, M. Gratzel, M. K. Nazeeruddin and S. A. Shivashankar, *J. Mater. Chem. A*, 2013, **2**, 1662–1667.

87. A. G. Kontos, K. A. I., D. S. Tsoukleris, V. Likodimos, J. Kunze, P. Schmuki and P. Falaras, *Nanotechnology*, 2009, **20**, 45603-45612.

88. G. K. Mor, M. A. Carvalho, O. K. Varghese, M. V. Pishko and C. A. Grimes, *Materials Research Society*, 2003, **19**, 628- 634.

89. J. Y. Huang, K. Q. Zhang and Y. K. Lai, *Int. J. Photoenergy*, **2013**, 2013, 761971.

90. Z. Y. Liu, Q. Q. Zhang, T. Y. Zhao, J. Zhai and L. Jiang, *J. Mater. Chem.*, 2011, **21**, 10354-10358.

91. Z. H. Zhang, M. F. Hossain and T. Takahashi, *Int. J. Hydrogen Energy*, 2010, **35**, 8528-8535.

92. K. Shankar, J. I. Basham, N. K. Allam, O. K. Varghese, G. K. Mor, X. J. Feng, M. Paulose, J. A. Seabold, K. S. Choi and C. A. Grimes, *J. Phys. Chem. C*, 2009, **113**, 6327–6359.

93. K. Zhu, N. R. Neale, A. Miedaner and A. J. Frank, *Nano Lett.*, 2007, **7**, 69-74.

94. G. K. Mor, S. Kim , M. Paulose, O. K. Varghese, K. Shankar, J. Basham and C. A. Grimes, *Nano Lett.*, 2009, **9**, 4250-4257.

95. M. S. Aw, K. Gulati and D. Losic, *J. Biomater. Nanobiotechnol.*, 2011, **2**, 477-484

96. C. Yao and T. J. Webster, *J. Biomater. Nanobiotechnol. B*, 2009, **91**, 587-595.

97. F. Schmidt-Stein, R. Hahn, J. F. Gnichwitz, Y. Y. Song, N. K. Shrestha, A. Hirsch and P. Schmuki, *Electrochem. Commun.*, 2009, **11**, 2077–2080.

98. M. S. Aw, J. Addai-Mensah and D. Losic, *Chem. Commun.*, 2012, **48**, 3348-3350.

99. Y. Song, Y., F. Schmidt-Stein, S. Bauer and P. Schmuki, *J. Am. Chem. Soc.*, 2009, **131**, 4230-4232.

100. J. M. Macak, H. Tsuchiya and P. Schmuki, *Angew. Chem. Int. Ed.*, 2005, **44**, 2100 –2102.

101. M. Zhang, Y. Bando and K. Wada, *National Institute for Research in Inorganic Material*, 2001, **20**, 167 – 170.

102. X. Wu, Q. Jiang, Z., Z. F. Ma, M. Fu and W. F. Shangguanb, *Solid State Commun.*, 2005, **136**, 513–517.

103. K. C. Sun, M. B. Qadir and S. H. Jeong, *RSC Ad*, 2014, **4**, 23223–23230.

104. D. B. Holt and D. C. Joy, *SEM Microcharacterization of semiconductors.*, Academic press limited., London, UK, 1989.

105. M. Wei, H. Zhou, Y. Konish, M. Ichihara, H. Sugihara and H. Arakawa, *Inorg. Chem*, 2006, **45**, 5684−5690.

106. Y. Y. Song, F. Schmidt-Stein, S. Berger and P. Schmuki, *Small*, 2010, **6**, 1180-1184.

107. X. D. Wang, Z. D. Li, J. Shi and Y. H. Yu, *Chem. Rev.*, 2014, **114**, 9346-9384.

108. M. Mohammadi, R., F. Ordikhani, D. Fray and F. Khomamizadeh, *Particuology*, 2011, **9**, 161–169.

109. T. Feng, G. S. Feng, L. Yan and J. H. Pan, *Int. J. Photoenergy*, 2014, **2014**, 563879.

110. W. Wen, J. M. Wu, Y. Z. Jiang, S. L. Yu, J. Q. Bai, M. H. Cao and J. Cui, Sci Rep, 2015, **2015**, 11804.

111. W. Oelerich, Y. Klassen and R. Bormann, *J. Alloys Compd.*, 2001, **315**, 237–242.

112. T. Wang, H. Jiang, L. Wan, Q. Zhao, T. Jiang, B. Wang and S. Wang, *Acta Biomater.*, 2015, **13**, 354–363.

113. P. K. Stoimenov, R. L. Klinger, G. L. Marchin and K. J. Klabunde, *Langmuir*, 2002, **18**, 6679-6686.

114. N. Pinna, G. Neri, M. Antonietti and M. Niederberger, *Angew. Chem. Int. Ed.*, 2004, **43**, 4345-4349.

115. T. Luttrell, S. Halpegamage, J. Tao, A. Kramer, E. Sutter and M. Batzill, *Sci. Rep.*, 2014, **4**, 4043.

116. R. L. Stockbauer, S. Warren, T. K. Johal, S. Patel, D. Holland, A. Taleb and F. Wiame, *Phy. Rev. B*, 2007, **75**, 35105.

117. J. M. Macák, H. Tsuchiya and P. Schmuki, *Angew. Chem. Int. Ed.*, 2005, **44**, 2100-2102.

118. G. H. Li, S. Ciston, Z. V. Saponjic, L. Chen, N. M. Dimitrijevic, T. Rajh and K. A. Gray, *J. Catal.*, 2008, **253**, 105–110.

119. R. R. Bacsa and J. Kiwi, *Appl. Catal. B*, 1998, **16**, 19-29.

120. R. Bickley, T. G. Carreno, J. Lees, L. Palmisano and R. J. D. Tilley, *J. Solid State Chem.*, 1991, **92**, 178-190

121. D. Hurum, C., A. G. Agrios, K. A. Gray, T. Rajh and M. C. Thurnauer, *J. Phys. Chem. B*, 2003, **107**, 4545-4549.

122. R. Asahi, T. Morikawa, T. Ohwaki, K. Aoki and Y. Taga, *Science*, 2001, **293**, 269-271.

123. R. Abe, *J. Photochem. Photobiol. C*, 2010, **11**, 179–209.

124. M. G. Walter, E. L. Warren, J. R. McKone, S. W. Boettcher, Q. X. Mi, E. A. Santori and N. S. Lewis, *Chem. Rev.*, 2010, **110**, 6446-6473.

125. P. Pongwan, B. Inceesungvorn, K. Wetchakun, S. Phanichphant and N. Wetchakun, *Engin. J.*, 2012, **16**, 1.

126. S. Liu, Z. Min, D. Hu and Y. Liu *International Conference on Material and Environmental Engineering*, 2014.

127. L. Yu, X. Yang, J. He, Y. He and D. Wang, *Sep. Purif. Technol.*, 2015, **144**, 107-113.

128. L. C. Chen, C. M. Huang, M. C. Hsiao and F. R. Tsai, *Chem. Eng. J.*, 2010, **165**, 482-489.

129. W. Choi, A. Termin and M. R. Hoffmann, *Angen. Chem. Int. Ed. Engl.*, 1994, **33**, 1091-1092.

130. X. B. Chen, L. Liu, P. Y. Yu and S. S. Mao, *Science*, 2011, **331**, 746- 749.

131. G. M. Wang, H. Y. Wang, Y. C. Ling, Y. C. Tang, X. Y. Yang, R. C. Fitzmorris, C. C. Wang, J. Z. Zhang and Y. Li, *Nano Lett.*, 2011, **11**, 3026–3033.

132. A. A. Nada, M. H. Barakat, H. A. Hamed, N. R. Mohamed and T. N. Veziroglu, *Int. J. Hydrogen Energy*, 2005, **30**, 687 – 691.

133. F. Su, J. Lu, Y. Tian, X. Ma and J. Gong, *Phys.Chem. Chem. Phys.*,, 2013, **15**, 12026-12032.

134. P. S. Shinde, G. H. Go and W. J. Lee, *Int. J. Energy Res.*, 2013, **37**, 323–330.

135. D. M. Symes and L. Cronin, *Nat. Chem.*, 2013, **5**, 403-409.

136. W. Yue, W. JiHuai, L. Zhang, X. YaoMing, L. QingBei, P. FuGuo, L. JianMing and H. MiaoLiang, *Chinese Sci. Bull.*, 2011, **56**, 2649-2653.

137. K. Srinivas, *J. Nanosci. Nanotechnol.*, 2014, **2**, 32-39

138. Y. Y. Song, P. Roy, I. Paramasivam and P. Schmuki, *Angew. Chem.*, 2010, **122**, 361 –364.

139. K. N. Shrestha, J. M. Macak, F. S. Stein, R. Hahn, C. T. Mierke, B. Fabry and P. Schmuki, *Angew. Chem.*, **2008**, 120, 1-3.

140. Y. Y. Song, F. S. Stein, S. Bauer and P. Schmuki, *J. Am. Chem. Soc*, 2009, **131**, 4230–4232.

141. L. Peng, A. D. Mendelsohn, T. J. LaTempa, S. Yoriya, C. A. Grimes and T. A. Desai, *Nano Lett.*, 2009, **9**, 1932-1936.

142. O. K. Varghese, D. Gong, M. Paulose, K. G. Ong and C. A. Grimes, *Sens. Actuators B Chem.*, 2003, **93**, 338–344.

143. J. Chen and C. S. Poon, *Building and Environment*, 2009, **44**, 1899–1906.

144. A. Fujishima and T. N. Rao, *Pure Appl. Chem.*, 1998, **70**, 2177-2187.

145. Y. Ren, Z. Liu, F. Pourpoint, A. R. Armstrong, C. P. Grey and P. G. Bruce, *Angew. Chem. Int. Ed.*, 2012, **51**, 2164 –2167.

146. M. Zhi, C. Xiang, M. Li and N. Wu, *Nanoscale*, 2013, **5**, 72–88.

147. Y. G. Guo, Y. S. Hu, W. Sigle and J. Maier, *Adv. Mater*, 2007, **19**, 2087–2091.

148. H. Uchiyama, E. Hosono, H. Zhou and H. Imai, *Solid State Ionics*, 2009, **180**, 956–960.

149. J. H. Lee, M. H. Hon and Y. W. Chung, *Appl. Phys. A*, 2011, **102**, 545–550.

150. X. Su, Q. L. Wu, X. Zhan, J. Wu, S. Wei and J. Guo, *J. Mater. Sci.*, 2010, **47**, 2519–2534.

151. A. Kolodziejczak-Radzimska and T. Jesionowski, *Materials*, 2014, **7**, 2833-2881.

152. U. Ozgur, Y. I. Alivov, C. Liu, A. Teke, M. A. Reshchikov, S. Dogan, V. Avrutin, S. J. Cho and H. Morkoc, *J. Appl. Phys.*, 2005, **98**, 41301.

153. Y. Zhang, T. R. Nayak, H. Hong and W. Cai, *Cur. Mol. Med.*, 2013, **13**, 1633-1645.

154. C. Tian, Q. Zhang, A. Wu, M. Jiang, Z. Liang, B. Jiang and H. Fu, *Chem. Commun*, 2012, **48**, 2858–2860.

155. Q. F. Zhang, C. S. Dandeneau, X. Y. Zhou and G. Z. Cao, *Adv. Mater.*, 2009, **21**, 4087-4108.

156. C. Bauer, G. Boschloo, E. Mukhtar and A. Hagfeldt, *J. Phys. Chem. B*, 2001, **105**, 5585-5588.

157. F. C. S. Paschoalino, M. P. Paschoalino, E. Jordão and W. F. Jardim, *Open J. Phys. Chem.*, 2012, **2**, 135-140.

158. M. Skompska and K. Zarebska, *Electrochim. Acta*, 2014, **127**, 467–488.

159. Z. L. Wang, *Mat. Sci. Eng. R.*, 2009, **64**, 33-71.

160. S. S. Kumar, P. Venkateswarlu, V. R. Rao and G. N. Rao, *Int. Nano Lett.*, 2013, **3**, 46.

161. Y. Zhang, J. Chung, J. Lee, J. Myoung and S. Lim, *J. Phys. Chem. Solids*, 2011, **72**, 1548–1553.

162. Z. Chen, X. X. Li, G. P. Du, N. Chen and A. Y. M. Suen, *J. Lumin.*, 2011, **131**, 2072-2077.

163. D. Banerjee, J. Y. Lao, D. Z. Wang, J. Y. Huang, Z. F. Ren, D. Steeves, B. Kimball and M. Sennett, *Appl. Phys. Lett.*, 2003, **83**, 2061-2063.

164. Y. B. Hahn, *Korean J. Chem. Eng.*, 2011, **28**, 1797-1813.

165. R. Wahab, S. G. Ansari, Y. S. Kim, H. K. Seo and H. S. Shin, *Appl. Surf. Sci.*, 2007, **253**, 7622–7626.

166. X. Y. Kong, Y. Ding, R. Yang and Z. L. Wang, *Science*, 2004, **303**, 1348-1351.

167. J. J. Wu, S. C. Liu, C. T. Wu, K. H. Chen and L. C. Chen, *Appl. Phys. Lett.*, 2002, **81**, 1312-1314.

168. W. J. Chen, W. L. Liu, S. H. Hsieh and T. K. Tsai, *Appl. Surf. Sci.*, 2007, **253**, 6749–6753.

169. Y. Huang and J. He, *J. Mater. Sci.*, 2006, **41**, 3057-3062.

170. B. Nikoobakht, X. Wang, A. Herzing and J. Shi, *Chem. Soc. Rev.*, 2013, **42**, 342--365.

171. T. F. Xu, P. F. Ji, M. He and J. Y. Li, *J. Nanomater.*, 2012, **2012**, 797935.

172. W. S. Chiu, P. S. Khiew, M. Cloke, D. Isa, T. K. Tan, S. Radiman, R. Abd-Shukor, M. A. Abd. Hamid, N. M. Huang, H. N. Lim and C. H. Chiang, *Chem. Eng. J.*, 2010, **158**, 345–352.

173. X. Liu, X. Wu, H. i. Cao and R. P. H. Chang, *J. Appl. Phys.*, 2004, **95**, 3141-3147.

174. N. Zhang, R. Yi, R. Shi, G. Gao, G. Chen and X. Liu, *Mater. Lett.*, 2009, **63**, 496-499.

175. F. Q. He and Y. P. Zhao, *Appl. Phys. Lett.*, 2006, **88**, 193113.

176. L. N. Protasova, E. V. Rebrov, K. L. Choy, S. Y. Pung, V. Engels, M. Cabaj, A. E. H. Wheatley and J. C. Schouten, *Catal. Sci. Technol.*, 2011, **1**, 768–777.

177. G. Cao and Y. Wang, *Nanostructures and Nanomaterials: Synthesis, Properties, and Applications*, World Scientific Series, World Scientific, Singapore, 2011.

178. M. Niederberger and N. Pinna, *Metal Oxide Nanoparticles in Organic Solvents: Synthesis, Formation, Assembly and Application*, Springer, New York, 2009.

179. J. N. Lalena and D. A. Cleary, *Inorganic Materials Synthesis and Fabrication*, Wiley, New Jersey, 2008.

180. W. H. Zhong, B. Li, R. G. Maguire, V. G. Dang, J. A. Shatkin, G. M. Gross and M. C. Richey, *Nanoscience and Nanomaterials: Synthesis, Manufacturing and Industry Impacts*, Destech Publications Inc, Pennsylvania, 2012.

181. P. Yang, K. Wang, Z. Liang, W. Mai, C. X. Wang, W. Xie, P. Liu, L. Zhang, X. Cai, S. Tan and J. Song, *Nanoscale Materials in Chemistry : Environmental Applications*, 2012, 4, 5755–5760.

182. M. He, H. Jiu, Y. Liu, Y. Tian, D. Li, Y. Sun and G. Zhao, *Mater. Lett.*, 2013, **92**, 154–156.

183. R. Zhang, X. Yang, D. Zhang, J. Qin, C. Lu, H. Ding, X. Yan, H. Tang, M. Wang and Q. Zhang, *Cryst. Res. Technol*, 2011, **46**, 1189 – 1194.

184. K. Govatsi and S. K. Yannopoulos, *Proceedings of the Advanced Architectures in Photonics* 2014, **1**, 22-26.

185. L. L. Yang, Q. X. Zhao and M. Willander, *J. Alloys Compd.*, 2009, **469**, 623–629.

186. A. P. Larios, R. Lopez, A. H. Gordillo, F. Tzompantzi, R. Gómez and L. T. Guerra, *Fuel*, 2012, **100**, 139–143.

187. Z. Zheng, PhD Thesis, Queensland University of Technology, 2009.

188. P. Saravanan, R. Gopalan and V. Chandrasekaran, *Def. Sci. J.*,, 2008, **58**, 504-516.

189. M. M. Lohrengel, *Mat. Sci. Eng. R.*, 1993, **11**, 243-294

190. Y. T. Sul, C. B. Johansson, Y. Jeong and T. Albrektsson, *Med. Eng. Phys.*, 2001, **23**, 329–346.

191. L. V. Taveira, J. M. Macak, H. Tsuchiya, L. F. P. Dick and P. Schmuki, *J. Electrochem. Soc.*, 2005, **152**, B405-B410.

192. S. Joseph, T. M. David, C. Ramesh and P. Sagayara, *Int. J. Sci. Eng. R.*, 2014, **5**, 85- 90.

193. J. Wang and Z. Q. Lin, *J. Phys. Chem. C*, 2009, **113**, 4026-4030.

194. K. Shankar, G. K. Mor, H. E. Prakasam, S. Yoriya, M. Paulose, O. K. Varghese and C. A. Grimes, *Nanotech.*, 2007, **18**, 11.

195. A. Ghicov and P. Schmuki, *Chem. Commun.*, 2009, **20**, 2791-2808.

196. Z. Liu, X. Zhang, S. Nishimoto, M. Jin, D. A. Tryk, T. Murakami and A. Fujishima, *J. Phy. Chem. C*, 2008, **112**, 253-259.

197. V. Zwilling, E. Darque-Ceretti, A. Boutry-Forveille, D. David, M. Y. Perrin and M. Aucouturier, *Surf. Interface Anal.*, 1999, **27**, 629-637.

198. K. S. Raja, M. Misra and K. Paramguru, *Electrochim. Acta*, 2005, **51**, 154–165.

199. K. Nakayama, T. Kubo and N. Nishikitania, *Electrochem. Solid-State Lett.*, 2008, **11**, C23-C26.

200. K. Byrappa and T. Adschiri, *Prog. Cryst. Growth Charact. Mater.*, 2007, **53**, 117-166.

201. A. Rabenau, *Angew. Chem. Int. Ed. Engl*, 1985, **24**, 1026-1040

202. K. Yanagisawa and J. Ovenstone, *J. Phys. Chem. B*, 1999, **103**, 7781-7787.

203. M. Yoshimura and K. Byrappa, *J. Mater. Sci.*, 2008, **43**, 2085–2103.

204. K. Shimomura, T. Tsurumi, Y. Ohba and M. Daimon, *Jpn J. Appl. Phys.*, 1991, **30**, 2174-2177.

205. Q. Yang, Z. Lu, J. Liu, X. Lei, Z. Chang, L. Luo and X. Sun, *Prog Nat Sci: Mat Int*, 2013, **23**, 351.

206. R. S. Kler, PhD Thesis, University of Sussex, 2012.

207. K. Kolincio, K. Gdula, A. Mielewczyk, T. Izdebski and M. Gazda, *Acta Phys. Pol., A*, 2010, **118**, 326-327.

208. Z. Y. Cai, X. R. Xing, L. Li and Y. M. Xu, *J. Alloys Compd.*, 2008, **454**, 466–470.

209. Y. Wang, Y. Wang and F. Wang, *Nanoscale Research Lett.*, 2014, **9**, 197-212.

210. H. I. Hsiang and C. H. Chang, *J. Magn. Magn. Mater.*, 2004, **278**, 218–222.

211. X. Zhu, J. Zhou, M. Jiang, J. Xie, S. X. Liang, S. Li, Z. Liu, J. Z. Zhu and Z. Liu, *J. Am. Ceram. Soc*, 2014, **97**, 2223–2232.

212. M. Knoll, *Aufladepotentiel und Sekundäremission elektronenbestrahlter Körper*, Z Techn Physik, 1935.

213. E. Lee, *Scanning Electron Microscopy and X-ray Microanalysis*, PTR Prentice-Hall, New York, 1993.

214. R. Hirano, S. Iida, T. Amano, T. Terasawa, H. Watanabe, M. Hatakeyama, T. Murakami and K. Terao, *J. Micro. Nanolithogr.*, 2014, **13**, 13009-13009.

215. W. H. Bragg, *The X-ray Spectra Given by Crystals of Sulphur and Quartz*, The Royal Society, Proceedings of the Royal Society of London, 1914.

216. D. F. Swinehart, *J. Chem. Educ.*, 1962, **39**, 333-335.

217. A. A. Tahir, M. A. Ehsan, M. Mazhar, K. G. U. Wijayantha, M. Zeller and A. D. Hunter, *Chem. Mater.*, 2010, **22**, 5084–5092.

218. L. Miao, P. Jin, K. Kaneko, A. Terai, N. N. Gabain and S. Tanemura, *Appl. Surf. Sci.*, 2003, **212**, 255–263.

219. J. Tauc *Amorphous and Liquid Semiconductors*, Plenum, London, 1974.

220. V. Kumar, S. K. Sharma, T. P. Sharma and V. Singh, *Opt. Mater.*, 1999, **12**, 115-119.

221. S. N. Dolia, R. Sharma, M. P. Sharma and N. S. Saxena, *Indian J. Pure Appl. Phys.*, 2006, **22**, 774-776.

222. E. Knoesel, A. Hotzel and M. Wolf, *Phys. Rev. B*, 1998, **57**, 812-812.

223. K. P. S. Parmar, H. Y. Kang, A. Bist, P. Dua, J. S. Jang and J. S. Lee, *ChemSusChem*, 2012, **5**, 1926-1934.

224. X. Yang, A. Wolcott, G. Wang, A. Sobo, R. C. Fitzmorris, F. Qian, J. Z. Zhang and Y. Li, *Nano Lett.*, 2009, 9**,** 2331-2336.

225. R. Saito, Y. Miseki and K. Sayama, *Chem. Commun*, 2012, **48**, 3833–3835.

226. T. Shokuhfar, S. S. Ray, C. Sukotjo and A. L. Yarin, *RSC Adv.*, 2013, **3**, 17380–17386.

227. M. S. Aw, S. Simovic, J. A. Mensah and D. Losic, *J. Mater. Chem. A*, 2011, **21**, 7082–7089.

228. S. A. Bencherif, T. M. Braschler and P. Renaud, *J. Periodontal. Implant Sci.*, 2013, **43**, 251-261.

229. C. Moseke, F. Hage, E. Vorndran and U. Gbureck, *Appl. Surf. Sci.*, 2012, **258**, 5399–5404.

230. H. Han, Y. D. Wang and Y. F. Zheng, *Adv. Mat. Res.*, 2008, **47**, 1438-1441.

231. M. Ma, M. K. Narbat, Y. Hui, S. Lu, C. Ding, D. D. Y. Chen, R. E. W. Hancock and R. Wang, *J. Biomed. Mater. Res. A*, 2012, 278–285.

232. J. M. Macak, H. Tsuchiya, A. Ghicov, K. Yasuda, R. Hahn, S. Bauer and P. Schmuki, *Curr. Opin. Solid State Mater. Sci.*, 2007, **11**, 3–18.

233. H. Jia and L. L. Kerr, *J. Pharm. Sci.*, 2013, **102**, 2341-2348.

234. J. Wang and Z. Lin, *J. Phys. Chem. C*, 2009, **113**, 4026–4030.

235. Z. T. Y. Al-Abdullah, Y. Shin, R. Kler, C. C. Perry, W. Zhou and Q. Chen, *Nanotechnology*, 2010, **21**, 505601-505609.

236. C. Salome, O. Godswill and O. Ikechukwu, *Res. J. Pharm. Biol. Chem. Sci.*, 2013, **4**, 97-103.

237. Z. T. Al-Abdullah, PhD Thesis, University of Sussex, 2012.

238. P. K. Gillman, *Int. J. Obstet. Anesth.*, 2006, **61**, 113.

239. T. Shokuhfar, S. Sinha-Ray, C. Sukotjo and A. L. Yarin, *RSC Adv.*, 2013, **3**, 17380–17386.

240. M. Liu, N. L. Snapp and H. Park, *Chem. Sci.*, 2010, **2**, 80–87.

241. G. K. Mor, K. Shankar, M. Paulose, O. K. Varghese and C. A. Grimes, *Nano Lett.*, 2005, **5**, 191-195.

242. K. Shankar, J. I. Basham, N. K. Allam, O. K. Varghese, G. K. Mor, X. Feng, M. Paulose, J. A. Seabold, K. S. Choi and C. A. Grimes, *J. Phys. Chem. C*, 2009, **113**, 6327–6359.

243. J. L. Giocondi, P. A. Salvador and G. S. Rohrer, *Top. Catal.*, 2007, **44**, 529-533.

244. J. B. Lowekamp and G. S. Rohrer, *J. Phys. Chem. B*, 1998, **102**, 7323-7327.

245. O. I. Micic, Y. Zhang, K. R. Cromack, A. D. Trifunac and M. C. Thurnauer, *J. Phys. Chem. B*, 1993, **97**, 1211-1283.

246. P. Ghosh and A. K. Sharma, *J. Nanomat.*, 2013, **2013**, 9.

247. J. Luo, L. Ma, T. He, C. F. Ng, S. Wang, H. Sun and H. J. Fan, *J. Phys. Chem. C*, 2012, **116**, 11956−11963.

248. A. Kumar, A. R. Madaria and C. Zhou, *J. Phys. Chem. C*, 2010, **114**, 7787–7792.

249. M. Wu, J. Long, A. Huang and Y. Luo, *Langmuir*, 1999, **15**, 8822-8825.

250. M. Wu, G. Lin, D. Chen, G. Wang, D. He, S. Feng and R. Xu, *Chem. Mater.*, 2002, **14**, 1974-1980.

251. B. S. Buyuktas, *Transition Met. Chem.*, 2006, **31**, 786–791.

252. H. Honda, S. K. and Y. Sugahara, *J. Sol-Gel Sci. Technol.*, 2001, **22**, 133–138.

253. A. B. Murphy, P. R. F. Barnes, R. L. K., I. C. Plumb, I. E. Grey, M. D. Horne and J. A. Glasscock, *Int. J. Hydrogen Energy*, 2006, **31**, 1999 – 2017.

254. R. S. Sonawane, B. B. Kale and M. K. Dongare, *Mater. Chem. Phys.*, 2004, **85**, 52–57.

255. L. Xiong, J. Li, B. Yang and Y. Yu, *J. Nanomat.*, 2012, **2012**, 13.

256. J. Strunk, W. C. Vining and A. T. Bell, *J. Phys. Chem. C*, 2010, **114**, 16937–16945.

257. J. Liu, Y. Liu, N. Liu, Y. Ha, X. Zhang, H. Huang, Y. Lifshitz, S. T. Lee, J. Zhong and Z. Kang, *Science*, 2015, **347**, 970-974

258. E. L. Unger, E. T. Hoke, C. D. Bailie, W. H. Nguyen, A. R. Bowring, T. Heumuller, M. G. Christoforo and M. D. McGehee, *Energy Environ.*, 2014, **7**, 3690–3698.

259. W. Tress, N. Marinova, T. Moehl, S. M. Zakeeruddin, M. K. Nazeeruddin and M. Gratzel, *Energy Environ. Sci.*, 2015, **8**, 995–1004

260. B. Choudhury, M. Dey and A. Choudhury, *Int. Nano Lett.*, 2013, **3**, 25.

261. A. G. Santiago, S. A. Mayen, G. T. Delgado and R. C. Perez, *Mater. Sci. Eng., B*, 2010, **174**, 84–87.

262. Y. Hu, X. D. Song, S. Jiang and C. Wei, *Chem. Eng. J.*, 2015, **274**, 102–112.

263. B. Tian, C. Li, F. Gu, H. Jiang, Y. Hu and J. Zhang, *Chem. Eng. J.*, 2009, **151**, 220–227.

264. R. Dholam, N. Patel, A. Santini and A. Miotello, *Int. J. Hydrogen Energy*, 2010, **35**, 9581-9590.

265. M. Ni, M. K. H. Leung, D. Y. C. Leung and K. Sumathy, *Renew. Sust. Energ. Rev.*, 2007, **11**, 401–425.

266. C. C. Chan, C. C. Chang, W. Hsu, C., S. K. Wang and J. Lin, *Chem. Eng. J.*, 2009, **152**, 492–497.

267. S. Xu, A. J. Du, J. Liu, J. Ng and D. D. Sun, *Int. J. Hydrogen Energy*, 2011, **36**, 6560 e6568.

268. O. Kerkez and I. Boz, *J. Phys. Chem. Solids*, 2014, **75**, 611–618.

269. S. Xu, J. Ng, A. J. Du, J. Liu and D. D. Sun, *Int. J. Hydrogen Energy*, 2011, **36**, 6538-6545.

270. M. I. Litter and J. A. Navfo, *J. Photochem. Photobiol. A*, 1996, **98**, 171-181

271. D. Zhang, L. Qian, J. Ma and H. Cheng, *J. Mater. Chem.*, 2002, **12**, 3677–3680.

272. Y. Qian, Q. Chen, Z. Chen, C. Fan and G. Zhou, *J. Mater. Chem.*, 1993, **3**, 203-205

273. M. Wang, F. M. Ren, G. Cai, Y. Liu , S. Shen and L. Guo, *Nano Res.*, 2014, **7**, 353–364.

274. Y. Lei, L. D. Zhang, G. W. Meng, G. H. Li, X. Zhang, Y., C. H. Liang and W. Chen, *Appl. Phys. Lett.*, 2001, **78**, 1125- 1127.

275. H. W. Kim, H. S. Kim, H. G. Na, J. C. Yang and D. Y. Kim, *J. Alloys Compd.*, 2010, **504**, 217–223.

276. J. Rodríguez, F. Paraguay-Delgado, A. López, J. Alarcón and W. Estrada, *Thin Solid Films*, 2010, **519**, 729-735.

277. A. S. Huss, J. E. Rossini, D. J. Ceckanowicz, J. N. Bohnsack, K. R. Mann, W. L. Gladfelter and D. A. Blank, *J. Phys. Chem. C*, 2011, **115**, 2-10.

278. O. Bierwagen, *Semicond. Sci. Technol.*, 2015, **30**, 24001-24017.

279. J. Chandradass, D. S. Bae and K. H. Kim, *Adv. Powder Technol.*, 2011, **22**, 370-374.

280. S. S. Kim , S. Y. Choi, C. G. Park and H. W. Jin, *Thin Solid Films*, 1999, **347**, 155-160.

281. L. Hao, X. Diao, H. Xu, B. Gu and T. Wang, *Appl. Surf. Sci.*, 2008, **254**, 3504–3508.

282. M. D. Benoy, E. M. Mohammed and B. Pradeep, *Brazilian Journal of Physics*, 2009, **39**, 629-632.

283. H. Wagata, N. Ohashi, K. I. Katsumata, H. Segawa, Y. Wada, H. Yoshikawa, S. Ueda, K. Okada and N. Matsushita, *J. Mater. Chem.*, 2012, **22**, 20706–20712.

284. X. Han, K. Han and M. Tao, *J. Electrochem. Soc.*, 2010, **157**, H593-H597.

285. M. Thirumoorthi and J. T. J. Prakash, *J. Asian Ceram. Soc.*, 2016, **4**, 124-132.

286. S. P. Berglund, A. J. E. Rettie, S. Hoang and C. B. Mullins, *Phys. Chem. Chem. Phys.*, 2012, **14**, 7065–7075.

287. X. Chen, S. Shen, L. Guo and S. S. Mao, *Chem. Rev.*, 2010, **110**, 6503–6570.

288. V. Kumar, S. M. Panah, C. C. Tan, T. K. S. Wong and D. Z. Chi, *International Nanoelectronics Conference (INEC)*, 2013, 443-445.

289. A. G. Pinheiro, G. D. Saraiva, J. M. Filho and A. S. B. Sombra, *Mat. Sci. App.*, 2013, **4**, 549-555.

290. M. Hu, Z, C., G. A. Miller, E. A. Payzant and R. C. J., *J. Mat. Sci.*, 2000, **35**, 2927 – 2936.

291. J. Zeng, J. Lin and K. Li, *Mater. Lett.*, 1999, **38**, 112–115.

292. E. Brzozowski and M. S. Castro, *J. Eur. Ceram. Soc.*, 2000, **20**, 2347-2351.

293. D. Segal, *J. Mater. Chem.*, 1997, **7**, 1297-1305.

294. Z. Cai, X. Xing, L. Li and Y. Xu, *J. Alloys Compd.*, 2008, **454**, 466–470.

295. M. L. Hand, M. C. Stennett and N. C. Hyatt, *J. Eur. Ceram. Soc.*, 2012, **32**, 3211–3219.